

Calcium Carbonate Scale Formation under Multiphase Turbulent Conditions

A Thesis Submitted

By

Loubna A. Mohamed Gargoum

Submitted in accordance with the requirements for the degree of

Doctor of Philosophy

The University of Leeds

School of Mechanical Engineering

December, 2018

The candidate confirms that the work submitted is her own and that appropriate credit has been given where reference has been made to the work of others.

This copy has been supplied on the understanding that it is copyright material and that no quotation from the thesis may be published without proper acknowledgement.

Acknowledgement

I would like to express my sincere gratitude to all those who have contributed to this research work.

A special thanks to Professor Anne Neville for giving me the opportunity to be a researcher in the institute of functional surfaces at the University of Leeds. I am grateful for her guidance, supervision, patience and support. I am also very grateful to Dr Thibaut Charpentier who has been very supportive, motivated and for his always encouragement.

Thanks to the Flow Assurance and Scale Team (FAST) in Heriot Watt University for their financial support and technical contributions in this project.

Thanks also to Libyan ministry of higher education for financial support and Libyan academy for nominating me for this PhD.

Many thanks to the technical and administrative staff who were always available for help and support: Jordan Thomas, Andrew O' Brien, Michael Huggan and Fiona Slade. I would like also to thank Dr. Michael Johnson for FBRM training and help. Dr. Faith Bamiduro for XRD support. Dr. Lorraine Boak and Wendy McEwan from Heriot-Watt University for providing assistance with the ICP analysis.

Thanks also goes to my colleagues and friends; Mohsen for helping me with my first steps in the experiments, Ogbemi for XRD help and for his continuous support, Olujide for advice and support, Ghinwa for training me with the Rheometer, Mohamed Sikiru with the interferometer NPFLEX and Doris for caring.

My deepest appreciation goes to my family; my parents, my brother (Louay) and my sister (Lamyia) for giving me the courage to face all the difficulties to come and commence this study. To my lovely daughters; Arwa and Yasmin, I am sure you would be so proud of your mum!

Finally, I would like to dedicate this work to my father (Ashour Gargoum).

Abstract

Crystallization in multiphase systems is one of the major problems that is encountered during oil processing and oil transporting processes. In the petroleum industry oil and water are produced and transported together and this causes mixing of oil and water which may result in different flow behaviour. This study is concerned with the crystallization of calcium carbonate in oil-in-water emulsions.

The crystallization process is studied by following the kinetics in which different CaCO_3 polymorphic phases are developed on a surface and in the bulk solution using a combination of X-Ray Diffraction and Scanning Electron Microscopy. Kinetic measurements combined with microscopic observations have been monitored with time and found as a useful way for characterizing CaCO_3 scale formation on a surface and in the bulk solution. This new approach enables a better understanding of the different stages of CaCO_3 scale formation in single and multiphase systems. This includes the formation of different polymorphs, the kinetics of growth of each polymorph, the order of polymorphic appearance, the mechanisms of transformation of the metastable phase to the stable one and the prediction of the time required for a complete transformation to a stable phase.

The results suggest the importance of the early period of the crystallization process. This period of time represents the nucleation and the growth of the metastable phase which exhibits simultaneously with the transformation to the stable phase. The solution supersaturation ratio is found to reduce by about 96% during this period.

It is found that the formation of the more stable phase mainly depends on the formation and the transformation of the less stable phase. The results show the existence of an inhibition effect when adding an oil phase to the surface crystallization through retarding both the nucleation and the dissolution processes of the metastable phase. The oil phase impacts the dissolution process by changing the mechanism of transformation from surface-controlled to diffusion-controlled. This affects the kinetics of formation of the stable phase and results in a reduction in the overall surface deposition.

The inhibition effect has also been shown to take place in the bulk solution where less nucleation has been detected for homogeneous type nucleation. At the same time the oil provides an extra surface where heterogeneous nucleation takes place.

The presence of oil was shown to have more impact on surface crystallization kinetics than the bulk precipitation kinetics which showed similar bulk behaviour

between systems with and without oil at 30° C and 60° C. The results suggest the existence of two simultaneous processes for the precipitation kinetics; the first is the rapid dissolution of the metastable phase followed by the re-crystallization to the stable phase according to a surface-controlled mechanism. This process takes place and ceases rapidly. The second process is the slow dissolution of the metastable phase and this is followed by the re-crystallization of the stable phase according to a dissolution-controlled mechanism. This process is very slow and proceeds for a much longer time.

The existence of two processes in the bulk solution compared to only one process for the crystallization on a surface results in much faster kinetics on the surface than in the bulk solution. The results also suggest the similarity in the mechanism of formation and transformation of CaCO_3 scale between surface and bulk solution.

Table of Contents

Calcium Carbonate Scale Formation under Multiphase Turbulent Conditions.....	i
Acknowledgement	ii
Abstract iii	
Table of Contents	v
List of Figures ix	
List of Tables xx	
Nomenclature xxii	
1 Chapter One Introduction.....	1
1.1 Benefits and problems encountered with emulsions.....	3
1.2 Problems encountered with mineral scale formation	5
1.3 Reduction of scale potential	7
1.4 Objectives of the research	8
2 Chapter Two Background on mineral scale formation, theories and literature review;	11
2.1 Introduction.....	11
2.2 Thermodynamics of crystallization	11
2.2.1 CO ₂ -H ₂ O phase equilibria	14
2.2.2 Solute solubility.....	17
2.3 Crystallization process	19
2.4 Nucleation.....	20
2.4.1 Primary nucleation	20
2.4.2 Secondary nucleation	22
2.5 Crystal growth.....	23
2.6 Crystal polymorph.....	26
2.6.1 Polymorphic transformation	30
2.7 Solid-state kinetics	32
2.7.1 Models derivation.....	34
2.7.2 Methods for studying solid-state kinetics for isothermal systems	40
2.8 Bulk precipitation and surface deposition literature review	43

2.9	Mineral scale control strategies.....	47
3	Chapter Three Background on multiphase flow and oil/water emulsions;.....	50
3.1	Introduction.....	50
3.2	Petroleum fractions.....	50
3.3	Multiphase flow system.....	52
	3.3.1 Characterization of multiphase flow with particles.....	54
3.4	Oil/Water emulsions.....	57
	3.4.1 Emulsification process.....	58
	3.4.2 Physical properties of Emulsions.....	59
3.4.2.1	Interfacial tension.....	59
3.5	Emulsions stability.....	68
	3.5.1 Double-layer theory.....	69
	3.5.2 Steric stabilization.....	69
	3.5.3 Stability due to the presence of solids (Pickering stability).....	71
3.6	Emulsions instability.....	73
	3.6.1 Creaming.....	73
	3.6.2 Droplet flocculation.....	74
	3.6.3 Coalescence.....	75
3.7	Crystallization in emulsions.....	76
4	Chapter Four Methodology, materials and procedures of experiments;.....	80
4.1	Introduction.....	80
4.2	Materials used.....	81
	4.2.1 Brine composition.....	81
	4.2.2 Physical properties of the oil phase.....	83
4.3	Surface deposition methodology and experimental details.....	83
	4.3.1 Rotating Cylinder Electrode (RCE) methodology.....	84
	4.3.2 Surface deposition experiment details.....	88
4.4	Bulk precipitation methodology and experimental details.....	91
	4.4.1 Emulsion characterization.....	91
	4.4.2 Particle (crystals) and droplet size distribution.....	93
	4.4.3 Assessment of the precipitation process.....	98

	4.4.4 Characterization of the scale.....	100
5	Chapter Five The kinetics of calcium carbonate surface deposition in water and in oil/water emulsions;.....	103
5.1	Introduction.....	103
5.2	Assessment of surface crystallization process	103
	5.2.1 Mass deposition.....	103
	5.2.2 Mass Growth Rates	105
5.3	Characterization of calcium carbonate scale deposition.....	110
	5.3.1 Analysis of crystals morphology using SEM.....	110
	5.3.2 Characterization of CaCO ₃ scale using XRD.....	125
	5.3.3 Analysis of the polymorphic abundance:.....	126
	5.3.4 Effect of temperature on the polymorphic abundance	138
5.4	Concluding Remarks.....	141
6	Chapter Six The kinetics of the calcium carbonate bulk precipitation crystallization process in water and in oil/water emulsions;.....	142
6.1	Introduction.....	142
6.2	Characterization of oil-saline water systems	142
	6.2.1 Assessment of oil-in-water emulsions using Focused Beam Reflectance Measurement technique (FBRM).....	142
6.3	Assessment of bulk precipitation process	147
	6.3.1 Turbidity measurements.....	147
	6.3.2 The pH measurements	148
	6.3.3 Calcium concentration in solution.....	150
	6.3.4 Estimation of the de-supersaturation profile and the calcium carbonate produced based on measured pH and calcium concentration	152
	6.3.5 Assessment of the precipitation process using calcium carbonate concentration, pH and de-supersaturation profile	159
	6.3.6 Assessment of calcium carbonate precipitation process using Focused Beam Reflectance Measurement (FBRM) technique..	161
6.4	Characterization of calcium carbonate bulk precipitation.....	175
	6.4.1 Analysis of crystal morphology using SEM.....	175
	6.4.2 Analysis of CaCO ₃ scale using XRD	181
	6.4.3 Analysis of polymorphic abundance.....	183
6.5	Concluding Remarks.....	193

7	Chapter Seven Discussion;.....	194
7.1	Introduction.....	194
	7.1.1 Characterization of oil-water (brine) emulsions	194
	7.1.2 Comparing the pH and the free calcium ions in solution during the precipitation process	201
	7.1.3 The kinetics of CaCO ₃ surface deposition and bulk precipitation	204
	7.1.4 Linking between surface deposition and bulk precipitation	220
8	Chapter Eight Conclusions and future work;.....	226
8.1	Conclusions of the study.....	226
8.2	Suggestions for future research work.....	228
Appendix A-1		244
Appendix A-2		246
Appendix B-1		258
Appendix B-2		261
Appendix C		270
Appendix D		272
Appendix E		273

List of Figures

Figure 1-1 The world's consumption of different sources of energy at different sectors [1]	1
Figure 1-2 The world's consumption of different sources of energy [1].....	2
Figure 1-3 The displacement of oil by water and the entrapped oil in porous media during oil recovery [6].....	4
Figure 1-4 Schematic representation of calcium carbonate precipitation over clay particles adsorbed by asphaltene [11].....	6
Figure 1-5 Blocking of a pipeline due to the growth of mineral scale [12]	6
Figure 1-6 The hypothesis regarding the effect of oil-in-water emulsions on surface deposition	9
Figure 2-1 CO ₂ temperature-pressure phase diagram [24].....	14
Figure 2-2 The distribution of carbonates, bicarbonates and carbonic acids in the bulk solution according to solution pH.....	17
Figure 2-3 Solubility curves for some salts; discontinuity of the lines indicate a phase change [15]	18
Figure 2-4 Solubility curves for two polymorphs	19
Figure 2-5 Interfacial tensions between liquid, crystal and solid surface; the principle of heterogeneous nucleation [32].....	22
Figure 2-6 Growing crystal-solution interface [40].	24
Figure 2-7 Different polymorphs of CaCO ₃ ; (a) CaCO ₃ monohydrate [52], (b) vaterite, (c) aragonite, (d) calcite [53].....	27
Figure 2-8 Effect of temperature on the polymorphic percentage in the bulk solution as taken from [51]	29
Figure 2-9 Effect of pH on the polymorphic percentage in the bulk solution at T =24° C, Ca ²⁺ /CO ₃ ²⁻ =1, (O) vaterite, (Δ) aragonite and () calcite; as taken from [43]....	29
Figure 2-10 The change in the solubility of the different polymorphic crystalline forms of CaCO ₃ with temperature	31

Figure 2-11 The transformation of vaterite to calcite (a) CaCO_3 precipitated using fast mixing Y- nozzle [77], (b) CaCO_3 precipitated by mixing Na_2CO_3 (1M) and CaCl_2 (1M) [69]	32
Figure 2-12 The distribution of energetic sites between (a) homogeneous system, (b) heterogeneous system [79]	33
Figure 2-13 Nuclei growth restrictions; black dots are nucleation sites, shaded areas are growth regions [58]	36
Figure 2-14 The isothermal method for evaluating solid state kinetics, α - time curves [60]	41
Figure 2-15 Model-free method for evaluating solid-state kinetics; (a) activation energy $E_{a\alpha}$ for a specific conversion fraction, the data here plotted for $\alpha = 0.8$, (b) Activation energies at different conversion fractions α [79]	42
Figure 2-16 The change in the deposition rate with (a) pH at different temperatures, (b) SR at temperature of 23°C	45
Figure 3-1 Outline for the chapter content.....	50
Figure 3-2 Oil and water flow patterns in horizontal pipes [108]	53
Figure 3-3 Flow pattern map as detected by Angeli and Hewitt et al. (2000) [105].....	54
Figure 3-4 Flow pattern map as detected by A. Mukhaimer et al. (2015) [107].....	54
Figure 3-5 Coupling between particles and the fluid [114].....	55
Figure 3-6 Classification of flow relative to dispersed phase volume fraction [115]	56
Figure 3-7 Types of oilfield emulsions [121].	58
Figure 3-8 Emulsions formation under shear forces [130].....	59
Figure 3-9 Shear stress, τ , versus shear rate, $\dot{\gamma}$, for different volume fractions of water ϕ in paraffin crude oil emulsion at 20°C [133].....	61
Figure 3-10 Emulsions behaviour under the influence of applying an electrical field [25]	63
Figure 3-11 Steps of image analysis [138]	68
Figure 3-12 Emulsions stabilized according to double layer theory	69
Figure 3-13 Emulsions stabilized by a surfactant according to steric method.....	70
Figure 3-14 Pickering type stability; (Top) contact angle between the oil and water; (bottom) different solid wet-ability by oil and water [14]	72

Figure 3-15 Emulsions instability due to creaming; the particles are separated according to gravity effect [153]	74
Figure 3-16 Emulsions instability due to Flocculation; The droplets aggregate and form a network of connected particles [153].....	75
Figure 3-17 Droplet coalescence; the droplets increase in size upon coalescence and this lead to a complete creaming with time [153].....	75
Figure 4-1 The techniques used for the assessment of surface deposition	80
Figure 4-2 The techniques used for the assessment of bulk precipitation	80
Figure 4-3 Rotating cylinder shaft [175].....	85
Figure 4-4 The development of the boundary layers [176].	86
Figure 4-5 Schematic representation of the experiment setup	90
Figure 4-6 Fluid dynamics inside the stirred tank; (top) before, (bottom) after adding of the baffles	91
Figure 4-7 Schematic representation of FBRM probe [192].....	94
Figure 4-8 Chord length measurements of particles [193].....	94
Figure 4-9 Schematic representation of FBRM experiments	97
Figure 5-1 Surface deposition in (mg/cm ² .hr) for oil-brine emulsion system at 30° C, data collected over 1 hour period.....	104
Figure 5-2 Surface deposition in (mg/cm ² .hr) for oil-brine emulsion system at 60° C, data collected over 1 hour period.....	104
Figure 5-3 Mass gain curve fitting at different time intervals for oil-brine 2 (0.065M) at 30° C.....	106
Figure 5-4 Mass gain curve fitting at different time intervals for oil-brine 1 (0.1M) at 30° C.....	106
Figure 5-5 Mass gain curve fitting at different time intervals for oil-brine 3 (0.045M) at 60° C.....	108
Figure 5-6 Mass gain curve fitting at different time intervals for oil-brine 2 (0.065M) at 60° C.....	108
5-7 SEM images for oil-brine 2 (0.065M) at 30° C; (a) 0%, (b)10%, (c)17%, (d) 23% oil content; right images are higher magnification of the red square area.....	111

Figure 5-8 SEM images for oil-brine 1 (0.01M) at 30° C; (a) 0%, (b)10%, (c)17%, (d) 23% oil content; right images are higher magnification of the red square area	112
Figure 5-9 Surface deposit for oil-brine 2 (0.065M) at 30° C; 0% oil content (a) 10 min, (b) 20 min, (c) 40 min, (d) 60 min; 23% oil content (e) 10 min, (f) 20 min, (g) 40 min, (h) 60 min.....	113
Figure 5-10 Surface deposit for oil-brine 1 (0.1M) at 30° C; 0% oil content (a)10 min, (b) 20 min, (c) 40 min, (d) 60 min; 17% oil content, (e) 10 min, (f) 20 min, (g) 40 min, (h) 60 min.....	114
Figure 5-11 Image analysis show surface coverage for oil-brine 2 (0.065M) at 30° C; 0% oil content (a) 10 min, (b) 20 min, (c) 40 min; 23% oil content (d) 10 min, (e) 20 min, (f) 60 min; magnification of the images X200.....	115
Figure 5-12 Early stages of surface deposition for brine 2 (0.065M) at 30°C; (a) 1 min, (b) 5 min, (c) 10min	118
Figure 5-13 Early stage of surface deposition for 23% oil-brine 2 (0.065M) at 30°C (a) 1 min, (b) 5 min, (c) 10min.....	119
Figure 5-14 The transformation of vaterite to calcite for oil-brine system at 30° C, (a) 10% oil content, sample at minute 40. (b) 23% oil content, sample at minute 60 .	120
Figure 5-15 The transformation of vaterite to calcite; (a) 17% oil-brine 1 (0.1M), rough calcite surface which represent the final stage of the transformation. (b) 23% oil-brine 2 (0.065M), calcite growth where a kink site has appeared on the surface	120
Figure 5-16 Surface deposit for oil-brine 2 (0.065M) at 60° C; (a) 0%, (b) 10%, (c) 17%, (d) 23% (e) 30% oil content.....	121
Figure 5-17 Surface deposit for oil- brine 3 (0.045M) at 60° C; 0% oil content (a) 10 min, (b) 20 min, (c) 40 min, (d) 60 min; 23% oil content (e) 10 min, (f) 20 min, (g) 40 min, (h) 60 min.....	122
Figure 5-18 Calcite occupy a similar surface area with a similar orientation to aragonite after transformation; sample is taken at 60 minutes for 10% oil-brine 2 (0.065M) at 60° C.....	123
Figure 5-19 Early stages of scale deposition for brine 3 (0.045M); (a) 1min, (b) 5min	124
Figure 5-20 Early stages of scale deposition for 23% oil-brine 3 (0.045M); (a) 1min, (b) 5min	124

Figure 5-21 Comparing XRD patterns for oil-brine 2 (0.065M) at 30° C; LHS, 0% oil content; RHS, 23% oil content	125
Figure 5-22 Comparing XRD patterns for oil-brine 1 (0.1M) at 30° C; LHS, 0% oil content; RHS, 17% oil content	126
Figure 5-23 Polymorph abundance on the surface for brine 2 (0.065M) at 30° C ..	128
Figure 5-24 Polymorph abundance on the surface for brine 1 (0.1M) at 30° C	128
Figure 5-25 Polymorph mass gain (mg/cm ²) for brine 2 (0.065M) at 30° C at different times	129
Figure 5-26 Polymorph mass gain (mg/cm ²) for brine 1 (0.1M) at 30° C at different times.....	130
Figure 5-27 Polymorph abundance on the surface for 23% oil-brine 2 (0.065M) at 30° C	131
Figure 5-28 Polymorph abundance on the surface for 17% oil-brine 1 (0.1M) at 30° C.....	131
Figure 5-29 Polymorph mass gain (mg/cm ²) for 23% oil-brine 2 (0.065M) at 30° C	132
Figure 5-30 Polymorph mass gain (mg/cm ²) for 17% oil-brine 1 (0.1M) at 30° C ..	133
Figure 5-31 Polymorph mole% and the total CaCO ₃ mass gain (mg/cm ² .hr) for oil-brine 2 (0.065M) system at 30° C.....	134
Figure 5-32 Polymorph abundance on the surface for brine 3 (0.045M) at 60° C ..	135
Figure 5-33 Polymorphic mass gain profile (mg/cm ²) for brine 3 (0.045M) at 60° C	136
Figure 5-34 Polymorph abundance on the surface for 23% oil-brine 3 (0.045M) at 60° C.....	137
Figure 5-35 Polymorphic mass gain (mg/cm ²) for 23% oil-brine 3 (0.045M) at 60° C	137
Figure 5-36 Polymorph mole% and total CaCO ₃ mass gain (mg/cm ² .hr) for different oil content at 60° C; samples at 60 minutes	138
Figure 5-37 Effect of temperature on CaCO ₃ scale deposition morphology in oil-free system; (a) 30° C, (b) 40° C, (c) 50° C, (d), 60° C; samples taken at 60 minutes ..	139

Figure 5-38 Effect of temperature on CaCO ₃ scale deposition morphology in the presence of oil; (a) 30° C, (b) 40° C ,(c) 50° C, (d), 60° C; samples are taken at 60 minutes	139
Figure 5-39 Effect of temperature on the polymorph abundance on the surface in the absence of oil.....	140
Figure 5-40 Effect of temperature on the polymorph abundance on the surface in the presence of 23% oil	140
Figure 6-1 Effect of rotation speed for 23% oil- (0.3M) NaCl solution at 60° C	143
Figure 6-2 Effect of rotation speed for 10% oil- (0.3 M) NaCl solution at 60° C	143
Figure 6-3 Droplet size distribution for oil-(0.3M) NaCl solution at different times, mixing speed of 550 rpm; top, 10% oil content; bottom, 17% oil content	144
Figure 6-4 Frequency curves for 17% oil- (0.3M) NaCl solution, stirred at 550 rpm	145
Figure 6-5 Applying square weight to chord length distribution for different oil contents at 60° C	146
Figure 6-6 Comparing average total number of counts as estimated by applying square- weighted method and droplet density as estimated by square-weighted mean droplet diameter for different oil contents at 60° C	147
Figure 6-7 Turbidity (FAU); (a) brine 2 (0.065M) at 30° C, SR of 115, (b) brine 3 (0.045M) at 60° C, SR of 97, (c) brine 1 (0.1M) at 30° C, SR of 211.....	148
Figure 6-8 The pH profile for oil-brine 2 (0.065M) at 30° C.....	149
Figure 6-9 The pH profile for oil-brine 1 (0.1M) at 30° C.....	149
Figure 6-10 The pH profile for oil-brine 3 (0.045M) at 60° C.....	150
Figure 6-11 The concentration of calcium ions in mg/l for oil-brine 1 (0.1M) at 30° C	151
Figure 6-12 The concentration of calcium ions in mg/l for oil-brine 3 (0.045M) at 60° C.....	151
Figure 6-13 Comparing the amount of calcium carbonate produced as calculated by the reacted calcium ions detected by ICP to the amount produced as calculated by the reacted calcium ions detected from supersaturation dependent on pH for oil-brine 1 at 30° C; (a) 0% oil content, (b) 17% oil content	158

Figure 6-14 Comparing the amount of calcium carbonate produced as calculated by the reacted calcium ions detected by ICP to the amount produced as calculated by the reacted calcium ions detected from supersaturation dependent on pH for oil-brine 3 at 60° C; (a) 0% oil content, (b) 23% oil content	158
Figure 6-15 Comparing the amount of CaCO ₃ formed with the change in supersaturation ratio and pH for oil-brine 1 (0.1M) at 30° C; (a) 0% oil content, (b) 17% oil content	159
Figure 6-16 Comparing the amount of CaCO ₃ formed with the change in supersaturation ratio and pH for oil-brine 2 (0.065M) at 30° C; (a) 0% oil content, (b) 23% oil content	160
Figure 6-17 Comparing the amount of CaCO ₃ formed with the change in supersaturation ratio and pH for oil-brine 3 (0.045M) at 60° C; (a) 0% oil content, (b) 23% oil content	160
Figure 6-18 Chord counts for brine 3 (0.045M) at 30° C, agitated at 550 rpm.....	162
Figure 6-19 Chord counts for 10% oil- brine 3 (0.045M) at 30° C, agitated at 550 rpm	163
Figure 6-20 Chord length distribution (un-weighted) for brine 3 (0.045M) at 30° C	164
Figure 6-21 Chord length distribution (un-weighted) for 10% oil-brine 3 (0.045M) at 30° C.....	165
Figure 6-22 Chord length distribution (un-weighted) for 23% oil-brine 3 (0.045M) at 30° C.....	165
Figure 6-23 Chord length distribution (square-weighted) for 10% oil-brine 3 (0.045M) at 30° C.....	166
Figure 6-24 Chord length distribution (square-weighted) for 23% oil-brine 3 (0.045M) at 30° C.....	167
Figure 6-25 Total chord counts for oil-brine (3) at 30° C; LHS: total counts including oil droplets; RHS: total counts excluding oil droplets	168
Figure 6-26 Crystals chord length counts for brine 3 (0.045M) at 60° C, agitated at 550 rpm	169
Figure 6-27 Change of chord counts with time for 10% oil-brine 3 at 60°C, agitated at 550 rpm	170
Figure 6-28 Chord length distribution for brine 3 (no oil) at 60° C.....	171

Figure 6-29 Chord length distribution for 10% oil-brine 3 (0.045M) at 60° C.....	171
Figure 6-30 Chord length distribution for 17% oil-brine 3 (0.045M) at 60° C.....	172
Figure 6-31 Chord length distribution (square-weighted) for 10% oil-brine 3 (0.045M) at 60° C.....	173
Figure 6-32 Chord length distribution (square-weighted) for 17% oil-brine 3 (0.045M) at 60° C.....	173
Figure 6-33 Total chord counts for oil-brine 3 at 60° C; LHS: total counts including oil droplets; RHS: total counts excluding oil droplets.....	174
Figure 6-34 SEM images for CaCO ₃ bulk precipitate for oil-brine 2 (0.065M) at 30° C; 0% oil content (a) 5 min, (b) 15 min, (c) 30 min, (d) 60 min; 23% oil content (e) 5 min, (f) 15 min, (g) 30 min, (h) 60 min.....	176
Figure 6-35 SEM images for CaCO ₃ bulk precipitate for oil-brine 1 (0.1M); 0% oil (a) 2 min, (b) 5 min, (c) 15 min, (d) 30 min, (e) 45 min, (f) 60 min; 17% oil content, (h) 2 min, (i) 5 min, (j) 15 min, (k) 30 min, (l) 45min, (m) 60 min.....	178
Figure 6-36 The appearance of flat and smooth surface on a side of vaterite in oil-brine systems at 30° C; (a) 23% oil-brine 2 (0.065M) sample at 60 min, (b) 17% oil-brine 1 (0.1 M) sample at 45 min, (c) 17% oil-brine 1 (0.1M) sample at 60 min....	179
Figure 6-37 SEM for oil-brine 3 (0.045M) at 60° C; 0% oil content (a) 2 min, (b) 5 min, (c) 15min, (d) 30 min, (e) 60 min; 23% oil content (f) 2 min, (g) 5 min, (h) 15 min, (i) 30 min, (j) 60 min.....	181
Figure 6-38 XRD patterns for oil-brine 2 (0.065M) at 30° C; LHS, 0% oil content; RHS, 23% oil content.....	182
Figure 6-39 XRD patterns for oil-brine 3 (0.045M) at 60° C; LHS, 0% oil content; RHS, 23% oil content.....	183
Figure 6-40 Polymorph abundance in the bulk solution for brine 2 (0.065M) at 30° C and at different times.....	184
Figure 6-41 Polymorph abundance in the bulk solution for brine 1 (0.1M) at 30° C and at different times.....	185
Figure 6-42 CaCO ₃ polymorph concentrations in (mg/l) for brine 2 (0.065M) at 30° C and at different times.....	186
Figure 6-43 CaCO ₃ polymorph concentrations in (mg/l) for brine 1 (0.1M) at 30° C and at different times.....	187

Figure 6-44 Polymorph abundance in the bulk solution for 23% oil-brine 2 (0.065M) at 30° C and at different times	187
Figure 6-45 Polymorph abundance in the bulk solution for 17% oil-brine 1 (0.1M) at 30° C and different times	188
Figure 6-46 CaCO ₃ polymorph concentration in (mg/l) for 23% oil-brine 2 (0.065M) at 30° C and different times	189
Figure 6-47 CaCO ₃ polymorph concentration in (mg/l) for 17% oil-brine 1 (0.1M) at 60° C and different times	189
Figure 6-48 Polymorph abundance in the bulk solution for 0% oil-brine 3 (0.045M) at 60° C	190
Figure 6-49 CaCO ₃ polymorph concentration in (mg/l) for 0% oil-brine 3 (0.045M) at 60° C and different times	191
Figure 6-50 Polymorph abundance in the bulk solution for 23% oil-brine 3 (0.045M) at 60° C and different times	192
Figure 6-51 CaCO ₃ polymorph concentration in (mg/l) for 23% oil-brine 3 (0.045M) at 60° C and different times	193
Figure 7-1 Comparison of different FBRM weighting methods of chord length distribution for aluminium particles (sieved 45-53 µm) to laser diffraction volume-weighted distribution [191]	196
Figure 7-2 Varied behaviour of the colloidal system is shown when mixing stops; LHS, un-stabilized emulsion layer; RHS, stabilized emulsion layer	199
Figure 7-3 Effect of O/W emulsion on calcium carbonate scaling process at 30° C; (a) the impact of interfacial tension (b) the impact on total number of calcium carbonate crystals in bulk solution at 60 minutes; (c) the impact on mean particle size at 60 minutes	200
Figure 7-4 Comparing the reaction progress for oil-brine 1 at 30° C (0.1M) using two different techniques; LHS: by normal drift of pH during the reaction; RHS: by measuring the amount of unreacted calcium using ICP	202
Figure 7-5 The change in pH during the dissolution process of vaterite at different temperatures [73].....	203
Figure 7-6 Polymorphic thickness versus time for brine 2 (0.065M) at 30° C; (a) calcite and vaterite thickness (µm), (b) curve fitting at an early stage of the crystallization process	205

Figure 7-7 The hypothesis of surface crystallization kinetics for oil-free system at 30° C; Calcite growth controls the transformation process	208
Figure 7-8 Polymorphic thickness versus time for 23% oil-brine 2 (0.065M) at 30° C; (a) calcite and vaterite thickness (μm), (b) the slope of curves at an early stage of the crystallization process	209
Figure 7-9 The hypothesis of surface crystallization kinetics for oil systems at 30° C; vaterite dissolution controls the transformation process	211
Figure 7-10 (a) The change in the ionic activity product with time at 25° C; (I) unstable stage, (II) metastable stage, (III) Stable stage; (b) The change in polymorphic abundance with time; (1) amorphous phase, (2) vaterite, (3) calcite [202]	212
Figure 7-11 The hypothesis of formation and transformation of CaCO ₃ in oil-free system which shows the dissolution of vaterite to calcite according to growth-control mechanism (process 1).....	213
Figure 7-12 The hypothesis of formation and transformation of CaCO ₃ in oil-free system which shows the growth of vaterite and the crystallization of calcite at surface of vaterite according to dissolution-control mechanism (process 2)	214
Figure 7-13 Comparing the total amount of CaCO ₃ produced for oil-brine 1 at 30° C	215
Figure 7-14 The hypothesis of formation and transformation of CaCO ₃ in the presence of oil which shows the existence of three processes simultaneously; S _o and S _c denotes the surface area for an oil droplet and a crystal, respectively.....	216
Figure 7-15 Comparing deposition and precipitation polymorphic abundance for brine 2 (0.065M) at 30° C; (a) on a surface, (b) in the bulk solution.....	221
Figure 7-16 Comparing deposition and precipitation polymorphic abundance for brine 1 (0.1M) at 30° C; (a) on a surface, (b) in the bulk solution.....	221
Figure 7-17 Comparing deposition and precipitation polymorphic abundance for oil-brine 2 (0.065M) at 30° C; (a) on a surface, (b) in the bulk solution.....	222
Figure 7-18 Comparing deposition and precipitation polymorphic abundance for oil-brine 1 (0.1M) at 30° C; (a) on a surface, (b) in the bulk solution.....	222
Figure 7-19 Comparing the polymorphic growth for 23% oil-brine 2 (0.065M) at 30° C; (a) on a surface, (b) in the bulk solution.....	223

Figure 7-20 Comparing the polymorphic growth for 17% oil-brine 1 (0.1M) at 30° C; (a) on a surface, (b) in the bulk solution	223
Figure 7-21 Comparing deposition and precipitation polymorph abundance for brine 3 (0.045M) at 60° C; (a) on a surface, (b) in the bulk solution.....	224
Figure 7-22 Comparing deposition and precipitation polymorph abundance for 23% oil-brine 3 (0.045M) at 60° C; (a) on a surface, (b) in the bulk solution	225

List of Tables

Table 2-1 Physical and crystallographic properties of CaCO ₃ polymorphs	28
Table 2-2 Different solid-state reaction models [58]	40
Table 3-1 Surface tensions of some materials and their interfacial tensions relative to water at 20° C [117].....	60
Table 3-2 Summary of some of scale formation studies in the presence of an organic phase.	78
Table 4-1 Brine 1 compounds and compositions.....	81
Table 4-2 Brine 2 compounds and compositions.....	81
Table 4-3 Brine 3 compounds and compositions.....	82
Table 4-4 Brine 4 compounds and compositions.....	82
Table 4-5 Brine 5 compounds and compositions.....	82
Table 4-6 Saturation ratios of the brines at different temperatures	82
Table 4-7 Physical properties of the oil phase [169].....	83
Table 4-8 Physical properties and hydrodynamic conditions at different temperatures.....	90
Table 4-9 Water and oil superficial velocities at different oil content and different temperatures; mixture velocity= 2.72 m/s at 30° C and 3.37 m/s at 60° C	92
Table 5-1 Curve fitting parameters and growth rate constants (mg/cm ² .min) for oil-brine 2 (0.065M) at 30° C.....	107
Table 5-2 Curve fitting parameters and growth rate constants (mg/cm ² .min) for oil-brine 1 (0.1M) at 30° C.....	107
Table 5-3 Curve fitting parameters and growth rate constants (mg/cm ² .min) for oil-brine 3 (0.045M) at 60° C.....	109
Table 5-4 Curve fitting parameters and growth rate constants (mg/cm ² .min) for oil-brine 2 (0.065M) at 60° C.....	109
Table 5-5 Analysis of the scale formed on a surface using image analysis for 0% oil-brine 2 (0.065M) at 30° C	116

Table 5-6 Analysis of the scale formed on a surface using image analysis for 23% oil-brine 2 (0.065M) at 30°	116
Table 6-1 Mean diameter, droplet density and interfacial area for different fractions of saline water- emulsion at 60 °C	145
Table 6-2 The calculation for correcting calcium ion that has reacted to form calcium carbonate for 0% oil-brine 1 (0.1M) at 30° C	154
Table 6-3 The calculation for correcting calcium ion that has reacted to form calcium carbonate for 17% oil-brine 1 (0.1M) at 30° C	155
Table 6-4 The calculation for correcting calcium ion that has reacted to form calcium carbonate for 0% oil-brine 3 (0.045M) at 60° C	156
Table 6-5 The calculation for correcting calcium ion that has reacted to form calcium carbonate for 23% oil-brine 3 (0.045M) at 60° C	157
Table 6-6 The change in precipitate average crystal size (μm) with time for oil-brine 2 (0.065M) system	178
Table 6-7 The change in precipitate average crystal size (μm) with time for oil-brine 1 (0.1M) system	179
Table 7-1 Comparing the difference in the system characteristic as calculated by un-weighted and square-weighted mean droplet diameter	195
Table 7-2 Applying weighting methods to the mean particle size for 10% oil-brine emulsion at 30° C	197
Table 7-3 Applying weighting methods to the mean particle size for 10% oil-brine emulsion at 60° C	200
Table 7-4 The growth profile fitted function for brine 2 (0.065M) at 30° C	205
Table 7-5 The polymorphic growth constants in the early stages of the deposition process for brine 2(0.065M) at 30° C	206
Table 7-6 The growth rate constants at 30 and 40° C and the growth activation energy for oil-free systems	206
Table 7-7 The growth profile fitted function for 23% oil-brine 2 (0.065M) at 30° C	209
Table 7-8 The polymorphic growth constants in the early stages of the deposition process for 23% oil-brine 2(0.065M) at 30° C	209
Table 7-9 The growth rate constants at 30 and 40° C and the growth activation energy for oil systems	210

Nomenclature

Latin letters

A: Aragonite

ACC: Amorphous Calcium Carbonate

a_{CO_2} : Activity of CO₂ in aqueous solution (M)

a_i : Activity of i^{th} ionic species (M)

C: Calcite

C_i : Ionic concentration (mole/l) of i^{th} ionic species

Cs: Molar concentration of surfactant

D: Diffusivity (m²/s)

d_{cyl} : Cylinder diameter (cm)

d_p : Pipe diameter (cm)

E: Eddy kinematic viscosity (m²/s)

E_a : Activation energy (kJ/mol)

F: Rotation per minute (rpm)

f : Friction factor

f_{CO_2} : Fugacity of CO₂ gas

f_j : Frequency of j^{th} channel per second

IS: Ionic strength (mol/l)

K: Boltzmann constant

K_A : Solubility product of aragonite (M²)

K_C : Solubility product of calcite, aragonite and vaterite (M²)

k_d : Mass transfer coefficient for diffusion (cm²/s)

K_H : Henry's law constant

k_r : Mass transfer coefficient (cm²/s)

K_{SP} : Solubility product (M²)

K_V : Solubility product of vaterite (M^2)

K_w : Ionization constant of water.

l_j : Chord length of j^{th} channel (μm)

N_A : Avogadro number

N_j : Number of chord count of j^{th} channel per second

$N_{j,0}$: Raw un-weighted chord count of the j^{th} channel per second (s^{-1})

$N_{j,n}$: Weighted chord count of the j^{th} channel per second ($\mu\text{m}^n \cdot s^{-1}$)

R : Gas constant ($\text{J/mol}\cdot\text{K}$)

r_c : Critical size radius

Re : Reynolds number

Sc : Schmidt number

Sh : Sherwood number

SR : Supersaturation Ratio

T : Temperature (K)

u_{cyl} : Peripheral velocity of RCE (cm/s)

V : Vaterite

v_{ms} : Mixture velocity (cm/s)

v_{os} : Oil superficial velocity (cm/s)

v_{ws} : Water superficial velocity (cm/s)

U_p : Pipe velocity (cm/s)

v : Molecular volume (m^3/mol)

X_A : Mole fraction of aragonite

X_C : Mole fraction of calcite

X_V : Mole fraction of vaterite

x_i : Mole fraction of i^{th} component

Z_+ : Valence of the cations

Z_- : Valence of the anions

Greek letters

α : Conversion fraction

α_o : Oil volume fractions

α_w : Water volume fractions

γ : Interfacial tension (J/m²)

γ : Activity coefficient

γ_{cl} : Interfacial tension between a crystal and a liquid phase (J/m²)

γ_{cs} : Interfacial tension between a crystal and a solid surface (J/m²)

μ : Solution viscosity (g/cm. s)

μ_c : Viscosity of the continuous phase (g/cm. s)

μ_i : Chemical potential of the i^{th} component in the mixture

ΔG_{crit} : Overall critical free energy (J/mol.K)

ΔH_{cryst} : Heat of crystallization (kJ/mol)

ΔH_{dil} : Heat of dilution (kJ/mol)

ΔH_{sol}^{sat} : Heat of solution for saturated solution (kJ/mol)

ΔH_{sol}^{∞} : Heat of solution for infinite dilute solution (kJ/mol)

τ_y : Shear stress at distance y from the wall (N/m²)

θ : Angle of wetting of two systems

ρ : Density (g/cm³)

ρ_d : Density of the dispersed phase (g/cm³)

Γ_s : Surface excess of surfactant (mole/cm²)

1 Chapter One Introduction

Due to the global economic growth, the increase in the world population and the rise in living standards for people worldwide means there has been a sharp rise in demand for consuming energy. Although alternative energy sources such as wind and solar energy have got much attention during the last decade due to being environmentally friendly and this helps to manage the risks of climate change, the world demand for crude oil has stayed at the top. According to ExxonMobil's 2018 outlook for energy demand and supply through 2040 [1], petroleum fluids including oil and natural gas are the most consumed source of energy at the present time and will continue for the next two decades due to the growing demand driven by commercial transportation and chemical industry. Figure 1-1 highlights the global energy request in various sectors; a wide variety of energy types support the need for electricity generation, which is the largest and fastest growing sector. Natural gas demand increased in almost all sectors whereas the world's oil demand is growing to support the fuel supply for transportation and is considered dominant in this sector. Oil resources will continue to provide the largest consumable source of energy followed by natural gas as illustrated in Figure 1-2 where the global crude oil demand was 86.4 million barrels per day in 2010 [2] and has increased to approximately 99 million barrels per day in 2018 [3] with a growth rate of 15%.

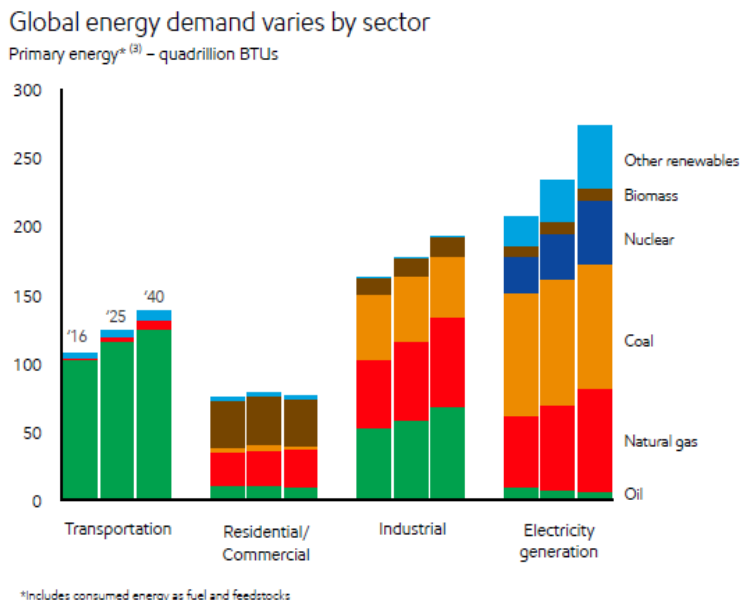


Figure 1-1 The world's consumption of different sources of energy at different sectors [1]

Energy supply evolves to meet diverse demand

Global demand by fuel - quadrillion BTUs

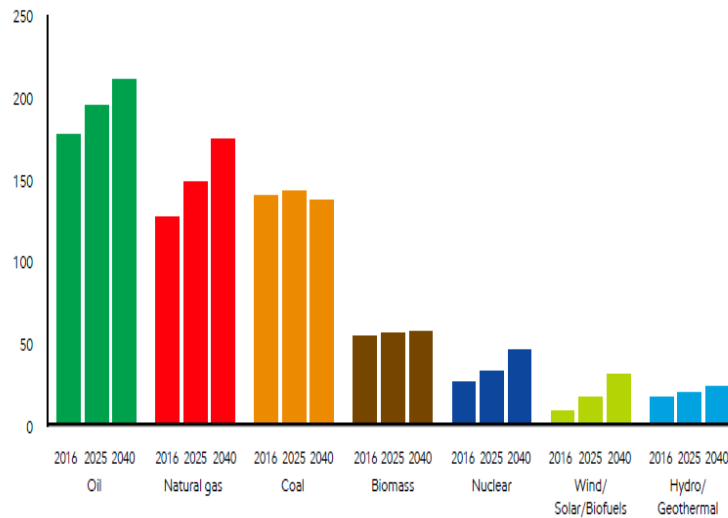


Figure 1-2 The world's consumption of different sources of energy [1]

Oil reserves are an estimate of the amount of crude oil located in a particular region in this world that can be extracted. The ratio of the reserve amount to the production amount is used to predict the number of years an oil reserve will last at a particular production rate. According to British oil annual report 2017 [4], the world oil reserve is 1696.6 billion barrels. This would be sufficient to meet 50.2 years of global production at 2017 levels. The reserve to production ratio can be changed when new technologies that enable extraction of oil emerge and this may extend the life of a reserve. A combination of hydraulic fracturing with horizontal drilling have opened up recently many unconventional resources such as shale oil and gas shale [5]. In addition to the emerging of new Enhanced Oil Recovery (EOR) technologies [6] which enable the extraction of heavy oils but these should be implemented while maintaining economic oil production rates.

The most efficient way for transporting hydrocarbon products to the market is by a network of pipelines. Pipeline transporting of petroleum fluids allows continuous flow, enables the transportation of the products from remote areas and harsh environment, in addition to being economical. The most severe operational problems associated with pipeline transportation are the risks of flowing of multiphase fluids. When water, oil and gas are flowing together, flow assurance problems can occur; formation of hydrates, waxes, asphaltenes and emulsions occurs due to mixing of hydrocarbon fluids with water. Scale and corrosion are issues associated with water.

Mineral scale formation is known as an undesirable phenomenon that is exhibited due to the disturbances in thermodynamics and chemical equilibria of the water

system. This phenomenon may cause many operational problems and it is considered as a costly problem and it is found to occur at different stages and various applications in the oil and gas industry. Moreover, when water is found to flow with crude oils, emulsions may take place. Emulsions are considered desirable in one stage of oil productions and undesirable in the others in which they are known to exhibit serious operating and flow assurance problems.

As the world is expected to rely on oil and gas as primary source of energy for decades to come, commercial operation of this industry is required to determine the long-term technical and economic viability of this technology. Studying the mechanism of scale formation in petroleum industry is more realistic in the presence of oil than in the single water phase as oil and water are accompanied together in the different stages of production and processing. This would impact the identifying, quantifying, and mitigating of the flow assurance risks associated with scale formation in the oil industry.

1.1 Benefits and problems encountered with emulsions

Emulsions are found to form within various stages of the petroleum recovery and processing industry. During oil recovery, water is injected into the reservoir to help maintaining the pressure needed for creating a pressure gradient within the reservoir. This causes the flow of the oil into the well bore. The injected waters displace the oil and leave it entrapped in the porous media as oil-in-water emulsions as shown in Figure 1-3. This is called water flooding which is a cheap technique particularly for offshore applications because of the availability of sea water. The only concern with water flooding is the incompatibility between the injected brine with the formation water in the reservoir which may result in scale formation. The scale formed in the reservoir may affect the rock permeability and result in adverse effects.

Emulsions can also be injected into the reservoir such as in recovery of heavy oils to improve the mobility of high-viscosity oils and hence to increase the production rate. In another application, the emulsions are formed in the reservoir such as in micellar-polymer or alkali-surfactant polymer flooding; the injection of surfactant results in lowering the interfacial tension between the oil and the water and this allows the recovery of residual oils which is left entrapped in the porous media.

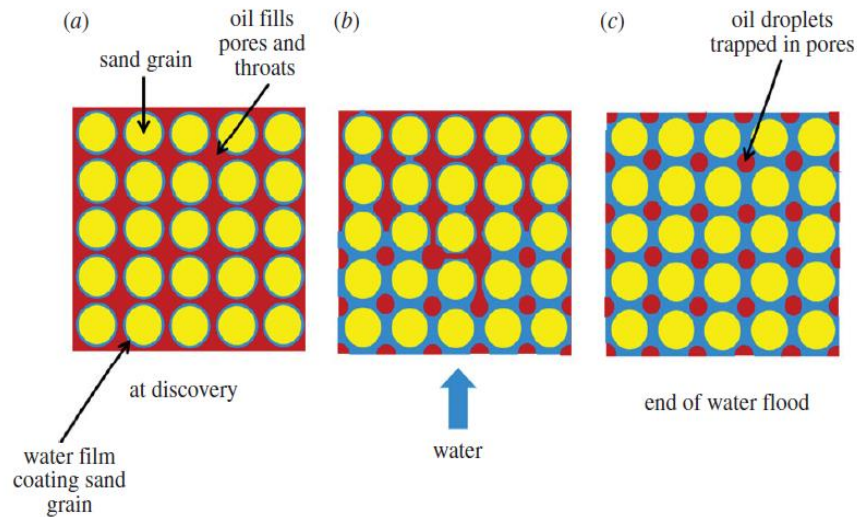


Figure 1-3 The displacement of oil by water and the entrapped oil in porous media during oil recovery [6]

Emulsions can also be useful for heavy crude oils pipeline transportation through using surfactant and waters to form oil-in water emulsions. The principle is to reduce the viscosity of the flowing fluid when the oil phase which has a very high viscosity is converted to droplets inside the water phase forming an emulsion. This is due to the shear thinning property of the emulsions where the challenges associated with this technology are the costs and the selection of the surfactant which has the ability to maintain the stability of the emulsion during transportation [7]. These are some of the applications in which the presence of emulsions is considered desirable.

Most of the emulsions that are created in the reservoir or during the production process by previous applications or by different conditions can be turned into an undesirable type of emulsion which is a water-in-oil emulsion when produced at the wellhead. Oil-in-water emulsions are also found to form and sometimes both types of emulsions can be found together. The stability of the emulsions formed depends on the concentrations and the type of the surfactant added to the emulsions. These surfactants are sometimes naturally found in crude oils such as asphaltene and resin which stabilize the emulsions by means of forming protective films around the emulsion droplets. The presence of fine divided solids such as clay or sand particles and inorganic solids could also stabilize emulsions according to their wettability properties. Emulsions could also be caused by applying mechanical energy and the stability in this case is a result of the reduction in the droplets size. According to the way that different type of emulsions are formed, determining the most effective and economic method for breaking an emulsion is generally made according to the physical properties of the fluids forming the emulsion such as

viscosity, density difference and water percentage. In addition to the way of emulsification [8]. Produced oils should contain a minimum amount of waters to meet pipeline specifications and regulations. To achieve the required quality of oils it is often necessary to treat the crude oil by various processes before proceeding to refineries. The first process is the desalting process in which the crude oil is washed by fresh waters to reduce salt content. The increase in the water content increases the probability of forming emulsions as mixing of phases is applied through mixing valves. The separation of the oil, the water and the inorganic salts then take place in a desalting vessel or treater but a complete separation of water from oil could not be achieved within this stage. A further treatment is required usually by heating to reduce water content. To break emulsions various methods can be applied such as gravitational separation, applying chemicals (demulsifiers), thermal treatments and applying electrical fields that promote coalescence. Other problems encountered with emulsions are oil spills on the ocean which form very stable emulsions and cause an increase in the quantity of pollutant to the environment.

1.2 Problems encountered with mineral scale formation

Mineral scales form in the early stages at the pores between rocks where sub-surface waters become saturated with some divalent minerals such as calcium and magnesium. These minerals are present in calcite sandstones which are rich with those ions, causing deposit on the pores' throats and a reduction in permeability and hence retard the flow of fluids. Mineral scales may also occur in reservoirs; it is well known that oil, gas and water are the three components of the reservoir fluids and during the trip of the crude oil from the reservoir to the wellbore, gases which contain carbon dioxide will come out of solution due to the reduction in pressure during extraction. Releasing of carbon dioxide gas is known as a major factor for carbonate scale formation. Moreover, during oil recovery processes, it is well known that sea water is injected in wells which are called injection wells to increase or maintain the pressure in the reservoir. Mixing of the formation water which is originally found in the reservoir with the injected sea water is the main reason for sulphate scale formation near the well bore. Sulphate scale is very difficult to remove by chemical or mechanical treatment. Mineral scale formation in the reservoir is one of the main causes of formation damage which is undesirable and can be considered as an economical problem [9, 10].

Mineral scale formation in conjunction with clay particles adsorbed by asphaltene in crude oils may act as mechanical stabilizers to emulsions, where particles are

found to collect at the water-oil interface and add stability to emulsions. It was also reported the presence of both organic and inorganic materials in the deposit layers can be found inside the production tubing. It was shown by [11] that the adsorbed asphaltene on suspended clay particles may act as seeds for calcium carbonate precipitation by lowering the activation energy needed for crystallization and hence decreasing the induction time.

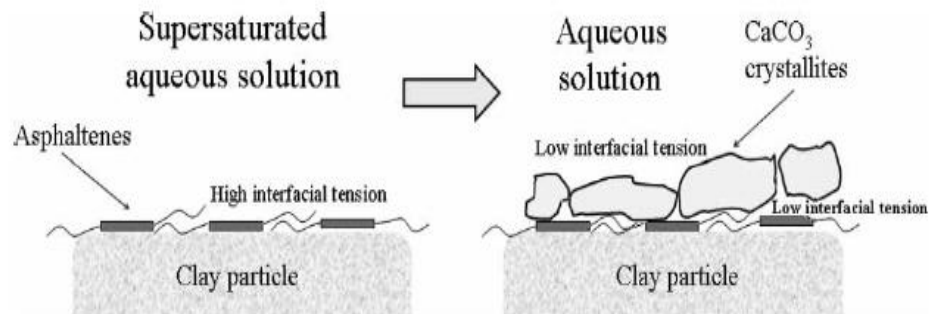


Figure 1-4 Schematic representation of calcium carbonate precipitation over clay particles adsorbed by asphaltene [11]

Scale may also be found to take place in the production tubing and surface facilities; it may affect these processes either by increasing the surface roughness of the internal tubing and hence reducing the production rates or if crystal growth persists then a complete blockage can cause serious operating problems. Scale formation may also cause chokes in the flow lines sometimes so large that the flow line needs to be closed. Blockage of safety valves may cause serious safety problems.



Figure 1-5 Blocking of a pipeline due to the growth of mineral scale [12]

In heat transfer equipment such as in heat exchangers tubes or condensers tubes, water is brought into contact with hot surfaces causing the inverse solubility scaling

salts with respect to temperature such as calcium carbonate and calcium sulphate to deposit. Scaling can also occur in boiler tubes due to evaporation of water causing scaling species to concentrate and because of the low solubility of these scaling matters at high temperatures, deposition takes place. Scale deposition may interface with the different heat transfer processes causing local overheating due to the increase in fouling resistance to heat transfer. This is as a result of an increase in scale thickness which causes a severe reduction in heat transfer efficiencies [13]. Surface localized corrosion which may form under fouling layers may also take place. A reduction in the cross sectional area of tubes or flow channels for the heat exchangers may also lead to an increase in pressure drop or may even lead to total flow blockage [14].

Mineral scale formation may cause problems in many other areas such as in water desalination plants; high pressure water treatment systems such as in reverse osmosis membranes which allow the pass of the pure waters while rejecting inorganic species, leading to supersaturation conditions nearby the membrane surface or concentration polarization. This condition leads to inorganic scale precipitation in the bulk solution which may accumulate on the membrane surface in conjunction with microbial fouling leading to sludge like deposits. Fouling of membranes causes serious problems such as minimizing in the flux, loss of production and membrane degradation [15, 16].

1.3 Reduction of scale potential

Scale prevention is technically and economically more effective than scale removal. In practice, an effective prediction of the scaling tendency by predicting the nature and extent of scale formation using chemical models that rely on thermodynamic principles is not enough and will not lead to accurate estimates of scaling rates. Studying the kinetics of mineral scale formation by assessing the time required for the crystallization to elapse and the rate at which it is taking place, such information about the nucleation and the growth rates for precipitation and deposition can provide a better characterization for the entire scaling process. Another important kinetic consideration is the thermodynamic instability of some types of scales and the transformation to a stable phase can also provide valuable information in understanding the mechanism of scale formation and an effective way to enable the development and selecting of the most efficient chemical inhibitors at different conditions for both scale prevention and controlling.

Scale prevention or removal by adding certain types of chemicals which act through retarding nucleation or crystal growth is the most applied method and preferable

because of its low cost, effectiveness and applicability for inaccessible locations such as in down-hole completion equipment. Squeeze treatment is one of the most used techniques to treat producing wells by squeezing a high concentration scale inhibitor to ensure a maximum amount of the chemical is retained at the reservoir rock surface. These chemicals are then slowly released with the produced fluid and inhibit scale formation and hence ensure well productivity. Treatment of scale formation in tubing surfaces is strongly affected by strength and texture of the formed scales [17], where low porosity crystals for example may exhibit a small surface area to large mass of deposit which will affect how well the chemicals gain access to the scale.

To minimize scaling potential in heat transfer processes, water treatment is needed to reduce the amount of scaling constituents that enter the heat transfer equipment such as by evaporation of water which is then condensed and used as feed water or by water softening techniques or chemical treatment through additives which is the main method utilized to retard or control the formation of scale on process equipment.

It can be concluded that mineral scale formation is a serious problem that imposes massive costs each year in the oil and gas industry. An understanding of the mechanisms of its formation and inhibition is required to eliminate its occurrences and complications.

1.4 Objectives of the research

The kinetics of scale formation is extensively studied in the literature in a single water phase. In reality, water and oil accompany each other during different stages in the petroleum industry. Studying the kinetics of scale formation on the surface and in the bulk of the fluid when the oil phase is present has not yet received much attention and is considered as a gap in the literature.

Since calcium carbonate can form in three different polymorphs and the transformation from the metastable to the stable polymorph is exhibited during the crystallization process, the kinetics at which each polymorph is formed and the mechanism of the transformation of phases has also not received much attention and usually has been ignored in oil and gas industry.

This work is concerned with the formation of calcium carbonate in the presence of oil-in-water emulsions. The impact of adding an oil phase to both surface deposition and bulk precipitation is not clear and needs to be studied. In this case the surface of oil droplets may act as a foreign surface at which nucleation may occur according

to heterogeneous type nucleation. The presence of oil may also affect the scaling characteristics in the bulk solution which in-turn may affect the deposition process. On the other hand, the oil phase could also impact the deposition process either by retarding the diffusion of scaling species to the surface or by continuously wetting the surface and in both cases a decrease in surface deposition is expected. A schematic representation of the possible scenarios of the effect of the existence of oil droplets in the bulk solution on scale deposition is presented in Figure 1-6.

Therefore, to what extent does the presence of oil enhance or alter surface deposition? Does the presence of oil droplets enhance bulk precipitation? Does a relationship between bulk precipitation and surface deposition exist under such conditions?

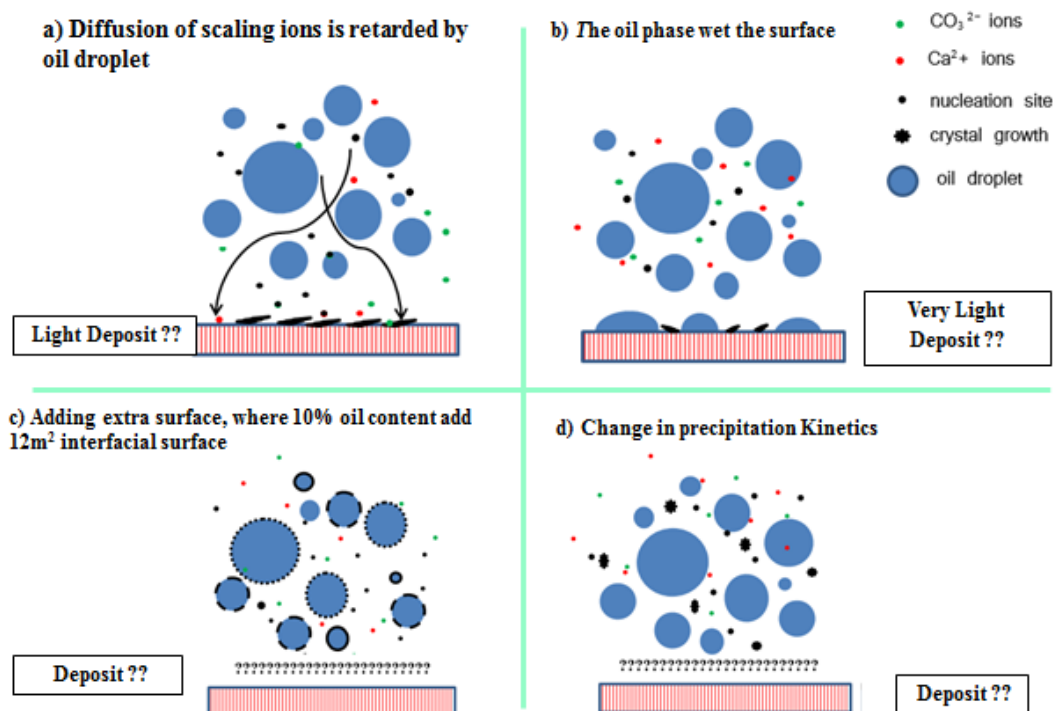


Figure 1-6 The hypothesis regarding the effect of oil-in-water emulsions on surface deposition

It is the aim of this research to integrate a detailed description of the kinetics of calcium carbonate scale formation on the surface and in the bulk solution when oil and water is mixed together. The objectives of the study are summarized as the following:

- 1- To develop a methodology for studying multiphase scale formation in oil-water systems.
- 2- To identify the impact of oil-in-water emulsions on the crystallization process.

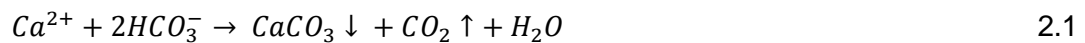
- 3- To understand the kinetics of calcium carbonate scale precipitation in the bulk and scale deposition on a surface in oil /water systems under turbulent conditions.
- 4- To quantify the kinetics of polymorphic formation and transformation and its effect on the overall scale formation both in single and multiphase conditions.
- 5- To detect the relationship between surface deposition and bulk precipitation kinetics in single and multiphase conditions.

2 Chapter Two Background on mineral scale formation, theories and literature review;

2.1 Introduction

Oilfield waters often contain high concentrations of alkaline earth metal cations such as Ca^{2+} , Ba^{2+} , Mg^{2+} and Sr^{2+} . These inorganic ions can react under specific conditions to form mineral scales. Scale formation in oil field reservoirs, producing wells, pipelines and other topside facilities can lead to serious problems, reductions and sometimes a complete shutdown in the production. In addition to flow problems and damage to safety valves. These make mineral scale formation one of the major flow assurance problems that require extensive study. In addition to the economic consideration which arises from decreased or even complete shutdown of the production, scale prevention and removal costs.

Calcium carbonate and barium sulphate are among the most common types of scale encountered with oilfield brines [18, 19]. Calcium carbonate inverse solubility property is responsible for its formation in heat transfer processes [20], while the evolution of carbon dioxide gas due to pressure reduction is the main reason for CaCO_3 formation in oil producing wells. Carbon dioxide reacts to form bicarbonate ions which react with calcium ions according to the following reaction:



Barium sulphate is formed when two incompatible waters are mixed such as injection sea water which is rich with sulphate anions and formation water which contains barium cations during oil recovery. Barium sulphate scale is formed according to the following reaction:



Many other types of mineral scale are found in association with water in various industries such as in water desalination [21] and petroleum industry [22]; sulphate based scales such as calcium sulphate (CaSO_4) and strontium sulphate (SrSO_4) are mainly formed due to mixing of incompatible waters. Iron carbonate or siderite (FeCO_3) forms a layer on the surface and provides protection from corrosion.

2.2 Thermodynamics of crystallization

When a solute dissolves in a solvent, heat is usually absorbed from the surrounding and the solution temperature will decrease. This is referred to as the heat of solution. On the other hand, when a solute crystallizes out of the solution, heat is

usually released and the solution temperature will increase. This heat is referred to as the heat of crystallization. However, the reverse is true in some cases. The heat of crystallization is defined as the following equation:

$$-\Delta H_{\text{Cryst}} = \Delta H_{\text{Sol}}^{\text{sat}} = \Delta H_{\text{Sol}}^{\infty} + \Delta H_{\text{dil}} \quad 2.3$$

where:

ΔH_{Cryst} is the heat of crystallization (kJ/mol)

$\Delta H_{\text{Sol}}^{\text{sat}}$ is the heat of solution for saturated solution (kJ/mol)

$\Delta H_{\text{Sol}}^{\infty}$ is the heat of solution for infinite dilute solution (kJ/mol)

ΔH_{dil} is the heat of dilution (kJ/mol)

The driving force for crystallization is the difference in chemical potential of the crystallizing compounds in the saturated solution (μ_1) and in crystalline form (μ_2).

$$\Delta\mu = \mu_2 - \mu_1 \quad 2.4$$

According to classical Gibbs-thermodynamic theory a general solubility equation can be obtained from the chemical potential of the i^{th} component in the mixture according to the following:

$$\mu_i = \mu_i^0 + RT \times \ln(a_i) \quad 2.5$$

where: μ_i^0 is the standard chemical potential (for pure substances at the system T&P), R is the gas constant and a_i is the activity of i^{th} component in the mixture.

In ideal solutions where the dissolved substances and the solute do not influence each other a_i is replaced by the concentration c_i , or mole fraction x_i . In non-ideal solutions the activity coefficient gives a measure of the deviation from the ideality and it is presented by:

$$a_c = \gamma C \quad 2.6$$

For electrolyte solutions that are completely dissociated, mean ionic concentration $a_{\mp C}$ and mean ionic activity coefficient γ_{\mp} are used where:

$$a_c = a_{\mp C}^v = (C_{\mp} \gamma_{\mp})^v = (QC \gamma_{\mp})^v \quad 2.7$$

where:

v is the number of moles of ions in 1 mole of electrolyte, $v = v_+ + v_-$

and

$$Q = (v_+^{v_+} v_-^{v_-})^{\frac{1}{v}}$$

The mean ionic activity coefficient can also be estimated by the Debye-Huckel (1923) correlation for infinitely dilute electrolyte, where the effect that leads to this deviation is that of interionic attraction which is between ionic charges of unlike signs:

$$\log \gamma_{\mp} = -A |z_+ z_-| \times I^{\frac{1}{2}} \quad 2.8$$

where:

I is the solution ionic strength (mole/l), $I = \frac{1}{2} \sum C_i z_i^2$

A is a constant which is a function of the temperature, the elementary charges and the dielectric constant of the solvent.

C_i is the ionic concentration (mol/l) of i^{th} ionic species.

z_+ and z_- are the valences of the cations and anions, respectively.

The Debye-Huckel equation is modified by many other theoretical correlations for ionic strengths ranged from 0 to 0.1 [23]. These correlations differ only in the ionic valance or in the choice of common ion size parameters such as the Guntelberg (1927) correlation for sparingly soluble electrolyte:

$$\log \gamma_{\mp} = -A |z_+ z_-| \left[\frac{I^{\frac{1}{2}}}{1 + I^{\frac{1}{2}}} \right] \quad 2.9$$

or the Davis (1962) equation:

$$\log \gamma_{\mp} = -A |z_+ z_-| \left[\frac{I^{\frac{1}{2}}}{1 + I^{\frac{1}{2}}} \right] - 0.3I \quad 2.10$$

Therefore, substituting the activity for an electrolyte solution into equation 2.5, results in the following equation:

$$\mu_i = \mu_{i^0} + RT [\ln(QC\gamma_{\pm})^v] \quad 2.11$$

According to equation 2.7:

$$\mu_{i^0} + RT [\ln(a_{\mp}^v)] - \mu_{i,eq}^0 - RT [\ln(a_{\mp,eq}^v)] = 0 \quad 2.12$$

$$\text{or } -\frac{\Delta\mu}{RT} = v \times \ln\left(\frac{a_{\mp}}{a_{\mp,eq}}\right) \quad 2.13$$

The solubility product for an electrolyte solution is:

$$K_{SP} = a_{+,eq}^+ \times a_{-,eq}^- = (QC\gamma_{\mp,eq})^v \quad 2.14$$

and the solubility is:

$$C^* = \left(\frac{K_{SP}}{v_+^{V_+} v_-^{V_-}} \right)^{\frac{1}{V}} \quad 2.15$$

For a salt which produces two ions per molecule such as CaCO_3 , the solubility is:

$$C^* = \left(\frac{K_{SP}}{1^{11} 1^1} \right)^{\frac{1}{1+1}} = K_{SP}^{\frac{1}{2}} \quad 2.16$$

2.2.1 $\text{CO}_2\text{-H}_2\text{O}$ phase equilibria

It is well known that saturation is the main cause of scale formation and the system has to reach to some level of supersaturation to scale up. Other factors that are crucial for alkaline scale formation are pH, temperature and pressure. Temperature and pressure have a high influence on carbonate scale through affecting the amount of CO_2 dissolved in the aqueous phase which has a direct effect on the solution pH. According to CO_2 -temperature-pressure equilibrium diagram which is shown in Figure 2-1, high pressures and temperatures keep CO_2 in the solution allowing it to react with water and form carbonic acids according to the following equation:

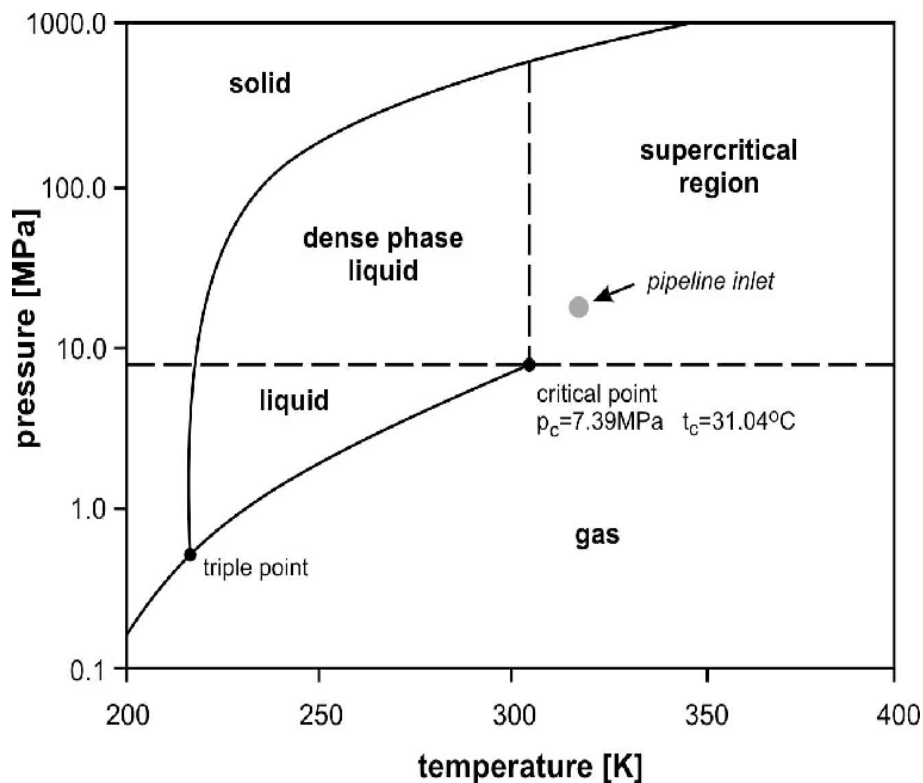


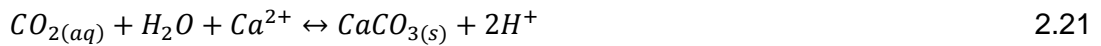
Figure 2-1 CO_2 temperature-pressure phase diagram [24]



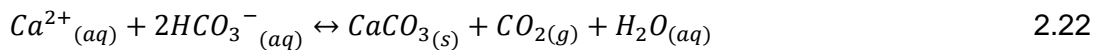
In the presence of cations such as Ca^{2+} ions in the formation waters, the dissociation of carbonic acids and bicarbonate ions are associated with the reaction to form $CaCO_3$. In this case, lowering of pH occurs due to the release of H^+ ions during the dissociation reaction to form $CaCO_3$ scale according to the following reactions:



and the overall reaction is:



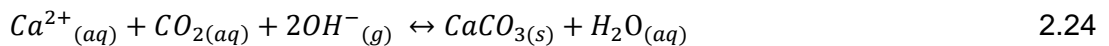
Since the formation of the carbonic acids is followed by hydrogen ion dissociation where this will generally decrease the pH of the solution and increase calcium carbonate solubility which in turn will decrease carbonate scale tendencies. According to Hasson et al. [25] carbonate scale is formed in this case according to acidic mechanism in which CO_2 is released out from the reaction and pH is decreased and the overall reaction is:



The existence of equilibrium between dissolved CO_2 and bicarbonate ions is the normal condition but in reservoir conditions different pressures and temperatures can be encountered such as lowering pressure during production or during enhanced oil recovery. In this case releasing or degassing of CO_2 from solution will result in an increase in pH and a decrease in $CaCO_3$ solubility and hence an increase in supersaturation and scaling tendencies. $CaCO_3$ solubility is also decreased with temperature and because of this, high scale deposition on hot surfaces such as on heat exchangers tubing can be found. The degassing of CO_2 from the solution occurs according to the following equation:



Therefore, less carbonic acids and hydrogen ions are formed and the reaction to form calcium carbonate occurs according to alkaline mechanism [25] where CO_2 is consumed and pH is increased and the overall reaction is:



The formation of calcium carbonate is controlled by the quantity of the overall carbonate compounds formed in the solution. These quantities are a function of the

solution pH as shown in Figure 2-2. Therefore, it is necessary to calculate the concentration of chemical species in the solution as a function of pH to accurately determine the supersaturation.

The equilibrium constants for the crystallization reactions in equations 2.17 to 2.19 and 2.23 are estimated by [26] and the ionization constant of water is estimated by [27] and are defined as the following:

$$K_1 = \frac{a_{H^+} a_{HCO_3^-}}{a_{CO_2(aq)} a_{H_2O}} \quad 2.25$$

and,

$$\log K_1 = -356.3094 - 0.060919464T + \frac{21834.37}{T} + 126.8339 \log T - \frac{1684915}{T^2} \quad 2.26$$

$$K_2 = \frac{a_{H^+} a_{CO_3^{2-}}}{a_{HCO_3^-}} \quad 2.27$$

and,

$$\log K_2 = -107.8871 - 0.03252894T + \frac{5151.79}{T} + 38.92561 \log T - \frac{563713.9}{T^2} \quad 2.28$$

$$K_H = \frac{a_{CO_2(aq)}}{f_{CO_2(g)}} \quad 2.29$$

and,

$$\log K_H = -108.3865 + 0.01985076T - \frac{6919.53}{T} - 40.45154 \log T + \frac{669365}{T^2} \quad 2.30$$

$$K_W = \frac{a_{H^+} a_{OH^-}}{a_{H_2O}} \quad 2.31$$

and,

$$\log K_W = 22.801 - 0.010365T - \frac{4787.3}{T} - 7.1321 \log T \quad 2.32$$

where:

$$a_{H^+} = 10^{-pH}$$

$a_{HCO_3^-}$, $a_{CO_3^{2-}}$ are the activities of bicarbonate and carbonate ions in the solution, respectively.

K_H is the Henry's law constant which is derived from the experimental measurement of CO_2 gas solubility in water and is available tabulated in the literature for varied temperatures and pressures.

K_w is the ionization constant of water.

a_{CO_2} is the activity of CO_2 in aqueous solution.

and f_{CO_2} is the fugacity of CO_2 gas.

The activity coefficients for the individual ions can be calculated using Debye-Huckel correlation or using its modified correlations as shown in equations 2.8 to 2.1.

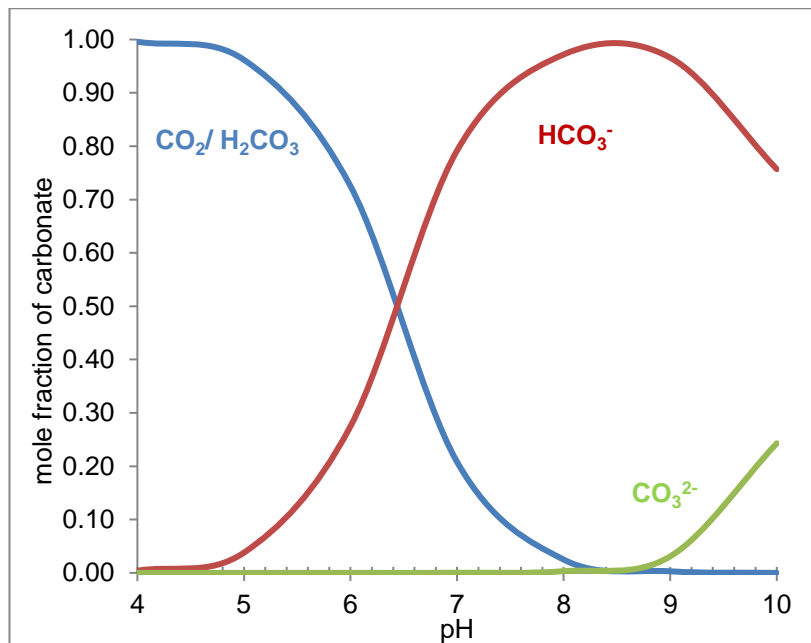


Figure 2-2 The distribution of carbonates, bicarbonates and carbonic acids in the bulk solution according to solution pH

2.2.2 Solute solubility

It is well known that solubility is directly related to temperature where for normal solute solubility, the solute is dissolved in its saturated solution with absorption of heat and the decrease in the temperature will result in a decrease in the solubility. In this case the precipitation will occur upon cooling; barium sulphate is known to behave as a normal solubility substance. Some other solutes exhibit an inverted solubility effect; this occurs when a solute is dissolved in its saturated solution with evolution of heat and an increase in temperature will result in a decrease in the solubility; calcium carbonate and calcium sulphate are known to exhibit a reverse solubility [20, 28]. In this case the precipitation will take place upon heating or in the warm regions of the solution or on hot surfaces such as in heat exchangers. Solubility curves such as shown in Figure 2-3 show the relationship between solute

concentration and temperature. Some curves show discontinuity which infer a phase change such as in the case of some hydrous salts which have different solubility behaviour from the anhydrous form of the same salt.

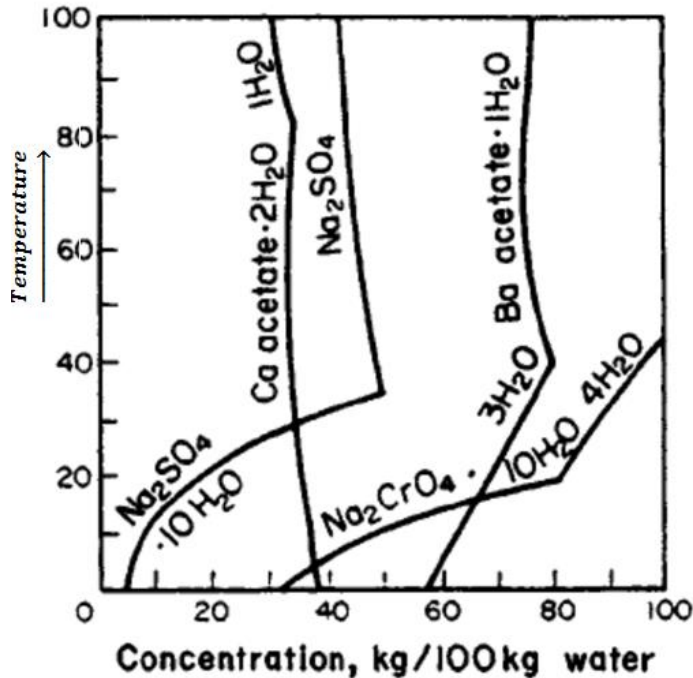


Figure 2-3 Solubility curves for some salts; discontinuity of the lines indicate a phase change [15]

Many correlations have been proposed for prediction of the solubility data. The most commonly used expressions are the empirical equations which are based on thermodynamic relationships relating to phase equilibria. For CaCO_3 polymorphs Plummer and Busenberg [26] developed equations for estimating the solubility product of calcite, aragonite and vaterite. The correlations are based on experimental data for $\text{CO}_2\text{-H}_2\text{O}$ solution between 0 and 90°C and are expressed as following:

$$\log K_C = -171.9065 - 0.077993T + \frac{2839.319}{T} + 71.595 \log T \quad 2.33$$

$$\log K_A = -171.9773 - 0.077993T + \frac{2903.293}{T} + 71.595 \log T \quad 2.34$$

$$\log K_V = -172.1295 - 0.077993T + \frac{3074.688}{T} + 71.595 \log T \quad 2.35$$

Where: K_C , K_A , K_V are the solubility product of calcite, aragonite and vaterite in M^2 , respectively. T is the temperature in K.

The solubility-temperature dependence curve can provide information about the phase transformation as shown in Figure 2-4. A solution with composition X_i at temperature T_A is supersaturated with respect to both the metastable and the stable

phases, in this case the initial phase to form is the metastable phase and once it precipitates, the solution composition would fall to the solubility of the metastable phase X_1 . Since the system is also supersaturated with respect to the stable phase, some of the stable phase crystals may also appear in this stage. When the system is saturated with respect to the metastable phase, it starts to dissolve and this causes a further reduction in the solubility. The crystallization of the stable phase will take place until all the metastable phase has disappeared and the transformation is complete.

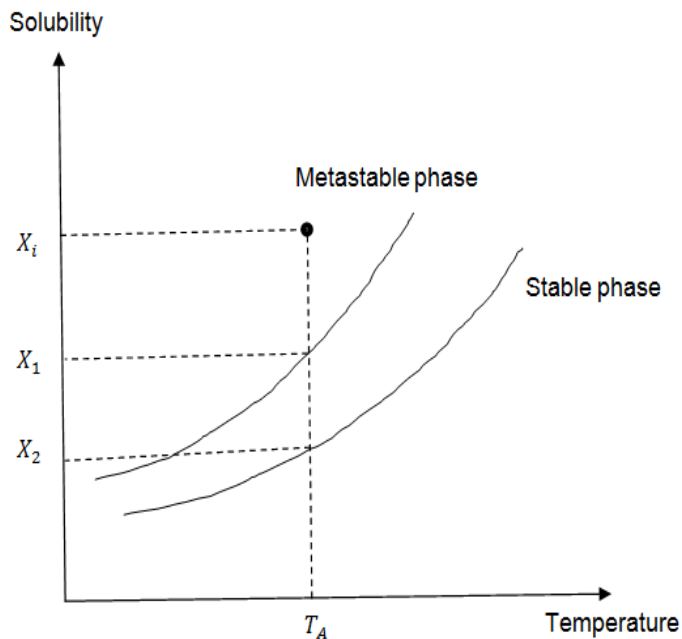


Figure 2-4 Solubility curves for two polymorphs

2.3 Crystallization process

The crystallization process generally takes place when solutions that contain reacting species become supersaturated and are mixed. The solubility of the precipitating compounds at specific temperatures and the concentrations of the reactant ions must be known in order to predict the probability of scaling. These quantities are usually presented by the activities of the reacting species and the solubility product of the formed crystals. During the crystallization process, the dissolution of an electrolyte into x of z^+ ions and y of z^- ions in a solution occurs according to:



The solubility product is:

$$K_{SP} = a_{M,eq}^{z+} a_{N,eq}^{z-} \quad 2.37$$

where: a_M and a_N are the activities of M and N reacting ions. The saturation ratio is the product of the activities of the reacting ions over the solubility product.

$$SR = \frac{a_M^{z_+} a_N^{z_-}}{K_{SP}} \quad 2.38$$

Supersaturation is achieved when $SR > 1$; a period of time is elapsed between the moment of achievement of supersaturation and the appearance of nuclei of detectable sizes. This period of time is called the induction time. In general crystallization processes are encountered in three stages: (i) achievement of supersaturation, (ii) appearance of nuclei and (iii) crystal growth.

For stationary systems; there may be regions of supersaturation and others of under-saturation. If a region of supersaturation exists at a solution-surface interface, deposition on the surface may occur. Otherwise, crystals may precipitate in the bulk solution. The precipitate may then be swept from the bulk into regions of under-saturation where it may either re-dissolve or accumulate at certain surfaces forming loose agglomerates.

Supersaturation usually declines during the process of crystallization and this is particularly the case for batch systems. If the system is running in such a way that the rate at which supersaturation is produced is equal to the rate of crystallization such as in continuous systems, supersaturation will be kept constant throughout the process.

2.4 Nucleation

Nucleation denotes the process of nuclei formation in which molecules are interacting to form short chains which continue to build into a crystal lattice by the addition of individual molecules. If these nuclei are present at regions of high saturation and have sizes greater than the critical size (the minimum size required to stabilize) it will grow, if not, it may re-dissolve into solution [29]. Some studies focused on detecting the size of which a nucleus must reach to grow into a crystal, one suggested a critical size of 200 μm and another between 200-500 μm [30]. However, according to the classic theory of nucleation [30, 31], nucleation is classified into two mechanisms:

2.4.1 Primary nucleation

Primary nucleation can take place either homogeneously (without the presence of any solids) or heterogeneously (induced by the presence of foreign solids).

The critical radius for homogeneous nucleation is obtained by determining the critical overall free energy change as represented by the following equation:

$$\Delta G_{\text{crit}} = \frac{4\pi\gamma r_c^2}{3} \quad 2.39$$

where: r_c is the critical size radius, γ is interfacial tension between the developing nuclei and the supersaturation solution.

Because of the energy distribution throughout the solution due to fluctuation in supersaturation, there is no amount of energy change required to form stable nuclei such as in the case of the critical sizes.

The overall critical free energy change can also be described in terms of solubility based on Gibbs- Thomson equation for non-electrolyte as follows:

$$\Delta G_{\text{crit}} = \frac{16\pi\gamma^3 v^2}{3(KT \ln S)^2} \quad 2.40$$

Where: v is the molecular volume, K is Boltzmann constant; S is the saturation ratio and γ is the interfacial tension.

The rate of homogeneous nucleation can be expressed in the form of the Arrhenius equation as the following:

$$J = A \times \exp\left(-\frac{\Delta G}{KT}\right) = A \times \exp\left(-\frac{16\pi\gamma^3 v^2}{3K^3 T^3 \ln S^2}\right) \quad 2.41$$

According to this equation, there are three main variables affecting nucleation rate; temperature, interfacial tension and supersaturation. However, the main difficulty in studying the kinetics of homogeneous nucleation is the preparation of impurity free systems.

Heterogeneous nucleation is easier to occur and requires less free energy change to nucleate. The overall critical free energy change for heterogeneous nucleation $\Delta G'_{\text{crit}}$ is less than for homogeneous nucleation according to the following:

$$\Delta G'_{\text{crit}} = \varphi \Delta G_{\text{crit}} \quad 2.42$$

where: the factor φ is <1

As nucleation rate is a function of the interfacial tension and since heterogeneous nucleation occurs in the presence of a solid as shown in Figure 2-5, the interfacial tension between the crystalline solid, the foreign solid surface and the solution is related by contact angle θ , and can be defined by Young's equation:

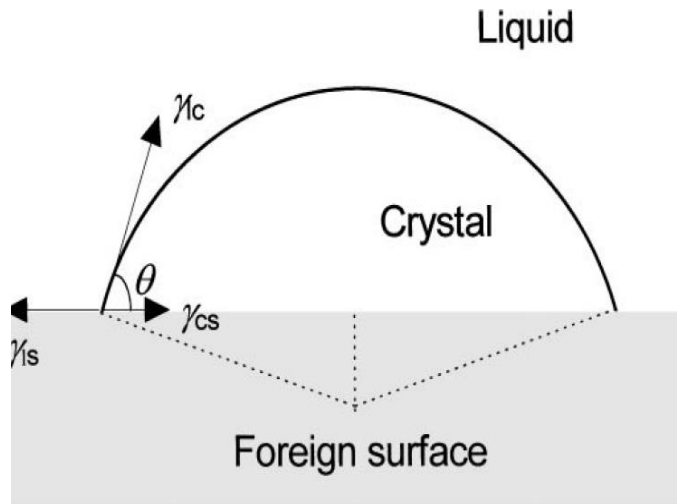


Figure 2-5 Interfacial tensions between liquid, crystal and solid surface; the principle of heterogeneous nucleation [32]

$$\cos\theta = \frac{\gamma_{sl} - \gamma_{cs}}{\gamma_{cl}} \quad 2.43$$

Where: θ is the angle of wetting for liquid and solid systems, γ_{sl} is the interfacial tension between a solid surface and a liquid phase, γ_{cs} is the interfacial tension between a crystal and a solid surface and γ_{cl} is the interfacial tension between a crystal and a liquid phase.

The factor φ can be expressed by Volmer (1939) equation:

$$\varphi = \frac{(2 + \cos\theta)(1 - \cos\theta)^2}{4} \quad 2.44$$

For the case of non-affinity between a crystalline solid and a foreign surface, $\theta=180^\circ$, $\varphi=1$ and $\Delta G'_{\text{crit}} = \Delta G_{\text{crit}}$

If $0^\circ < \theta < 180^\circ$ and $\varphi < 1$, the overall energy change is less for heterogeneous nucleation.

For the case of a complete affinity between a crystalline solid and a foreign surface, $\theta=0^\circ$, $\varphi=0$, and $\Delta G'_{\text{crit}} = 0$, no heterogeneous nucleation will occur.

2.4.2 Secondary nucleation

Secondary nucleation is the nucleation in the presence of solute crystals in the solution where it can occur in low supersaturation conditions. In the crystallization industry, continuous nucleation is typically undesirable because it results in the production of bad product size distribution which is difficult to control. In this case seeding can help prevent spontaneous nucleation by reducing the supersaturation

through inducing secondary nucleation where the operation is usually undertaken in the metastable zone and thus avoids spontaneous nucleation. Secondary nucleation is also used as a method for producing selective crystal polymorph; the seeding operation provides a surface for the selective growth of the desired polymorph and suppresses the nucleation of the undesired one [33]. Some of the conditions that promote the occurrence of secondary nucleation are [30, 31]: (i) hydrodynamic forces nearby stationary crystals which shear the loosely bonded units from crystal-solution interface such as the dendritic needle shaped crystals. These units reproduce sub-nuclei which develop into stable ones if settled at regions of supersaturation. (ii) contact or collision between crystals such as in the case of agitation. This may cause fragments to break off the crystals due to fractures at the point of contact or at the crystal–agitator contact [34]. (iii) breakage fragments may also be produced through growing of crystals containing defects which strain and crack the crystals [35]. (iv) cracks and defects in the vessel surface which could retain some fragments from previous batch. Secondary nucleation was also found to have relation with solute solubility; sparingly soluble substances promote secondary nucleation while intermediate and readily soluble substances may not [31]. This is as a result from crystals size where small crystals are less subject to the above conditions whereas aggregate of crystals in which large particles are formed promote the onset of secondary nucleation by forming a crystalline bridge between particles and form agglomerate. Some studies [36, 37] indicate the similarity in supersaturation dependency between secondary nucleation and crystal growth. Secondary nucleation rate can be expressed using a power law empirical relation of the form [38]:

$$B_{Tot} = k_N M_T^a N^b \Delta c^m \quad 2.45$$

where: k_N is the nucleation constant. M_T is the suspension density (g/l). N is the mixing speed (rev/min). Δc is the concentration driving force (g/l). a , b and m are constants.

2.5 Crystal growth

Once stable nuclei are found in a supersaturation solution, they will start to grow to visible sizes. There are many proposed growth mechanisms in the literature, the most acceptable two theories are [31]: (i) the diffusion process in which molecules transport from solution to crystal surface by diffusion or convection or both. (ii) surface reaction process in which species incorporate into the surface of the crystal lattice, also called surface integration process.

Growth rates were first proposed by Noyes and Whitney (1897) and then modified by Berthoud (1912) and Valeton (1924) who suggested the previous two processes for crystal growth and estimating the rate of growth for each process by the equations [30]:

$$R_G = k_d(C - C_i) \quad (\text{Diffusion process}) \quad 2.46$$

and,

$$R_G = k_r(C_i - C_{eq})^n \quad (\text{Surface integration process}) \quad 2.47$$

where: R_G is the growth rate, k_d and k_r are the mass transfer coefficient for diffusion and surface integration, respectively, n is the order of the integration process, C is solute bulk concentration, C_i is solute concentration at the crystal-solution interface and C_{eq} is the equilibrium concentration.

The growth rate can also be expressed by relative supersaturation dependency [39]:

$$G = k_p(S - 1)^n \quad 2.48$$

where: G is the overall linear growth rate, k_p is the precipitation rate constant, S is the saturation ratio. n is the order of the reaction which can take a value of 1 for the diffusion process and 2 for the surface integration process.

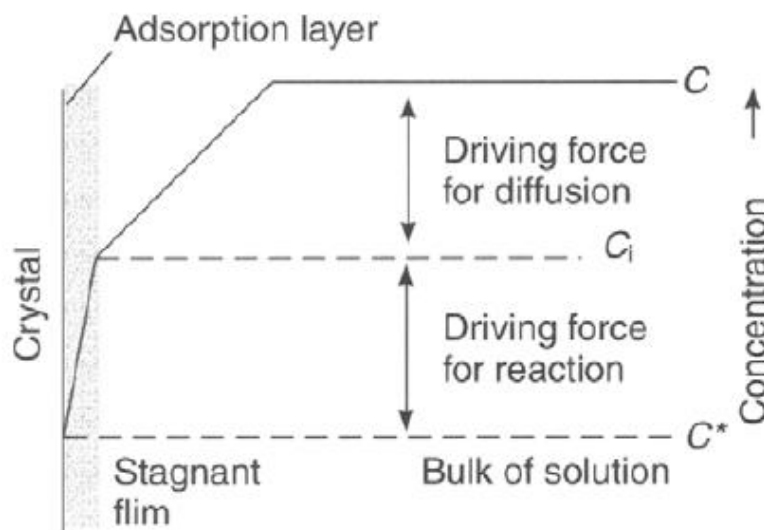


Figure 2-6 Growing crystal-solution interface [40].

Each of these processes can be the rate determining step of the overall growth process where linear growth rate in which the SR dependency is first order indicates the diffusion growth control and parabolic growth rates where the SR dependency is second order indicate surface reaction control.

The trend of the crystal growth versus time then could be converted to a model which describes the growth rate at certain conditions. Zhang et al. [39, 41] studied the growth mechanism of seeded calcite and found that calcite growth rate can be described according to Davies and Jones [42] with reaction order of 2 for solution pH >7 as the following:

$$R = k_p(S^{0.5} - 1)^2 \quad 2.49$$

$$S = [Ca^{2+}][Co_3^{2-}]/K_{SP} \quad 2.50$$

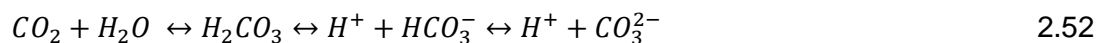
where: R is the precipitation rate (mmol/m².kg.hr), K_{SP} is the solubility product for calcite (mmol²/kg²), $[Ca^{2+}]$ and $[Co_3^{2-}]$ are the concentrations of calcium and carbonate ions in the solution (mmol/kg), S is the saturation ratio and k_p is the precipitation rate constant. The overall rate constant was estimated as a function of temperature, ionic strength and over the range of Mg²⁺/Ca²⁺ of 0.1 and 0.5. The presence of Mg²⁺ ions was found to cause an average reduction in crystal growth rate by about 48% and to affect the morphology of the crystals. The calcite growth constant was found to increase with temperature and ionic strength as shown in the following equation:

$$\text{Log}(K_p) = 0.1257(IS)^{0.5} - 2504/(T) - 2.03 \quad 2.51$$

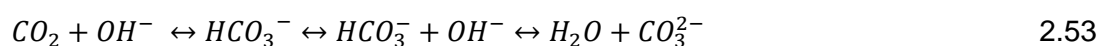
where: IS is the Ionic strength, T is the temperature (° C)

The growth rate has also been found to be affected by solute solubility such that the growth rate of a sparingly soluble solute is lower by an order of 2 than that of a readily soluble solute [43]. However studies [25, 44] suggested if mass transfer to the crystals has much higher rate than that of surface incorporation, then the growth rate is controlled by the surface integration process. On the other hand, if surface integration rate is much faster than the diffusional rate, the deposition is low and the growth rate is controlled by the diffusion process. If the rate constants are nearly equal for both processes then both are important in determining the rate of crystal growth. Hasson et al. [25] suggested that pH has an important role on detecting the dominant mechanism for the crystal growth of calcium carbonate, where the hydration and dehydration of CO₂ in the solutions occur by the following parallel reactions:

The acidic reaction mechanism:



The alkaline reaction mechanism:



The rate limiting step is the acidic reactions for pH range of 7 to 8, alkali reactions for pH range of 9.2 to 10 and both reactions are important and cannot be neglected when pH is ranged between 8 and 9.2. The relative extent of the CO₂ reaction and diffusion was evaluated by comparing the reaction time with the diffusion time required by the CO₂ species and the dominant effect is the process which occurs more rapidly. Diffusion and reaction controlled growth processes and their effect on calcium carbonate polymorphs have been studied by [45]. The diffusion mechanism was achieved using a special designed reactor comprising of three cells separated by movable baffles and microspores sponge. The reactive species are placed in the side cells and pure water is placed in the middle cell in which the precipitation will take place. The diffusion of calcium and carbonate ions is well controlled in order to obtain different compositions of different calcium carbonate polymorphs due to the change in the crystal growth rates. A reaction-controlled growth process was achieved by direct mixing of reactant in a glass vessel stirred at 300 rpm. The precipitate from both experiments at 40° C shows different polymorphs; the decrease in the diffusion of reactants during the diffusion-controlled process led to a massive decline in supersaturation and the major polymorph formed was rhombic calcite whereas spherical vaterite was the major phase in direct mixing experiments.

2.6 Crystal polymorph

Polymorphism is usually encountered in crystalline matter and is caused by the change in the molecular arrangement inside the crystal unit, or due to the change in the spacing of the lattice points. Different polymorphs exhibit different physical properties such as density, solubility, hardness, thermal and optical properties [30]. Different types of scale may exhibit different polymorphs; calcium sulphate for example which is the most common type of scale among the non-alkaline scales known to present in water desalination processes can be present in three polymorphs [21]; calcium sulphate dihydrate CaSO₄.H₂O (gypsum), calcium sulphate hemihydrates (α or β CaSO₄. 1/2 H₂O) and calcium sulphate anhydrate CaSO₄. At ambient temperature gypsum is found to be the most common type and can be present in two morphologies, needle like or plate like depending on supersaturation. Needle-like crystals are found to form under low saturation ratio while platelets are found under high saturation conditions. The morphology is found also to depend on the substrate nature [46]. Unlike other types of mineral scale, barium sulphate (barite) exhibits an orthorhombic structure which is the only form that can be found.

Calcium carbonate is known to exhibit six various forms. Three of which are anhydrous and these are considered as the more stable phases (calcite, aragonite and vaterite), and three hydrated forms which are less stable (amorphous calcium carbonate (ACC), calcium carbonate monohydrate ($\text{CaCO}_3 \cdot \text{H}_2\text{O}$) and calcium carbonate hexa-hydrate ($\text{CaCO}_3 \cdot 6\text{H}_2\text{O}$)).

Amorphous calcium carbonate is described as a gelatin structure [47-49] which consists of spherical particles with an average diameter of 600 nm [48]. ACC is also described as a nano-sized spherical particles [50, 51]. Calcium carbonate monohydrate are shown to have branch leaf-like structure [52]. Calcite crystals have sharp edges which are rhombohedral in structure and usually appear as individual crystals. Aragonite which has an orthorhombic structure usually appears as agglomerate with outward oriented needles, emerging from a central point. Vaterite is described as a polycrystalline sphere consisting of individual rounded nano-sized particles clustered together with an overall diameter ranging from 0.5-5 μm [21]. Figure 2-7 and Table 2-1 show the difference in the shape and the characteristics of the three CaCO_3 crystalline polymorphs.

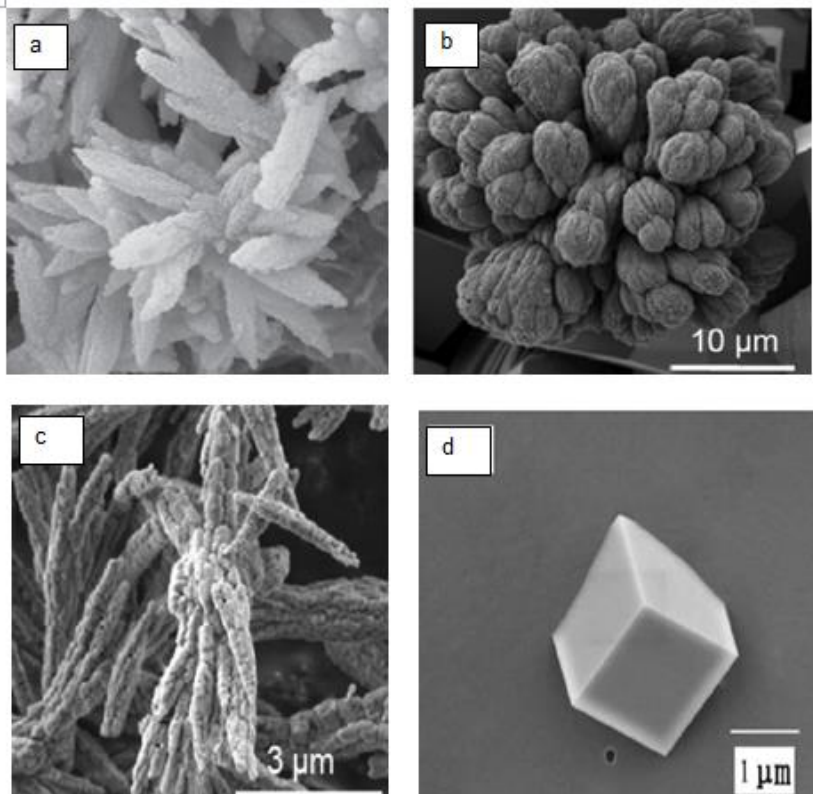
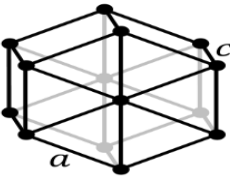
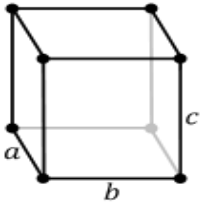
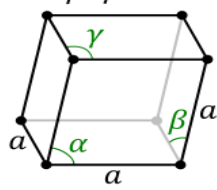


Figure 2-7 Different polymorphs of CaCO_3 ; (a) CaCO_3 monohydrate [52], (b) vaterite, (c) aragonite, (d) calcite [53]

Table 2-1 Physical and crystallographic properties of CaCO ₃ polymorphs			
properties	Vaterite	Aragonite	Calcite
Stability	Least stable (metastable)	More stable (metastable)	Most stable
Density (g/cm ³)	2.66	2.83	2.711
Solubility at 25° C [26]	1.107×10 ⁻⁴	6.799×10 ⁻⁵	5.761×10 ⁻⁵
Refractive index	1.65	1.70	1.66
Crystal structure	Hexagonal 	Orthorhombic $a \neq b \neq c$ 	Cubic- Rhombohedral $\alpha = \beta = \gamma \neq 90^\circ$ 

Among the three anhydrous forms, calcite is the most thermodynamically stable phase and vaterite is the least stable one. Amorphous calcium carbonate is known as a template for CaCO₃ crystalline phases [54]. ACC is transformed to vaterite and calcite at low temperatures of 14 to 30° C and to aragonite and calcite at high temperatures of 60 to 80° C [51]. All the three polymorphs are observed at intermediate temperatures of 40 to 50° C [51]. However, certain conditions such as temperature [51, 55] as shown in Figure 2-8, solution pH [56] as shown in Figure 2-9, reactant concentration ratio [39, 52], mixing conditions [45, 47] and the presence of certain additives such as cations, solvents and some chemical inhibitors are all found to affect the abundance of crystal polymorphs [52, 57-62].

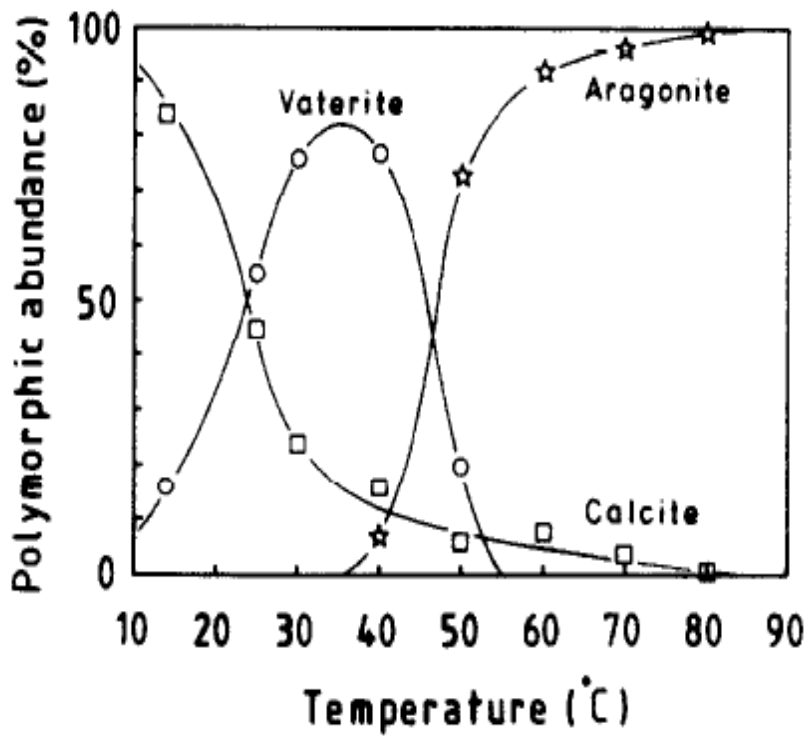


Figure 2-8 Effect of temperature on the polymorphic percentage in the bulk solution as taken from [51]

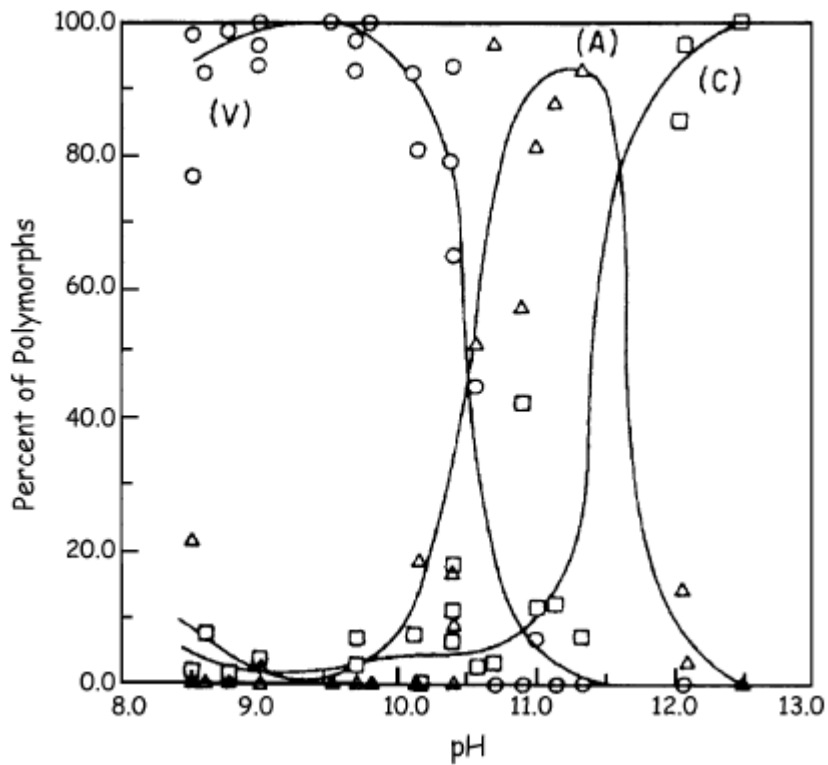


Figure 2-9 Effect of pH on the polymorphic percentage in the bulk solution at $T = 24^\circ \text{C}$, $\text{Ca}^{2+}/\text{CO}_3^{2-} = 1$, (O) vaterite, (Δ) aragonite and (\square) calcite; as taken from [43]

The different factors that affect the formation of different polymorphs, solution pH, temperature, concentration ratio of components, ionic strength, supersaturation and different additives were studied by [56]. According to this study the influence of the concentration ratio and supersaturation is less significant than pH and temperature which are found as the most important factors. The effect of initial supersaturation and solution pH on the polymorphic formation of CaCO_3 was also studied by [63] for equal concentrations of calcium chloride and sodium carbonate solution at 25° C and for a range of pH between 8 and 11. It was shown that the transformation of ACC is highly influenced by the initial SR and pH; for high initial SR and low solution pH, high vaterite abundance is present initially followed by calcite appearance due to aging whereas for low SR and high pH, calcite is observed from early stages and during the whole experiment time. The importance of initial SR and pH of the solution on the phase transformation of CaCO_3 was also showed by [48].

2.6.1 Polymorphic transformation

The crystallization process of CaCO_3 starts from thermodynamically unstable hydrated form to anhydrous polymorphic stable forms [54, 64]; the order of the transformation is from the more hydrated ACC, to the less hydrated ACC, to dehydrated ACC, then to the crystalline form which takes the order of vaterite, aragonite then calcite. According to [64] the transformations involve a series of ordering, dehydration, and crystallization processes, each lowers the enthalpy of the system where the crystallization of the dehydrated amorphous material lowers the enthalpy the most. The change in the solubility of different CaCO_3 crystalline phases with temperature which is calculated using Plummer and Busenberg [26] equations 2.36 to 2.38 shows that the transformation takes place from the higher solubility crystalline form to lower solubility one as shown in Figure 2-10.

There are two theories regarding the polymorphic transformation of a solid structure. The first suggests the transformation occurs through a direct solid transition in which the metastable phase exhibits a rearrangement of its molecules or atoms to a more stable form [65]. The second is valid in the presence of a solvent which allows the dissolution and the re-nucleation and grow of the stable phase [66]. However, in the presence of water the second theory is applied and in this case two kinetic processes are observed; (i) the dissolution of the metastable phase (ii) the growth of the stable phase.

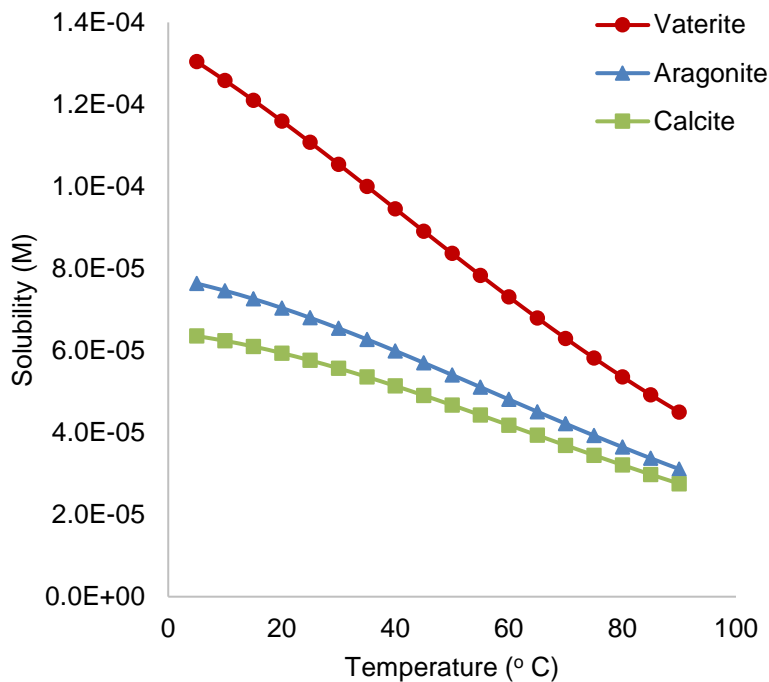


Figure 2-10 The change in the solubility of the different polymorphic crystalline forms of CaCO₃ with temperature

Figure 2-11 show some evidences of the transformation of vaterite to calcite. Extensive studies have been reported in the literature investigating which of these processes is controlling the transformation of CaCO₃. The most accepted kinetic mechanism suggested that the growth of calcite is the controlling mechanism of the transition of vaterite to calcite [67-69]. Others such as [70, 71] suggested the controlling of the vaterite dissolution process. Kralj et al. [68, 72, 73] studied the rate of vaterite growth, vaterite dissolution and calcite growth each independently by a series of unseeded and seeded experiments. Both vaterite and calcite growth with respect to relative supersaturation of the solution were found to follow a parabolic growth rate whereas the dissolution of vaterite was found to follow a linear growth rate. The growth rate of calcite is found to be lower than vaterite growth rate and is considered as the rate determining step.

Some others such as [74, 75] studied the kinetic of polymorphic transformation of CaCO₃ based on solid state reaction kinetics. Different models have been proposed based on mechanistic assumptions which are classified as nucleation models which account for both nucleation and growth rates such as power law and Avrami-Erofeyev models, geometric contraction, diffusion and reaction-order models [76].

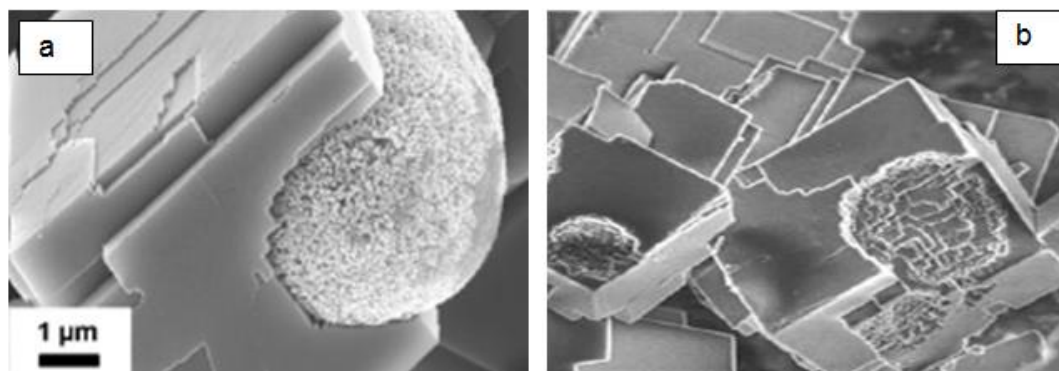


Figure 2-11 The transformation of vaterite to calcite (a) CaCO_3 precipitated using fast mixing Y- nozzle [77], (b) CaCO_3 precipitated by mixing Na_2CO_3 (1M) and CaCl_2 (1M) [69]

The degree of transformation at different time intervals and at different constant temperatures are then fitted to the different models where the model which best fits the data is selected and the rate constant and hence the activation energy and the frequency factor can be determined using the Arrhenius equation. The activation energy is used as an indication of what mechanism controls the transformation process where calcite growth is considered as a surface-controlled process and is characterized by a relatively high activation energy >34 kJ/mol [41, 68, 69] whereas vaterite dissolution is a diffusion-controlled process and is characterized by lower activation energy [73]. In the presence of certain additives such as some chemical inhibitors or solvents it is reported that these additives change the growth rate mechanism and prolong the life of vaterite [60-62, 78].

2.7 Solid-state kinetics

Solid-state chemistry has gained much interest in pharmaceutical sciences as the degradation of many drugs due to the de-solvation or polymorphic transformation affects its solubility and performance. Therefore, the solid state stability of polymorphic drugs and the kinetics of transformation are considered in the development of such products.

Khawam and Flangan [76, 79] provided a comprehensive review on the solid-state reaction kinetic concepts and the mathematical development of the different models available in the literature. The basic mathematical principles of solid-state kinetics arise from those of homogeneous reactions in solution or in gas such as in using the Arrhenius equation. However, solid-state kinetics differs as it takes into account particle size and geometric shape which are variables mainly addressed for heterogeneous reactions. In addition the rate of a homogeneous reaction is usually studied by following the decrease in the reactant concentration or the increase in the product concentration. However, concentration has little meaning in solid-state

kinetics due to the change in the reactivity distribution throughout the solid surface. Defects at the crystal surface or crystal lattice such as in the case of dislocations in the lattice structure during crystal growth or due to the presence of foreign atoms or ions, in addition to the edges and corners are all energized sites in which the activation energy is least and hence considered as a high reactive sites such as shown in Figure 2-12.

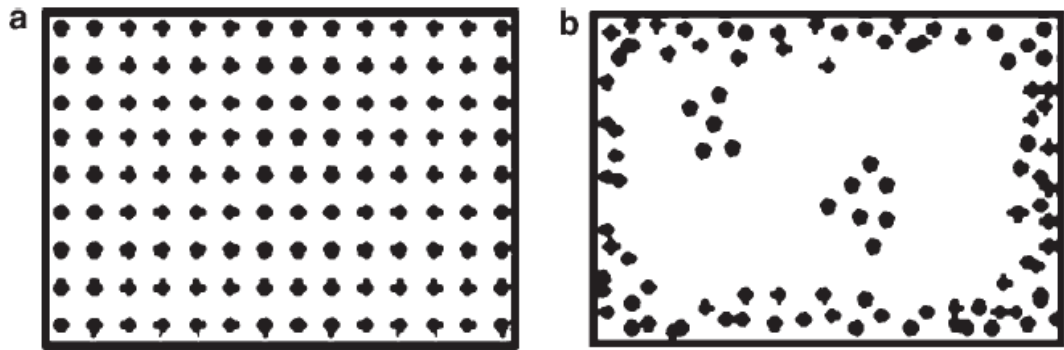


Figure 2-12 The distribution of energetic sites between (a) homogeneous system, (b) heterogeneous system [79]

Solid-state kinetics can be studied with thermal analytical methods such as by measuring the change in a sample specific properties as it is heated or held at constant temperature such as by measuring the evolution or consumption of heat using differential scanning calorimetry (DSC) or differential thermal analysis (DTA). If the reaction involves weight loss, the weight loss can then be followed throughout the reaction and the kinetics can be studied by thermo-gravimetry analysis (TGA). Reaction kinetics in solid-state can also be studied using X-ray diffraction (XRD) and nuclear magnetic resonance (NMR).

Weight loss or heat flow can be described as conversion fraction (α) which is a measure of the reaction progress. The conversion fraction for the case of weight loss is calculated by the following equation:

$$\alpha = \frac{m_o - m_t}{m_o - m_\infty} \quad 2.54$$

where: m_o is the initial sample weight, m_t is the weight at time t, m_∞ is the final sample weight.

The conversion factor is plotted against time for different solid-state models and is classified based on the shape of the curves to; accelerator in which the reaction rate increases with the reaction progress, decelerator in which it decreases with the reaction progress, linear which shows a constant reaction rate or sigmoidal models which show a bell-shaped reaction rate. The most appropriate models for a

particular reaction can be visually determined from the shape of α -time plot. The rate law for solid-state reaction can be expressed as the following:

$$\frac{d\alpha}{dt} = kf(\alpha) \quad 2.55$$

$$\frac{d\alpha}{f(\alpha)} = g(\alpha) = kt \quad 2.56$$

where: $f(\alpha)$ is the differential reaction model, g_α is the integral reaction model, k is the rate constant which is expressed using the Arrhenius equation:

$$k = Ae^{-\frac{E_a}{RT}} \quad 2.57$$

where: A is the frequency factor, E_a is the activation energy, R is the gas constant which is equal to 8.314 J/mol. K and T is the temperature in K.

2.7.1 Models derivation

Different models have been proposed based on mechanistic assumptions which are summarized in Table 2-2 and are classified as:

2.7.1.1 Nucleation and nuclei growth models

Nucleation is the process of formation of a new product at the reactive sites in the lattice of the reactant. The nucleation rate is derived based on the assumption of single-step nucleation or multistep nucleation; in single-step nucleation once the nuclei N are formed, they grow and the nucleation rate can be described as the following:

$$N = N_o(1 - e^{-k_N t}) \quad 2.58$$

$$\frac{dN}{dt} = k_N N_o e^{-k_N t} \quad 2.59$$

where: N is the number of growth nuclei at time t , N_o is the initial nucleation sites, k_N is the nucleation rate constant.

In multistep nucleation, several steps are required to generate a growth nucleus, where a molecule or a crystal is formed by a series of steps of addition of sub-nuclei until a critical size is formed, the rate of nucleation follows a power law which is defined as:

$$\frac{dN}{dt} = D\beta t^{\beta-1} \quad 2.60$$

where: β is the successive event to form a growth nucleus, $D = N_o(k_i t)^\beta / \beta$.

Growth of nuclei $G(x)$ is a size dependence growth where small nuclei (sub-microns) have low growth rate compared to large nuclei. The radius of a growth nucleus at time t is:

$$r(t, t_0) = \int_{t_0}^t G(x) dx \quad 2.61$$

where: t_0 is the formation time of a growth nucleus.

Nucleus shape factor σ and growth dimension λ are also important in nuclei growth process, where the nuclei growth rate can be expressed by the volume occupied by individual nucleus $v(t)$. Therefore, a stable nucleus formed at time t_0 and occupies a volume $v(t)$ is described according to:

$$v(t) = \sigma [r(t, t_0)]^\lambda \quad 2.62$$

The volume occupied by all nuclei $V(t)$ can be estimated by combining nucleation rate $\frac{dN}{dt}$ and the growth rate of a nucleus and is expressed as:

$$V(t) = \int_0^t v(t) \left(\frac{dN}{dt}\right)_{t=t_0} dt_0 \quad 2.63$$

This equation can be integrated for any combination of nucleation or growth rate to give a rate expression of the form $g(\alpha) = kt$ as listed in Table 2-2. However, the nucleation and growth nuclei models are based on assumptions and are summarized as the following:

2.7.1.1.1 Power law (P) models

In this model the nucleation rate is assumed to follow the power law equation 2.60 and nuclei growth is assumed constant $G(x) = k_G$, therefore equation 2.63 is represented as:

$$V(t) = \int_0^t \sigma (k_G (t - t_0))^\lambda (D\beta t_0^{\beta-1}) dt_0 \quad 2.64$$

By integration

$$V(t) = \sigma k_G^\lambda D' t^n \quad 2.65$$

where D' is function of β and $n = \beta + \lambda$

Since $V(t)$ is directly proportional to the reaction progress α , therefore:

$$\alpha = C \times V(t) = (kt)^n \quad 2.66$$

where: C is a constant which is equal to $1/V_0$ and $k = (\sigma k_G^\lambda C D')^{1/n}$

or the power law models are described as:

$$(\alpha)^{1/n} = kt \quad 2.67$$

Since power law models assume a constant nuclei growth, these models are usually applied to the analysis of accelerator type of curves.

2.7.1.1.2 The Avrami-Erofeyev (A) models

Nuclei growth rates in this case take into account the growth restrictions such as ingestion, which is the elimination of a potential nucleation site by the growth of an existing nucleus, or coalescence, which is the loss of reactant/ product interface when the reaction zone of two or more growing nuclei is merged. Growth restrictions are illustrated in Figure 2-13:

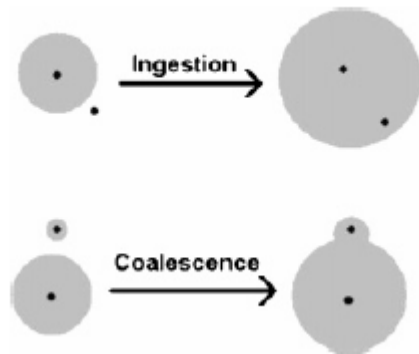


Figure 2-13 Nuclei growth restrictions; black dots are nucleation sites, shaded areas are growth regions [58]

The number of nuclei sites is described as:

$$N_1(t) = N_0 - N(t) - N_2(t) \quad 2.68$$

where:

N_0 is the total number of possible nuclei-forming sites, $N_1(t)$ is the actual number of nuclei at time t , $N_2(t)$ is the number of ingested nuclei and $N(t)$ is the number of activated nuclei into a growth nuclei.

In this case an extended conversion fraction α' is related to the actual conversion fraction α and is expressed as:

$$d\alpha' = \frac{d\alpha}{(1-\alpha)} \quad 2.69$$

where by integration:

$$\alpha' = -\ln(1 - \alpha) \quad 2.70$$

Substituting the value of α by α' from equation 2.66 gives the Avrami-Erofeyev model which is described as

$$(kt)^n = -\ln(1 - \alpha) \quad 2.71$$

or,

$$kt = [-\ln(1 - \alpha)^{1/n}] \quad 2.72$$

2.7.1.2 Geometrical contraction (R) models

These models assume that the nucleation occurs rapidly on the surface of the a crystal. The reaction progresses towards the centre of the crystal and depends on the crystal shape. Different mathematical models have been derived based on the following equation:

$$r = r_o - kt \quad 2.73$$

where: r is the radius at time t, r_o is the radius at time t_o and k is the rate constant.

According to this equation, the mathematical models are classified as:

2.7.1.2.1 Contracting area (R2) model

For cylindrical solid particles in which the weight of n cylindrical particles is:

$$m = n\rho h\pi r^2 \quad 2.74$$

where:

n is the number of particles, ρ is the density, h is the cylinder height and r is the cylinder radius.

By substituting the weight of particles into equation 2.54

$$\alpha = \frac{n\rho h\pi r_o^2 - n\rho h\pi r^2}{n\rho h\pi r_o^2} \quad 2.75$$

By substituting the value of r from equation 2.73

$$\alpha = 1 - \left(\frac{r_o - k t}{r_o}\right)^2 \quad 2.76$$

By rearranging equation 2.76 and by setting $k_o = k/r_o$, the contracting cylinder R2 model will be simplified as the following:

$$1 - (1 - \alpha)^2 = k_o t \quad 2.77$$

2.7.1.2.2 Contracting volume (R3) model

If the solid particles have spherical or cubic shape, the general formula for the model is derived in a similar approach to the cylindrical model and the contracting volume model is described as:

$$1 - (1 - \alpha)^{1/3} = k_o t \quad 2.78$$

2.7.1.3 Diffusion (D) models

In solid-state kinetics, the diffusion of reactants into the reaction sites or the products away from the reaction sites depends on the motion of the molecules into or out of the crystal lattice. This may be restricted by the presence of lattice defects. In diffusion-controlled reactions, the rate of product formation is proportion to the thickness of the product layer.

Considering for an infinite flat plane that does not have a shape factor (one-dimensional), l is the product layer thickness, A and B are the reactants and AB is the product. The mass of B moving to form AB is:

$$\frac{dl}{dt} = -\frac{DM_{AB}}{M_B\rho} \frac{dC}{dx} \quad 2.79$$

where: M_B and M_{AB} are the molecular weight of the reactant B and the product AB, respectively. D is the diffusion coefficient, ρ is the product density, C is the concentration of B in AB and x is the distance from interface to AB.

Assuming a linear concentration gradient of B in AB product layer, $\left. \frac{dC}{dx} \right|_{x=l} = -\frac{(C_2-C_1)}{l}$ and by integrating equation 2.79:

$$l^2 = kt \quad 2.80$$

where $k = 2D \frac{M_{AB}(C_2-C_1)}{M_B\rho}$

2.7.1.3.1 One-dimensional diffusion-controlled model D1

Since α is directly proportional to the product layer thickness l thus from equation 2.80:

$$\alpha^2 = k't \quad 2.81$$

where k' is a constant

2.7.1.3.2 Three-dimensional diffusional (D3) model

Applying equation 2.54 for n spherical particles where the diffusion occurs radially, the conversion fraction is:

$$\alpha = \frac{\frac{4}{3}n\rho\pi R^3 - \frac{4}{3}n\rho\pi(R-x)^3}{\frac{4}{3}n\rho\pi R^3} = 1 - \left(\frac{R-x}{R}\right)^3 \quad 2.82$$

where: x is the thickness of the reaction zone

By rearranging equation 2.82 and assuming $x^2 = l^2 = kt$, the D3 model is described as:

$$[1 - (1 - \alpha)^{1/3}]^2 = k't \quad 2.83$$

where: $k' = k/R^2$

2.7.1.3.3 Two-dimensional diffusional (D2) model

Similarly, the conversion factor for n cylindrical particles is:

$$\alpha = \frac{n\rho h\pi R^2 - n\rho h\pi(R-x)^2}{n\rho h\pi R^2} = 1 - \left(\frac{R-x}{R}\right)^2 \quad 2.84$$

and the D2 model is:

$$[1 - (1 - \alpha)^{1/2}]^2 = k't \quad 2.85$$

where: $k' = k/R^2$

2.7.1.4 Reaction order (F) models

These models are similar to homogeneous kinetic rate expressions where the reaction rate is proportional to the fraction of remaining reactants raised to a power which is the reaction order. These models are in general derived from the following equation:

$$\frac{d\alpha}{dt} = k(1 - \alpha)^n \quad 2.86$$

where

$\frac{d\alpha}{dt}$ is the rate of the reaction, k is the rate constant and n is the reaction order.

According to this equation, the mathematical models are classified as:

2.7.1.4.1 Zero-order (F0) reaction model

$$\frac{d\alpha}{dt} = k \quad 2.87$$

and by integration:

$$\alpha = kt \quad 2.88$$

2.7.1.4.2 First-order (F1) reaction model

$$\frac{d\alpha}{dt} = k(1 - \alpha)^1 \quad 2.89$$

and by integration:

$$-\ln(1 - \alpha) = kt \quad 2.90$$

2.7.1.4.3 Second-order (F2) reaction model

$$(1 - \alpha)^{-1} - 1 = kt \quad 2.91$$

and,

2.7.1.4.4 Third-order (F3) reaction model

$$0.5((1 - \alpha)^{-2} - 1) = kt \quad 2.92$$

Table 2-2 Different solid-state reaction models [58]

Model	Integral Form $g(\alpha) = kt$
Nucleation models	
Power law (P2)	$\alpha^{1/2}$
Power law (P3)	$\alpha^{1/3}$
Power law (P4)	$\alpha^{1/4}$
Avrami- Erofeyev (A2)	$[-\ln(1 - \alpha)^{1/2}]$
Avrami- Erofeyev (A3)	$[-\ln(1 - \alpha)^{1/3}]$
Avrami- Erofeyev (A4)	$[-\ln(1 - \alpha)^{1/4}]$
Geometrical Contraction models	
Contracting area (R2)	$[1 - (1 - \alpha)^{1/2}]$
Contracting volume (R3)	$[1 - (1 - \alpha)^{1/3}]$
Diffusion models	
1-D Diffusion	α^2
2-D Diffusion	$[(1 - \alpha)\ln(1 - \alpha)] + \alpha$
3-D Diffusion	$[1 - (1 - \alpha)^{1/3}]^2$
Ginstling- Brounshtein (D4)	$1 - \left(\frac{2\alpha}{3}\right) - (1 - \alpha)^{2/3}$
Reaction-order models	
Zero-order (F0/R)	α
First-order (F1)	$-\ln(1 - \alpha)$
Second-order (F2)	$(1 - \alpha)^{-1} - 1$
Third-order (F3)	$0.5((1 - \alpha)^{-2} - 1)$

2.7.2 Methods for studying solid-state kinetics for isothermal systems

Solid state kinetics are studied for isothermal and non-isothermal systems by both experimental and computational methods; in isothermal methods, the system is studied at several constant temperatures and a set of α -time curves is plotted at

each temperature as shown in Figure 2-14. The data is then analysed using model-fitting or model-free methods.

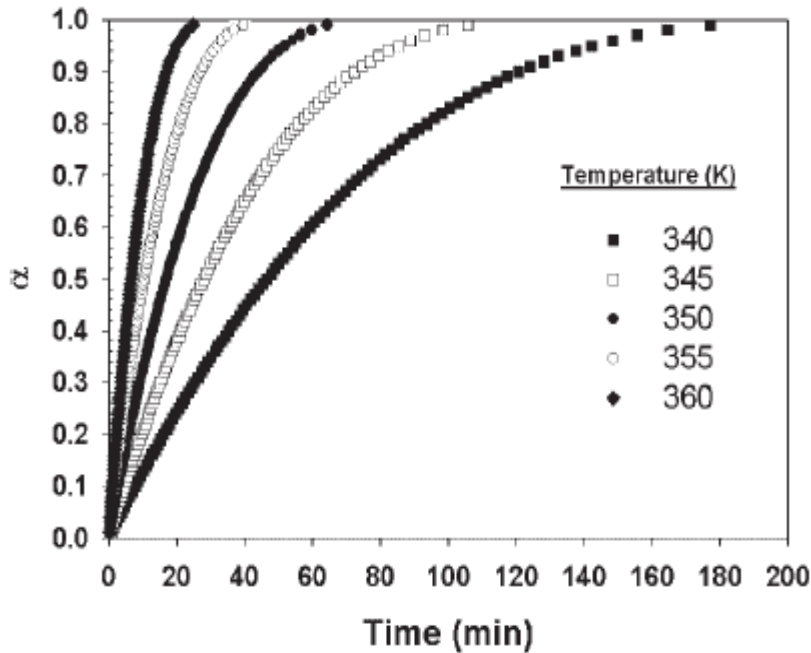


Figure 2-14 The isothermal method for evaluating solid state kinetics, α -time curves [60]

2.7.2.1 Model-fitting methods

In this method, the data is fitted into different models according to equation 2.56 where the model that gives the best fit to the data is chosen and the rate constant is calculated. The activation energy and frequency factor is then calculated from the rate constants at different temperatures using the Arrhenius equation 2.57

2.7.2.2 Model-free methods

In this method, the activation energy is the only kinetic parameter that is calculated without the need for the mechanistic assumptions of different models. This method requires several kinetic α -time curves to perform the analysis as shown in Figure 2-14.

The calculations are made from several curves at the same conversion fraction, the activation energy for each conversion point is calculated by taking the logarithm of the isothermal rate law equation 2.56 to give:

$$\ln g(\alpha) = \ln A - \frac{E_{\alpha}}{RT} + \ln t \quad 2.93$$

and this can be rearranged to:

$$-\ln t = \ln \left(\frac{A}{g(\alpha)} \right) - \frac{E_{\alpha}}{RT} \quad 2.94$$

Then a plot of $-\ln t$ versus $\frac{1}{T}$ for each α results in activation energy E_a for a specific α regardless of the model as shown in Figure 2-15(a). A plot of α versus the activation energy is generated as shown in Figure 2-15(b)

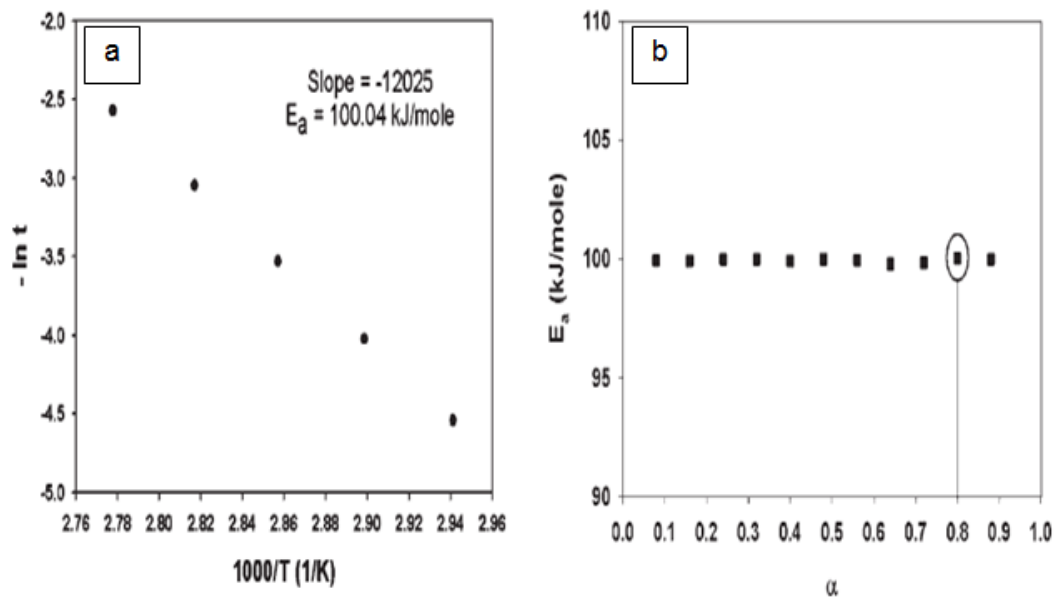


Figure 2-15 Model-free method for evaluating solid-state kinetics; (a) activation energy $E_{a\alpha}$ for a specific conversion fraction, the data here plotted for $\alpha = 0.8$, (b) Activation energies at different conversion fractions α [79]

However, Figure 2-15(b) shows a slight variation in the activation energy as the reaction progresses. This variation appears to be in conflict with chemical kinetic principles. Khawam and Flanagan [80] have shown that the variation in the activation energy is for two reasons: true variations and artificial variations. True variations of the activation energy are due to the complex nature and the different reaction mechanisms of a solid sample. The reactivity in solid-state may change due to the existence of crystal defects. The reactivity could also be affected by the variation of the experiment conditions such as temperature which could affect the kinetics not only through the reaction constant but also through the mechanistic changes in the elementary reaction kinetics. For instance, for complex reactions where two or more elementary steps are taking place at the same time, they have their own activation energy which may affect the rate of product formation.

The artificial variations of the activation energy result from errors in calculating the kinetic parameters such as when performing isothermal experiments, care should be taken to run them under the same experimental conditions for sample weight, sample size distribution and particles morphology. This means the temperature is the only variable for each run.

There are many kinetic models for solid-state in the literature and this is due to the non-isotropic nature of the solid-state which is affected by many factors such as

particle size, crystal defects, crystal strain, and other solid properties not relevant to liquid or gas phase processes.

For the processes of nucleation, crystal growth and transformation, they may take place either in the bulk solution where it is called scale precipitation or on a surface where it is called surface deposition.

2.8 Bulk precipitation and surface deposition literature review

Nucleation and crystal growth mechanisms in the bulk solution and on surfaces can be studied by various methods. Precipitation is usually studied by either microscopic observations where crystal size increase is measured directly, or by indirect measurement of the particle size distribution by different light scattering techniques. The assessment of scale precipitation and the estimation of the induction time could also be done by measurement of the change in the solution properties upon crystallization such as turbidity, pH and conductivity. Determining the amount of scale precipitated through tracking the amount of reactant ions in the solution with time using analytical techniques such as inductively coupled plasma-optic emission spectroscopy, or through monitoring the change in the solution pH with the estimation of different equilibrium constants and the activity coefficients for the reactions that are taking place within the crystallization process.

Surface deposition can be studied using an electrochemical technique in which the change in the rate of oxygen reduction due to crystallization at a metallic surface which is cathodically polarized is used to quantify surface deposition. Or by non-electrochemical techniques such as dynamic tube blocking tests in which scale is built up on the surface of a thin tube while flowing through it. The differential pressure between the inlet and the outlet of the tube as function of time is measured and translated to scale thickness. Rotating cylinder electrode, this technique could be operated either by electrochemical or non-electrochemical approach and is widely used in corrosion and scaling studies. In this technique scale is accelerated due to the high turbulence condition which is generated by moving the sample instead of the fluid. The mass gain due to deposition of the scale on the surface is then measured during different time intervals.

In the past, there was a belief that precipitation is a preliminary process that leads to deposition by secondary nucleation but recently it was found that deposits formed on a metal surface and precipitates formed in the bulk solution are due to two different processes, each has its own mechanism and kinetics regarding the induction time, nucleation, growth rates and crystal morphology [57]. The surface

may encounter CaCO_3 deposition without the solution being precipitated, this particularly occurs at low saturation ratios where the conditions are below the level at which homogeneous nucleation occurs [81]. The effect of bulk precipitation on scale deposition is examined for both CaSO_4 and CaCO_3 by [78]. It was found that bulk precipitation had a considerable effect on CaSO_4 enhanced deposition but not significantly affecting the deposition of CaCO_3 .

Studying the surface deposition process combined with bulk precipitation recently has been the focus of many researchers who conducted both the crystallization processes together *in-situ* and *in-real* time. In such studies bulk precipitation was assessed using turbidity measurement while surface deposition was assessed by image recording of the surface scaling at different times or by electrochemical analysis of the oxygen reduction reaction at a rotating disc electrode which is then translated to surface coverage percentage, nucleation and growth rates using image analysis. Different brine saturations at different temperatures are usually used and the initial rate for each process assessed by estimating the rate constants for bulk precipitation and surface deposition. An agreement between the various studies suggested the existence of different mechanisms due to the differences in the rate constants detected for bulk precipitation to that for surface deposition [82] or due to the differences in the induction times [57].

As mentioned previously, the process crystal growth involve two steps; diffusion followed by surface incorporation of reactant species where the dominant effect is the slower process. Studies show that the effect of solution pH is of great importance on the crystallization process; Andritsos [44] investigated the deposition rate in a flow loop using a stainless steel substrate. A continuous injection of sodium hydroxide solution was applied to create different pH conditions in the range between 8 and 13 and hence different supersaturation with respect to CaCO_3 is achieved. The deposition was varied between high pH solutions of greater than 9.5 to those with pH of less than 9. High pH solutions exhibited an immediate deposition (low induction time) and a high deposition amount which was nearly constant. Low pH solutions exhibited low deposition and high induction times and the deposition is increased with pH. These results suggested the existence of a critical supersaturation at which the deposition increases sharply between low and high pH solutions as shown in Figure 2-16. The scaling process was found to be surface-controlled for low pH solutions and diffusion-controlled for high pH solutions.

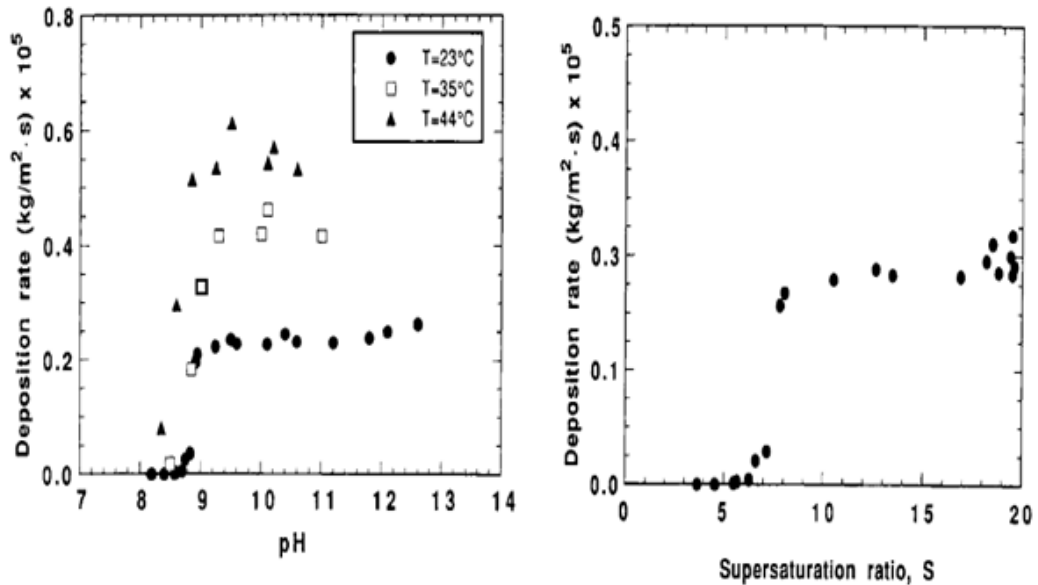


Figure 2-16 The change in the deposition rate with (a) pH at different temperatures, (b) SR at temperature of 23° C

This is in agreement with [53] in which the effect of changing the water chemistry (pH and supersaturation) on the scaling deposition of CaCO_3 was investigated; the brine supersaturation was varied by controlling the pH through continuous inline injection using different amount of KOH solution at 40°C. It was found that low supersaturation solutions of 5 and pH of 8 exhibited less deposition and a higher induction time than a reference solution of supersaturation of 9 and pH 9. A supersaturation solution of 10 and pH of 11 exhibited a similar order of deposition as the pH 9 reference solution of relatively similar supersaturation but lower pH. Calcite growth rate was studied by [39] using a pH-free-drift method in a closed system. It was found that calcite growth constant was not affected by an initial solution pH of greater than 7 but it was affected by an initial solution pH of less than 7, where the growth rate constant increased with the decreasing of the initial pH value and this became more significant when the solution supersaturation was lowered. The increase of the growth rates in low pH solutions and very low saturation ($S=1.5-2.5$) is also observed by [83] who claimed that, surface nucleation of calcite under such conditions resulted in high rate constants and low reaction orders which yield to high precipitation.

Supersaturation ratio is also found to have an important impact on both nucleation and growth processes. Although supersaturation is directly affected by the change in the solution pH and the temperature, it can also be affected by varying the initial concentrations of calcium and carbonate ions. The effect of supersaturation ratio on CaCO_3 scale precipitation and deposition show that brines of low supersaturation ratio exhibit short induction and rapid growth rate for surface deposition while bulk

precipitation may exhibit long or short induction and growth [57]. Another study suggests that the scale process is surface control under low supersaturation conditions while it is diffusion control under high supersaturation [44]. However, SR alone does not permit to predict the induction time and the kinetics of bulk and surface scale processes [82]. The role of fluid dynamics and mixing in addition to high supersaturation ratio may have a direct effect on crystal structure, according to [84] high SR induce rapid growth which may result in a change in the crystal habit. It was also suggested that the change in crystal structure may also be due to the presence of impurities or due to the diffusion field limitations especially at high growth rates.

Temperature has been reported to have a significant impact on the formed crystal polymorph through affecting the solubility [51, 55]. Temperature has also been reported to have a direct effect on the induction time, kinetics of the crystallization and nucleation mechanism. The induction time is decreased, the kinetics is faster and the amount of precipitation is high when the temperature is increased [85]. Temperature has also influenced the kinetics of crystallization and increased the homogeneous precipitation whereas heterogeneous deposition was increased at low temperatures [85, 86].

Hydrodynamics have been proved to have a direct effect on mineral scale formation. Studies have shown that calcium carbonate is surface-controlled at low Reynolds number while transport-controlled at high turbulent conditions [25]. Abdul Qudus et al. [46, 87-92] used a rotating cylinder electrode RCE to study the role of hydrodynamic conditions on scale deposition of different mineral scales in a once through continuous flow system at 60°C, for the deposition of BaSO₄, CaSO₄ and CaCO₃ on Stainless steel 316 [87-89] and the deposition of CaSO₄ (gypsum) on different substrates; Aluminium [90], brass [92], copper [91], polymer coated carbon steel and titanium [46]. It was claimed that the deposition rate increased linearly with the increase of the rotational speed. This result is in close agreement with Levich theory [93] which suggested that mass transfer coefficient is proportional to the square root of Reynolds number and the deposition at all specimen are governed by diffusional process at high rotating speeds. However, no significant effect of the rotation speed on the rate of deposition is observed when scale inhibitors are present [78]. According to this study, the presence of inhibitors acts by shift the growth mechanism from mass-control to surface-control so that retards the rate of deposition and reduces the effect of hydrodynamics; the study examined the effect of adding polycarboxylic acid, phosphonate and Inorganic polyphosphate

based chemical inhibitors on the mechanism of surface deposition of two scaling species CaSO_4 and $\text{Mg}(\text{OH})_2$.

2.9 Mineral scale control strategies

The potential of scaling can be controlled according to different strategies and can be classified into three categories [94]; those that affect the solubility, change the operating conditions and the characteristics of a surface to foul and those which alter the growth mechanisms.

1- Those which affect the water characteristics such as the solution solubility. Solubility can be influenced by reducing supersaturation levels through eliminating scale forming species and hence reducing the hardness ions such as Ca^{2+} , Mg^{2+} , Ba^{2+} ...etc. in the solution and replacing them by univalent ions such as Na^+ and H^+ . This is called water softening. This technique is effective and can provide 100% scale control but it is less attractive due to its highly costs compared to other techniques.

Acidification or pH control is a simple way to control scale formation by adding acids and lowering pH and hence affecting alkaline scales by increasing their solubility and reduce their supersaturation. Generally, sulphuric acid or hydrochloric acid are used for pH adjustment. However, due to the tendency for sulphuric acid to form sulphate scales, hydrochloric acid is preferred [21] although it is very corrosive.

Other methods include the use of magnetic devices to treat water [95]. It was claimed that the magnetic fields influence scaling kinetics by lowering the energy of nuclei, modify the local ionic concentration and chemical equilibria. Although this technique has been used widely as an environmentally sustainable method for water treatment but lack of reproducibility and agreed identification by which magnetic field influence scale inhibition have limited the credibility of the treatment.

2- Optimizing of the operating conditions and system design: such as operating a reverse osmosis system at temperature and pressure below the saturation level of calcium sulphate scale which is known for being the most frequent type of scale to form at membrane surfaces in water desalination [21]. Material selection in which the physical nature of the surface material at which deposition occurs is carefully selected. For example CaSO_4 scale has greater affinity towards aluminum and titanium substrates than stainless steel [46, 89]. Surface modification such as by applying surface coatings or changing the physical/chemical nature of a surface is also found to be effective. In general, parameters such as surface chemistry,

surface roughness, surface energy and surface hydrophobicity are all known to play a major role in the scale formation process on a surface [96]. A surface with low surface energy shows a significant reduction in scale formation [97].

3- Methods which act by delaying nucleation or retarding crystal growth through adding different chemicals (scale inhibitors) at different dosage rates; the presence of certain ions in solution may adsorb on the crystal growth sites and block the energetic sites of surfaces such as in the presence of phosphates and polyphosphates compounds. Some inhibitors such as carboxylic acids work by weakening the crystal structure and some have a chelating effect such as EDTA which bind up ions forming species in solution and reduce crystal growth. The presence of metallic ions such as zinc, Iron, magnesium, copper and many other also may have an inhibition effects but the mechanisms differ depends on how the ion interacts with the inhibitor.

The optimal dosing of chemicals is generally conducted by laboratory tests prior to full scale trials. The major concern associated with addition of chemical additives for managing the scale formation is the environmental impact. Commercially available chemical inhibitors can be classified into three major categories; phosphates, phosphonates and polycarboxylates. These non-organic inhibitors are considered aggressive to nature and alternative friendly inhibitors are important to find. These friendly inhibitors act as a non-toxic, bio-accumulate and bio-degradable chemicals [98].

Synthetic inhibitors derived from petrochemicals have been recently examined such as Poly aspartic acid PASP. This is a green inhibitor that has a biodegradable property and many studies [99, 100] has shown its effectiveness towards scale formation by acting on the crystal growth sites and modifying the morphology of the crystals formed. It was claimed by [100] that PASP based inhibitors are the most promising green scale inhibitors. Polyepoxysuccinic acid PESA is a biodegradable scale inhibitor in which 10 mg/l has an efficiency of 90% at varied water content making it suitable and alternative to PASP in water treatment processes as the latter is found to have less inhibition efficiency as temperature is increased.

CarboxyMethyl Inulin CMI is a biodegradable and non-toxic inhibitor which has significant inhibition effects on CaCO_3 due to the presence of carboxylic groups in its structure. Studies show that CMI is a good inhibitor for CaCO_3 over a wide range of concentrations; for high concentrations of 10000 ppm, CMI has the scale cleaning effect by dissolving CaCO_3 deposits [101]. A study showed that the higher the number of carboxylic groups, the higher the efficiency of the inhibitor towards

CaCO₃ precipitation [102]. Another study compared the efficiency of non-green Phosphinopolycarboxylic acid PPCA, a conventional inhibitor widely used in oilfields, with the green inhibitors PolyMaleic Acid PMA, PolyAspartate PA and CMI. The results showed that surface deposition requires higher inhibitor concentration than bulk precipitation and that the green scale inhibitors need to be presented at higher concentrations to have the same effect as PPCA [103].

3 Chapter Three Background on multiphase flow and oil/water emulsions;

3.1 Introduction

This chapter aims to define the system characteristics of the multiphase systems in which oil and water are mixed together under turbulent conditions. A brief description of petroleum fractions, followed by multiphase flow and different flow patterns that are expected to exist when the phases are flowing in horizontal pipes, in addition to particles based multiphase flow. As turbulent conditions will promote mixing of phases, oil/water emulsions are expected to form, the different physical characteristics of petroleum emulsions and the methods of emulsions stability and instability are also illustrated in this chapter. The outline of this chapter is illustrated in the following figure:

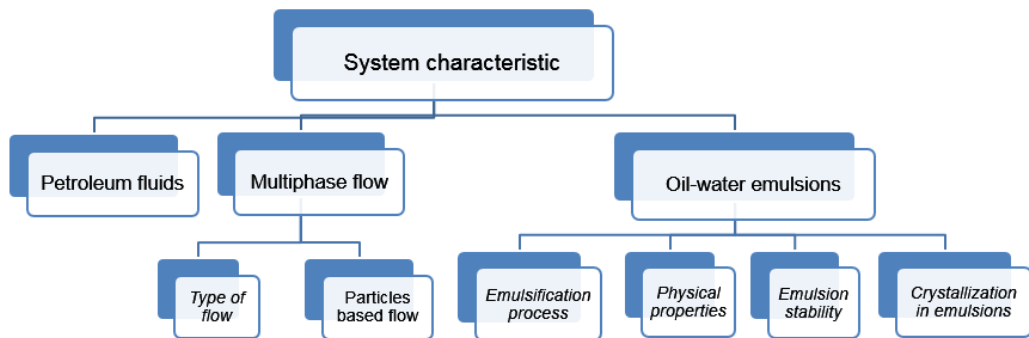


Figure 3-1 Outline for the chapter content

3.2 Petroleum fractions

Petroleum fluids are complex mixtures of hundreds of different hydrocarbon compounds that can be present as gas (natural gas), liquid (crude oil), semisolids (bitumen) and solids (wax or asphaltene). The carbon numbers of these components range from 1 for methane to as high as 50 for asphaltene. Generally hydrocarbons are divided into four groups [104]:

- Paraffins or alkanes which are divided into two groups of paraffins (straight chain) such as butane and iso-paraffins (branched-type) such as iso-butane. Both paraffins and iso-paraffins are saturated hydrocarbons which have a general formula of C_nH_{2n+2} .
- Olefins are unsaturated and have at least one double bond between two carbon atoms and in this case the compounds are called mono-olefins or

alkenes such as ethene $CH_2 = CH_2$ which have a formula of C_nH_{2n} . The olefins is called di-olefin when the compounds have two double bonds such as butadiene $CH_2 = CH = CH = CH_2$. These compounds are unsaturated due to the presence of the double bonds and are more reactive than saturated compounds. Because of the high reactivity of olefins with hydrogen which converts them to saturated compounds, olefins are not found in crude oils.

- Naphthenes or cycloalkanes are cyclic saturated hydrocarbons such as cyclohexane C_6H_{12} and have a formula of C_nH_{2n} . Naphthenic compounds are normally found in the crude oils.
- Aromatics are cyclic and have more than one double bond such as benzene C_6H_6 . These compounds can form derivatives with attached methyl, ethyl, or higher alkyl group. Aromatics have a formula of C_nH_{2n-6} and are considered saturated and unreactive due to the unique arrangement of the electrons in its structure. The attachment of benzene rings and naphthenic rings can form many combinations of compounds. These compounds are found in almost all crude oils. Other compounds such as sulfur, oxygen and nitrogen may also be found in high molecular weight aromatic compounds usually in heavy crude oils.

Because of the wide range of compositions, crude oils can exhibit a wide range of properties such as viscosities and densities. These properties are used to classify crude oils as light, heavy, and bitumen. Crude oils could also be categorized according to the gas-to-oil ratio (GOR) into black oil, volatile oil, gas condensate, wet gas and dry gas. Or into many other classifications based on the composition of the petroleum mixture that it contains such as: PONA classification which is Paraffins, Olefins, Naphthenes and Aromatics or SARA classification which is Saturates, Aromatics, Resins and Asphaltene.

A produced crude oil is transferred to a refinery after a series of treatment, separation (water from oil) and processing where it is converted in refineries into various useful products. In general petroleum products can be classified into [104]:

- Fuel products: such as liquid petroleum gas (LPG) which mainly contains propane and butane and is used for heating and cooking. Gasoline which contains hydrocarbons of C_4 to C_{11} and is used as car fuel. Kerosene and jet fuels which are used as a lighting source and for jet engines, respectively.
- Non-fuel products: solvents such as white spirit, benzene, toluene and xylene which are used for glue and adhesive products or for petrochemical

industry. Naphtha: this could also be categorized as solvents as it has properties corresponds to white spirit and is used as a raw material for petrochemicals. In addition to Lubricants, waxes and asphalt.

Petroleum iso-paraffinic hydrocarbon, naphtha solvent produced by treating a petroleum fraction with hydrogen in the presence of a catalyst is used as model oil in this study. The product consists of a mixture of aliphatic compounds and very low aromatics content. The physical properties of this oil are presented in chapter 4.

3.3 Multiphase flow system

Oil and water are often produced and transported together and the water fraction increases during the production life of a well. High fractions of water may be present in upstream facilities causing scaling threats. Mixing of oil and water may result in different flow behaviour due to the differences in the densities, viscosities and volume fractions as well as flow conditions and pipeline configurations. Figure 3-2 illustrates some different flow patterns in horizontal pipes which are mainly classified to:

Separated or stratified flow: In which phases flow in a semi-continuous mode with interface between the different phases. The relative movement of phases results in the development of turbulence at the interface and this tends to mix the phases.

Dispersed flow: in which one phase is totally dispersed into the other and results in discontinuous phase flow. An emulsion is a stable dispersion which can form a homogeneous mixture at sufficient high mixture velocity. An emulsion can be oil-in-water emulsion for high water fractions or water-in-oil emulsion for low water fractions. But this also depends on many other factors such as the type of the oil, the presence of fine solids and the different chemical additives.

Flow pattern maps are initiated for different cases of pipe diameters and materials and for different flowing fluids at different volume fractions and superficial velocities or mixture velocities. Crude oils tend to form dispersions of one phase into another which are found to exist over a wide region in the flow pattern maps. Generally, the type of the flow regime depends mainly on the phase fraction and the superficial velocities of water (v_{sw}) and oil (v_{so}). Oil-in-water (O/W) emulsions are found when conditions in the pipe are of high water cuts \approx (0.6-0.99) and high mixture velocities or high superficial water velocities [105-107] as shown within the red circles in Figures 3-3 and 3-4.

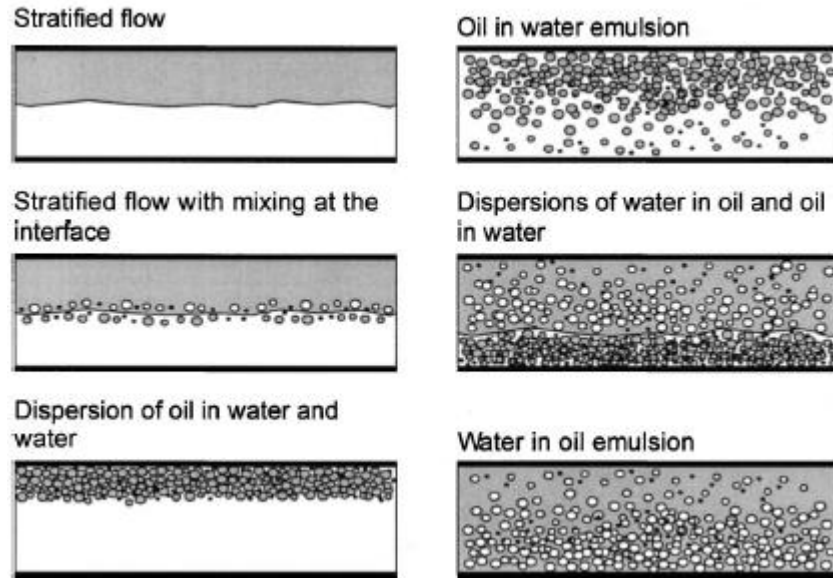


Figure 3-2 Oil and water flow patterns in horizontal pipes [108]

Oil-in-water emulsions are considered homogeneous under high shear conditions; these emulsions are unstable and separate immediately when lowering or stopping the mechanical energy unless some chemical additives or solid particles are presented and stabilize the emulsions. It was reported that mineral particles can collect at water/oil interface and contribute to emulsions stability [109-111]. Oil mineral aggregate (OMA) is a natural phenomenon that occurs when oil and mineral particles are present together in high turbulence conditions such as during oil production or after oil spills. Physical properties of mineral particles such as size, density and concentration; oil properties such as viscosity, droplets size, composition, density and concentration and other conditions such as temperature, pH, salinity, and hydrodynamic conditions are all factors affecting OMA formation [112, 113].

However, oil-in-water emulsion is the type of flow regime that this study is concerned with. A background about emulsions will be presented in section 3.4 of this chapter.

○ Stratified wavy (SW); ■ three layers; △ stratified mixed/oil; ---- phase continuity boundaries; ● stratified mixed/ water; ▲ stratified wavy/ drops; + mixed.

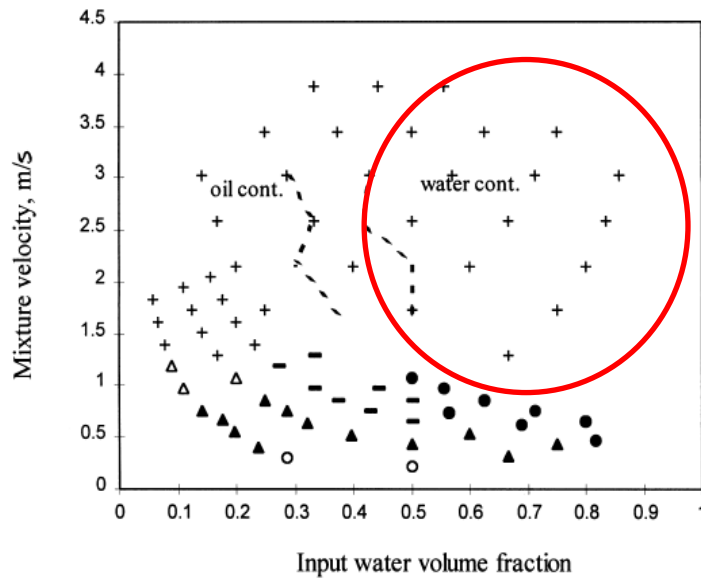


Figure 3-3 Flow pattern map as detected by Angeli and Hewitt et al. (2000) [105]

ST: Stratified flow, ST&MI: Stratified with mixing at interface, DO/W: oil-in-water emulsion, DW/O: water-in-oil emulsion, DO/W&O: dispersion of oil-in-water over water, DW/O&O: dispersion of water-in-oil under an oil layer, DO/W&DW/O: dispersion of oil-in-water and dispersion of water-in-oil

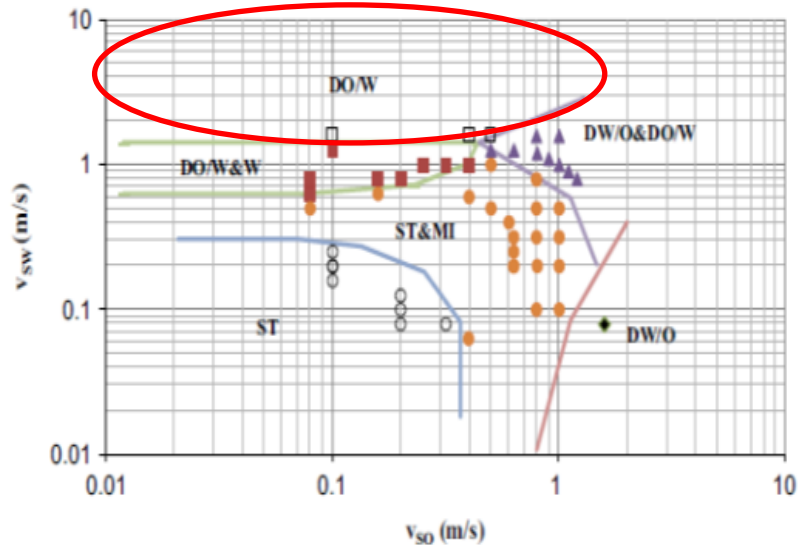


Figure 3-4 Flow pattern map as detected by A. Mukhaimer et al. (2015) [107]

3.3.1 Characterization of multiphase flow with particles

In order to characterize multiphase flow and to determine appropriate numerical method to solve for momentum, heat and mass transfer equations, coupling between particles which are in this case oil droplets and the continuous liquid phase must be defined. Generally multiphase flow can be considered as [114]:

Dilute flow when the effect of particle-fluid interactions dominates the overall transport of particles. The relative velocity of particles is diminished due to the effect

of drag forces which cause particles path tend towards the continuous fluid path. In this case different coupling between the particles and the continuous phase may take place as illustrated in Figure 3-5 and is defined as:

- One way coupling: dispersed phase is affected by continuous phase but not the reverse.
- Two way coupling: dispersed phase may have an effect on the continuous phase.
- Three way coupling: particle wakes and other continuous phase disturbances affect the motion of particles.
- Four way coupling: collision and other particle-particle interactions affect the motion of particles but do not dominate the overall flow.

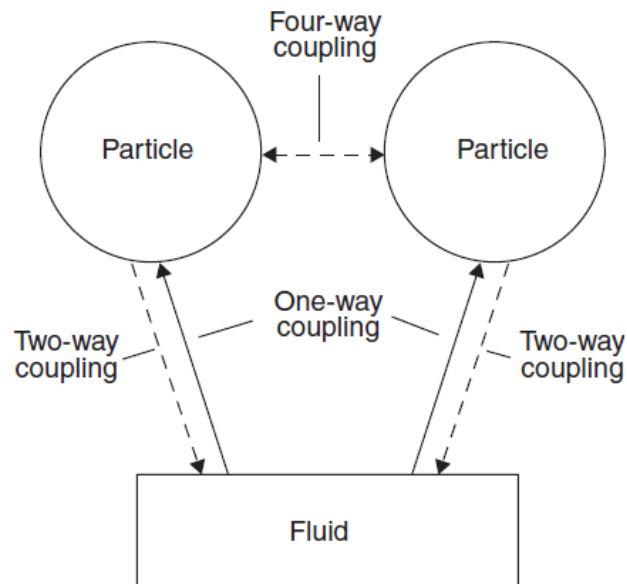


Figure 3-5 Coupling between particles and the fluid [114]

Dense flow when the effect of particle-particle interactions dominates the flow. In this case coupling between particles and the continuous phase is considered as four way coupling and can occur due to two separate mechanisms:

- 1- Particle-particle collision dominates the flow such as in fluidized bed.
- 2- Contact dominates the flow such as in granular flow.

A qualitative estimate of the nature of flow can be made by comparing the ratio of momentum response time τ_v and time between collision τ_c , so that

If $\frac{\tau_v}{\tau_c} < 1$, dilute flow

$\frac{\tau_v}{\tau_c} > 1$, dense flow

The response time can be estimated using the following equation:

$$\tau_v = \frac{\rho_d d_p^2}{18\mu_c} \quad 3.1$$

where; ρ_d is the density of dispersed phase, d_p is particle diameter and μ_c is the continuous phase viscosity. The time between collisions τ_c can be estimated using kinetic theory of gases.

The particle volume fractions can also provide a general indication for dilute or dense flow as illustrated in Figure 3-6. For particle volume fractions of 0.001 or smaller, the flow can be regarded as dilute flow. The dense flow is divided into collision-dominated flow in which the particles collide and results in a change in its trajectory. Contact-dominated flow in which the particles are in continuous contact and the contact forces are responsible for the particles motion.

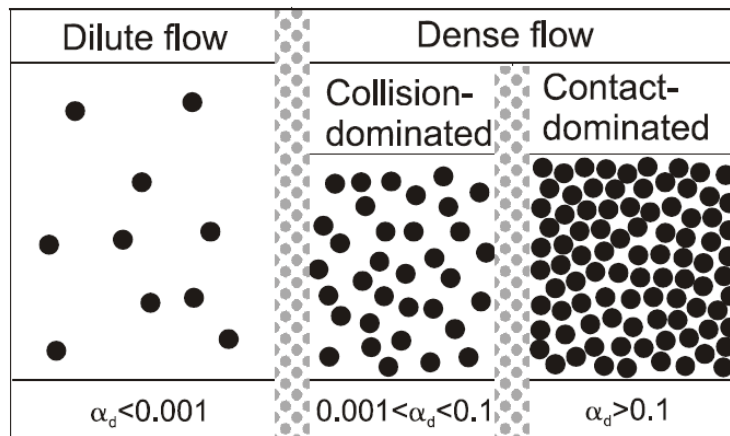


Figure 3-6 Classification of flow relative to dispersed phase volume fraction [115]

However, the presence of droplets or particles may or may not affect the turbulence of the carrier phase. For dilute system, particle motion has no effect and turbulence can be represented by models for single phase flow and this is the case of one way coupling. On the other hand in many disperse flow systems; the presence of particles may affect turbulence properties such as Reynolds stresses and turbulent kinetic energy. Most frequently the change occurs in turbulent kinetic energy by either suppression or enhancement. This effect is called turbulence modulation. Turbulence modulation can have a significant effect on rate of heat and mass transfer and chemical reaction rate. In fact many factors are found to contribute to turbulence modulation due to particles [116]; particles with low Reynolds number tend to suppress the turbulence while those with high Reynolds number tend to enhance it. Other factors include particle size where the particle wake plays an increasing role with an increase of particle size and particle density where turbulent

modulation is less observed when the density ratio between the particles and the external carrier is low. In addition to particle response time (the time required to change the flow velocity) or stoke number (the ratio between the characteristic time of a particle to the characteristic time of the flow) and particle-particle/ particle-wall interactions.

Defining the extent of coupling between the dispersed phase and the dispersion media is important in selecting the appropriate model to solve for multiphase flow. The extent of coupling can be analysed by comparing the length scale of motion to the particle diameter or by comparing the distance between the particles and the particle relaxation time. Many numerical models have been developed to solve wide ranges of multiphase flows systems. The derivation of the equations to solve Navier–Stokes equations for dispersed multiphase flow is far more complicated than for single phase flow due to the presence of interfaces, discontinuity of fluid properties across the interfaces and complicated flow characteristic.

3.4 Oil/Water emulsions

Emulsions are stable forms of dispersions (stability is a time dependent factor) that are produced from mixing of two immiscible liquids in which one forms liquid droplets called the dispersed phase or discontinuous or internal phase, which disperse into another liquid called the dispersion medium or the continuous or external phase [117]. Emulsions can be water-in-oil (W/O) or oil-in-water (O/W) and sometimes multiple emulsion in which tiny droplets of the external phase are tripped inside large droplets of the internal phase and both are suspended in the outer external phase [118] as illustrated in Figure 3-7.

As a rule of thumb, the phase with higher volume fraction is considered as the continuous phase but this is not always the case. Other factors that affect the type of formed emulsions are the presence of fine divided solids [119], the type of emulsifying or surface active agents if present and the type of oil (polar or non-polar). Inversion of emulsions may also be encountered in some cases such as in the presence of an electrolyte in which O/W emulsions are converted to W/O emulsions [120].

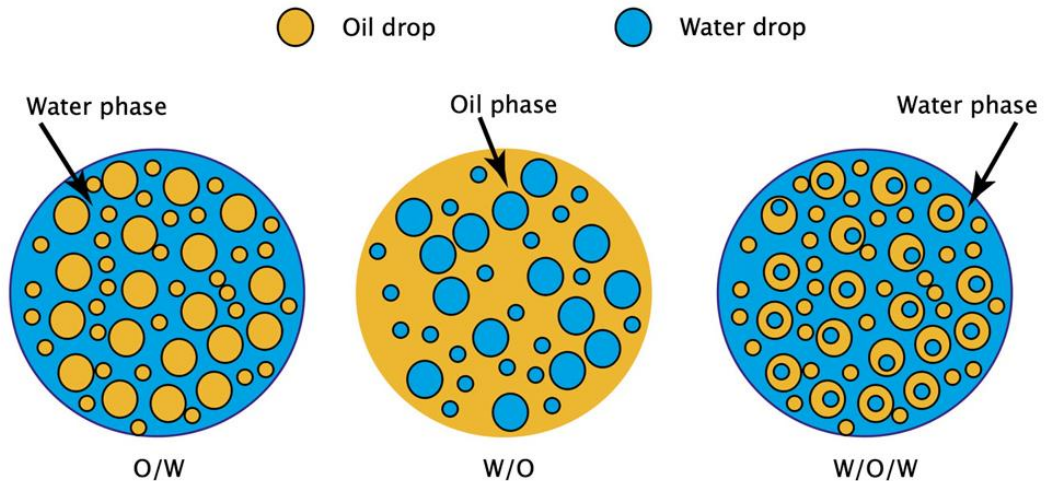


Figure 3-7 Types of oilfield emulsions [121].

In the petroleum industry emulsions may be considered desirable in some cases such as in handling and transporting asphalt for roadway coating or transporting of heavy crude oils and bitumen in long distance pipelines which is very difficult especially in cold weather due to their high viscosities. Under these conditions, the forming of oil-in-water emulsions was introduced as a method to reduce crude oil viscosity due to the shear thinning property of emulsions and hence enable easier transporting and saving of pumping power [122, 123]. Under most conditions, emulsions are considered undesirable and should be broken to avoid many processing problems and to improve oil quality.

3.4.1 Emulsification process

Emulsification or homogenization is the process of mixing two liquids together in order to form an emulsion. When two immiscible liquids are brought into contact, a layer between the two liquids will separate them according to their densities; the interfacial tension between the two liquids prevents the interaction between their molecules. Emulsions can occur naturally due to the presence of natural surfactant such as asphaltene and resins in crude oils [124], or due to the presence of fine solids [111, 125]. Emulsions can be also formed artificially by adding certain types of chemicals called surfactant or surface active agents. Generally, when the system is subject to hydrodynamic forces, the increased kinetic energy of individual molecules will tend to overcome the net attractive forces between the molecules. This results in disturbances in interfacial tension and break up of interface leading to dispersion of phases [126]. The formed emulsified droplets will have large interfacial area and low interfacial tension. Figure 3-8 illustrates the breakage process for the formation of an emulsion under hydrodynamic conditions.

In oil fields, transporting of crude oil in association with both water and gas from the wellbore into the well head through choke valves and pumps will result in high turbulence condition and will lead to fluid emulsification which further stabilise by the presence of divided solids [125]. Emulsions may also be formed at earlier stages in the reservoir either due to flow of oil and water in porous media [127] or during oil recovery such as in Micellar-polymer flooding or Alkaline-surfactant-polymer (ASP) oil recovery. These techniques are based on the injection of surfactant into the reservoir to reduce the interfacial tension between oil and water and hence reduce the capillary forces and recover the residual oil [128, 129]. ASP oil recovery was found to enhance oil recovery by 15-20% but the produced fluid contains a highly stabilised form of both O/W emulsion and W/O emulsion where the separation of such emulsions is difficult. It was claimed that the presence of alkaline components is responsible for this emulsion stability [129].

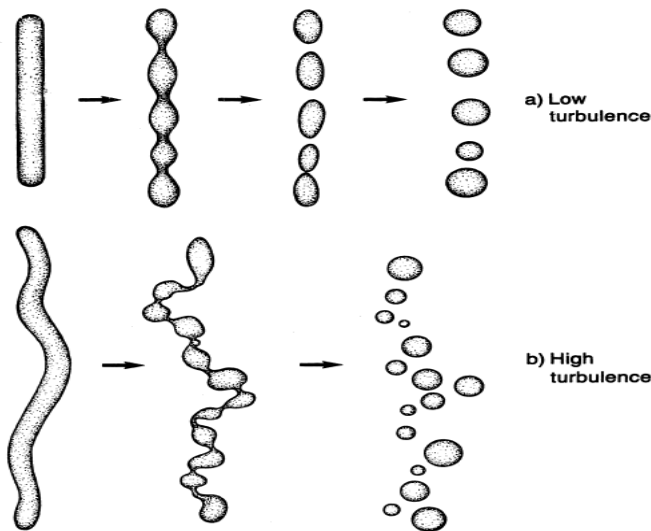


Figure 3-8 Emulsions formation under shear forces [130]

3.4.2 Physical properties of Emulsions

3.4.2.1 Interfacial tension

When two liquids are brought into contact a boundary between the two phases separating them according to their densities is formed and is called an interface. The interactions between the molecules of the same phase at interface are less than the interactions between the molecules of the same phase in the bulk solution. Therefore molecules at interface have higher free energy than molecules in the bulk solution. The work required to change the shape of a given interface or the work required to generate a surface area of 1m^2 is called Interfacial tension and is expressed as (N/m) or (J/m^2) . It is distinguishing between interfacial tension and

surface tension, as the latter is formed between liquid and air interface. Table 3-1 shows examples of some surface and interfacial tensions of some liquids:

Table 3-1 Surface tensions of some materials and their interfacial tensions relative to water at 20° C [117]

Material	Surface tension (mN/m)	Interfacial tension (mN/m)	Density (g/cm ³)
Water	72.80	-	0.998
Paraffin oil	30.00	50.00	0.800
Benzene	28.86	35.00	0.877
Toluene	28.40	36.10	0.866
n. Hexane	18.43	51.10	0.661

Temperature can have a significant effect on interfacial tension through an increase of the kinetic energy of individual molecules with a rise in temperature. This intermolecular energy tends to overcome the net attractive forces between molecules at interface and thus decrease the interfacial tension. Adding a small amount of solute to solution may have a substantial effect on interfacial tension either by lowering or increasing. Fatty acids and most soaps and detergent for example have the effect of lowering surface tension and are called surface active agents. On the other hand, compounds that contain large number of hydroxyl group such as sugar may slightly increase surface tension [117].

3.4.2.2 Emulsion rheology

Emulsions can exhibit Newtonian behaviour for very dilute to moderate systems or non-Newtonian for highly concentrated systems; a non-Newtonian behaviour may be shear thinning or shear thickening. As the viscosity of the external phase may be the essential factor of the final emulsion viscosity, other factors such as internal phase viscosity, temperature, shear rate, internal phase volume fraction and emulsifying agent may all have an important role towards the apparent viscosity of an emulsion [131-133].

Emulsions behave Newtonian at low volume fractions of the internal phase and in this case shear rate has no effect on emulsion viscosity. Non-Newtonian behaviour appears at high ranges of volume fractions and in this case viscosity changes with changing shearing rate. Temperature has a strong effect on emulsions viscosity where the viscosity decreases upon increasing of temperature. Emulsifying agents and its concentrations affect emulsions rheology by: (i) affecting the droplet size

and size distribution where, the smaller the droplet radius and the more homogeneous with respect to particle size, the more viscous is the emulsion. (ii) the surfactant molecules may form an interfacial film around droplets, this film may inhibit the internal circulation of the droplet and let it behave as a rigid solid which increases the interfacial viscosity and hence increases the emulsion apparent viscosity. Moreover, electrostatic effect by charging the droplets by an ionic surface active agent which tend to enhance the viscosity by repulsive forces of a nearby droplets. This is called electro-viscous effect in which the kinematic viscosity of the fluid μ can be expressed as a function of electric potential gradient E by an equation of the form [134]:

$$\mu = \mu_o(1 + fE^2) \quad 3.2$$

Where: μ_o is the bulk kinematic viscosity, E is the electric field charge (V^2), f is the visco-electric coefficient of the fluid ($V^{-2}m^2$). According to this equation, the effect of charges will always be to increase the viscosity irrespective of the sign of the charge.

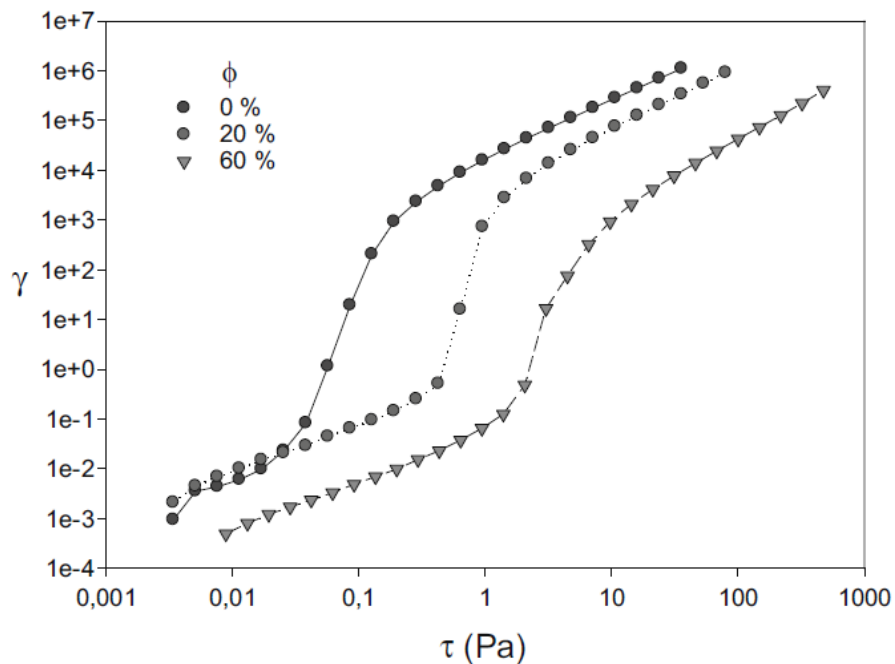


Figure 3-9 Shear stress, τ , versus shear rate, γ , for different volume fractions of water ϕ in paraffin crude oil emulsion at 20°C [133]

Generally, viscosity measurement apparatus are based on measurement of shear rate by increasing the shear stress in a given time interval such as shown in Figure 3-9; the measured shear stress and shear rate data can be used to construct models. Many theoretical and empirical correlations are available in literature for estimating emulsions viscosities. Some of these correlations are considered

classical and based on the internal phase volume fraction as the control parameter such as in Einstein model (1906):

$$\mu = \mu_o(1 + 2.5\phi) \quad \text{applicable for } 0.02 < \phi < 0.1 \quad 3.3$$

where: μ is the emulsion viscosity, μ_o is the external phase viscosity, and ϕ is the internal phase volume fraction. In this equation the relative viscosity is found to increase linearly with the dispersed phase concentration.

Many correlations have been proposed to enhance the volume fraction limitation of Einstein model. The most widely used was Arrhenius correlation (1917):

$$\mu_r = \exp(2.5\phi) \quad 3.4$$

This equation is found to be applicable to moderate internal phase concentrations where the relative viscosity μ_r increases exponentially with the internal phase concentration ϕ and the emulsions in this case remain Newtonian.

When the internal phase concentration increases, other factors need to be considered such as droplet interaction forces, droplet internal circulation and droplet size distribution. Models also considered that there is a limit for the internal phase content at which the emulsion viscosity is at highest it can tolerate and phase inversion will then occur upon a further increase in internal phase volume fraction. An adjustable parameter describes the maximum internal phase content becomes to appear in the empirical equation such as in the moony correlation (1951):

$$\mu_r = \exp\left(\frac{2.5\phi}{1 - (\phi/\phi_m)}\right) \quad 3.5$$

where: μ_r is relative viscosity which is the ratio of the emulsion viscosity to external phase viscosity, ϕ is volume fraction of the dispersed phase. ϕ_m is the maximum packing concentration.

Pal and Rhodes [135] used an empirical approach to correlate the viscosity data of both Newtonian and non-Newtonian emulsion using an expression $\phi_{\mu_r=100}$ which is the dispersed phase concentration at which the relative viscosity is equal to 100.

$$\mu_r = \left[1 + \frac{0.8415\phi/\phi_{\mu_r=100}}{1 - 0.8415\frac{\phi}{\phi_{\mu_r=100}}} \right]^{2.5} \quad 3.6$$

Both W/O and O/W emulsions for different oils with electro-viscous effect (electrically charged droplets) and with a range of dispersed phase concentrations of less than 74% are used to correlate this equation. The use of this empirical equation can be in conjunction with experimental determinations of shear stress versus shear rate curves at specific volume fractions of the dispersed phase ϕ .

3.4.2.3 Conductivity

Because water has a high dielectric constant, emulsions in which water is the continuous phase may be expected to show a high conductivity. On the other hand, emulsions in which the oil phase is the continuous phase may be expected to show a low conductivity. The electrical properties of the emulsions allow different types of emulsions (O/W or W/O) to be studied using a high frequency impedance or conductivity probes [105]. The conductivity can also be used as a method of separation for water-in-oil emulsions through enhancement of flocculation and coalescence of water droplets as a result of applying an electric field as shown in Figure 3-10 or as a method of measuring the stability of a water in oil emulsion [136]

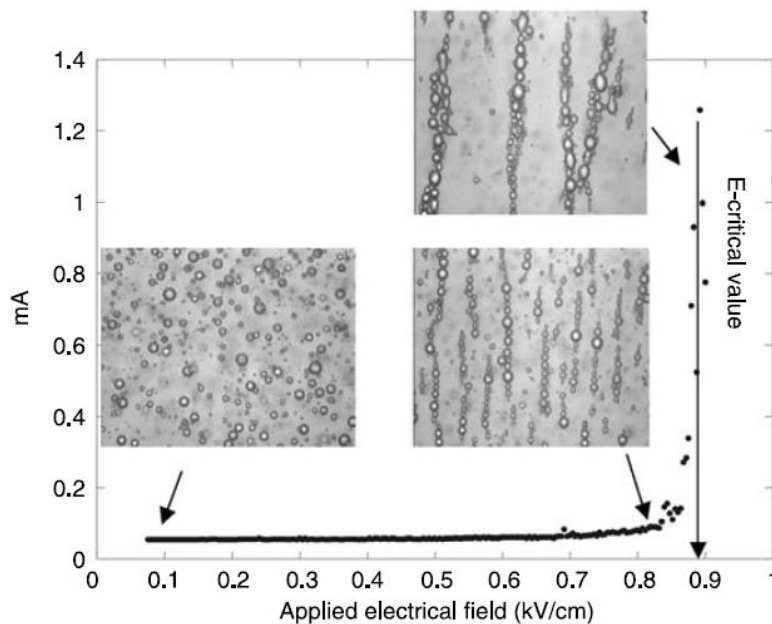


Figure 3-10 Emulsions behaviour under the influence of applying an electrical field [25]

3.4.2.4 Droplet size and size distribution

Oil field emulsions may have droplet diameters larger than $0.1 \mu\text{m}$ and may exceed $50 \mu\text{m}$ [137]. The size of droplets and its distribution depends on many factors such as hydrodynamics of flow, Interfacial tension between phases and also the type and the concentration of emulsifiers which directly affect the interfacial tension. Other factors such as the presence of solids and the bulk properties for both phases may also have a direct effect. Generally, emulsions that containing small droplets are more stable and more difficult to separate and greatly affect the size of the separation equipment [137].

Most size measurement theory is based on particles not on droplets. However, what applies to particles can be applied to droplets. A droplet usually has a spherical shape and the term diameter represents the diameter of a sphere unless there might be some degree of flocculation, which would give irregular shape and different diameters. A particle may have an irregular shape and the term diameter may be interpreted differently in this case. However, the shape of a droplet can be described using an overall shape factor, SF [138] which is defined as

$$SF = \frac{\sqrt{\text{roundness}^2 + \text{aspect}^2 + \text{radius ratio}^2}}{3} \quad 3.7$$

where: Roundness is $\frac{P^2}{4\pi S}$, P is the perimeter of a droplet and S is its surface area.

Aspect shape factor is the ratio between the major and minor axis of the ellipse and the radius ratio is the ratio between the maximum and the minimum radius of each shape. For a perfectly sphere shape, the overall shape factor is equal to one.

The droplet size and size distribution measurements can be classified into groups in which a mean diameter represents the entire group. These groups can be related to number, surface area or volume depending on the importance of the given property. The mean diameter \bar{D} is described as:

$$\bar{D} = \frac{\sum D_i d\phi}{\sum d\phi} \quad 3.8$$

where ϕ is the given property, such as if number of particles or droplets is important, then the number mean diameter and number distribution should be used and $d\phi = dN$ and the mean diameter described as:

$$D(1,0) = \frac{\sum D_i dN}{\sum dN} \quad 3.9$$

If the surface area is important such as in measuring the amount of surfactants or other additives or in the case of presence of solids at the droplet interface, then the surface mean diameter (Sauter mean diameter) and surface distribution should be used:

$$D(3,2) = \frac{\sum D_i^3 dN}{\sum D_i^2 dN} \quad 3.10$$

where: $d\phi = dS = D_i^2 dN$, S is the surface area.

Or if the amount of the dispersed phase is important such as in the oil industry where the amount of oil-in-water should meet the regulations, then volume mean diameter and volume distribution should be considered:

$$D(4,3) = \frac{\sum D_i^4 dN}{\sum D_i^3 dN} \quad 3.11$$

Where $d\phi = dV = D_i^3 dN$

Consideration must be taken when describing a system with the number of particles distribution from that based on volume distribution as the latter will increase this by a factor of 3 [139].

Particle size distribution functions are mathematical expressions used to characterize particles without the need for detailed plotting of the experimental data. These expressions also enable the extrapolation of information about particle size outside the measured range of values [140]. Several types of particle distribution can be determined depending on the nature of the system such as the normal distribution function:

$$f(d) = \frac{1}{\sigma\sqrt{2\pi}} \exp\left[-\frac{(d-\mu)^2}{2\sigma^2}\right] \quad 3.12$$

or,

Log-normal distribution function:

$$f(d) = \frac{1}{\ln\sigma\sqrt{2\pi}} \exp\left[-\frac{(\ln d - \ln\mu)^2}{2\ln\sigma^2}\right] \quad 3.13$$

where

μ is the mean of the distribution described by:

$$\mu = \sum \frac{d_i}{N} \quad 3.14$$

σ is the standard deviation:

$$\sigma^2 = \sum \frac{(d_i - \mu)^2}{N-1} \quad 3.15$$

N is the number of samples and d is the particle diameter.

Measuring particle size is important for many industries such as in the manufacturing of metallic powders, tribology, control of taste and texture of food, spray characterizations, pharmaceutical manufacturing control and in controlling of different nanomaterial properties such as chemical reactivity, diffusivity and permeability [141, 142]. Many methods have been developed for measuring particle size and size distribution, each method contains various techniques and each has its advantage and limitation according to the system being studied; these methods may be classified into the following [143]:

3.4.2.4.1 Electrical properties based technique (Coulter counter)

The difference in the dielectric constants and hence the conductivity between the two phases can be used to measure droplet size and size distribution through measuring and analysing the electrical pulses which are converted into digital data to produce information on droplet size distribution. Generally, this technique cannot differentiate between a droplet and a solid, the signal is proportional to the total solids and droplets content. This limits its applicability to systems with no or negligible solid content.

3.4.2.4.2 Physical separation technique

Such as gravitational /centrifugal sedimentation which measures the particle size according to its gravity force. As a particle settles due to gravitation or centrifugation, the intensity of the light beam will be changed due to the change in the concentration of the suspension. The rate at which droplets sediment may be measured by analysing for the droplet velocity using Stokes' equation for gravity sedimentation or sedimentation coefficient for centrifugal sedimentation. The droplet size distribution may then be determined.

3.4.2.4.3 Ultrasonic technique

Ultrasonic based or acoustic technique can provide reliable particle size for low dispersed volume fractions (below 0.1%) or concentrated emulsion (above 40%) without the need for system dilution [144]. Sound pulses are generated using an ultrasound detector which passes through the sample and this causes the signals to change in intensity. The sound speed and the energy attenuation of ultrasound are measured and the signals are then converted into amplitude-time relation. Converting the data into particle size distribution requires analysing and fitting the experimental data to theoretical models.

3.4.2.4.4 Light scattering technique

Light Scattering is the most common commercial technique that is widely used in detecting the sizes of various particles in suspensions. Generally when a beam of light enters a dispersion media, some of light is absorbed, some is scattered (reflected), and some is transmitted (refracted). This technique can be classified based on the dimensionless size parameter α which is defined as [145]:

$$\alpha = \frac{\pi m d_p}{\lambda}$$

where: d_p is the particle diameter, λ is the wave length of the incident radiation and m is the refractive index of the particles. Three domains may exist in this case:

$\alpha \ll 1$; small particles compared to wavelength of incident light; there will be scattered radiation due to diffraction (Rayleigh scattering method). This method can provide a direct measurement of particle size and can be used in the measurement of molecular mass of particles.

$\alpha \approx 1$; particles of about the same size to that of incident light wavelength; in this case radiation is partly reflected and partly absorbed (Mie scattering method); particle size and its distribution measurement are based on this method.

$\alpha \gg 1$; large particles compared to wavelength of incident light (Geometric scattering method). This technique is applicable for non-spherical geometries of known shapes.

These methods characterize the interaction of light with particles and provide physical basis and explanation for the operation of the various methods of particle-size analysis [146].

A Laser beam is widely used as a source of light because it has useful properties such as a monochromatic nature, coherence and spectral power which describes the intensity per unit wave length of the laser, so that the range of wave length is small and intense. This means that large amounts of power can be concentrated in narrow wavelength bands [146]. Laser systems can further be classified into different groups such as light backscattering which is based on Mie scattering principles. This predicts the way that light passes through or is absorbed by spherical particles. The Focused Beam Reflectance Measurement FBRM instrument is based on this method. A further description of the methodology of the FBRM technique will be illustrated in chapter four. Another laser system based group is the Fraunhofer diffraction theory which is based on the measurement and interpretation of an angular distribution of light diffracted by droplets. This predicts the way that light is scattering when a particle is passed through a laser beam. In fact a combination of Mie scattering and Fraunhofer diffraction techniques forms the basis of every modern "laser diffraction" instrument that provides the optimal method for analysing most samples over a wide range of sizes [147]. A Malvern Mastersizer is an instrument that operates according to these two methods.

3.4.2.4.5 Optical and video microscopy

Optical microscopy is a popular technique but requires sample dilution so that only a small part of the emulsion is analysed. Recently, there has been an increased

tendency to use the video microscopy technique due to the development of image analysis software which provides a wide range of analytical capabilities for acquiring, enhancing and analysing images [138] as shown in Figure 3-11. Many parameters can be determined for each droplet such as diameter, area, roundness, aspect, and radius ratios, in addition to droplet size distribution. The limitation of this technique is that the sample must be transparent and both phases must have different refractive indices or different colours to make them distinguishable. In addition to how concentrated the emulsion must be.

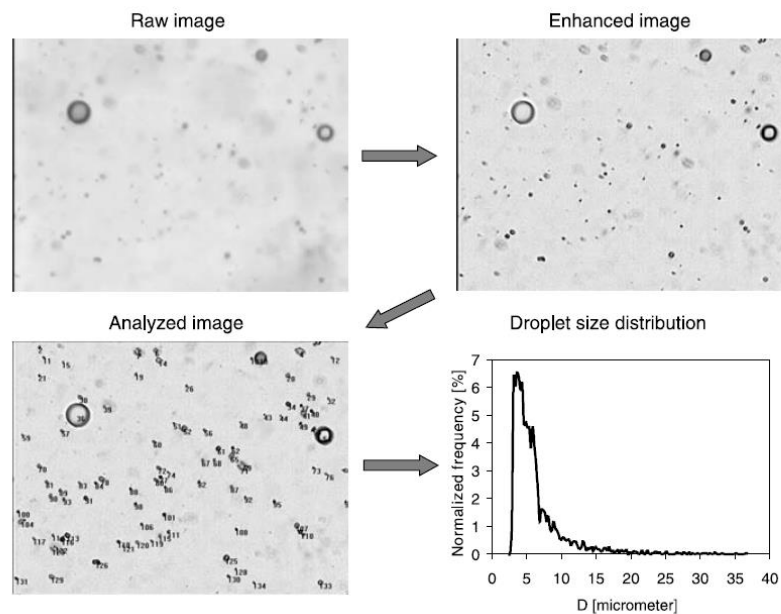


Figure 3-11 Steps of image analysis [138]

Each of the previous techniques have different size regions which they can detect [148]. However the suitability of each technique depends on the system to be studied and its ability to provide sufficient representation of the system. Data acquisition and processing are then required to reproduce the mean droplet properties, their distribution and the standard deviation in a histogram or as a distribution function if sufficient data are available [140].

3.5 Emulsions stability

Emulsions are dispersions of one liquid in another liquid in which the total interfacial area between both liquids is large. This high interfacial area results in high free energy and this makes the system thermodynamically unstable. A stable emulsion is the one in which its droplets do not exhibit creaming or sedimentation which naturally occurs from the density differences between the oil and water. To have an emulsion that can persist for a long time then it is necessary to add a certain type of modifier to reduce the interfacial tension between the phases and increase the

activation energy to prevent instability. Emulsion stability is based on three methods [117]:

3.5.1 Double-layer theory

Stabilization by this method occurs due the presence of charges (*+ve*, or *-ve*) at the surface of the droplets. These charges bring as many of the opposite charges around it, forming a double layer. If two particles surrounded by double layers approach each other, the double layer will interact and lead to repulsion between particles and hence add stability to the emulsions. Addition of an ionic surface active agent generally stabilizes the emulsions according to this method. Usually oil-in-water emulsions stabilise according to this method because the double layer thickness is much greater in water than in oil due to its highly dielectric nature.

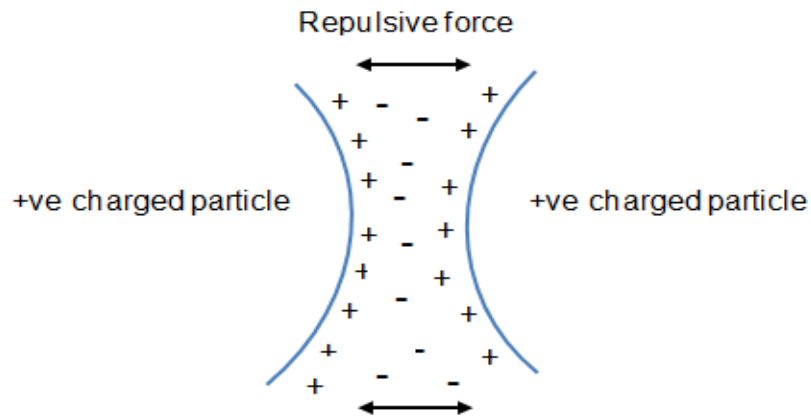


Figure 3-12 Emulsions stabilized according to double layer theory

3.5.2 Steric stabilization

Stability exerts in this case due to the presence of an adsorbed layer, usually polymeric in nature, at the oil-water interface. These compounds have a dual solubility and called amphiphilic when the continuous phase is water and this contains one part that has a strong affinity to water (hydrophilic) and another part that has little or no affinity to water (hydrophobic). These units incorporate onto the surface by some kind of chemical bonding. Usually water-in-oil emulsions stabilise according to this method. The hydrophilic portion will dissolve in water while the lyophobic portion will extend into the dispersion medium as a tail as shown in Figure 3-13. There are two approaches for the repulsion process by this method:

1- Volume restriction effect: in which a second particle is excluded from the volume occupied by the adsorbed layer.

2- Osmotic pressure effect: when the adsorbed layer on two particles interact with each other, the increased polymer segment concentration creates a local osmotic pressure which acts as a repulsion force.

However, steric stabilisation is found to have an effect when small distances between the droplets are existed as illustrated in Figure 3-13.

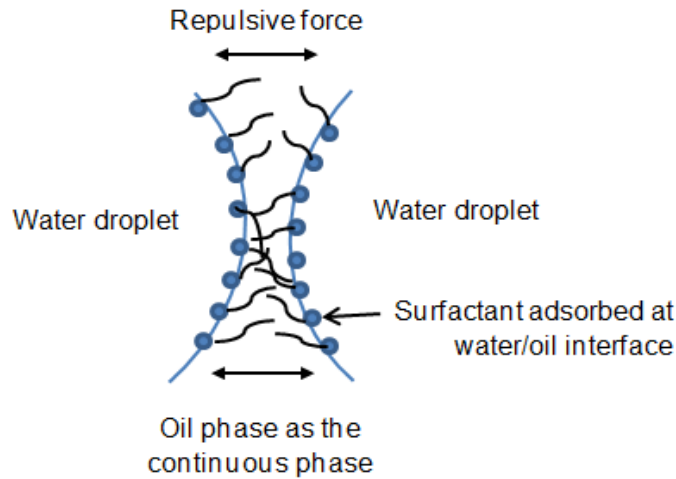


Figure 3-13 Emulsions stabilized by a surfactant according to steric method

Surfactants or surface active agents are compounds that possess the ability to adsorb onto the interface and reduce the interfacial tension. Both asphaltenes and resins have hydrophobic and hydrophilic parts, which give them surfactant character [149].

Emulsions are thermodynamically unstable structures but may exhibit kinetic stability by the adsorbed material at the interface [150]. Adsorbed surfactants at interface provides expanding surface force π which acts against the normal interfacial tension and lowers the surface free energy according to the following:

$$\gamma = \gamma_i - \pi \quad 3.17$$

Where: γ_i is the initial surface tension.

If $\pi \approx \gamma_i$ a low value of γ is reached and the emulsification can take place as a consequence of a small increase in surface free energy. Surfactant adsorption is thermodynamically described by Gibbs adsorption equation for dilute binary system with monolayer adsorbed film:

$$\Gamma_S = - \frac{d\gamma}{RT d \ln c_s} \quad 3.18$$

Where: Γ_s is surface excess of surfactant (mole/cm²), C_s is the molar concentration of surfactant which is replaced by surfactant activity for a concentrated solution and γ is surface or interface tension (mN/m).

A plot of γ versus $\log c_s$ gives a descending curve with a negative slope due to a lowering in the surface tension upon increasing the surfactant concentration. This slope enables the estimation of the surface excess of surfactant (Γ_s) and hence the area occupied per surfactant molecule (a):

$$a = \frac{10^{16}}{N_A \Gamma_s} \quad 3.19$$

Where: N_A is the Avogadro number, a is the area occupied per molecule of surfactant (A²), 10^{16} is a conversion from cm² to A².

Increasing the concentration of surface active agent beyond that needed to form a complete monolayer of adsorbent molecules which is termed Micelles, may yield anomalies in some bulk properties of the solution such as surface tension, vapour pressure, osmotic pressure and conductivity [117].

3.5.3 Stability due to the presence of solids (Pickering stability)

Crude oil emulsions are stabilised naturally due to the presence of asphaltene. Asphaltene can be precipitated in light hydrocarbons such as alkanes when it presents in high percentage or due to pressure reduction during production. Asphaltene aggregates add stability to water-in-oil emulsions according to the Pickering method [11]. Other solid particles such as wax, hydrates and inorganic solids can also stabilize oilfield emulsions. The mechanism of stabilization in this case depends on solid wet-ability by both phases. Particles that do not wet by both phases cannot be considered as stabilisers. Solid particles may be wetted by one phase more than the other and this can be used as an indication of the type of the emulsion formed; for instance particles which are more wetted by water than oil stabilise O/W emulsions, while particles which are more wetted by oil stabilise W/O emulsions as shown in Figure 3-14.

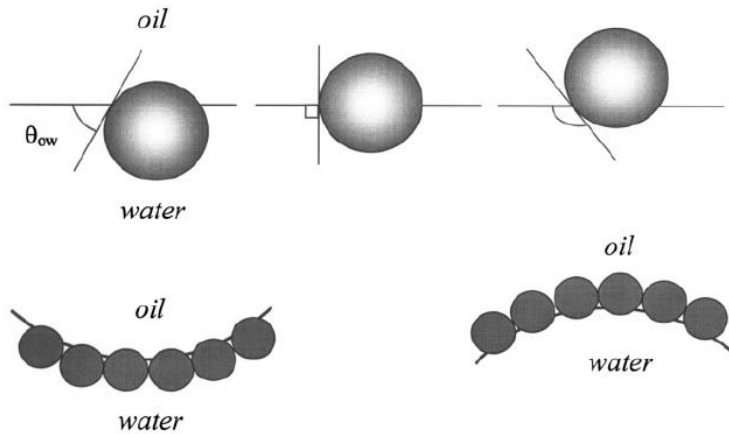


Figure 3-14 Pickering type stability; (Top) contact angle between the oil and water; (bottom) different solid wet-ability by oil and water [14]

For emulsions, three interfaces can exist between the two immiscible phases and a solid, where they all meet at a point, and a contact angle between the two liquids can be estimated by:

$$\cos\theta = \frac{\gamma_{so} - \gamma_{ws}}{\gamma_{wo}} \quad 3.20$$

If $\gamma_{so} > \gamma_{sw}$, $\theta < 90^\circ$, in this case the solid will be mainly in water.

If $\gamma_{so} < \gamma_{sw}$, $\theta > 90^\circ$, in this case the solid will be mainly in oil.

However, the factors that enhance emulsions stability can be summarized as the following:

- Lowering of interfacial tension such as in the presence of acidic compounds in crude oils especially asphaltic crude oils. These acids react with strong alkali and form petroleum soaps which reduces interfacial tension between the oil and water and has a large effect on emulsion stability[136, 151].
- Mechanically strong films around droplets surface may act as a barrier to coalescence and this could be enhanced by adsorption of fine solids or closed packed surfactant molecules.
- Small volume of dispersed internal phases or dilute systems which reduces the frequency of collisions and aggregation.
- Small particle sizes can improve the stability such as microemulsions can be considered thermodynamically stable. Phase inversion method in which emulsions may be suddenly changed from O/W to W/O emulsions when stabilised by certain types of surfactant. In this case an extremely small droplets may be produced and add stability to emulsions [117].

- Physical properties of the external phase such as increasing of pH [152] and high viscosity medium are showed to affect emulsion stability and slow the rate of creaming and coalescence.

3.6 Emulsions instability

Demulsification is the conversion process of an emulsion to the separate forms of oil and water and therefore it is the reverse of emulsions stability. Generally, when the mechanical agitation which is used for creating an emulsion from pure oil and pure water (no chemical stabilizing agents) is removed or stopped, the two phases tend to return to their normal thermodynamic stability state by reducing their contact area. Since oil density is less than water density, a layer of oil is created on the top of a layer of water. A more kinetically stabilized emulsion could be created by using a sufficient amount of emulsifier during the emulsification process. The role of an emulsifier is to prevent oil droplets merging together for a reasonable period of time. Therefore, knowledge of the most efficient method for breaking the emulsion requires knowledge about the physical nature of its stability and the type of the stabilizer used. There are three methods of emulsion instability:

3.6.1 Creaming

In this type of emulsions instability, the oil droplets tend to move upwards and collect at the top surface. This occurs due to the oil droplets having a lower density than the dispersion media which is water in oil-in-water emulsions. If the density of the dispersed phase is higher than that of its surroundings such as in water-in-oil emulsions, the water droplets will tend to move downwards and collect at the bottom of the vessel and this is called sedimentation. These phenomena occur according to Stokes' law in which a balance between the forces acting on a spherical particle and the surrounding liquid may determine whether the particle will cream up or sediment down and the rate at which these occur.

The two forces acting on a particle are the gravity force F_g which acts by pulling the particle downward but when the density of the particle is less than the density of its surroundings, this force acts by pushing the particle upward. The drag force or frictional force F_f which acts against the particles direction of travel is shown in Figure 3-15. Stokes' law is defined as:

$$v_{stokes} = -\frac{2gr^2(\rho_p - \rho_f)}{9\eta_f} \quad 3.17$$

Where: r is the radius of the particle (μm), g is the gravity acceleration constant (m/s^2), ρ_p and ρ_f is the density of the particle and the surrounding fluid in (kg/m^3), respectively and η_f is the fluid shear viscosity in ($\text{mPa}\cdot\text{s}$).

Gravity separation by Stokes' law is known as one of the techniques used for treating oil. According to Stokes' law equation, the larger the particle size and the higher the density difference between the phases, the faster the separation. Thus the lighter the crude oil is, the easier it is to separate. In addition, the higher the temperature, the lower the emulsion viscosity and hence the faster the separation.

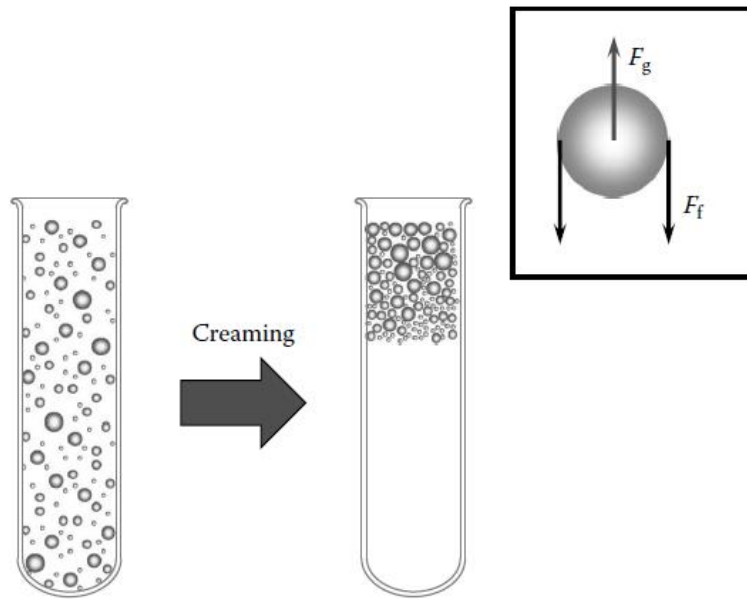


Figure 3-15 Emulsions instability due to creaming; the particles are separated according to gravity effect [153]

3.6.2 Droplet flocculation

In which the droplets aggregate to form clusters of droplets without changing in their integrity. Flocculation accelerates the rate of gravitational separation in dilute emulsions due to the increase in the droplets size. Many mathematical models were derived to account for droplet flocculation rate in dispersion systems [154]. These models account for the collision frequency and the fraction of collisions that lead to aggregation. Generally, oil-in-water emulsions which are stabilised with an ionic type surfactant are stabilized against flocculation. The electrical charge on the surface of the oil droplets in this case generates an electrostatic repulsion between the droplets. Sterically stabilized emulsions are also stabilised against flocculation, however there are some conditions such as increasing temperature which promote flocculation [153].

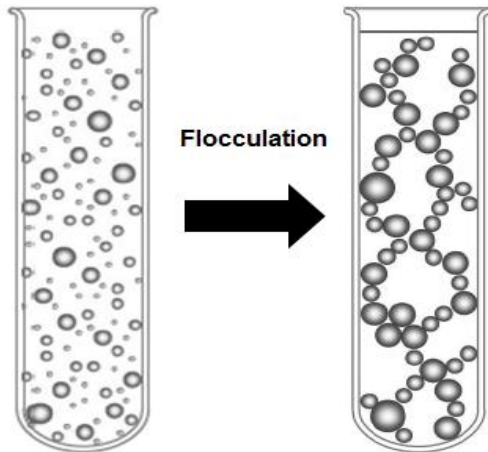


Figure 3-16 Emulsions instability due to Flocculation; The droplets aggregate and form a network of connected particles [153]

3.6.3 Coalescence

In this type of emulsions instability, two or more droplets merge together forming a single larger droplet. Coalescence causes the emulsion to cream or sediment much faster due to the resulting larger droplets. This process occurs when the droplets come in close contact and the thin film around the droplets ruptures and the fluid inside the droplets merge together. The time required for the droplets to come into contact is a function of the mechanism of the droplets movement. When the droplets come into a very close position, a relative thin film of the surrounding liquid forms between the droplets and this film continues to thin to a certain point where other factors such as hydrodynamic interaction forces and nature of the colloidal system may lead to the droplet to move apart, or flocculate or coalesce.

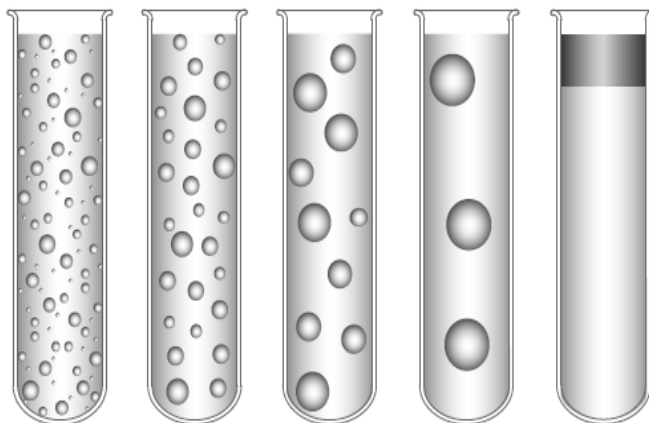


Figure 3-17 Droplet coalescence; the droplets increase in size upon coalescence and this lead to a complete creaming with time [153]

3.7 Crystallization in emulsions

Crystallization in emulsions has been widely studied in the food industry for dairy products to ensure a favourable texture for ice creams and whipped toppings [155] and in pharmaceuticals for emulsions based delivery systems which are used for encapsulating crystalline bioactive components for oral consumption [156]. The feasibilities of this technique are the encapsulation, the protection and the controlled-release of active ingredients. Encapsulation is also used in the food industry for various vitamins, minerals and preservatives. Fat crystallization in emulsions is found to take place upon cooling inside the droplets due to the presence of fat or lipid in the dispersed phase which is oil. The nucleation in this case may take place according to four mechanisms [157]:

(i) In the bulk of a droplet and it is called volume homogeneous nucleation; a high degree of sub-cooling is required before the small solid phase can grow to macro-size. (ii) In the bulk of the droplet due to the presence of some impurities which will act as the starting point for nucleation and is called volume heterogeneous nucleation; a lower degree of sub-cooling is required and nucleation in this case occurs more rapidly. (iii) Surface heterogeneous nucleation, due to the presence of adsorbed polymeric stabilizers, where the hydrophobic part may have the same structure as oil and act as a heterogeneous surface [158] or (iv) due to the collision of solid droplets (crystallized ones) with liquid droplets (non-crystallized ones) and this may induce nucleation and this is called inter-droplet heterogeneous nucleation [159].

Adding an organic phase to change the characteristic of inorganic materials has attracted attention in various industries such as in paper and ceramic manufacturing. Such studies were particularly directed into improving the mechanical properties of CaCO_3 particles by changing the particles morphology. The aragonite polymorph of calcium carbonate for example has received much attention in the paper industry due to its ability to form thick and compact layers more than calcite, making it preferable as a filler material. A study by [160] investigated the important role of adding different organic additives onto the morphology of CaCO_3 particles in the presence of surface active compounds to ensure emulsification. Others such as [161, 162] studied the influence of different surfactants on the polymorph and morphology of calcium carbonate in water-in-oil emulsions.

In the petroleum industry, organic crystallization in the presence of emulsions has been extensively studied such as asphaltene precipitation which enhances the

stability of emulsions, wax precipitation and deposition which can lead to severe problems in pipelines and processing equipment. Particle-stabilized emulsions were given special attention in petroleum science. In fact there are several types of solid particles that can be found to flow with crude oils such as silica, clays, waxes, asphaltene, corrosion products and mineral scales.

CaCO₃ scale has also been studied in the presence of the mono-ethylene glycol (MEG) solvent which is usually injected to prevent hydrate formation during the transportation of natural gas and condensate in long subsea pipelines. It was suggested by [163] that the solubility of most of the salts were decreased with the increasing MEG concentrations and the existence of alkaline conditions enhance the precipitation of calcium carbonate. Another study [164] suggested the increase in the induction time of CaCO₃ precipitation with the increase in the MEG concentration whereas [62] suggested that the presence of MEG inhibited calcite crystal growth. Table 3-2 summarise some of the studies concerned with mineral scale formation in the presence of an organic phase.

There is a lack of the understanding with respect to the mechanism by which CaCO₃ scale precipitates and deposits in the presence of oil. The conditions in the field allow both the oil and the water to mix during different stages of the production and transportation. This results in emulsions formation combined with scale formation. Calcium carbonate scale formation in oil-in-water emulsions is studied here in order to develop a better understanding of the crystallisation mechanism in such a system. The next chapter will discuss the various methodologies and techniques which are used in this study.

Table 3-2 Summary of some of scale formation studies in the presence of an organic phase.

First and last author's name (year)	Non miscible phase and concentration	Set-up, hydrodynamic, and conditions	Results: main findings
Beck, R. and Andreassen, J. P. (2013) [62]	mono-ethylene glycol (MEG), 0 and 65wt%	Seeded stirred batch experiments, stirring speed of 500rpm, temperature of 40 and 70° C	The presence of MEG inhibits calcite crystal growth by affecting the growth order from two in pure water to one in the presence of the solvent.
Bukuaghangin, O. and Cherpentier, T. (2015) [165]	Isoparaffinic oil (Isopar M), 0, 5, 20, 50 % v/v	Overhead dissolver stirrer rotated at 500 rpm to create the emulsion. temperature of 80° C	The presence of various quantity of paraffinic oil reduces BaSO ₄ surface deposition by about 45%. Hydrophobic surfaces show an improved antifouling performance in multiphase condition
Jaho, S. and Paraskeva C. (2016) [166]	n- dodecane	Flow through a narrow channel where the displacement of the organic phase by the supersaturated solution allows the formation of oil drops within the channel. Experiment temperature of 25° C	The precipitation of CaCO ₃ in the presence of n-dodecane results in shorter induction time and smaller crystals size. The nucleation of crystals at oil-water interface is also detected

<p>Natsi, P. and Koutsoukos P. G. (2016) [167]</p>	<p>mono-ethylene glycol (MEG), 10-80% v/v and n-dodecane</p>	<p>Bulk jar test at 25°C, two conditions of stirring: slow rates in which interface between the organic and the aqueous phase is created and rapid stirring in which an oil-in-water emulsion is created</p>	<p>In the presence of MEG the rate of precipitation decreased for MEG concentrations between 10-20% v/v, while for higher MEG concentrations between 30-80% v/v, precipitation was completely suppressed. In the presence of n-dodecane; the rate of CaCO₃ precipitation increased with the increasing amounts of the organic phase in the presence of water-oil interface; The rate of precipitation were unaffected in emulsions</p>
<p>Keogh, W. and Cherpentier, T. (2017) [168]</p>	<p>Light synthetic distillate (C11-C16 iso-alkanes), 5% v/v</p>	<p>A bladed impeller rotated at 400 rpm to emulsify the oil and water phases. Cylindrical samples rotated at 400 rpm to create turbulence at the surface interface. The experiments were conducted in sour conditions at 25° C</p>	<p>The deposition of CaCO₃ and BaSO₄ increases for hydrophilic surfaces whereas oil wetting of hydrophobic surfaces acted as a barrier to deposition.</p>

4 Chapter Four Methodology, materials and procedures of experiments;

4.1 Introduction

Studying the kinetics of scale formation on a surface and in the bulk solution under multiphase conditions is necessary to establish a better understanding of the scaling process under normal field conditions where water and oil exist together. Several methodologies and techniques have been used to characterize the crystallization process. These techniques are divided into two categories; surface deposition and bulk precipitation as shown in Figures 4.1 and 4.2. In this chapter a description of different methodologies, apparatus and materials which are used in this study are presented. The details and the procedures for the experiments conducted are also described in this chapter.

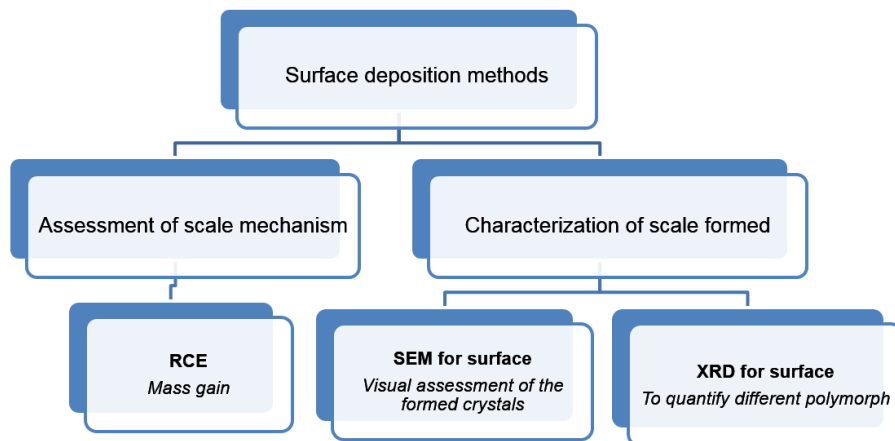


Figure 4-1 The techniques used for the assessment of surface deposition

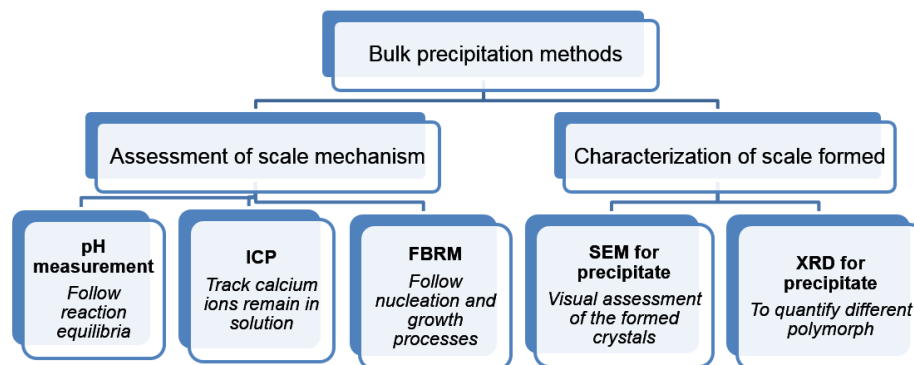


Figure 4-2 The techniques used for the assessment of bulk precipitation

4.2 Materials used

4.2.1 Brine composition

The brine is formed from two solutions prepared separately by dissolving the required amount of salts into distilled water; solution A which contains calcium ions in the form of calcium chloride dihydrate and solution B which contains bicarbonate ions in the form of sodium bicarbonate. Stock solutions A and B were filtered for any impurities prior to use. These solutions are mixed once starting the experiment with a ratio of 1:1 to form the brine solution to be studied. Five brine solutions are prepared with different concentrations to obtain different saturation brines as shown in Tables 4-1 to 4-5. Supersaturation (SR) of the brines were estimated based on a single phase model using MultiScale™ software. This is a thermodynamic scale prediction model based on Soave-Redlich-kwong (SRK) equation of state and PVT models for water mixtures. The initial SR for the brines at different condition are presented in Table 4-6.

Table 4-1 Brine 1 compounds and compositions

Inorganic Salt	Solution A		Solution B	
	(g/l)	(M)	(g/l)	(M)
NaCl	17.12	0.29	17.12	0.29
CaCl ₂ .2H ₂ O	14.70	0.1	-	-
NaHCO ₃	-	-	8.40	0.1

Table 4-2 Brine 2 compounds and compositions

Inorganic Salt	Solution A		Solution B	
	(g/l)	(M)	(g/l)	(M)
NaCl	11.69	0.2	11.69	0.2
CaCl ₂ .2H ₂ O	9.56	0.065	-	-
NaHCO ₃	-	-	5.46	0.065

Table 4-3 Brine 3 compounds and compositions

<i>Inorganic Salt</i>	Solution A		Solution B	
	(g/l)	(M)	(g/l)	(M)
NaCl	17.12	0.29	17.12	0.29
CaCl ₂ .2H ₂ O	6.62	0.045	-	-
NaHCO ₃	-	-	3.78	0.045

Table 4-4 Brine 4 compounds and compositions

Inorganic Salt	Solution A		Solution B	
	(g/l)	(M)	(g/l)	(M)
NaCl	17.12	0.29	17.12	0.29
CaCl ₂ .2H ₂ O	8.82	0.06	-	-
NaHCO ₃	-	-	5.04	0.06

Table 4-5 Brine 5 compounds and compositions

Inorganic Salt	Solution A		Solution B	
	(g/l)	(M)	(g/l)	(M)
NaCl	17.12	0.29	17.12	0.29
CaCl ₂ .2H ₂ O	7.35	0.05	-	-
NaHCO ₃	-	-	4.20	0.05

Table 4-6 Saturation ratios of the brines at different temperatures

Saturation ratio (SR)	30°C	40°C	50°C	60°C
Brine 1	211	-	-	-
Brine 2	115	-	-	198
Brine 3	-	-	-	97
Brine 4	-	120	-	-
Brine 5	-	-	105	-

4.2.2 Physical properties of the oil phase

The oil used is an iso-paraffinic hydrocarbon, Naphtha solvent purchased from VWR chemicals. The physical properties of the organic phase used are presented in Table 4-4.

Table 4-7 Physical properties of the oil phase [169]

Chemical name	Light distillate
Commercial name	Isopar M
Carbon number	C ₁₃ -C ₁₅
Average Molecular weight (g/mol)	206
Colour	Colourless
Sp. gr. @ 15° C	0.803
viscosity @ 25°C (mm ² /s)	2.9
Surface tension at 20° C (mN/m)	28
Paraffins wt%*	55
Naphthenes wt% *	45
Aromatics (mg/kg) **	200
Benzene (mg/kg)*	<3

Method of measurement; *Gas Chromatography, ** SMS 2728

Different fractions of oil to a fixed amount of the brine were prepared by adding the following amounts of oil 0, 100, 200, 300 and 400 ml to 1000 ml of brine. These represent the oil fractions of 0, 10, 17, 23 and 30 vol%, respectively. Some Mass gain experiments were conducted for oil content of 50 and 70 vol% to detect the effect of high oil fractions on surface deposition.

4.3 Surface deposition methodology and experimental details

The amount of scale deposition is assessed by measuring the weight gain for a surface that encounters scale fouling using a Rotating Cylinder Electrode (RCE) apparatus. This apparatus enables the production of high turbulence conditions for laboratory scale studies instead of using complicated pipe flow loops. Flow conditions similar to the wall shear stresses and mass transfer coefficient of the field conditions can be generated around the sample and hence relatively similar mass transfer and shear conditions in the surface can be estimated.

4.3.1 Rotating Cylinder Electrode (RCE) methodology

This apparatus is used in many industrial applications that require small scale simulation in high turbulent conditions. It can be used combined with electrochemical techniques to study corrosion[170], metal ion recovery [171], electro deposition [172], or as a non-electrochemical technique to study mineral scale deposition.

The RCE enables the production of highly turbulent conditions in relatively low rotation speeds and the control of the mass transfer through the control of the hydrodynamics of the flowing conditions by adjusting the rotation speed. In addition it has the advantage of being a simple setup, easy to use and cheap compared to other techniques and laboratory complicated flow loops. The Rotating Cylinder Electrode device is simply a metal sample of cylindrical shape attached to the end of a vertically oriented shaft by an insulating material such as Teflon as shown in Figure 4-3. The vertical shaft is connected to a control unit to enable adjusting of the rotation speed from 0 to 2000 rpm.

The flow regime is usually characterized by Reynolds number and for RCE the Reynolds number is:

$$Re = \frac{d_{cyl} u_{cyl} \rho}{\mu} \quad 4-1$$

Where: d_{cyl} is the substrate cylindrical diameter (cm), ρ is the solution density (g/cm³), μ is the solution viscosity (g/cm.s), $u_{cyl} = \pi d_{cyl} F / 60$ is the peripheral velocity of RCE (cm/s) and F is the rotation per minute (rpm).

The mass transport conditions can be described by a dimensionless correlation of the following form [173]:

$$Sh = \frac{K_m d_{cyl}}{D} = a Re^b Sc^{0.356} \quad 4-2$$

Where: Sherwood number (Sh) describes mass transport by forced convection, Reynolds number (Re) describes the fluid flow profile, and Schmidt number (Sc) characterizes the phase transport properties, K_m is the mass transfer coefficient (cm/sec), D is the diffusivity of mass transfer species (cm²/s), a and b are empirical constants that can be measured by fitting experimental data. In fact there are many different values in the literature for these constants and these depend on the nature of the substrate, the solution composition, the experiment conditions and the nature of the scale deposit. However, most of the RCE correlations are in agreement with the 0.356 power for the Schmidt number [174].



Figure 4-3 Rotating cylinder shaft [175].

Under turbulent flow conditions, the presence of circulating streams or eddy currents create a high increase in the momentum transfer in all three directions of the stream flow, and these eddies are responsible for the random fluctuations in velocity and high wall shear stresses [176].

$$\tau_y = - \left(\frac{\mu}{\rho} + E \right) \frac{d(\rho U_x)}{dy} \quad 4-3$$

Where: τ_y is the shear stress at distance y from the wall, μ and ρ is the fluid viscosity and density, respectively. E is the eddy kinematic viscosity of the fluid which depends on the degree of turbulence. $d(\rho U_x)/dy$ is the velocity gradient.

However, in the turbulent boundary layer, streamline flow continues in a thin layer close to the surface which is called the laminar sub-layer. In this layer and at the wall, the eddy effect is very small and can be neglected and the wall shear stress in this case can be defined as steady laminar flow. The laminar sub-layer is where the resistance to heat and mass transfer exists where, the thinner the laminar sub-layer is, the more the heat and mass transfer to the surface exist. The laminar sub-layer is separated from the turbulent part of the boundary layer by a buffer layer. In the buffer layer, the average size of the eddies or the turbulent circulating currents become progressively smaller as the surface is approached [176]. The mass transfer layer (diffusion layer) lies within laminar sub-layer. This layer becomes very thin with increasing average wall shear stresses. It was also reported that the Schmidt number has an inverse influence on the diffusion layer thickness [174]. Figure 4-4 illustrates the turbulent boundary layer.

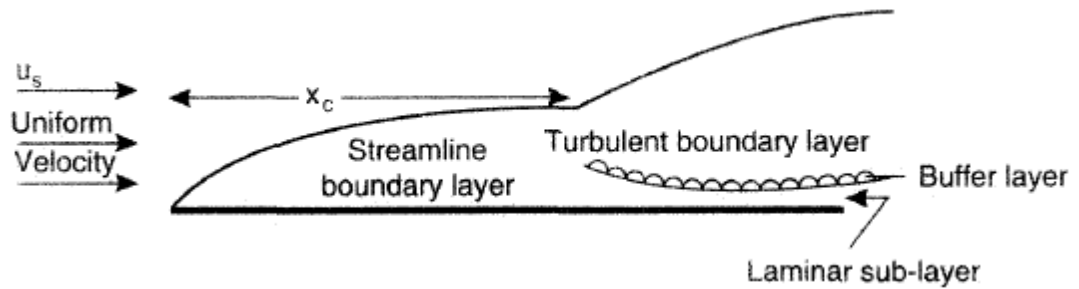


Figure 4-4 The development of the boundary layers [176].

The majority of the changes in the fluid stress characteristics due to turbulence and fluid interactions with wall occurs at the boundary layer. Therefore estimating the wall shear stresses are necessary for estimating both the momentum and mass transfer acting on solid surfaces under turbulence condition. For RCE the transition from laminar to turbulent conditions occurs at low Reynolds number of around 200 [177], The high rate of transfer in turbulent flow is accompanied by high shear stresses for a given velocity gradient [178]. Eisenberg (1954) was able to derive an acceptable correlation for estimating wall shear stress on the surface of a cylinder under turbulent conditions and this relation was confirmed by Silverman [175] and many other studies which used the same correlation under multiphase conditions [178, 179]:

$$\tau_{cyl} = 0.0791\rho Re^{-0.3}U_{cyl}^2 \quad 4-4$$

However, studies such as [180, 181] show that the fluctuation in the velocity and the wall shear stress due to the presence of circulating or eddies in turbulent condition or due to the presence of a second phase in a form of particles such as bubbles or droplets will not lead to accurate estimation of wall shear stresses for the system. The two components of the fluctuating wall shear stress and the Reynolds stress were defined by [180] as:

The stream-wise wall shear stress

$$\tau'_{w,s} = \mu r \frac{\partial u'}{\partial r} \quad 4-5$$

and span-wise wall shear stress

$$\tau'_{w,z} = \mu \frac{\partial w'}{\partial r} \quad 4-6$$

The average wall shear stress

$$\tau'_w = \sqrt{\tau'_{w,s} + \tau'_{w,z}} \quad 4-7$$

Reynolds stresses is the average fluctuating velocities

$$Re_s = \overline{u' w'} \quad 4-8$$

where: (') refers to the fluctuating component, u and w refer to stream wise and span wise velocities respectively. Computational fluid dynamics CFD can calculate average fluctuating in wall shear stresses as well as Reynolds stresses [181].

For emulsions, the effect of emulsions on the friction factor under turbulent flow conditions is found to exhibit differently between un-stabilised emulsions and surfactant-stabilised emulsions. Two phase dispersions are found to exhibit a drag reduction behaviour in the turbulent flow regime. This affects the friction factors and hence the wall shear stresses where drag reduction effect increases as the volume fraction of the dispersed phase increases [182]. For surfactant-stabilized emulsions, the friction factor was found to reasonably follow the Blasius equation for turbulent flow of Newtonian fluid over a smooth pipe [183]:

$$f = 0.079 Re^{-0.25} \quad 4-9$$

Surfactant-stabilized emulsions exhibit small or negligible drag reduction activity in turbulent flow conditions [183, 184].

For un-stabilised emulsion the system exhibits a strong drag reduction. These drag forces result in lower friction factors than that would be expected from Blasius equation. It was claimed that the increase in the droplet size will cause such behaviour [184]. Turbulence modulation of the dispersion medium in the presence of dynamic coalescence/ breakup processes [183] can also cause drag reduction. The drag reduction is found to be more significant in W/O emulsions than in O/W emulsions. The drug reduction is increased with the increase in the dispersed phase volume fraction. However, it has been shown by [182] that the drag reduction tend to diminish at high Reynolds number for un-stabilised W/O emulsions due to the decrease in the droplet size distribution as droplets break up at high flow conditions. Un-stabilised O/W emulsions may exhibit coalescence resistance due to the existence of electrical double layer and hence it may exhibit less significant drag reduction [183].

The aim of using RCE is to introduce similar mass transport conditions and wall shear stresses to those found in a horizontal pipe and therefore to reproduce field conditions. This based on the assumption of that the boundary layer thickness is much smaller than the radius of the curvature of the pipe geometry and therefore the boundary layer is assumed to be independent of flow geometry. Many studies compared the two flow geometries in terms of hydrodynamics and mass transfer and obtained good agreement between them [185, 186]. Such studies enable the selection of RCE velocity which corresponding to that of a straight horizontal pipe

which gave approximately equal wall shear stresses and similar mass transfer conditions. Such as a velocity of 2 m/s will lead to shear stresses of 12 and 16 Pa for straight pipe and RCE, respectively and approximately equal mass transfer coefficient of 0.0004 m/s [185], but this study showed that this will be true only if both diameters are of the same order of magnitude ($d_p=15$ mm and $d_{cyl}=10$ mm). Silverman [175, 186, 187] suggested the existence of some combinations of pipe diameter, pipe velocity, rotating cylinder diameter and rotation rate exist so that the mass-transfer coefficients and the wall shear stresses can be similar for both geometries; if water is flowing through a smooth 10-inch schedule 40 pipe at 152 cm/s, an RCE should be operated at about 1113 rpm or peripheral velocity of 87.4 cm/s to match the conditions in the pipe. This estimated according to the following equation [186]:

$$U_{cyl} = 0.1185 \left(\frac{\rho}{\mu}\right)^{\frac{1}{4}} (d_{cyl}^{\frac{3}{7}}/d_p^{\frac{5}{28}}) Sc^{-0.0857} U_p^{5/4} \quad 4- 10$$

However, a study [179] used an apparatus design to allow the comparison of three test methods (rotating cylinder, pipe flow and jet impingement). In terms of flow-accelerated corrosion for carbon steel under CO₂-brine containing solution, a general equation describing the effect of wall shear stress on carbon steel corrosion rate for the three methods is generated in the following form:

$$r_{corr} = a \times \tau_w^{0.1} \quad 4- 11$$

Where a is a constant which was found to be, 7.7 for 12.7 mm pipe flow, 6.8 for jet impingement and 2.8 for RCE. The results showed that the RCE did not correlate with both pipe flow and jet impingement methods in terms of wall shear stresses or mass transfer under similar condition. The corrosion rate for the rotating cylinder was about three times less than that for the pipe flow at similar wall shear stresses. The explanation was that the actual shear stress at the RCE was lower than estimated by equation 4-11 for carbon steel under experimental conditions.

4.3.2 Surface deposition experiment details

4.3.2.1 Substrate

The substrate (RCE sample) at which the deposition took place is a cylindrical piece of stainless steel (SS 316L) with an outer diameter of 12 mm, length of 10 mm and total exposed area of 3.768 cm². The roughness of the substrate (R_a) is 1.07 μm, assessed by interferometer NPFLEX. Before each test the samples were cleaned with 36% HCl solution and rinsed with distilled water and acetone and then

allowed to dry at 35° C for 24 hrs. The samples were then weighted using a high precision balance (Mettler XP26) with resolution of 1 µg.

4.3.2.2 Mass gain using Rotating cylinder electrode

The experiment was conducted in a 2 litre beaker containing 500 ml of sodium bicarbonate solution and between 0 and 500 ml of oil to represent different oil fractions of 0, 10, 17, 23, 30 and 50%. Both phases were allowed to settle and saturate with CO₂ gas at a flow rate of 0.2 litre per minute. CO₂ gas was then stopped and both phases mixed using an impeller (dissolver stirrer R 1300 from IKA) at 520 rpm which is considered high enough to allow homogeneous dispersion of phases. The impeller blade was kept at a constant distance of 1 cm from the bottom of the vessel. Two baffles of width 20 mm and thickness of 4 mm were added to the vessel. The baffles were fixed at a distance of 4mm from the vessel bottom and the walls. Figure 4-5 shows a schematic representation of the experiment setup. Figure 4-6 illustrates the importance of inserting the baffles to the system. The aim of using baffles is to achieve adequate mixing and to avoid vortices and hence to minimize any possible effect of high turbulence on the precipitation characteristic. The vessel is covered over by a Teflon lid to minimize the interaction with air which may affect the pH of the solution. The RCE is then immersed and the experiments were conducted under turbulent conditions in which the RCE was allowed to rotate at 2000 rpm. Table 4-5 illustrates the flowing conditions around the RCE for an oil- free system at different temperatures.

The pH is adjusted to 8 prior to the experiment and left to drift normally within the experiment which lasts for one hour. 500 ml of brine A is then added and the experiment is started. Both brines were heated separately to the specified experiment temperature prior to mixing and the temperature was kept constant during the experiment. Once the experiment was completed, the sample was carefully removed from the apparatus using tweezers to avoid touching or removing the scale. The sample is then well rinsed with distilled water and allowed to dry at 35° C for 24 hrs. The amount of scale deposited was measured by subtracting the sample weight after and prior to the experiment. The samples were then analysed using SEM (Hitachi TM3030 Bench Top) and XRD (Philips X' Pert X- Ray diffraction) with CuK α type radiation at a voltage of 40 kV and an intensity of 40 mA.

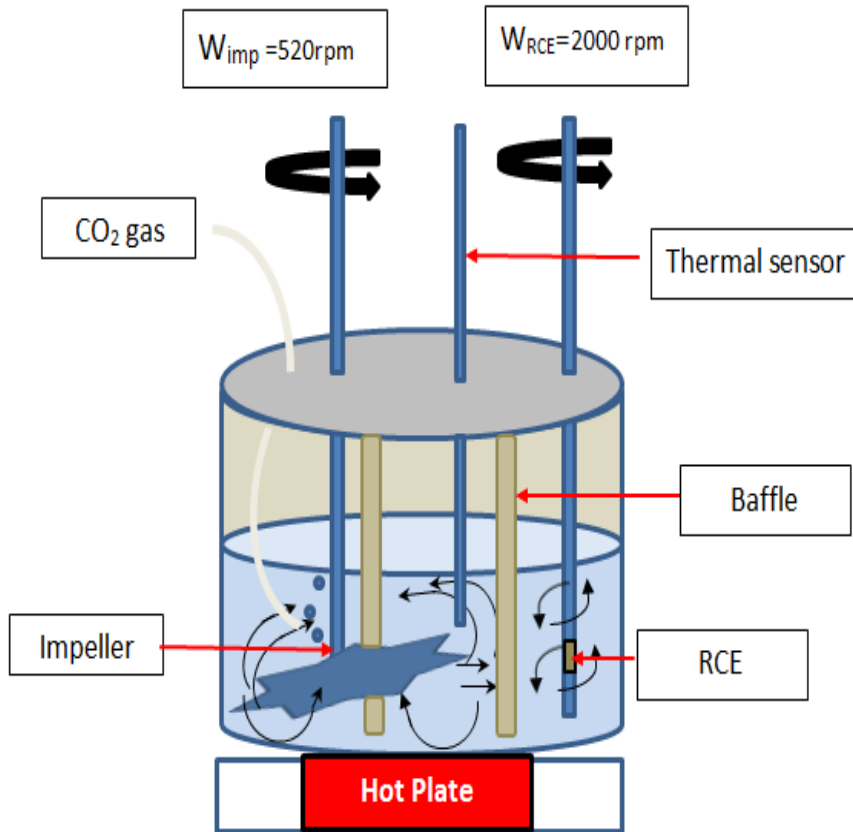


Figure 4-5 Schematic representation of the experiment setup

Table 4-8 Physical properties and hydrodynamic conditions at different temperatures

Flowing conditions	30° C	60° C
Density of water (g/cm ³)	1.036	1.023
Viscosity of water (mPa. s)	0.833	0.493
Viscosity of oil (mPa. s)	2.813	1.34
Reynolds number around RCE	18,748	31,275
Wall shear stress (Pa)	6.76	5.72

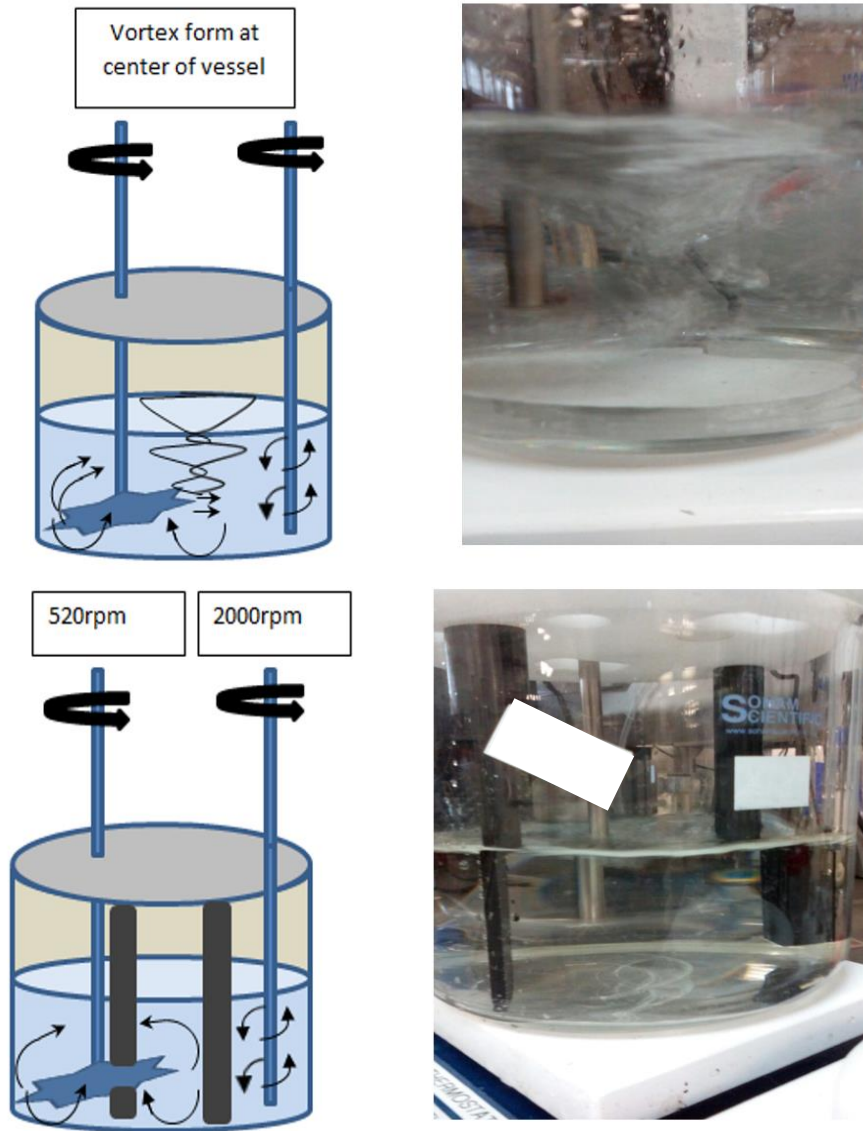


Figure 4-6 Fluid dynamics inside the stirred tank; (top) before, (bottom) after adding of the baffles

An analogy between flowing velocities in the RCE to that in a horizontal pipe for single phase at an equivalent flow to field conditions is estimated using equation 4-10. For RCE rotating at 2000 rpm which is equivalent to 1.25 m/s, the brine physical properties at 30 shown in Table 4-5 and a pipe diameter of 25.4 cm, the pipe velocity which is equivalent to the RCE velocity is calculated to be 2.72 m/s at 30° C and 3.37 m/s at 60° C.

4.4 Bulk precipitation methodology and experimental details

4.4.1 Emulsion characterization

Since adding the oil phase under turbulent condition results in emulsions formation, it was necessary to investigate the type of the emulsion formed, whether it is O/W or W/O emulsion. A simple drop test was conducted; two small flasks of 10 ml were

used, one filled with water and the other filled with oil. A drop of the emulsion was sampled using a pipette from the reaction vessel which contains the oil-saline water mixed at 520 rpm. The sample is then poured rapidly into each flask. If the drop diffused and disappeared immediately in the oil phase but dispersed in the aqueous phase then, the emulsion is O/W emulsion and vice versa. This test showed that the type of the emulsion formed during the mixing of the phases under experimental conditions is an oil-in-water (O/W) emulsion. The type of emulsion can also be detected using flow pattern maps which are initiated for different cases of pipe diameters and materials and for different flowing fluids at different volume fractions and superficial velocities of water (v_{ws}) and oil (v_{os}) or mixture velocities. Since the RCE velocity for the oil-free system is found to be equivalent to a pipe velocity of 2.72 m/s at 30° C and 3.37 m/s at 60° C and since the viscosity of the emulsion mainly depends on the viscosity of the external phase which is the brine, the mixture velocity for the oil system is assumed to be equal to the pipe velocity for an oil-free system and the superficial velocities at different oil content and conditions are presented in Table 4-6 which are calculated using the following equations:

$$v_{ms} = v_{os} + v_{ws} \quad 4.12$$

where:

$$v_{ws} = \alpha_w \times v_{ms} \quad \text{and} \quad v_{os} = \alpha_o \times v_{ms}$$

Where: v_{ws} and v_{os} are the water and oil superficial velocities, respectively. v_{ms} is the mixture velocity. α_o and α_w are the oil and water volume fractions, respectively.

Table 4-9 Water and oil superficial velocities at different oil content and different temperatures; mixture velocity= 2.72 m/s at 30° C and 3.37 m/s at 60° C

Oil fraction	30° C		60° C	
	v_{ws} (m/s)	v_{os} (m/s)	v_{ws} (m/s)	v_{os} (m/s)
0%	2.72	0.00	3.37	0
10%	2.45	0.27	3.00	0.37
17%	2.25	0.47	2.80	0.57
23%	2.1	0.62	2.60	0.77
30%	1.9	0.82	2.37	1.00

From the values of superficial water and superficial oil velocities which are shown in Table 4-6 and from the flow pattern which is presented in Figure 3-4, the type of

emulsion for a horizontal pipe of 25.4 cm diameter with a flowing velocity equivalent to the RCE rotating at 2000 rpm is shown to exist within the red circle which represents oil-in-water emulsions.

Emulsions are usually characterized by their rheological properties but because the system is unstable and separate immediately after mixing is stopped, these properties are difficult to assess. Droplet size and droplet size distribution are also important factors for the characterization of emulsions.

4.4.2 Particle (crystals) and droplet size distribution

Studying bulk precipitation in multiphase systems is far more complex than in single-phase systems. Two types of particles are presented in the solution, droplets of the dispersed phase and particles of the crystalline matter. Studying bulk precipitation in such a system may require the *in-situ* characterization of the system in which particle size distribution is detected in the presence and absence of oil. This may enable the tracking of the nucleation and growth of particles in the bulk solution. The FBRM device enables the *in-situ* and *real-time* measurements, so that the particle size and the change in the particle dimension and counts could be tracked with time. Droplet size and droplet size distribution are important for the estimating of the interfacial area between both phases and hence for understanding the impact of oil on the precipitation process. The FBRM was used by different studies to follow the crystal nucleation, growth and agglomeration processes [188, 189]. This technique has an advantage of being able to provide an immediate measurement of the particles as they actually exist in the system without the need of sample preparation or dilution. This makes it able to work in dense systems comparing to other size measurements techniques such as Mastersizer in which 10% suspension is its optimum sample density [190]. According to [146] particlesizing systems which depend on measuring the amplitude of the scattered light have the ability to work at high concentration of greater than 10^6 #/cm³. The FBRM has also the advantage of producing repeatable and reproducible results [191].

4.4.2.1 Focused Beam Reflectance Measurement (FBRM) methodology

FBRM has been widely used as a technique for *in-situ* characterization of different colloidal systems regardless of the shape and the concentration of the suspension particles. Its principle is that when a rotating laser beam passes through a particle, the laser light is scattered back and a chord length is measured. A chord length is simply defined as the straight line between any two points on the edge of a particle as shown in Figure 4-8. The chord length is estimated by the product of the

reflection time and the laser speed. Since the particles may take different shapes, chord length distributions were recorded rather than diameter based distributions. The chord length distribution then requires transformation procedures using empirical equations and algorithms [191]. However many studies assumed the particles to have spherical shape in order to simplify the mathematics, others used different chord weighting methods which are found to correlate well with other sizing techniques for different colloidal systems [191, 192].

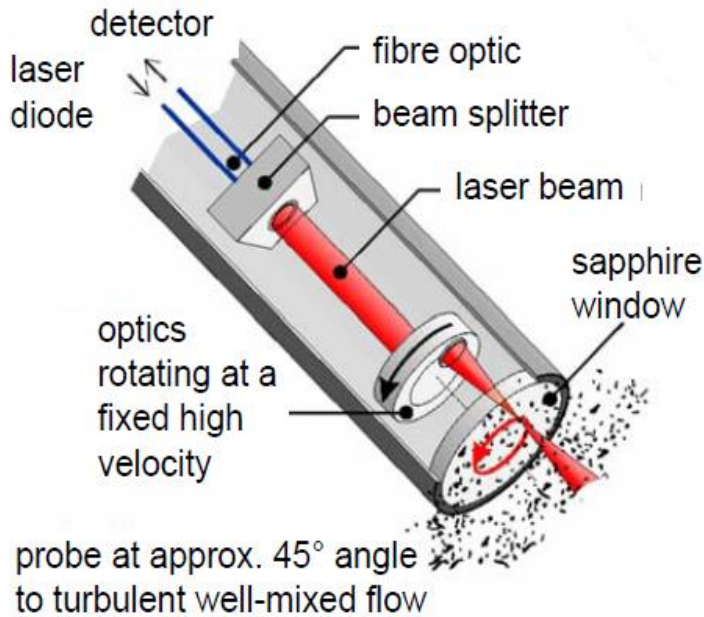


Figure 4-7 Schematic representation of FBRM probe [192]

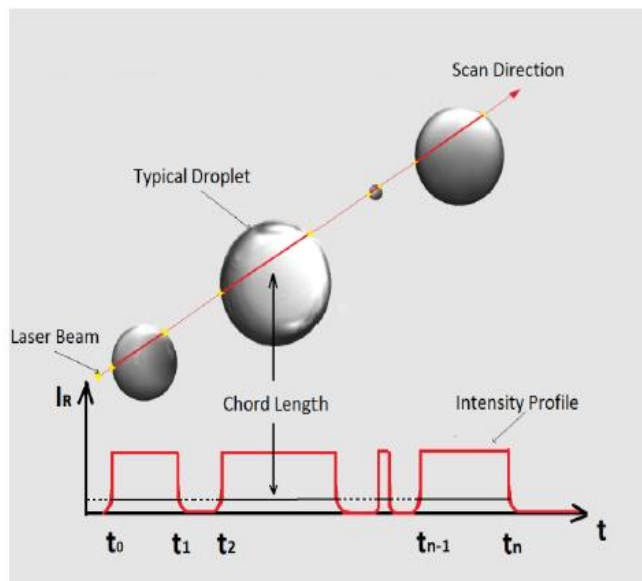


Figure 4-8 Chord length measurements of particles [193]

The size distribution at different frequencies is defined as particle size distribution which can be represented by cumulative density or frequency distribution. The frequency distribution in FBRM is expressed as the following:

$$f_j = \frac{N_j(l_j)}{\sum_j N_j(l_j)} \quad 4.13$$

where: N_j is number of chord count of j^{th} channel per second, l_j is chord length of j^{th} channel (μm).

The average of a distribution can be represented by the mean, mode and median size and these values can be expressed as number, surface or volume based depends on the area of interesting. Mode size represents the most frequent size in the distribution where it appears as a peak in the frequency curves. The median size is defined as the size in which half of the particles are larger than this size and half are smaller than it.

Various weighting statistics are used to approximate the measured particle size to the actual size. These methods are applied to increase the importance of specific size such as if large particles have more influence than smaller ones in the analysis. In FBRM software, chord counts, mean chord length, median chord length and chord length distribution can be expressed by either un-weighted or square-weighted averaging methods. The square-weighted chord counts have a mathematical expression of:

$$N_{j,n} = N_{j,0} l_j^n \quad 4.14$$

where: $N_{j,n}$ is the weighted chord count of the j^{th} channel per second ($\mu\text{m}^n \cdot \text{s}^{-1}$).

$N_{j,0}$ is the raw un-weighted chord count of the j^{th} channel per second (s^{-1})

l_j is the chord length of j^{th} channel (μm).

n is the type of weighting method, where: n of 1, 2 and 3 represent un-weighted, square-weighted and quadratic-weight, respectively.

The un-weighted and square-weighted mean chord lengths are defined as the following:

$$l_{mean} = \frac{\sum_{j=1}^n f_j l_j}{\sum_{j=1}^n f_j} \quad 4.15$$

$$l_{mean}^2 = \frac{\sum_{j=1}^n f_j l_j^3}{\sum_{j=1}^n f_j l_j^2} \quad 4.16$$

where: f_j is the frequency of j^{th} channel per second, l_j is the chord length of j^{th} channel (μm).

Droplet size and distribution are of importance in estimating the interfacial area between both phases and hence in detecting the relation between total interfacial area and the amount of precipitation. Therefore, it may help in finding an answer to whether increasing the oil content, increases or reduces the precipitation process. In the current work the mean droplet diameter has been estimated using FBRM with the assumption that oil droplets are spherical in shape [191]. By knowing the mean droplet diameter, the total interfacial area can be estimated according to the following equations [194]:

$$\text{Volume of a droplet} = \frac{4}{3}\pi r^3 \quad 4.17$$

$$\text{Number of droplets} = \frac{\text{total volume of dispersed phase } (\alpha)}{\text{volume of a droplet}} \quad 4.18$$

$$\text{Surface area of a droplet} = 4\pi r^2 \quad 4.19$$

where: r is mean droplet radius

Total interfacial area could be estimated by multiplying the total number of droplets by the surface area of a droplet.

$$\text{Total interfacial area} = \frac{3\alpha}{r} \quad 4.20$$

$$\text{Droplets density in solution} = \frac{\text{number of droplets}}{\text{volume of the continuous phase}} \quad 4.21$$

The aim of using this technique is to track the nucleation and the crystal growth processes in absence and presence of an oil phase. It could be considered as an attempt to characterize the system and to get a better understanding of the kinetics of the precipitation process. This could be achieved by measuring the number of counts for different chord length channels per unit time so that both nucleation and crystal growth could be tracked simultaneously.

4.4.2.1 Focused beam reflectance measurement (FBRM) experiment details

The LASENTEC FBRM D600 probe with diameter of 19 mm and length of 400 mm is inserted into a 2 litre beaker. This technique is used to characterize different oil fractions by adding 140, 280, 420 and 560 ml of oil to 1400 ml of 0.3 M NaCl solution to form emulsions of oil fractions 10, 17, 23 and 30%, respectively. The experiments were conducted at temperatures of 30 and 60° C. The fluid in the vessel is mixed at 700 rpm impeller speed for the case of 23 and 30% oil fractions to ensure homogeneous mixing between the phases. This rotation speed is considered higher than the usual speed of 520 rpm which is used at all other experiments as the level of the fluid is much higher at these oil fractions.

In the experiments conducted by FBRM to characterize the precipitation process, the probe is inserted in a similar beaker which contains 700 ml of sodium bicarbonate solution. An amount of 140 to 420 ml of the oil is then added and the phases are mixed at rotation speed of 550 or 700 rpm depending on the oil fraction. The solution is heated and maintained at the experiment temperature of 30° C or 60° C where the vessel is kept closed. 700 ml of calcium chloride solution is heated separately and then added to create a solution with oil fraction ranges from 10 to 23% by volume. The experiment is started after mixing the brines and lasted for 1 hour.

The FBRM probe is oriented with an angle of about 45° as recommended by [195] to minimize the scale particles from building up on the sapphire window of the probe which is mounted just above the impeller as shown in Figure 4-9. Throughout the experiment, the FBRM probe was cleaned regularly due to the tendency for scale to adhere at the sapphire window which may result in a high increase of the chord counts.

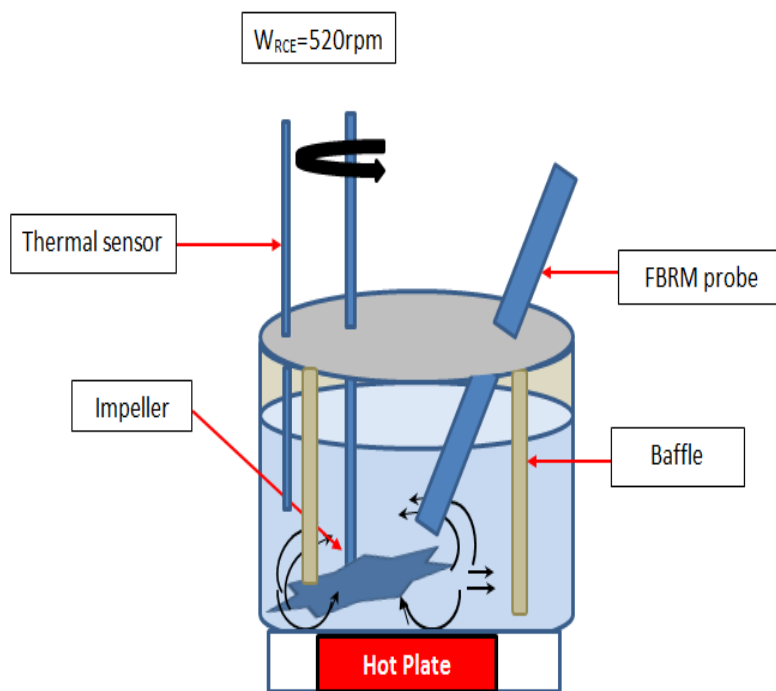


Figure 4-9 Schematic representation of FBRM experiments

The FBRM experiment was conducted without bubbling CO_2 gas prior to the experiments. This may create different conditions in-terms of pH and supersaturation from the other experiment conditions. The vessel was not securely closed as the FBRM probe needed to be removed from the vessel for regular cleaning. Moreover, mixing of the phases with an impeller speed of 700 rpm for

high oil fractions may also have had an influence on the precipitation rates for high oil fraction systems.

Brine 3 (0.045) was chosen to be used in the FBRM experiments. This brine is considered to have a medium tendency to scale at 30° C. Conducting the experiments with high saturation brines such as brine 1 (0.1 M) or brine 2 (0.065 M) is not recommended as the FBRM seems to lose its accuracy in a very high density medium.

4.4.3 Assessment of the precipitation process

4.4.3.1 Turbidity measurements

Turbidity is an indication of the clarity of a solution and refers to its cloudiness. As calcium carbonate precipitates, the solution will become cloudier. Turbidity meters measure the turbidity in Formazin Attenuation Unit (FAU). Its principle is based on measuring the amount of light that is scattered back by the particles in the solution.

Turbidity samples were taken from the reactor vessel at different time intervals during the experiment using a 10 ml pipette and then poured in a 10 ml cell which is part of the turbidity meter device. The cell is closed and the measurement was recorded and repeated for each sample three times where the average of the readings was taken. The cell is gently agitated between the measurements to ensure particle suspension and to avoid the formation of gas bubbles.

Since the oil-brine emulsions are highly unstable and separate easily once mixing stops and because the calcium carbonate particles have a great affinity to the oil phase so they collect at the oil-water interface, it was difficult to measure the turbidity in the presence of oil. Moreover, shaking of the cell in the presence of oil may disperse the oil phase and this affects the measurements. For these reasons the turbidity measurements were only conducted in an oil-free system to evaluate the precipitation tendency for the brines.

4.4.3.2 pH measurement

The solution pH is measured using a Thermo Scientific™ Orion Star™ A111 pH Benchtop Meter. The basic principle of the pH meter is to detect the concentration of hydrogen ions [H⁺] in the solution. Since the crystallization process consists of a series of chemical reactions in which the dissociation of hydrogen ions takes place, measurement of pH is important to follow the kinetics of the precipitation process.

pH has also been widely used as a method for characterizing scale formation particularly as a way for estimating the induction time. pH can also be used as a

method of identifying different stages of the crystallization process such as nucleation, growth and agglomeration stages [196]. In addition to identifying phase transition [49, 50, 68].

Different supersaturation conditions can be generated in CO₂ systems due to the high sensitivity of alkaline scales to changes in pH. This may affect the solubility, different deposition and precipitation kinetics shown by the same solution at the same temperature but different pH conditions. pH can also be changed upon contact with air and this could lead to a continuous rise of pH and hence shifts in the initial pH of the experiments. To minimize the effect of air interactions with the solution, the experiments have been conducted in a securely sealed vessel where CO₂ gas was bubbled over the night. The oil phase is left to settle on the bicarbonate brine while bubbling with CO₂. The gas is then stopped and the solution is left to release the excess CO₂ while starting the mixing of the phases where this process could take at least three hours until the pH of the bicarbonate solution is adjusted to 8. The reason for bubbling and stopping the CO₂ gas prior to the experiments is to saturate the system with CO₂ gas as much as possible to minimize the rapid change in pH as the loss of CO₂ makes the solution more alkaline. This procedure was performed to allow better control of the initial pH and to ensure a relatively similar starting point for all the experiments. Moreover, reproducing similar pH trends for each experiment is used as an indication for the consistency in the experiment conditions particularly in the case of experiments needed to detect polymorph change on the surface or in the bulk. The initial pH of the calcium chloride brine usually ranges between 6.7 and 7.0 whereas the pH of the bicarbonate brine is fixed to pH of 8. Measurements started once the two solutions were mixed and the initial pH is considered as the pH of the bicarbonate solution. The initial pH is also calculated using Multiscale software™ for the mixing of the two brines with a ratio of 1:1 and found to range between 7.6 and 7.8. This related to the fact that the individual pH of the solution containing the calcium ions has generally decreased the overall initial pH. The organic phase has also been found to interfere with the pH probe and shows fluctuation in the measurements therefore, calibration of the pH probe is essential and was done on a regular basis.

4.4.3.3 Detection of calcium ion concentration using Inductively Coupled Plasma- Optical Emission Spectrometry (ICP-OES)

This analytical technique enables the detection of a trace amount of metals in solutions. The principle is that each element emits energy as they return to their ground state after excitation by a high temperature plasma source of the range of

6000-10000 K. When the light that comes from the plasma source is passing through the aspirated sample, the sample will convert into free atoms in gaseous state. These atoms will adsorb the light where the intensity of the emitted energy at specific wavelengths is proportional to the concentrations of elements in the solution. The aim of using this technique is to measure the concentration of calcium ions that remain in solution and hence to calculate the amount of calcium ions which are produced during the experiment.

The experiments were conducted in a 2 litre beaker containing of 500 ml of sodium bicarbonate solution B. An amount of 100, 200 and 300 ml of the oil is added and the phases are mixed at a rotation speed of 520 rpm to ensure dispersion of phases. Carbon dioxide is bubbled and pH is adjusted prior to the experiments as described in the previous section. The experiments start after mixing brine solution A and B with a ratio of 1:1. About 5 ml of the scaling brine-emulsion was sampled at regular time intervals using a pipette and poured into 10 ml tube where the phases are rapidly separated. 1 ml of the aqueous phase (from the lower layer) was sampled and quenched immediately into 9 ml of 1000 ppm of polyvinyl sulfonate scale inhibitor (PVS) and 3000 ppm potassium as KCl solution [197]. The quenching solution is prepared by dissolving 1 g of PVS and 5.71 g of KCl into 1 litre of distilled water and adjusted to pH of 8-8.5 by adding drops of 0.1 M of NaOH solution prepared by dissolving 0.4 g of NaOH into 100 ml water. The reason of quenching the solution immediately after sampling is to stop the reaction and to allow measuring of the unreacted calcium ions that remain in the solution. This procedure of sampling was only performed for the experiments conducted with oil. In the absence of oil, 1 ml sample was directly pipetted from the reaction vessel. A control solution which is the sample represents the initial solution prior to any reactions is prepared by adding 5 ml of the calcium containing brine into a 100 ml volumetric flask that contains some of the quench solution and is well agitated. More quench solution and 5ml of the bicarbonate solution are then added to the flask, well agitated and the volume in the flask is completed to 100 ml. All samples were then filtered using a syringe type filter and sent for analysis using ICP-OES in order to track the change in Ca^{2+} concentration in the solution.

4.4.4 Characterization of the scale

Samples of the RCE substrate and the precipitate powder are sampled during different time intervals. The precipitate samples are filtered using 0.2 μm filter paper and rinsed well with distilled water. The samples are then left to dry in an oven at

35° C for 24 hours before they were analysed using Scanning Electron Microscopy (SEM) and X- Ray diffraction (XRD).

4.4.4.1 Scanning Electron Microscopy (SEM)

To assess the scale formed on the surface of the RCE sample and in the bulk solution, the Hitachi TM 3030 Bench Top Scanning Electron Microscope is used. The samples were placed in a vacuum chamber where they were subject to a beam of high energy electrons instead of a beam of light such as in conventional optical microscope. The focused beam scans the specimen and reflects back any secondary electrons which are emitted from the sample. The reflected beams are then collected and its intensity is measured and displayed as a large three dimensional image of a very small object. SEM allows the examination of the structure and morphology of materials with high magnification.

4.4.4.2 X-Ray Diffraction, XRD

The Philips PanAlytical X' pert X-Ray diffractometer is a quantitative technique used to identify different polymorphs of CaCO₃ crystals formed on the surface of a deposit sample or precipitated in the bulk solution. This technique is based on the fact that the distances separating the atoms are in the same order of size as the wavelengths of an X-ray radiation of Cu K α type anode of 1.54056 Å. Once the X-rays interact with the atoms in the crystals, it results in diffraction of the radiation in a way that corresponds to the arrangement of the atoms of a particular crystal and a diffraction pattern is generated. Crystalline matters are identified by peak positions ($^{\circ}2\theta$) and peak intensities (counts) of the diffraction pattern. XRD can measure the average spacing between layers of atoms, the orientation of a crystal, in addition to detecting the crystallites sizes, identifying unknown materials and internal stresses in a crystal lattice.

A quantitative measurement of the proportions of different polymorphs is determined using set of correlations developed based on the construction of an X-Ray calibration graph obtained from a crystal mixture of a purely synthesised calcium carbonate polymorph [198, 199]. The correlations are based on the intensity peaks of calcite (104) at 2θ of 29.4°, aragonite (221) at 2θ of 46.06° and vaterite (110) at 2θ of 25° and known mole fraction ratio for binary mixtures according to the following relationship:

$$\frac{I_1}{I_2} = A \frac{X_1}{X_2}$$

Where:

$\frac{X_1}{X_2}$ is the mole fraction ratio for a binary mixture, $\frac{I_1}{I_2}$ is the ratio of diffraction intensities for a binary mixture and A is an empirical constant from the fitting of the calibration graph.

The following correlations were determined by [199] and used in this study to measure the composition of a tertiary mixture of a calcium carbonate polymorph:

$$X_A = \frac{3.157 \times I_A^{221}}{I_C^{104} + 3.157 \times I_A^{221} + 7.691 \times I_V^{110}} \quad 4.22$$

$$X_C = \frac{I_C^{104} \times X_A}{3.157 \times I_A^{221}} \quad 4-23$$

$$X_V = 1.0 - X_C - X_A \quad 4-24$$

where: X_A , X_C and X_V are the mole fractions of aragonite, calcite and vaterite, respectively.

I_A^{221} , I_C^{104} and I_V^{110} are the intensities of aragonite, calcite and vaterite, respectively.

For a binary mixture of CaCO_3 polymorphs the following equations are used:

For vaterite-calcite mixture:

$$X_V = \frac{7.691 \times I_V^{110}}{I_C^{104} + 7.691 \times I_V^{110}} \quad 4-25$$

$$X_C = 1 - X_V \quad 4-26$$

For aragonite-calcite mixture:

$$X_A = \frac{3.157 \times I_A^{221}}{I_C^{104} + 3.157 \times I_A^{221}} \quad 4-27$$

$$X_C = 1 - X_A \quad 4-28$$

It is important to control the dynamics and the conditions of the experiments as small changes in the experiment conditions such as temperature, mixing speed or pH can lead to large differences in the rate of precipitation and deposition. The next chapter will present the results detected from surface deposition experiments.

5 Chapter Five The kinetics of calcium carbonate surface deposition in water and in oil/water emulsions;

5.1 Introduction

This chapter presents experimental results used to assess calcium carbonate surface deposition in the absence and presence of an organic phase. The methodology used is based on measuring the amount of scale deposition on a surface of a Rotating Cylinder Electrode (RCE). Surface scaling is assessed using X-Ray Diffraction (XRD) by which a quantitative correlation for the determination of CaCO_3 polymorphs is used. The different stages of the crystallization kinetics are assessed. The formation of different phases and the transformation from a metastable phase to a stable one are quantitatively determined to enable a better understanding for the overall crystallization process. The formation and transformation of different polymorphic phases are also characterized using Scanning Electron Microscopy (SEM).

5.2 Assessment of surface crystallization process

5.2.1 Mass deposition

The amount of mass deposition is determined by measuring the amount of scale deposit (mg) per RCE exposed surface area (cm^2) per experiment time of 1 hour. Figures 5-1 and 5-2 show the amount of deposition in $\text{mg}/\text{cm}^2\cdot\text{hr}$ collected over 1 hour at 30°C and 60°C for two different saturation brines and oil fractions up to 70%.

There is an overall reduction in the amount of scale deposition in the presence of oil at 30°C ; there is little change at the brine 2 (0.065M) deposition in the range of 10 to 23% oil content. The rate of deposition for both brines is decreased by an average of 40% for an oil content up to 23% whereas the reduction in the scale formed reaches an average of 90% for oil content up to 70% for brine 2 (0.065M). Systems at 60°C exhibit different behaviour when an oil phase is introduced to the system; the amount of surface deposition for oil fractions up to 30% is found to increase by one fold for brine 2 (0.065M) at 60°C . The amount of deposition is increased by two folds for oil fractions up to 23% Brine 3 (0.045M). This is followed by a clear reduction in the scale formed after 23% as shown in Figure 5-2.

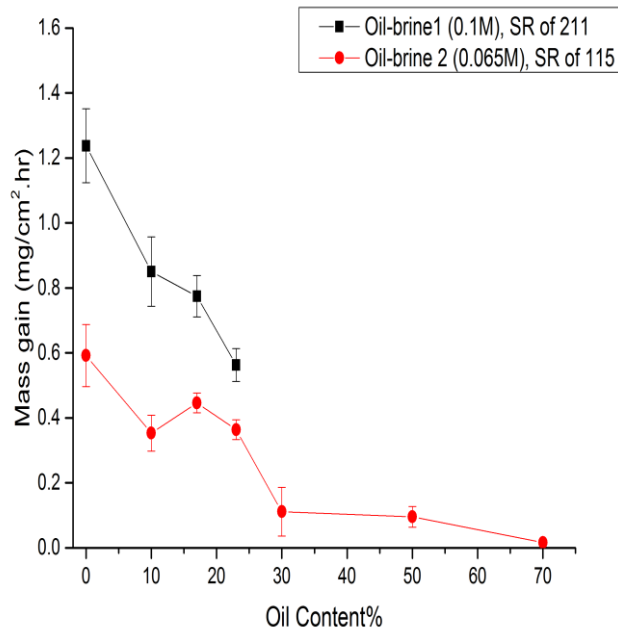


Figure 5-1 Surface deposition in (mg/cm².hr) for oil-brine emulsion system at 30° C, data collected over 1 hour period

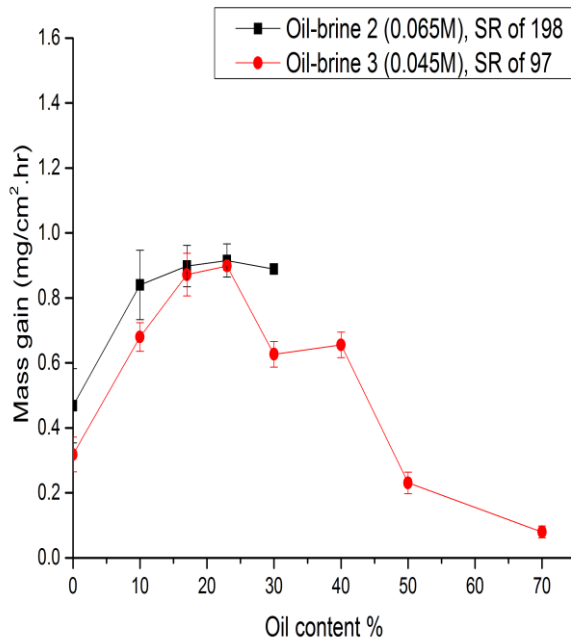


Figure 5-2 Surface deposition in (mg/cm².hr) for oil-brine emulsion system at 60° C, data collected over 1 hour period

However the amount of deposition seems to exhibit a maximum at certain oil fractions where the deposition is found to increase by up to 65% higher than the amount of deposition for oil-free system at 60° C. 50% and higher oil fractions show a decrease in the amount of deposition where the reduction reaches to about 80% for 70% oil fractions at 60° C. The mass gain experiments for brine 4 at 40° C and

brine 5 at 50° C have only been conducted in the presence of 23% oil content to estimate the effect of adding an oil phase to the deposition at different temperatures. Brine 4 (0.06M) at 40° C behaves similar to the brines at 30° C where the scale is reduced by about 40% when 23% oil is added whereas brine 5 (0.05M) at 50° C showed a slight deposition increase ($\approx 15\%$) when 23% oil is added to the system. This result is much similar to the brine behaviour at 60° C to that at 30° C.

A decrease in the deposition in the presence of an organic phase was the expected trend but this was only the case at the lower temperatures of 30°C and 40° C and the higher oil fractions at 60°C. The increase in the deposition for systems with oil content up to 40% at 60° C is unexpected. The extent of scale formed on the stainless steel surfaces when an organic phase is in the system needs more investigation. The next section will show the growth of scale at different time intervals for the one hour experiment time.

5.2.2 Mass Growth Rates

Growth rates can be expressed by different ways such as linear velocity (m/s), linear growth rate (m/s) and mass deposition rate in ($\text{kg}/\text{m}^2.\text{s}$) and this can be used to express the overall growth rates for population of crystals [2]. Mass deposition in (mg/cm^2) at different time intervals is used here to define the growth trends and to evaluate the growth rate constants.

5.2.2.1 Mass gain at different time intervals at 30° C

Figures 5-3 and 5-4 show the mass gain profiles for two different brine concentrations at 30° C and different oil fractions up to 23%. A similar trend of mass gain has been detected for systems with and without oil for brine 1 (0.1M) and brine 2 (0.065M). The mass gain profile shows different slopes which range between regions of high slopes usually at the beginning of the crystallization process to regions of low slopes and/ or steady state regions which are sometimes followed by another rise in the mass deposition. The mass gain profiles follow an exponential to polynomial growth functions where the slope of the curves in the early stages of the deposition process may represent the growth rate constants and are illustrated in Tables 5-1 and 5-2. The growth kinetics is higher for the oil-free system in the early stages of the crystallization process and this could clearly be observed from the slope of the curves in the first 10 minutes. The rate of the growth process is slowed down when the oil phase is introduced to the system by about 20 to 45% for oil-brine 2 (0.065M) and oil-brine 1 (0.1M) at 30° C.

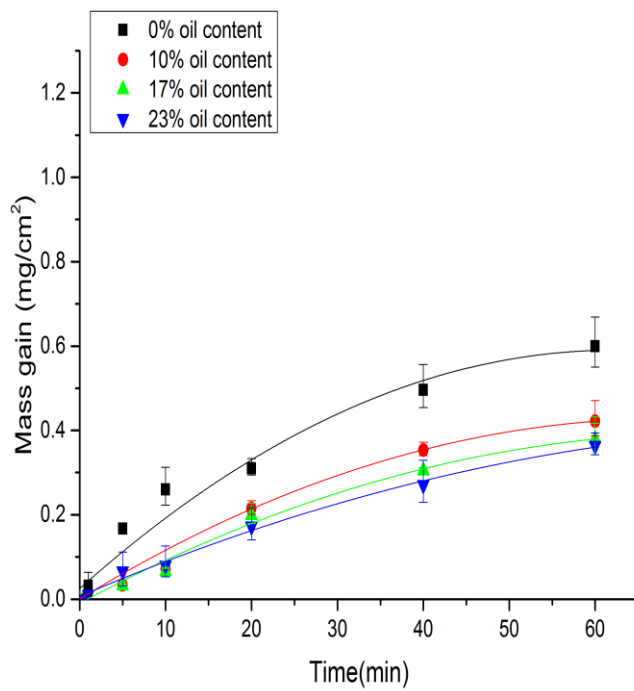


Figure 5-3 Mass gain curve fitting at different time intervals for oil-brine 2 (0.065M) at 30° C

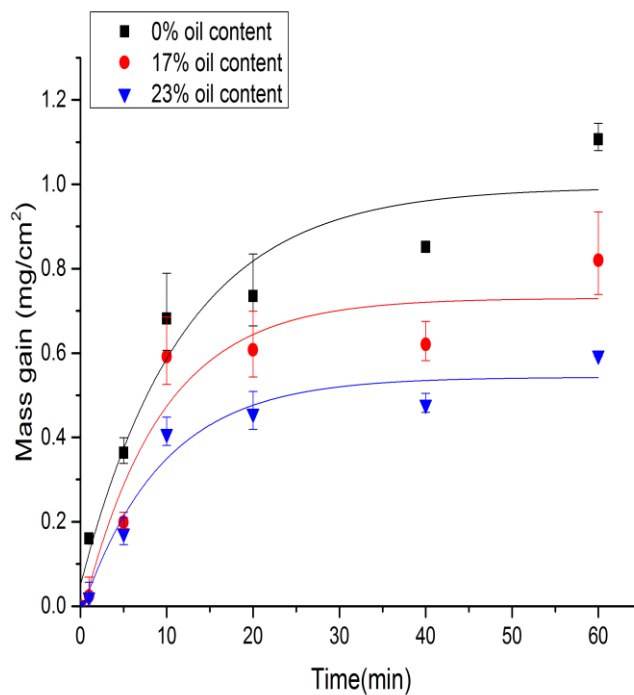


Figure 5-4 Mass gain curve fitting at different time intervals for oil-brine 1 (0.1M) at 30° C

Table 5-1 Curve fitting parameters and growth rate constants (mg/cm².min) for oil-brine 2 (0.065M) at 30° C

Second order polynomial, $y = A + B_1x + B_2x^2$					Growth rate constant (mg/cm ² .min)
Slope, $\frac{dy}{dx} = B_1 + 2B_2x$					
Oil content	A	B ₁	B ₂	R ²	Slope at 10 min
0%	0.02510	0.01817	-0.00015	0.978	0.015
10%	0.00040	0.01249	-0.00009	0.999	0.011
17%	-0.00956	0.01092	-0.00007	0.988	0.009
23%	0.00659	0.00875	-0.00005	0.994	0.008

Table 5-2 Curve fitting parameters and growth rate constants (mg/cm².min) for oil-brine 1 (0.1M) at 30° C

Exponential function, $y = A_1 - A_2 \exp(-kx)$					Growth rate constant (mg/cm ² .min)
Slope, $\frac{dy}{dx} = kA_2 \exp(-kx)$					
Oil content	A ₁	A ₂	k	R ²	Slope at 10 min
0%	0.99317	0.94446	0.08427	0.927	0.034
17%	0.73021	0.76497	0.10915	0.900	0.028
23%	0.54264	0.56277	0.10676	0.946	0.021

5.2.2.2 Mass gain at different time intervals at 60° C

Figures 5-5 and 5-6 present the mass gain for two different brine concentrations at 60° C and different oil fractions up to 23%. Similar trend have also been found for systems with and without oil where the mass gain profiles follow an exponential growth function. The mass gain reaches a steady state in most of the cases whereas it continued to build in some others. However the time required to reach a steady state differs between systems with and without oil. The steady state is an indication of stopping the reaction due to reaching the saturation state. The reaction stopped because it took place in a batch system in which there is no continuous flowing of the reactant into the system. This occurs simultaneously with the bulk precipitation reaction and these caused the supersaturation to decrease with time until a steady state is reached. Figure 5-5 represents the mass gain for oil-brine 3 (0.045M) at 60° C; the kinetics are different between systems with and without oil. It is very fast and reaches a steady state within 10 minutes for the oil-free system, whereas the kinetics are slower in the first 10 minutes for the oil systems before it

becomes faster and the mass gain continues throughout the experiment. The amount of deposition in 1 hour time when the oil phase is introduced into the system is higher than that for the oil-free system by about one fold even though it started with relatively slow kinetics.

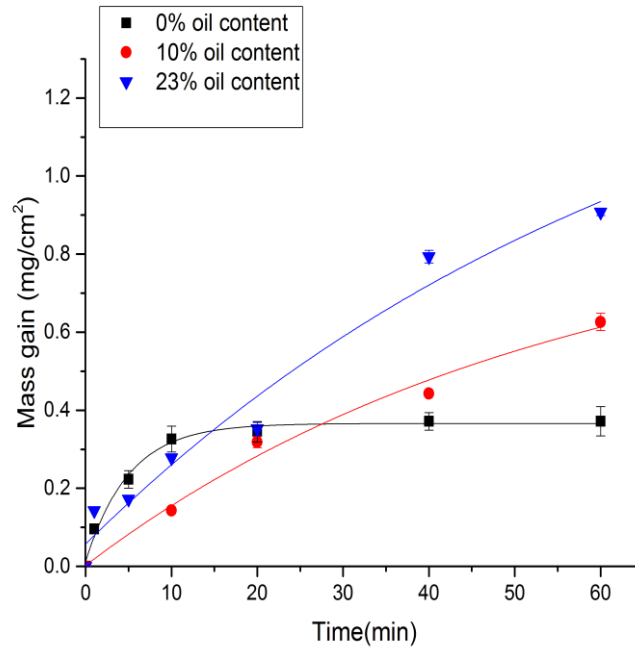


Figure 5-5 Mass gain curve fitting at different time intervals for oil-brine 3 (0.045M) at 60° C

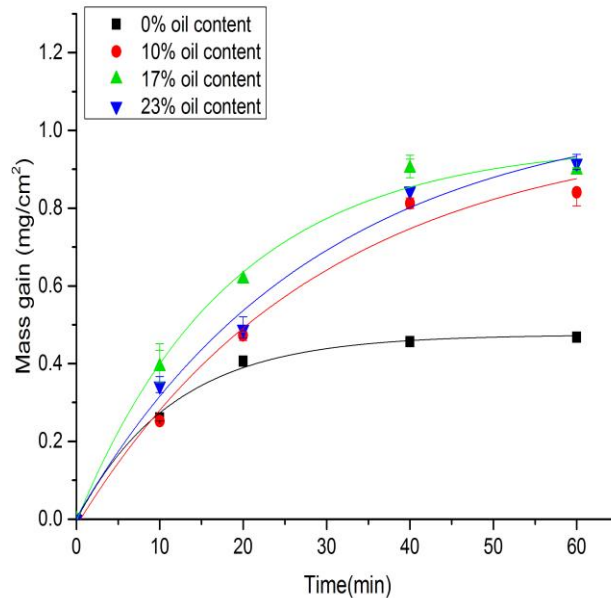


Figure 5-6 Mass gain curve fitting at different time intervals for oil-brine 2 (0.065M) at 60° C

The kinetics in the early stages of the crystallization process for the relatively higher SR brine is quite different as shown in Figure 5.6. The early stage of deposition is faster when the oil phase is in the system. In this case all the growth rate reach a

relatively steady state. It is much faster to reach steady state in the oil-free system after 20 minutes, whereas oil systems take about 40 minutes to reach steady state.

The slope of the curves in the early stages of the deposition process and the growth rate constant are illustrated in Tables 5-3 and 5-4. The rate of the growth process is higher by about 20 to 40% for the oil-free system compared to when the oil phase is introduced to the system for the lower brine concentration of 0.045M. The higher brine concentration exhibits differently where the growth rate is lower by about 10 to 30% for the oil-free system compared to those for the oil systems.

Table 5-3 Curve fitting parameters and growth rate constants (mg/cm².min) for oil-brine 3 (0.045M) at 60° C

Exponential function, $y = A_1 - A_2 \exp(-kx)$					Growth rate constant (mg/cm ² .min)=Slope
Slope, $\frac{dy}{dx} = kA_2 \exp(-kx)$					
Oil content	A ₁	A ₂	k	R ²	Slope at 5 min
0%	0.36619	0.35384	0.19865	0.992	0.026
10%	0.91997	0.91748	0.01824	0.988	0.015
23%	1.58050	1.52341	0.01430	0.970	0.020

Table 5-4 Curve fitting parameters and growth rate constants (mg/cm².min) for oil-brine 2 (0.065M) at 60° C

Exponential function, $y = A_1 - A_2 \exp(-kx)$					Growth rate constant (mg/cm ² .min)=Slope
Slope, $\frac{dy}{dx} = kA_2 \exp(-kx)$					
Oil content	A ₁	A ₂	k	R ²	Slope at 10 min
0%	0.47429	0.47690	0.0862	0.996	0.027
10%	1.00713	1.02439	0.03428	0.986	0.030
17%	0.96705	0.97218	0.05377	0.994	0.040
23%	1.06476	1.06143	0.03485	0.991	0.031

The change in the mass gain can provide us with information about the mechanism of the crystallization process in terms of the transformation of the metastable phase and the growth of the more thermodynamically stable phase and this will be illustrated in section 5.3.3 of this chapter.

5.3 Characterization of calcium carbonate scale deposition

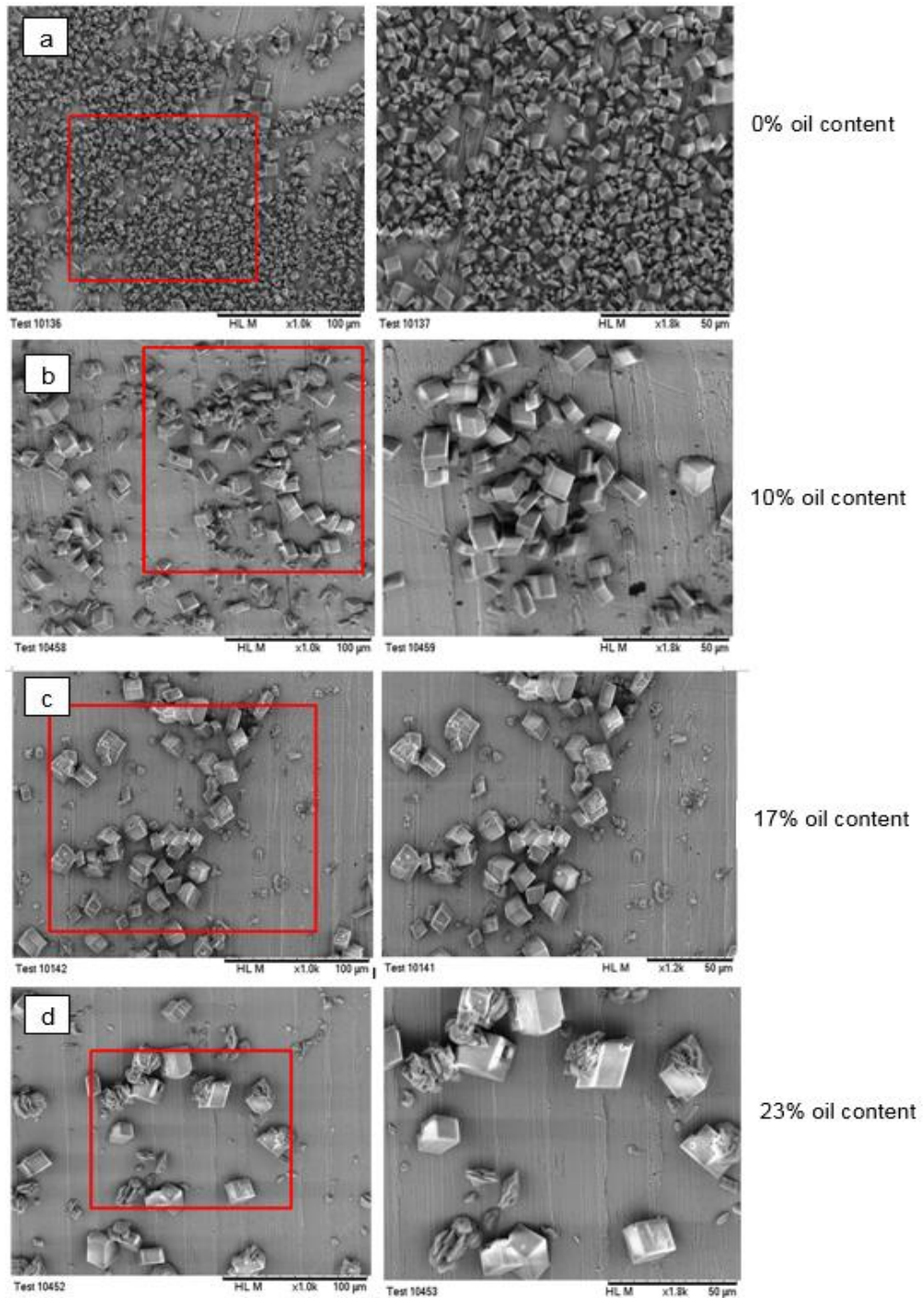
5.3.1 Analysis of crystals morphology using SEM

5.3.1.1 Morphology of crystals deposit at 30° C

The morphology of the scale formed on a stainless steel surface for systems with and without oil is analysed using Scanning Electron Microscopy (SEM) with the aid of image processing program (ImageJ). The microscopic evidence of the scale formed on surfaces enables the understanding of the different stages at which scales are formed; this includes the changes in morphology, crystal growth and surface coverage. Figures 5-7 and 5-8 present scale deposit at 30° C for brines 2 (0.065M) and brine 1 (0.1M), respectively in the presence of different oil fractions. It can be clearly observed that calcite is the major polymorph at this temperature with some vaterite which is mainly seen when the oil phase is presented. It can also be observed that nearly full surface coverage is formed for the oil-free system and less surface coverage for systems with the oil at 60 minutes. The presence of vaterite increases with oil percentage and this is combined with the increase of the size of calcite crystals. The rhombohedral calcite crystals have an average size of 2 and 3 μm in the oil-free system whereas they reach an average of 10 and 15 μm for 23% oil systems of brine 2 and brine 1, respectively.

Comparing vaterite presence, the calcite crystals size and surface coverage in the presence and absence of the oil phase at different time intervals can lead to discover the difference in the mechanism of formation and transformation of CaCO_3 . Figures 5-9 and 5-10 compare surface scale deposit morphology at different time intervals for systems with and without oil at 30° C. The crystals at 10 minutes are of approximately of the same size where both systems consist of calcite of about 5 μm . The only difference between both cases is the existence of small crystals of about 1 to 2 μm and this can be observed in the oil-free system as comparing Figure 5-9 (a) and (e). These are most probably a new generation of crystals that seem to nucleate and grow in a later stage to the old ones which already grew to a bigger size. The increase in nucleation sites continues in the oil-free system until a full coverage of a single layer of crystals is formed on the surface by 60 minutes as shown in Figures 5-9 (d) and Figure 5-10 (d). Vaterite (flower like shape) can be clearly observed in the presence of oil. This may be attributed to the retardation in the rate of its transformation to the more stable calcite. It can also be observed that fewer crystals exist on the surface and the crystals are bigger and reached an average size of 12 μm . Table 5-5 and 5-6 show

a quantitative estimation of the scale built on the surface at different time by analysing Figure 5-11 using ImageJ analysis.



5-7 SEM images for oil-brine 2 (0.065M) at 30° C; (a) 0%, (b)10%, (c)17%, (d) 23% oil content; right images are higher magnification of the red square area.

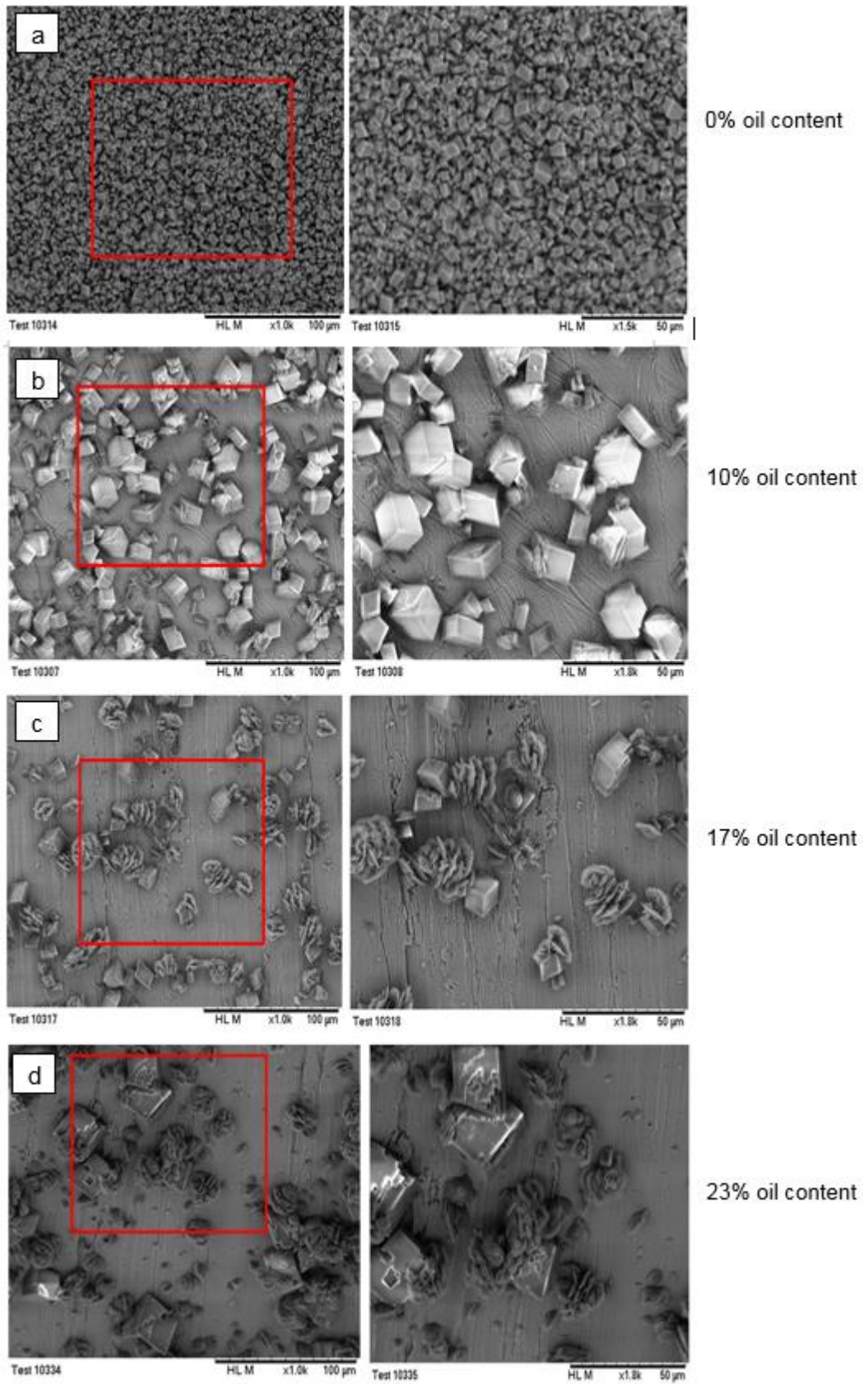


Figure 5-8 SEM images for oil-brine 1 (0.01M) at 30°C; (a) 0%, (b) 10%, (c) 17%, (d) 23% oil content; right images are higher magnification of the red square area

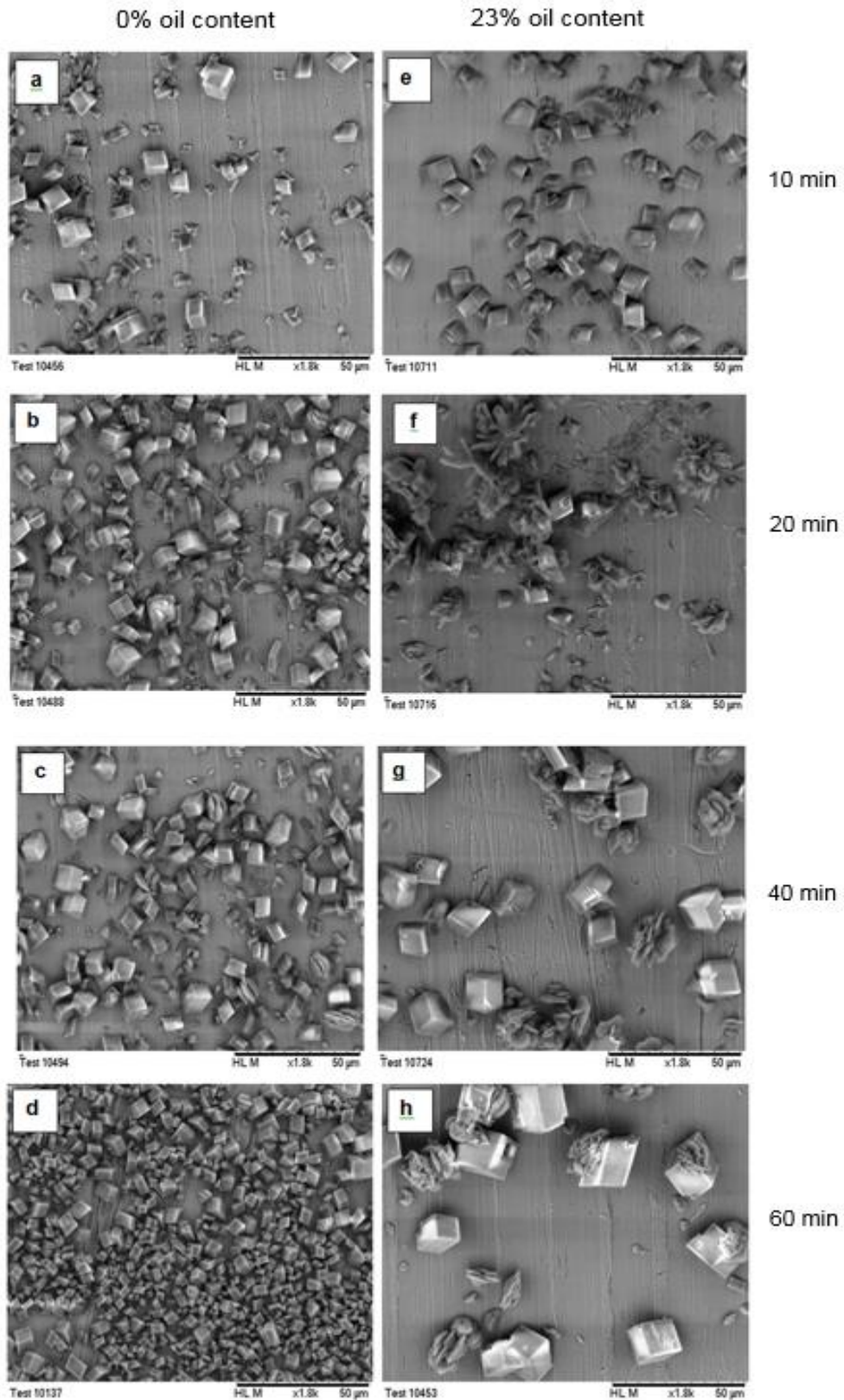


Figure 5-9 Surface deposit for oil-brine 2 (0.065M) at 30° C; 0% oil content (a) 10 min, (b) 20 min, (c) 40 min, (d) 60 min; 23% oil content (e) 10 min, (f) 20 min, (g) 40 min, (h) 60 min

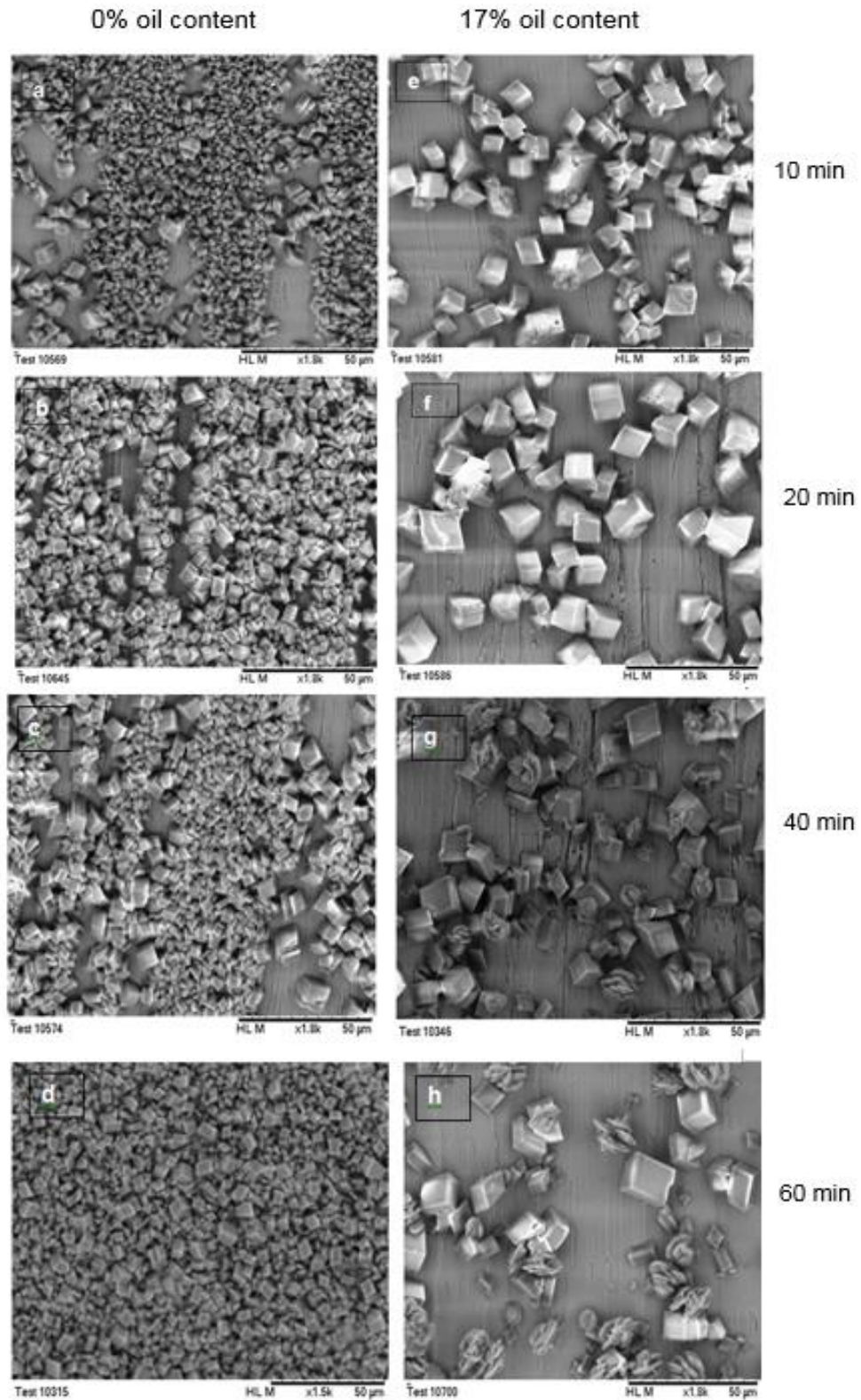


Figure 5-10 Surface deposit for oil-brine 1 (0.1M) at 30° C; 0% oil content (a)10 min, (b) 20 min, (c) 40 min, (d) 60 min; 17% oil content, (e) 10 min, (f) 20 min, (g) 40 min, (h) 60 min

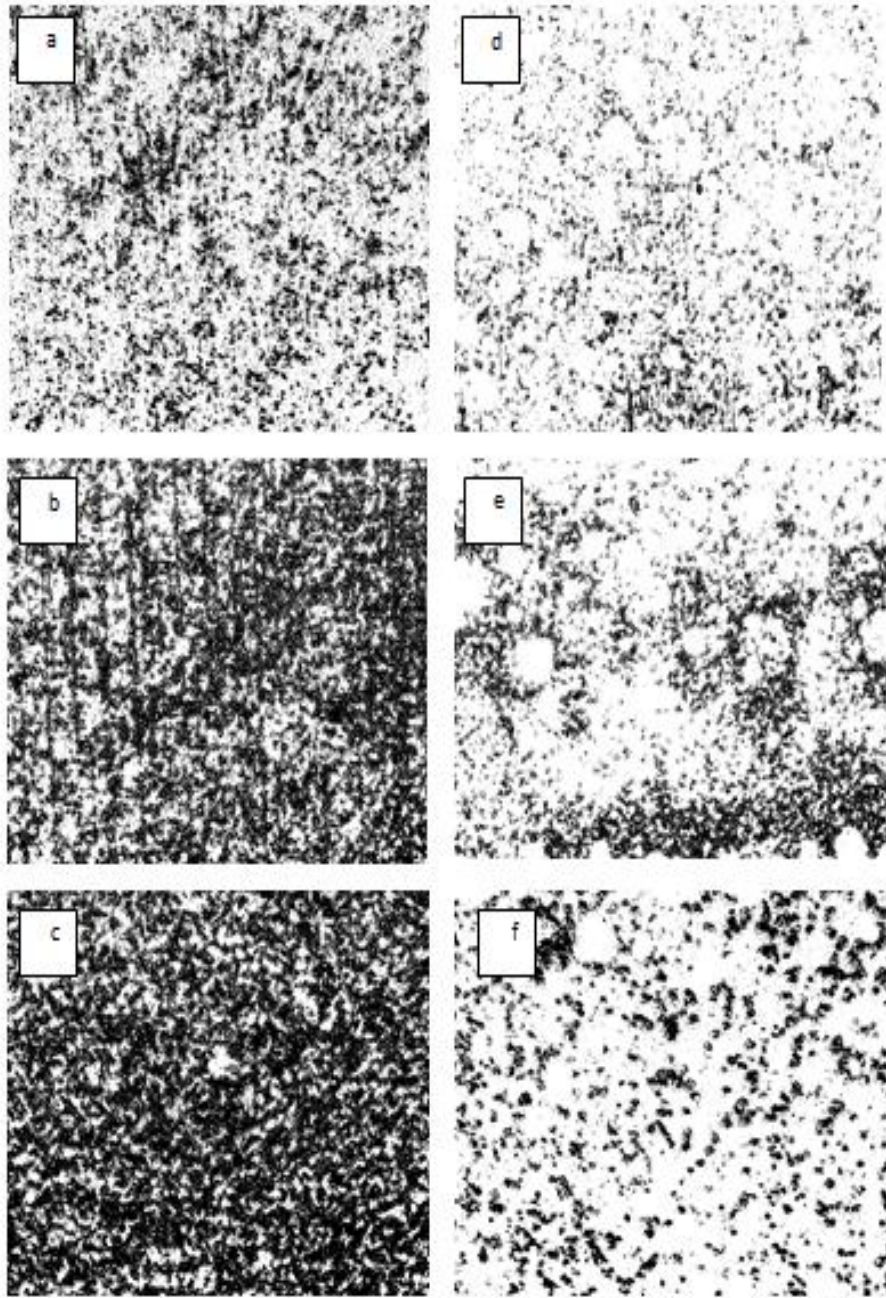


Figure 5-11 Image analysis show surface coverage for oil-brine 2 (0.065M) at 30° C; 0% oil content (a) 10 min, (b) 20 min, (c) 40 min; 23% oil content (d) 10 min, (e) 20 min, (f) 60 min; magnification of the images X200

Table 5-5 Analysis of the scale formed on a surface using image analysis for 0% oil-brine 2 (0.065M) at 30° C

Time (min)	Mass gain (mg/cm ²)	Total area analysed (µm ²) ¹	Surface coverage % ²	Area occupied by crystals (µm ²) ³	Avg. area occupied by a crystal (µm ²) ⁴	Number of crystals ⁵	Mass of the crystals for the analysed area (mg) ⁶	Volume of crystals (µm ³) ⁷	Avg. Volume of a crystal (µm ³) ⁸	Avg. Thickness of a crystal (µm) ⁹
10	0.260	1,139,118	26.384	300,544.89	21.35	14,077	0.002963	1093237.71	77.66	3.64
20	0.496	1,138,623	47.103	536,325.59	22.68	23,648	0.005651	2085169.55	88.18	3.89
40	0.599	1,138,024	51.537	586,503.43	21.89	26,793	0.006826	2518718.75	94.01	4.29

Table 5-6 Analysis of the scale formed on a surface using image analysis for 23% oil-brine 2 (0.065M) at 30°

Time (min)	Mass gain (mg/cm ²)	Total area analysed (µm ²) ¹	Surface coverage % ²	Area occupied by crystals (µm ²) ³	Avg. area occupied by a crystal (µm ²) ⁴	Number of crystals ⁵	Mass of the crystals for the analysed area (mg) ⁶	Volume of crystals (µm ³) ⁷	Avg. Volume of a crystal (µm ³) ⁸	Avg. Thickness of a crystal (µm) ⁹
10	0.080	1,137,428	12.78	145,363.30	32.9	4,418	0.000906	334168.10	75.63	2.29
20	0.173	1,138,631	25.92	295,133.16	87.86	3,359	0.001964	724796.65	215.77	2.46
60	0.295	1,138,782	17.74	202,019.93	97.41	2,074	0.003355	1237893.8	596.89	6.13

¹ Estimated by image analysis, the total pixel area of the images which is converted to µm²

² Surface coverage % is determined by threshold the images as shown in Figure 5-11

- ³ Area occupied by total crystals (μm^2)= total analysed area (μm^2) x (surface coverage/100)
- ⁴ Average area occupied by a crystal (μm^2) is estimated for a number of calcite crystals cross sectional area
- ⁵ Number of crystals= area occupied by total crystals/ avg. area occupied by a crystal
- ⁶ Mass of the crystals for the analysed area= (mass gain (mg/cm^2) x area analysed by the crystals (μm^2))/(10,000)²; where: 10,000 is the conversion from centimeter to microns
- ⁷ Volume of crystals (μm^3)= mass of the crystals (mg) for the analysed area/ density of the crystals (calcite)
- ⁸ Average volume of a crystal (μm^3)= volume of total crystals (μm^3)/ number of crystals
- ⁹ Average thickness of a crystal (μm)=volume of a crystal (μm^3)/ avg. area occupied by a crystal (μm^2)

5.3.1.2 Nucleation in the early stages at 30° C

SEM images for the surface as early as 1 minute indicate the instant reaction for surface scale formation as shown in Figures 5-12 (a) and 5-13 (a). The initial crystals have a spherical to cubic shape of 1 μm or less which may suggest that the initial phase mainly consists of vaterite in addition to some calcite. The population of crystals is clearly increased for the oil-free system by 5 minutes as shown in Figure 5-12 (b) while it remains the same but the crystals increase in size to about 5 μm for the oil system as shown in Figure 5-13 (b). At 10 minutes less surface coverage by cubic crystals of different sizes is observed in the absence of oil. On the other hand, the systems in the presence of oil continued with the same surface coverage of larger crystals size at 10 minutes.

Figure 5-14 (a) and (b) present some visual evidence of the transition of vaterite to calcite. It can be observed that the transition starts from one side of the vaterite spherulites (flower shape) followed by the growth of calcite polymorph which initially takes a cubic edge as indicated by the red circle 1 in the figure. The transformation of vaterite and the growth of calcite then continue until the entire calcite cubic crystal is formed. The red circles 2 and 3 illustrate the final stage of vaterite transformation to calcite where vaterite appears on the final edge and nearly a complete cubic calcite is formed.

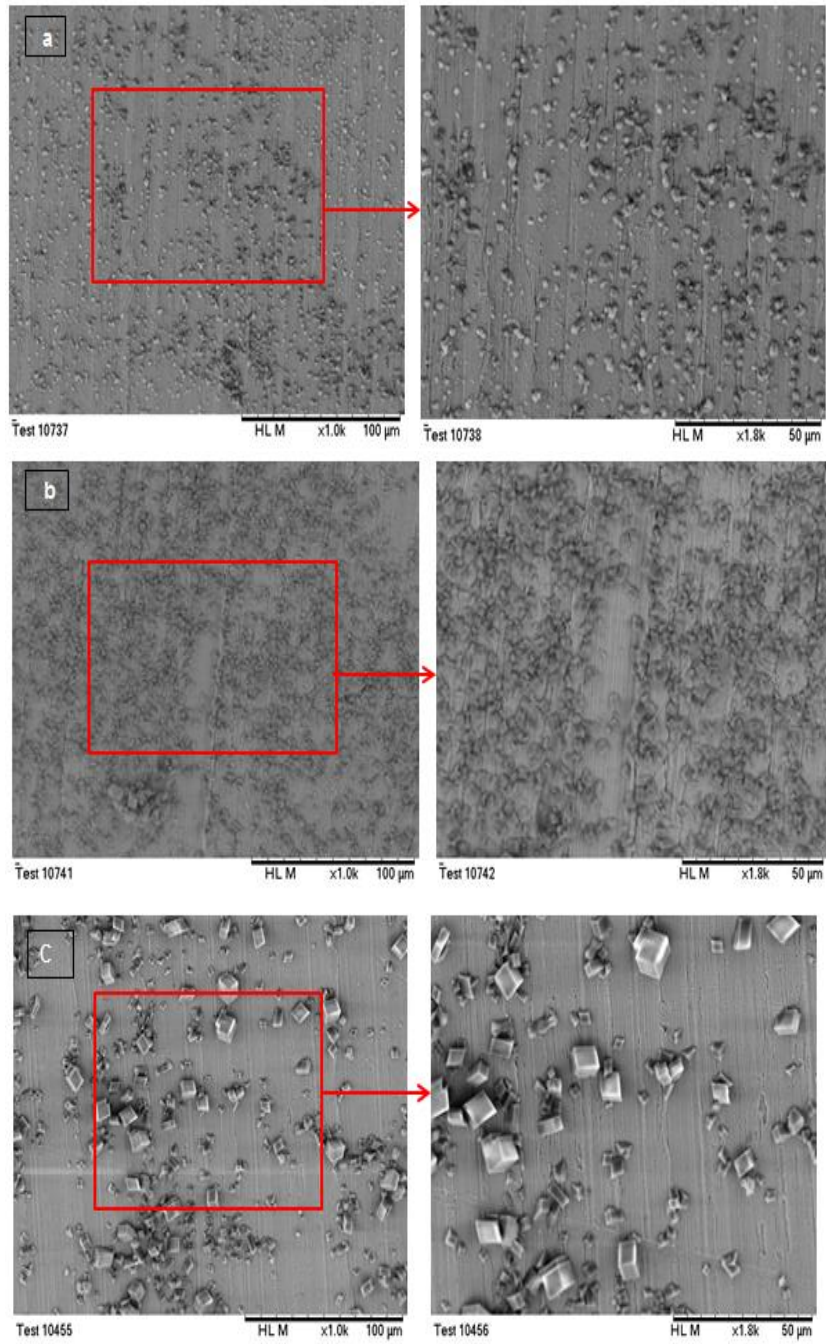


Figure 5-12 Early stages of surface deposition for brine 2 (0.065M) at 30°C; (a) 1 min, (b) 5 min, (c) 10min

The surface of calcite crystals is rough at its early stage before it becomes totally smooth as shown in Figure 5-15 (a). The mechanism of calcite growth can also be observed in Figure 5-15 (b) where a kink site on the surface of a crystal exists and this represents the site where the growth units incorporate and cause further growth of the calcite crystal.

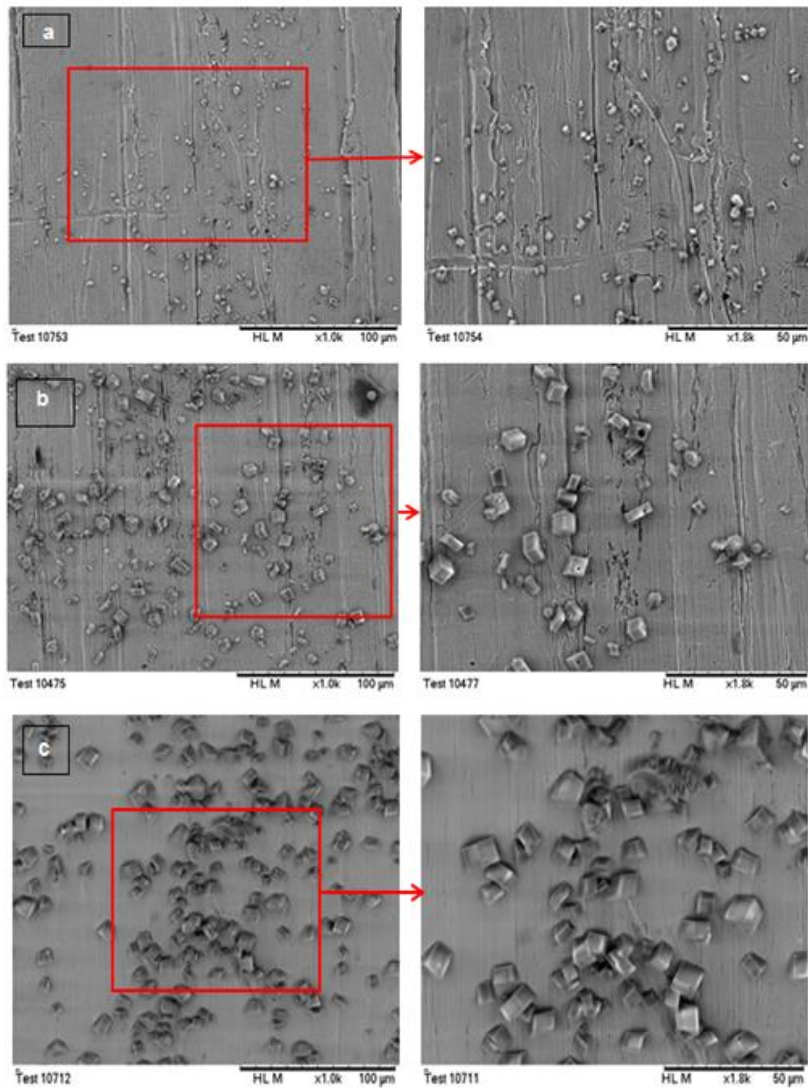


Figure 5-13 Early stage of surface deposition for 23% oil-brine 2 (0.065M) at 30°C (a) 1 min, (b) 5 min, (c) 10min

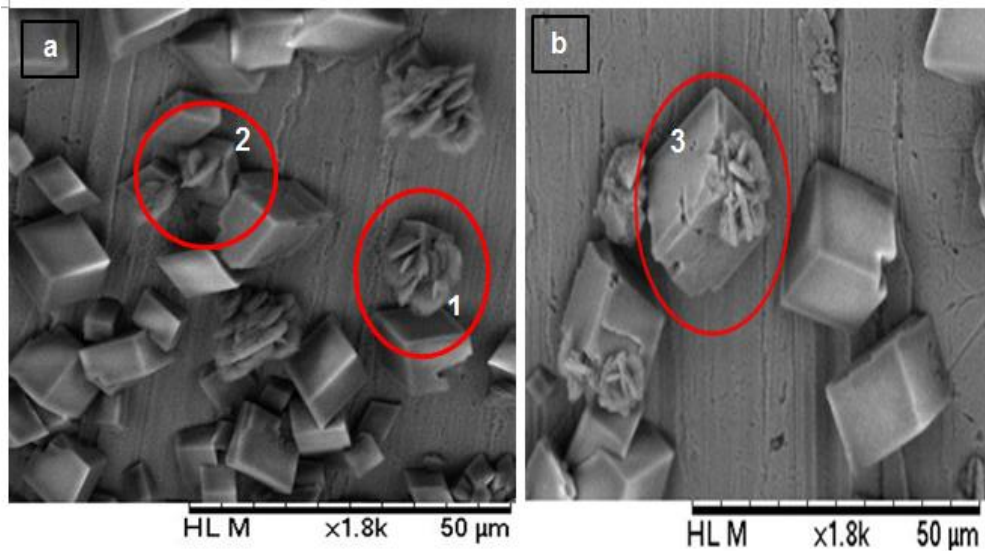


Figure 5-14 The transformation of vaterite to calcite for oil-brine system at 30° C, (a) 10% oil content, sample at minute 40. (b) 23% oil content, sample at minute 60

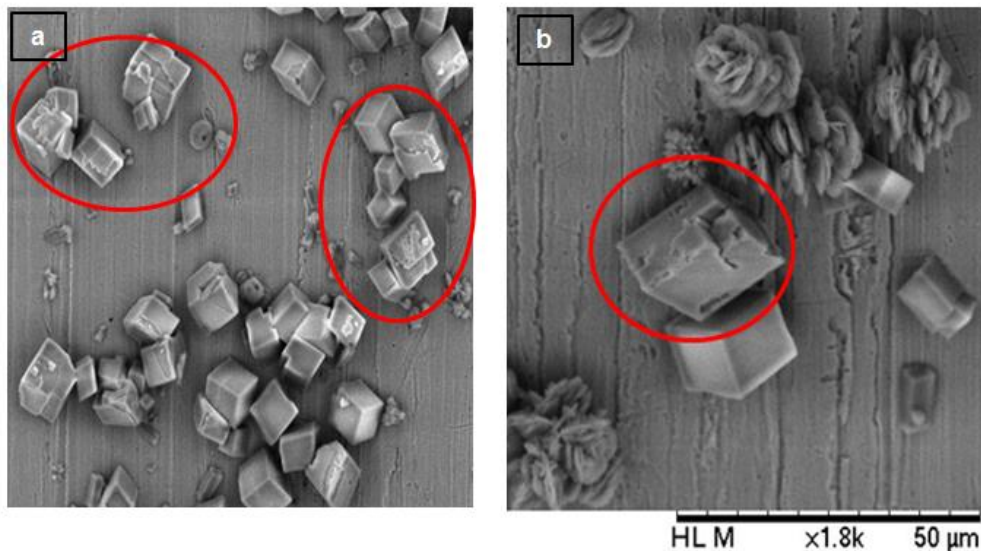


Figure 5-15 The transformation of vaterite to calcite; (a) 17% oil-brine 1 (0.1M), rough calcite surface which represent the final stage of the transformation. (b) 23% oil-brine 2 (0.065M), calcite growth where a kink site has appeared on the surface

5.3.1.3 Morphology of crystals deposit at 60° C

Figure 5-16 presents SEM images of the scale deposit on a stainless steel surface for brine 2 (0.065M) at 60° C. It can be clearly observed that aragonite is the major morphology at this temperature with some calcite. Aragonite crystals were formed as outward needles emerging from a central point and layers of aragonite appear to form and to grow on each other for the systems with oil. This is clearly observed in the higher oil fractions as shown in Figure 5-16(c) to (e).

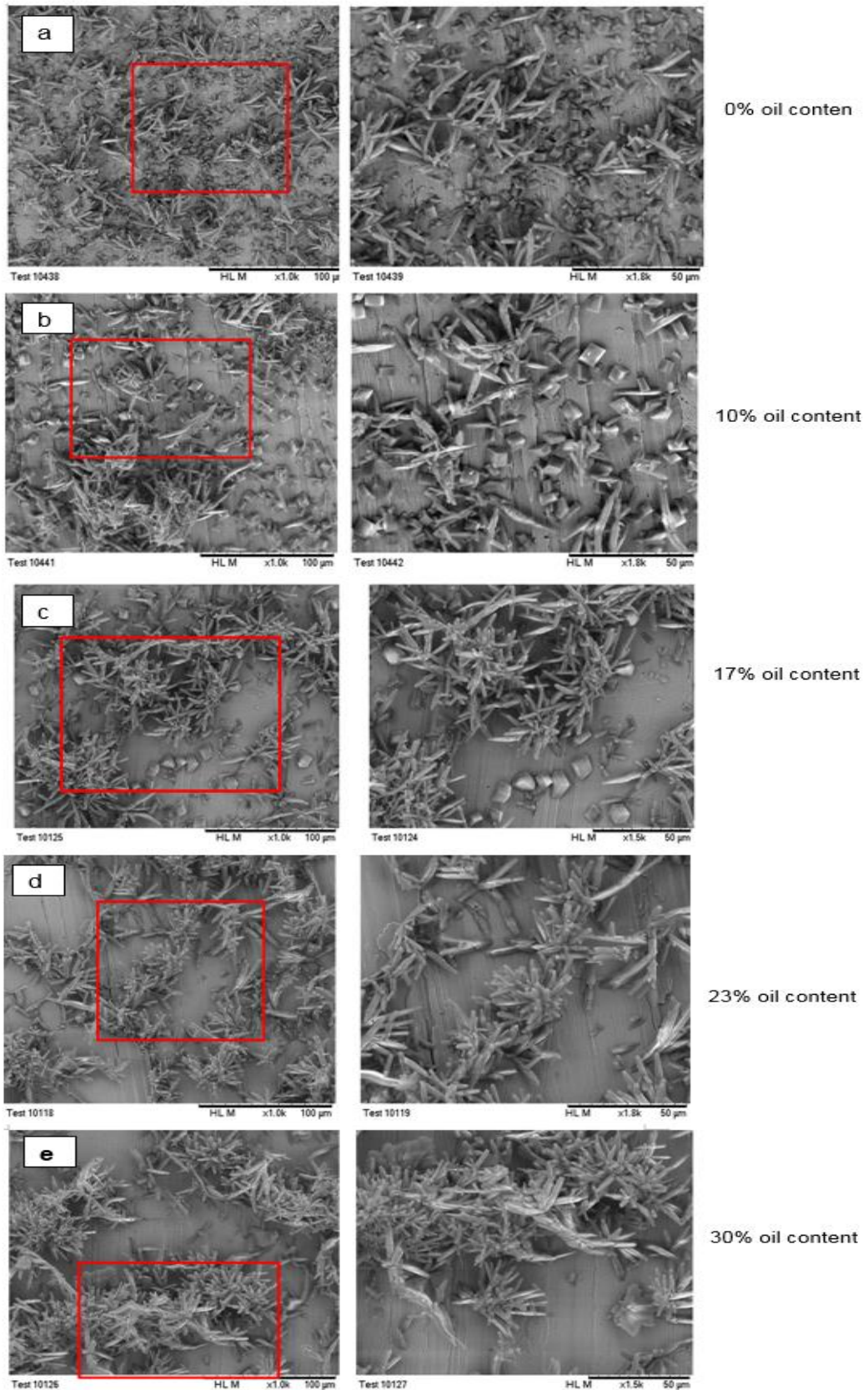


Figure 5-16 Surface deposit for oil-brine 2 (0.065M) at 60° C; (a) 0%, (b) 10%, (c) 17%, (d) 23% (e) 30% oil content

Figure 5-17 shows a comparison of the CaCO_3 scale built up on the surface during different times for oil-brine 3 (0.045M) at 60° C. Calcite is less dominant initially for

the oil-free system and then it starts to increase by 40 minutes compared to the system with oil where calcite crystals clearly appears at 10 minutes. On the other hand, aragonite clearly presents at 10 minutes for the oil-free system and it seems to grow to a bigger size.

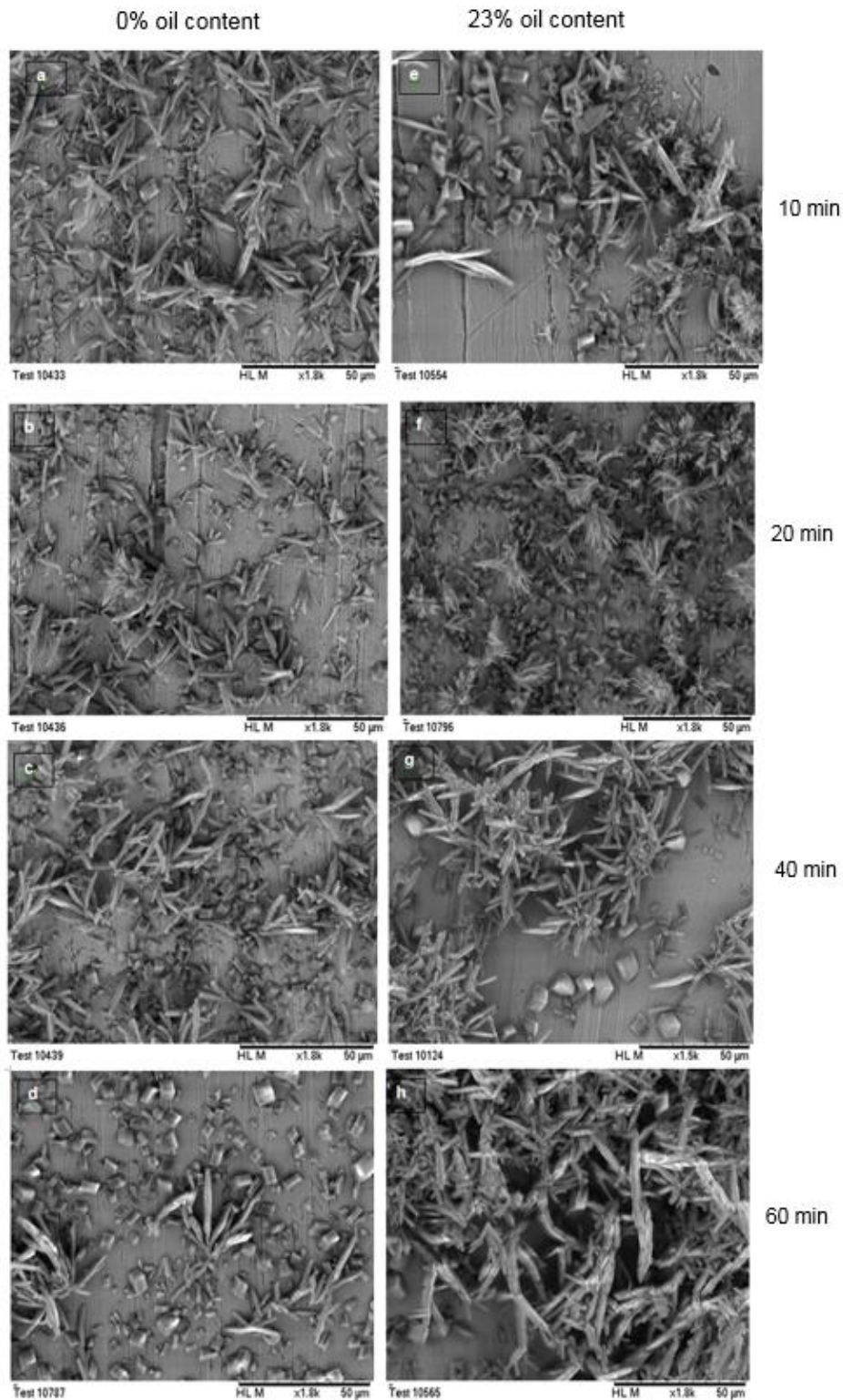


Figure 5-17 Surface deposit for oil- brine 3 (0.045M) at 60° C; 0% oil content (a) 10 min, (b) 20 min, (c) 40 min, (d) 60 min; 23% oil content (e) 10 min, (f) 20 min, (g) 40 min, (h) 60 min

For the oil system aragonite stays as thin needles until 20 minutes and layers of aragonite starts to accumulate at 40 minutes where they become thicker by 60 minutes as shown in Figure 5-17(g) and (h). The increase in the availability of calcite with time can be observed simultaneously to the decrease in the availability of aragonite for oil-free system. This may suggest the transformation of aragonite to calcite with time. The clear presence of calcite at 10 minutes with thin aragonite needles for the system with oil may indicate rapid transformation of the old formed aragonite to calcite. The rest of aragonite which did not transform is then grown by 40 minutes and layers of aragonite started to accumulate by 60 minutes.

Figure 5-18 may be considered as evidence of the transformation of aragonite to calcite where calcite is found to occupy similar position to aragonite as indicated in the figure.

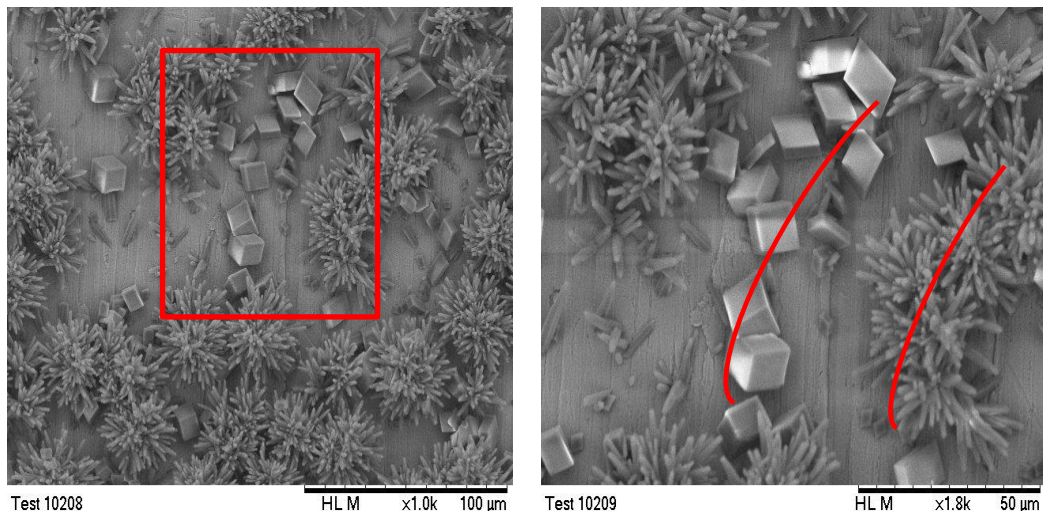


Figure 5-18 Calcite occupy a similar surface area with a similar orientation to aragonite after transformation; sample is taken at 60 minutes for 10% oil-brine 2 (0.065M) at 60° C

5.3.1.4 Nucleation in the early stages at 60° C

Figures 5-19 and 5-20 present the early stages of the surface crystallization for both systems at 60° C. The nucleation and growth processes seem to take place in a few seconds as a considerable amount of crystals is formed within the first minute. At 5 minutes, aragonite is observed to build up as aggregates of thin needles which emerged from a central point. These aggregates are bigger in size of an average size of 30 μm and are fewer in number for the oil-free system compared to an average size of 15 μm for the oil system. Calcite is found to spread over the surface with a high population of an average size of 2 μm for the system with the oil. Calcite is fewer in number and grew to an average size of 7 μm for the oil-free system. It can also be observed where calcite is presented there is no aragonite around it.

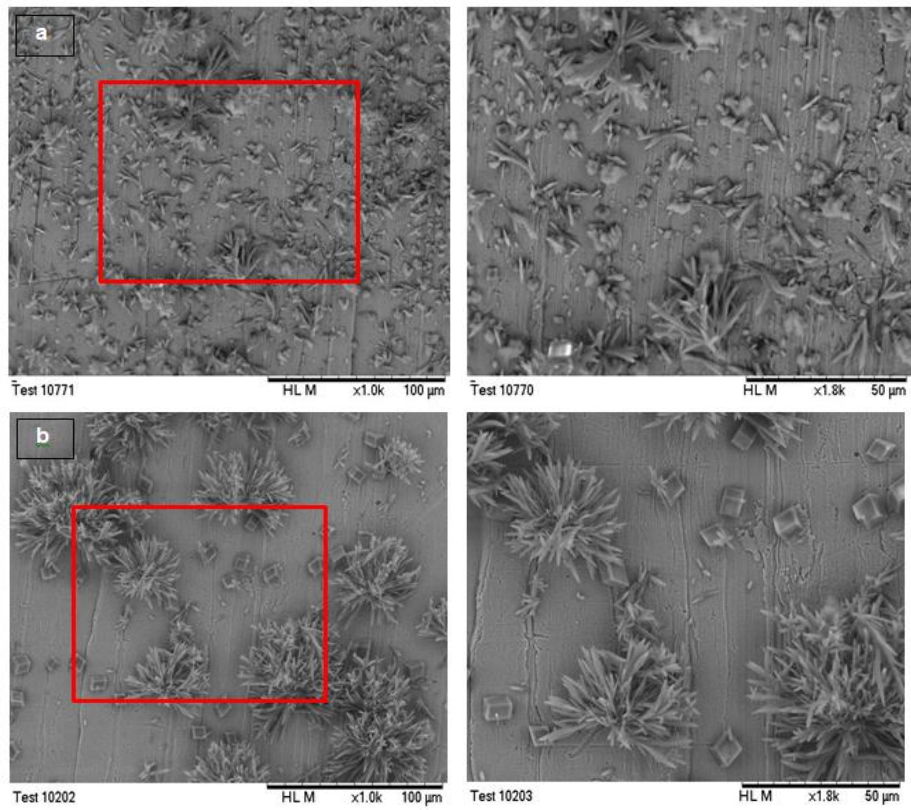


Figure 5-19 Early stages of scale deposition for brine 3 (0.045M); (a) 1min, (b) 5min

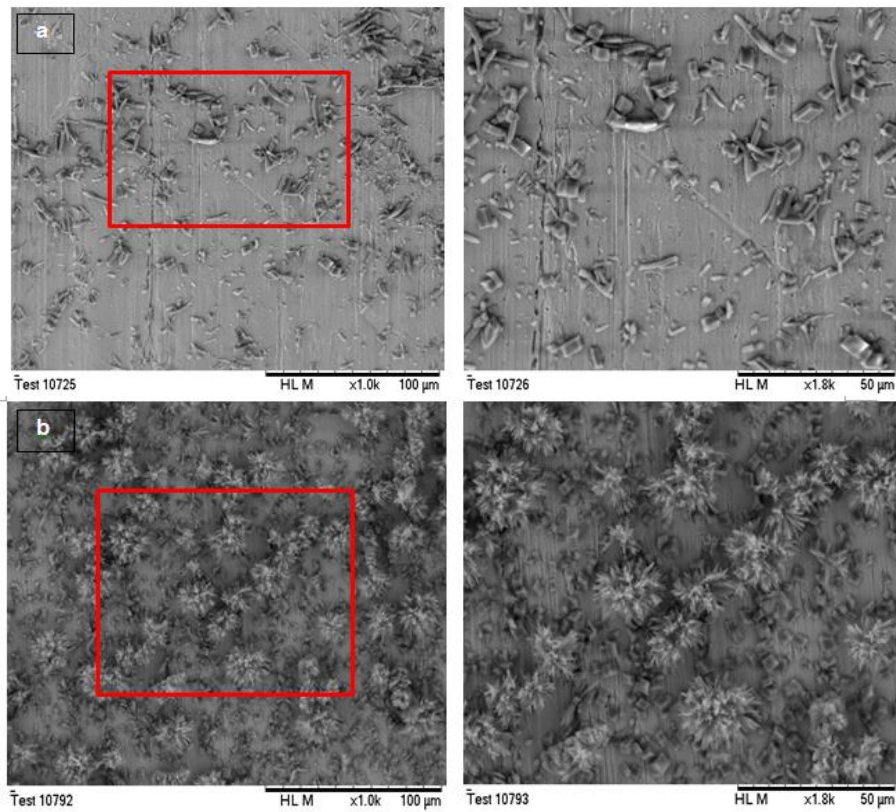


Figure 5-20 Early stages of scale deposition for 23% oil-brine 3 (0.045M); (a) 1min, (b) 5min

5.3.2 Characterization of CaCO₃ scale using XRD

Calcium carbonate scale deposits on RCE samples were characterized for scale polymorphic transformation using X Ray Diffraction (XRD). Figures 5-21 and 5-22 illustrate XRD patterns for oil-brine 2 (0.065M) and oil-brine 1 (0.1M) after 1 hour at 30° C, respectively. The two calcium carbonate polymorphs, calcite (C) and vaterite (V) have been detected and this is also confirmed by SEM in Figures 5-9 and 5-10. Calcite (104) with a strong intensity at 2θ of 29.4° can be easily identified for systems with and without oil whereas vaterite is presented with a relatively weak intensity at 2θ of 25.0°. The diffraction peak of calcite is clearly observed to increase with time due to the transformation process as in Figures 5-21 and 5-22.

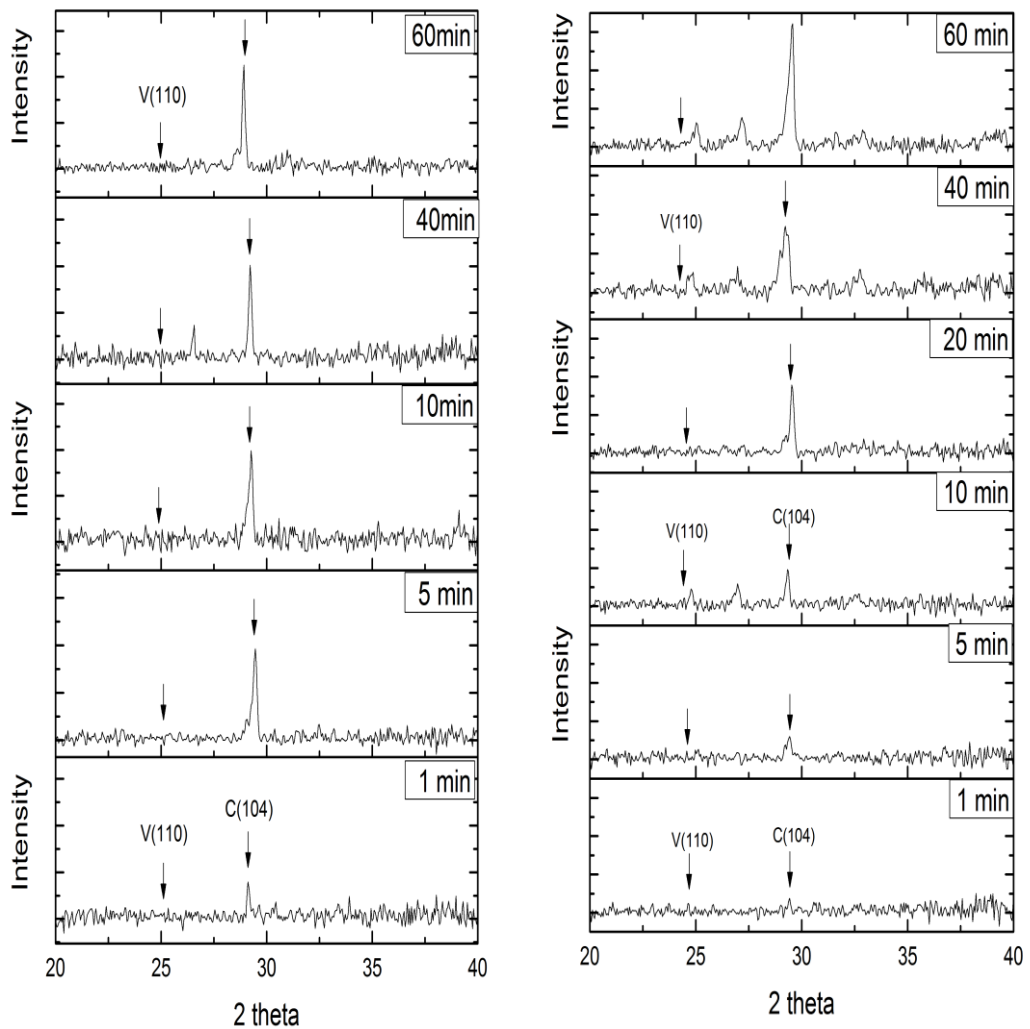


Figure 5-21 Comparing XRD patterns for oil-brine 2 (0.065M) at 30° C; LHS, 0% oil content; RHS, 23% oil content

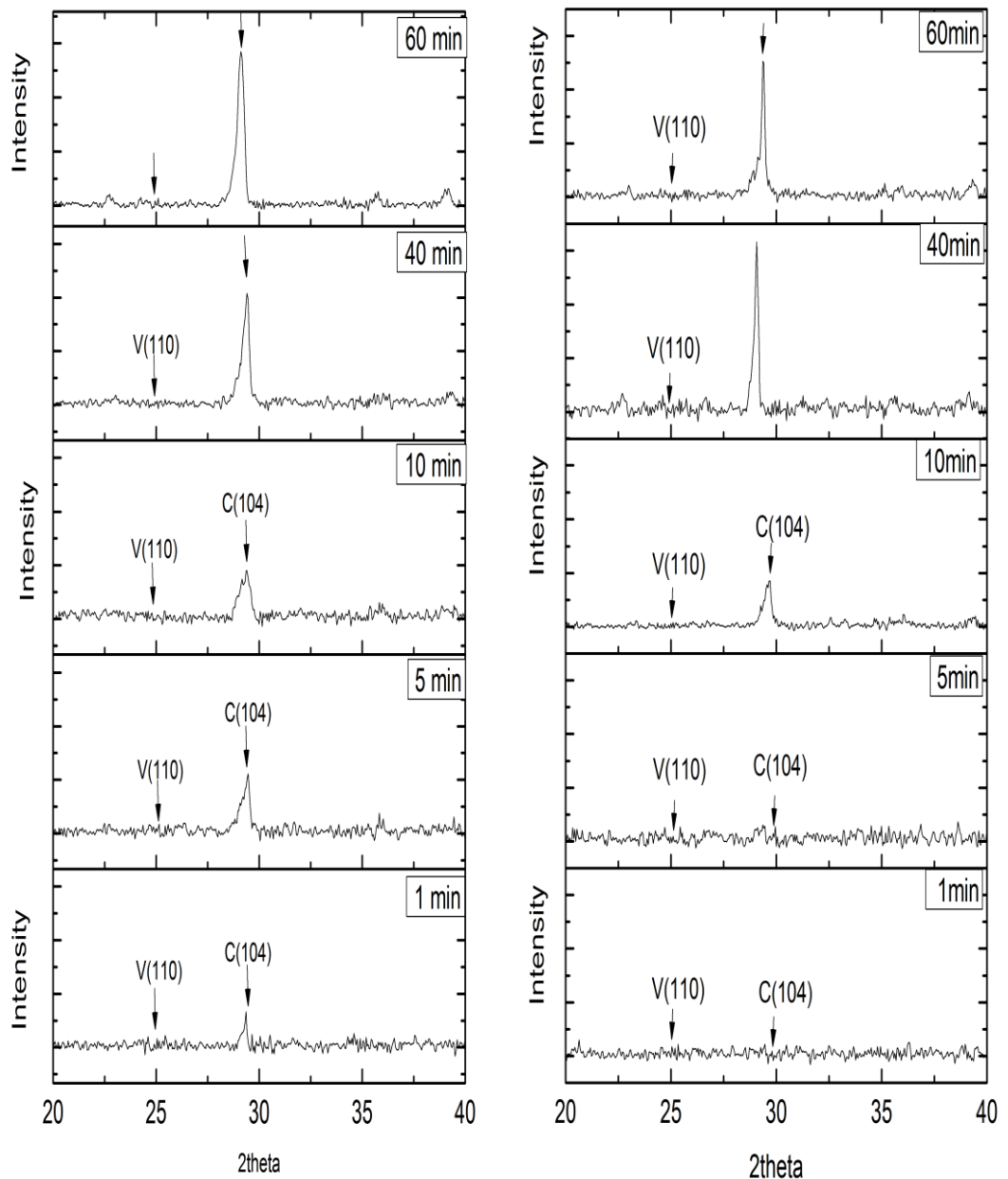


Figure 5-22 Comparing XRD patterns for oil-brine 1 (0.1M) at 30°C; LHS, 0% oil content; RHS, 17% oil content

5.3.3 Analysis of the polymorphic abundance:

Calcium carbonate crystals may be present in three different crystalline polymorphs and the three phases coexist under specific conditions of temperature, supersaturation and mixing conditions [47, 68].

Studying the kinetics of calcium carbonate nucleation and growth processes on a surface by tracking the kinetics of individual polymorphs is a complicated process

because of the continuous transformation of the unstable phases towards the more stable one. Since vaterite, the less stable polymorph, is known to act as a precursor for calcite and aragonite formation [51], it is expected and assumed that vaterite is formed initially and the other phases are formed as a consequence of vaterite transformation. It is also assumed a negligible presence of amorphous calcium carbonate ACC which is known as a highly unstable phase and can be totally transformed to the crystalline form in a few minutes [50, 200]. It was postulated by [48] that the lifetime of ACC is too short to distinguish the time between its formation and transformation. Based on these assumptions the mole fraction of each phase is estimated using equations 4-22 to 4-24. The number of mmole of each polymorph per 1cm^2 of surface is calculated by multiplying the total mmol/cm^2 of calcium carbonate that is formed by the mole fraction of each polymorph. The mass in mg/cm^2 of each polymorph is then calculated by multiplying the mmol/cm^2 of each polymorph by the molecular weight of CaCO_3 . By this way, the change in the abundance, in addition to the mass growth of each polymorph could be evaluated.

5.3.3.1 Assessment of the polymorphic abundance on a stainless steel surface at 30° C

Figures 5-23 to 5-26 show the mole fraction and the mass growth for each polymorph formed on a stainless steel surface for two different brine concentrations with and without oil at 30° C. Since only vaterite and calcite are known to form at this temperature [48, 51, 201], equations 4-25 and 4-26 are used for quantifying the polymorphic composition for binary mixtures of calcium carbonate, this was also confirmed by SEM in Figures 5-9 and 5-10 and XRD in Figures 5-21 and 5-22. The distribution of the phase fraction with time is shown in Figures 5-23 and 5-24 for oil-free system. An equal composition of vaterite and calcite are found to exist within the first minute and this not only indicates rapid nucleation but also a rapid transformation process. The decline in the vaterite composition which is accompanied with the rise in the calcite composition is an indication of the transformation reaction from vaterite to calcite. The rate of vaterite transformation and the rate of calcite growth are faster in the first ten minutes than later where the abundance of vaterite is decreased by about half of its initial value. The rate of vaterite transformation and calcite growth are slowed down beyond 10 minutes where the composition of vaterite and calcite are about 10 and 90%, respectively at the end of 1 hour.

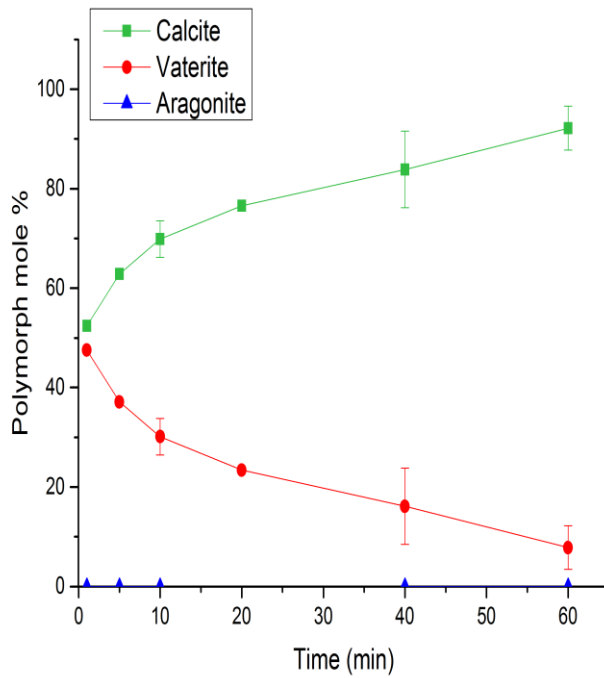


Figure 5-23 Polymorph abundance on the surface for brine 2 (0.065M) at 30°C

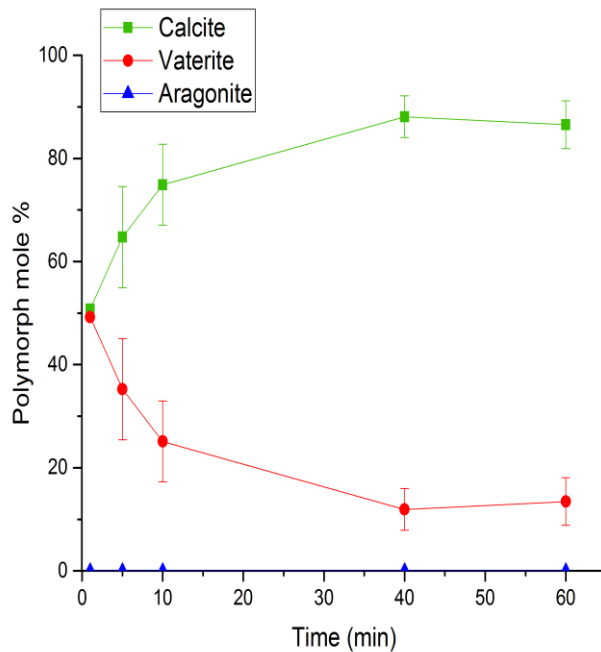


Figure 5-24 Polymorph abundance on the surface for brine 1 (0.1M) at 30°C

The polymorph fraction can then be translated to mass distribution in mg/cm^2 for each crystalline phase that is formed and compared to the mass gain of total CaCO_3 scale deposit as shown in Figures 5-25 and 5-26. A linear growth of calcite with time is clearly observed after 10 minutes which follows a trend similar to that of the overall CaCO_3 mass gain. This may indicate the control of calcite growth mechanism over the other polymorph. The linear growth of calcite with time has

also been reported in the literature [41, 81]. The amount of vaterite deposit remained low throughout the experiment time of 1 hour. The first 10 minutes may be considered as the period of continuous build-up of new vaterite which are then subject to a quick transformation to the more stable calcite. The change in the slope of lines for the total mass gain can also be observed at 10 minutes. This may be due to the change in the kinetic rates between the period of the appearance of vaterite simultaneous to the period of the nucleation and the growth of calcite.

SEM images in the left side of Figures 5-9 and 5-10 illustrate a clear increase in the number of calcite crystals with time in addition to the existence of a variety of sizes of crystals. This ensures the continuous formation of the new generation of calcite according to the polynuclear mechanism where the old crystals are bigger in size and can be distinguished from those which are formed later. However a nearly full coverage of the surface is shown to exist at 1 hour and the crystals may then be subject to further growth process. This is in agreement to [57] where an electrochemical technique in which the rate of oxygen reduction at the surface of a rotating disc electrode is used to quantify surface deposition on a stainless steel substrate. A surface coverage of about 60% in 1 hour was detected for an equimolar brine of 0.035M of Ca^{2+} and HCO_3^- ions. It was suggested that small particles (sub-microns) were distributed over the surface among large particles but the small crystals were the main contributors to the surface coverage.

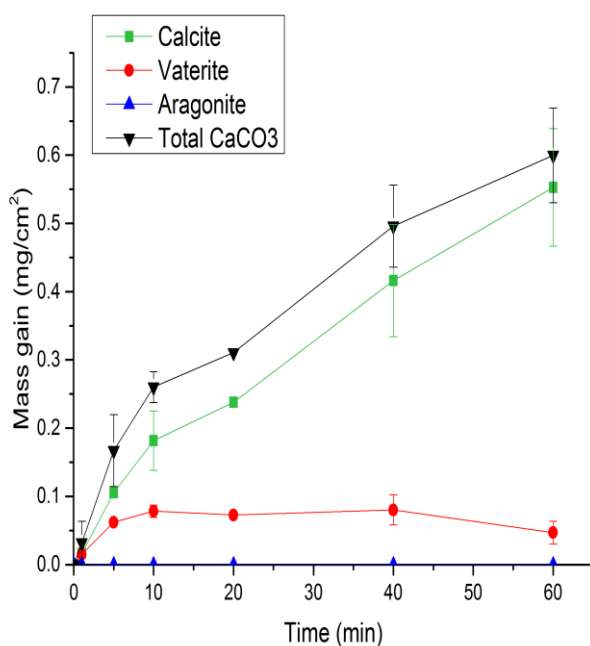


Figure 5-25 Polymorph mass gain (mg/cm²) for brine 2 (0.065M) at 30° C at different times

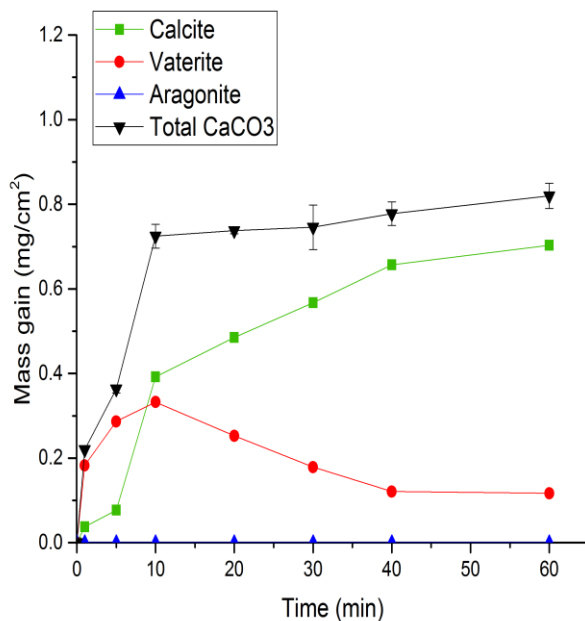


Figure 5-26 Polymorph mass gain (mg/cm²) for brine 1 (0.1M) at 30°C at different times

The assessment of polymorph abundance in the presence of an organic phase is illustrated in Figures 5-27 and 5-28. In the first minute, 28 mole% of calcite is found to form at the surface for the lower saturation brine 2 (0.065M) compared to 18 mole% of calcite in the case of higher saturation brine 1 (0.1M). However, this does not necessarily mean that the process of nucleation and transformation for brine 2 is higher and faster than that for brine 1, it could be because there is a lower nucleation rate initially for the lower saturation brine. The nucleation for brine 1 is most probably very intense during the first 5 minutes as can be observed from the slow decline of vaterite abundance within the first 5 minutes in Figure 5-28. It can also be noted that the change in the polymorphic composition exhibits a much lower rate for brine 2 (0.065M) than for brine 1 (0.1M) by observing the slope of the lines. Equal compositions of vaterite and calcite are found to exist within the first ten minutes for brine 1 whereas it requires 60 minutes for brine 2 to equilibrate. This also suggests the slow transformation process for the lower saturation brine compared to the higher saturated brine 1. The composition of vaterite and calcite for brine 1 are about 20 and 80%, respectively at 60 minutes.

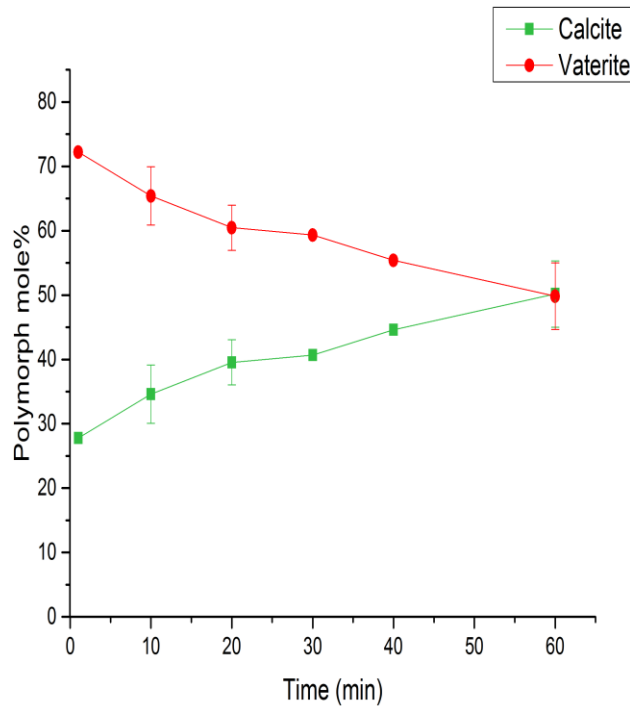


Figure 5-27 Polymorph abundance on the surface for 23% oil-brine 2 (0.065M) at 30° C

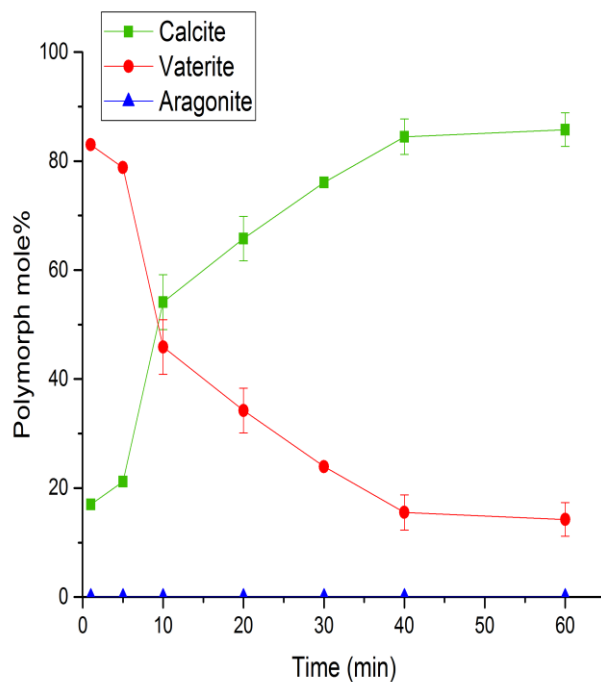


Figure 5-28 Polymorph abundance on the surface for 17% oil-brine 1 (0.1M) at 30° C

The mass distribution of each polymorph could better describe the crystallization process as shown in Figures 5-29 and 5-30. Both vaterite and calcite mass growth are found to build up parallel to each other and their presence is in equal amounts by the end of experiment for the case of brine 2 (0.065M) as shown in Figure 5-29. The continuous rise in vaterite amount indicates a long period of vaterite nucleation

and/or growth processes. The increase in vaterite amount occurs simultaneously with the increase in calcite nucleation and growth processes. This may lead us to suggest that the disappearance of vaterite due to the transformation of vaterite to calcite is a slow process which occurs in a gradual manner as it is combined with a gradual growth of calcite polymorph.

Brine 1 (0.1M) in Figure 5-30 exhibits a similar trend to the lower SR brine initially but with much faster rate where both polymorphs are present in equal amounts by 10 minutes compared to 60 minutes for brine 2 (0.065M). This is again due to vaterite nucleation and/or growth processes which occur in conjunction with calcite nucleation and growth processes. Further transformation of vaterite to calcite without the continuation in vaterite nucleation and/or growth processes results in a clear decrease in the vaterite amount and an increase in the calcite amount and this is what brine 2 is expected to behave like after 1 hour. The period from 10 to 40 minutes is presented as a steady state in the total CaCO_3 mass gain where equilibrium between the disappearance of vaterite and the nucleation and growth of calcite exists.

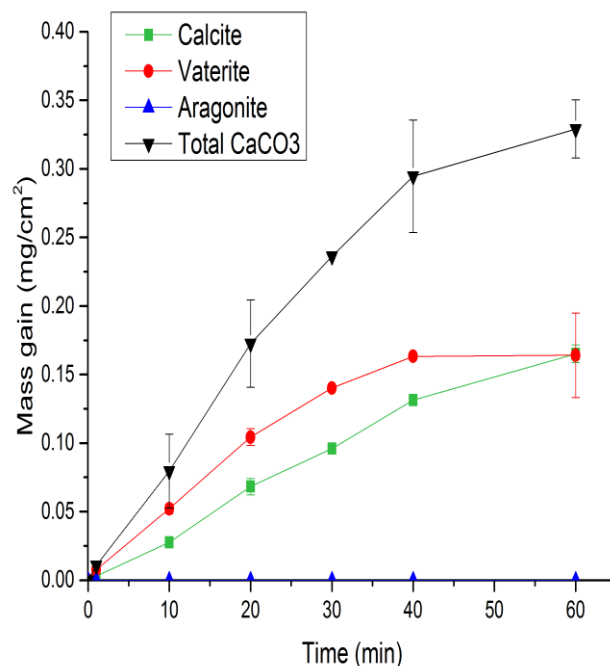


Figure 5-29 Polymorph mass gain (mg/cm^2) for 23% oil-brine 2 (0.065M) at 30° C

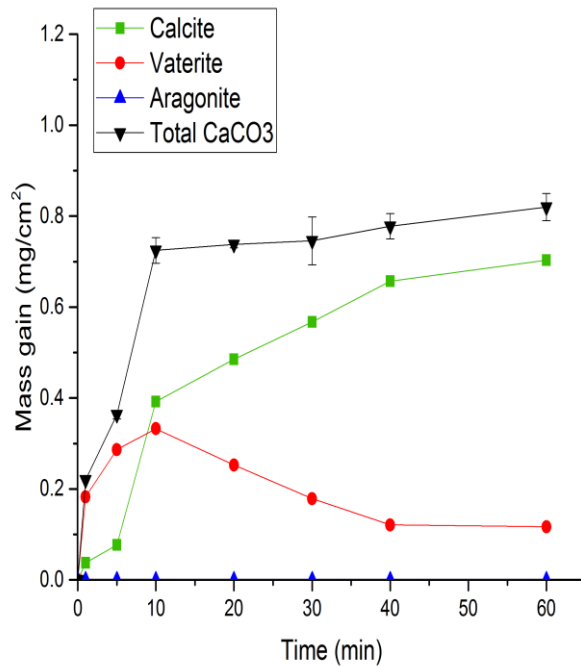


Figure 5-30 Polymorph mass gain (mg/cm²) for 17% oil-brine 1 (0.1M) at 30° C

SEM images in the right side of Figures 5-9 and 5-10 show a clear increase in the crystals size with time rather than crystals sites. It can also be observed the relatively equal size of the crystals which suggests that the initial nuclei are formed at the same time, according to the mononuclear mechanism. This first generation of vaterite crystals are then subject to grow in size rather than increase in numbers. This finding can explain the differences of the slope of the lines in the initial stage of the crystallization process between systems with and without oil which is shown in section 5.1.2 of this chapter.

The polymorphic composition of vaterite and calcite for the systems with and without oil for different oil fractions at 30° C is illustrated in Figure 5-31. The abundance of vaterite is much more in the presence of oil where it represents about 50 to 60% of the total polymorph abundance whereas it only represents by about 10% in the absence of oil.

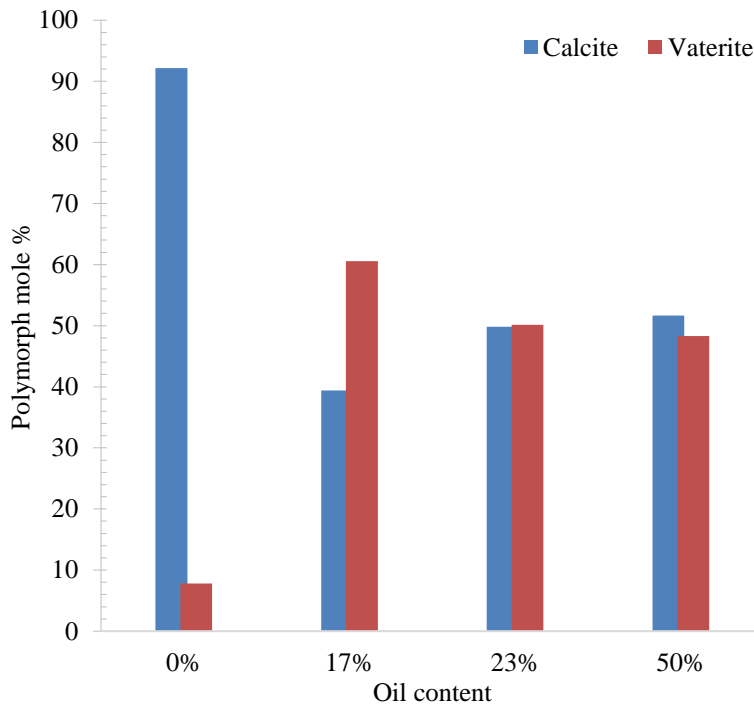


Figure 5-31 Polymorph mole% and the total CaCO_3 mass gain ($\text{mg}/\text{cm}^2\cdot\text{hr}$) for oil-brine 2 (0.065M) system at 30°C

5.3.3.2 Assessment of the polymorphic abundance on a stainless steel surface at 60°C

Figures 5-32 to 5-35 show the mole percentage and the mass growth for each of calcium carbonate crystalline phases that are formed on the substrate surface at 60°C for brine 3 (0.045M) in the presence and absence of oil. Aragonite is known to predominate at this temperature and its presence is combined with calcite and some vaterite [202]. This is also confirmed by SEM in Figure 5-16. The presence of vaterite is very low in which it could be ignored in this temperature and the equations used for quantifying the polymorphic composition in this case are equations 4-27 and 4-28 for binary mixture of aragonite and calcite only.

The distribution of the phase fractions with time for brine 3 (0.045M) is shown in Figure 5-32. In the first minute, aragonite is found to be about 80 mole% while calcite was about 20 mole%. This indicates the short induction time and the fast transformation rate where the transformation in this temperature is considered from the metastable aragonite to the stable calcite. The initial percentage detected for aragonite is 80% at 1 minute and it is fallen to about 40% in 60 minutes. Equal compositions of aragonite and calcite exist in about 50 minutes whereas a complete transformation may take around 240 minutes if the transformation continues at the same rate.

It is not clear whether aragonite has formed as a result of vaterite transformation or it formed directly from the amorphous calcium carbonate without a vaterite precursor. However, working with a lower saturation brine is recommended to discover more about the early stages of the crystallization process.

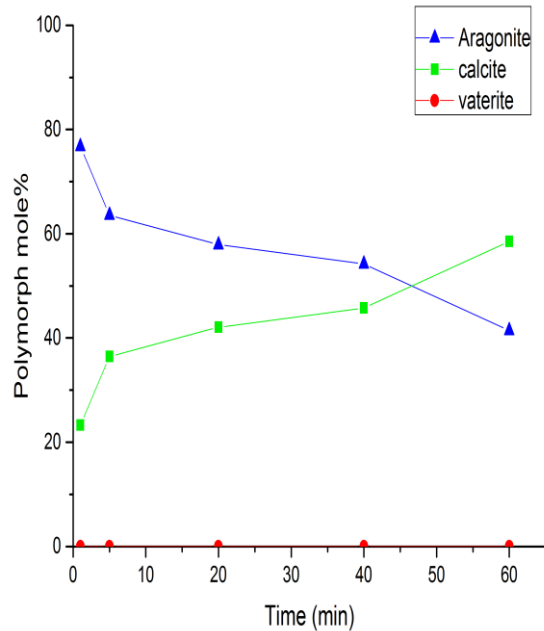


Figure 5-32 Polymorph abundance on the surface for brine 3 (0.045M) at 60° C

The mass profile in Figure 5-33 shows period of nucleation and growth for both the phases which take about 20 minutes and these represented by the parabolic region of the curves before a change in the trend is exhibited. In this region, transformation of aragonite to calcite is also taking place and can be clearly seen by the decline in the fractions of aragonite in Figure 5-32. The change in the slope of calcite beyond 20 minutes follows a linear growth which continues to the end of experiment whereas aragonite starts to decline gradually as a result of its transformation process. However, combining the nucleation, the transformation and the growth processes to the total CaCO_3 mass gain profile suggest that the first 20 minutes generally represents periods of nucleation and growth for both phases whereas reaching a steady state represents the region when nucleation of aragonite is stopped but the transformation of aragonite is continued which is combined with the nucleation and growth of calcite.

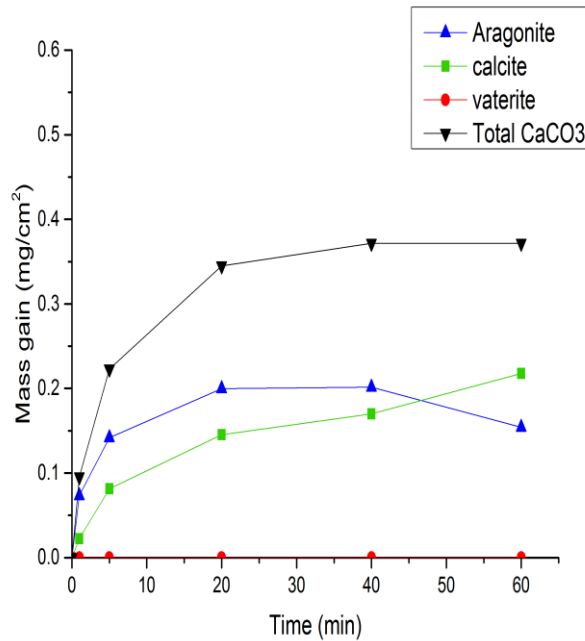


Figure 5-33 Polymorphic mass gain profile (mg/cm²) for brine 3 (0.045M) at 60° C

When an oil phase is introduced to the system a different trend is detected as illustrated in Figure 5-34. The metastable phase fraction of aragonite has encountered a decline followed by a rise. As a result of the increase in aragonite abundance, the mole percentage of calcite on the surface is decreased. A relatively equal polymorphic percentage is shown to exist at about 20 minutes but this rapidly diverged in opposite directions. The rise of aragonite fraction after 20 minutes is most probably due to the formation of a new generation of the metastable aragonite and this is confirmed by SEM in Figure 5-17 (g) and (h) where aragonite is found to build up on each other in a dendritic manner forming layers of aragonite.

The mass distribution in Figure 5-35 can obviously illustrate the elevation of aragonite mass growth making it controlling the whole process. There are two regions of aragonite mass gain; the first is within the first 10 minutes and this is accompanied by a linear growth of calcite phase which continues to about 40 minutes before it stabilizes. The second region of aragonite mass gain starts after 20 minutes and continues to 60 minutes. This is most probably the region of the re-nucleation and the growth of new crystals of aragonite which is expected to slow due to the stopping of nucleation, stabilize due to ceased growth then decline due to its transformation to calcite in a slow process which may take several hours. On the other hand, calcite will start to rise due to its re-nucleation and growth processes which will take place as a consequence of aragonite transformation.

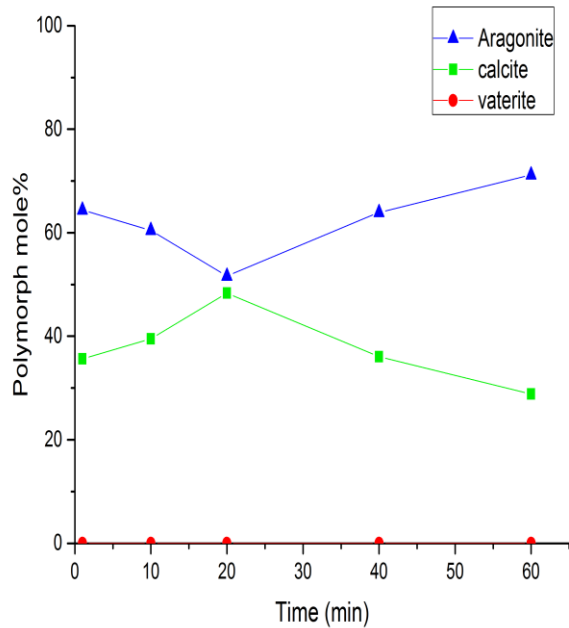


Figure 5-34 Polymorph abundance on the surface for 23% oil-brine 3 (0.045M) at 60° C

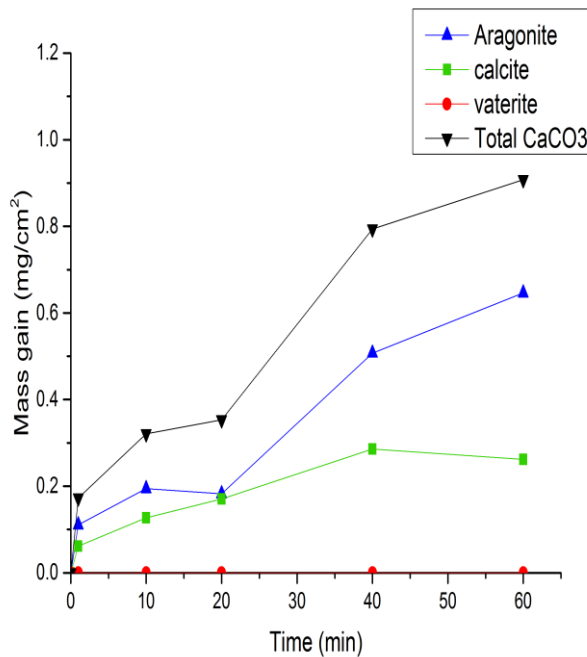


Figure 5-35 Polymorphic mass gain (mg/cm²) for 23% oil-brine 3 (0.045M) at 60° C

Comparing the percentage of aragonite to calcite for systems with and without oil at 60° C is illustrated in Figure 5-36. The percentage of aragonite is higher in the presence of oil where it represents about 60 to 70% of the total polymorphs abundance in the presence of oil whereas it represents about 50% in the absence of oil. The ratio of aragonite to calcite abundance is relatively similar for the whole oil fractions despite the difference in the amount of CaCO₃ deposit between systems at low and high oil fractions as shown for oil-brine 3 (0.045M) in Figure 5-2.

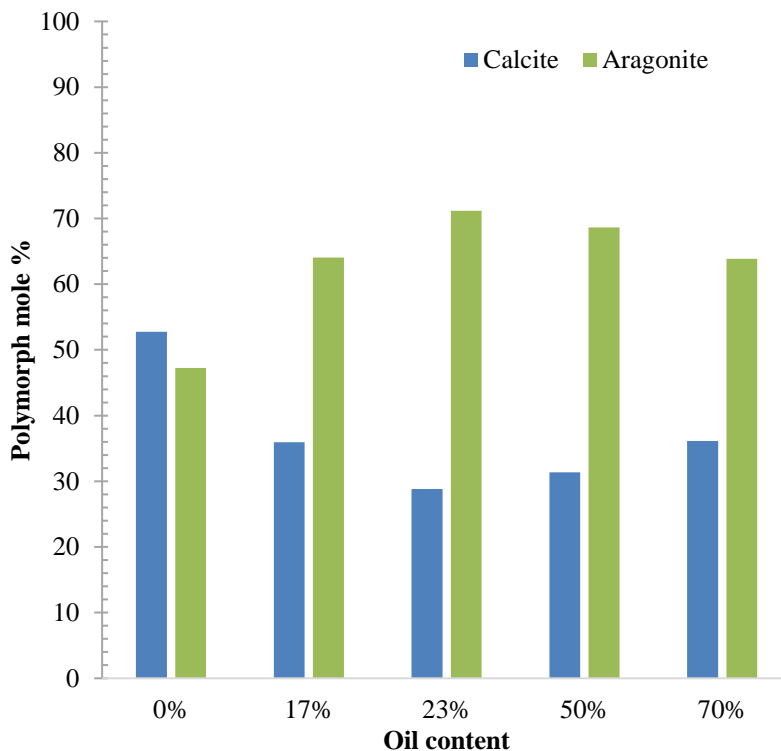


Figure 5-36 Polymorph mole% and total CaCO_3 mass gain ($\text{mg}/\text{cm}^2\cdot\text{hr}$) for different oil content at 60°C ; samples at 60 minutes

5.3.4 Effect of temperature on the polymorphic abundance

It has been shown in the previous two sections that vaterite and calcite are the polymorphic phases of CaCO_3 at 30°C and their abundance compromise the transformation of vaterite to calcite. On the other hand, aragonite and calcite are the polymorphic phases of CaCO_3 at 60°C and their abundance compromise the transformation of aragonite to calcite. All the three polymorphs of crystalline CaCO_3 is known to form at intermediate temperature of 40 to 50°C [51] and this is confirmed by SEM images in Figures 5-37 and 5-38

The presence of the three polymorphic together makes the system quite complex as the condition allows more than one metastable phase to form in parallel to each other where the formation of the stable phase can be a consequence of the transformation of both phases simultaneously.

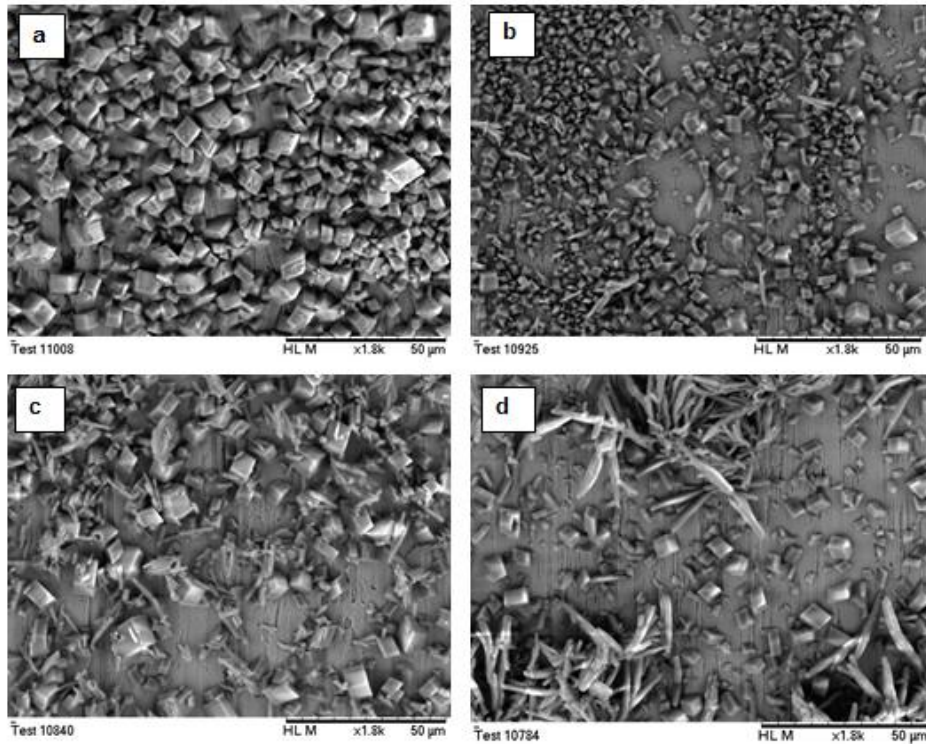


Figure 5-37 Effect of temperature on CaCO_3 scale deposition morphology in oil-free system; (a) 30° C, (b) 40° C, (c) 50° C, (d), 60° C; samples taken at 60 minutes

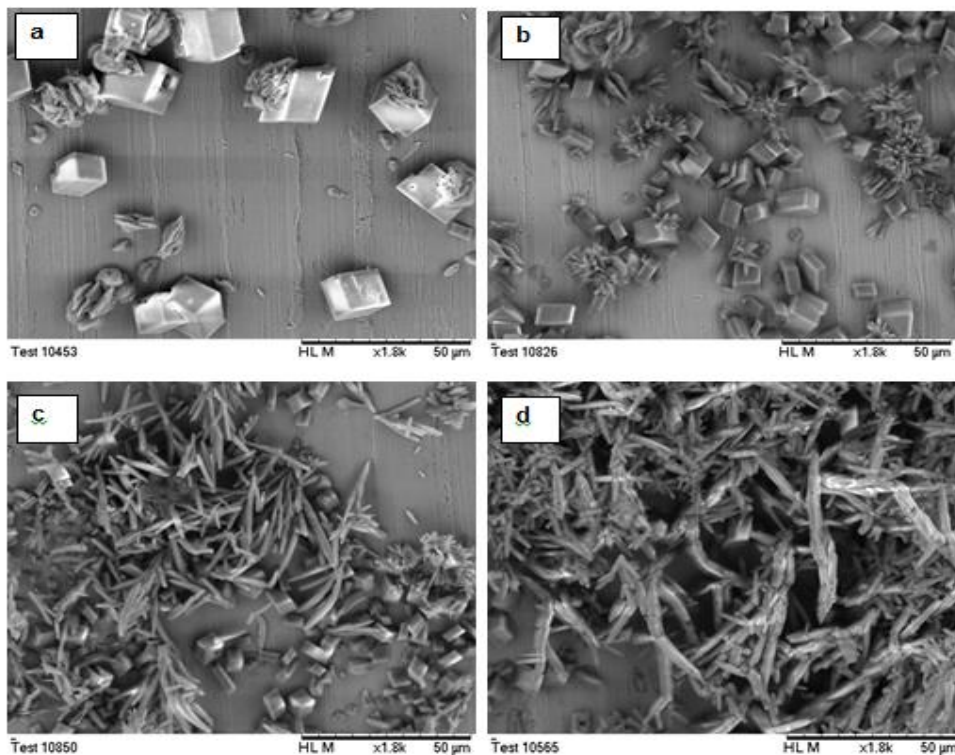


Figure 5-38 Effect of temperature on CaCO_3 scale deposition morphology in the presence of oil; (a) 30° C, (b) 40° C, (c) 50° C, (d), 60° C; samples are taken at 60 minutes

Figures 5-39 and 5-40 show the effect of temperature on the polymorph abundance at 60 minutes for approximately similar brine saturations at different temperatures. The brines used are brine 2 (0.065M), SR of 115 at 30° C, brine 4 (0.06M), SR of

120 at 40° C, brine 5 (0.05M), SR of 105 at 50° C and brine 3 (0.045M), SR of 97 at 60° C.

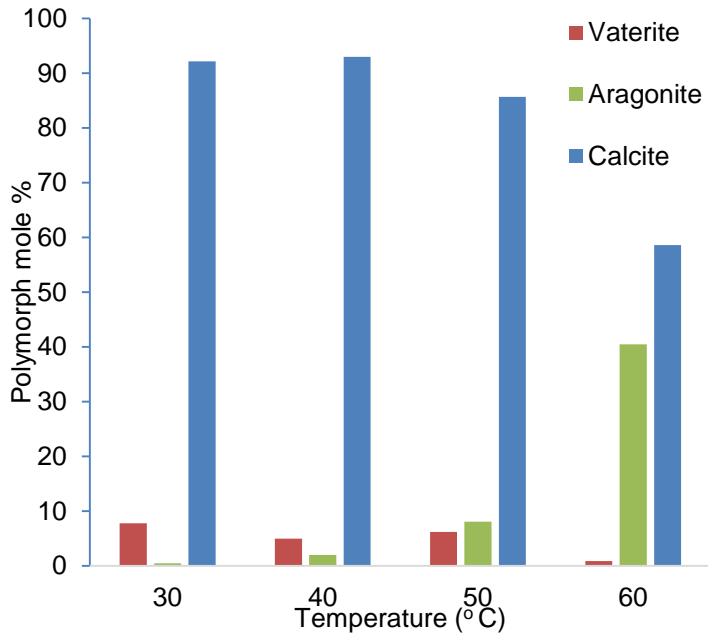


Figure 5-39 Effect of temperature on the polymorph abundance on the surface in the absence of oil

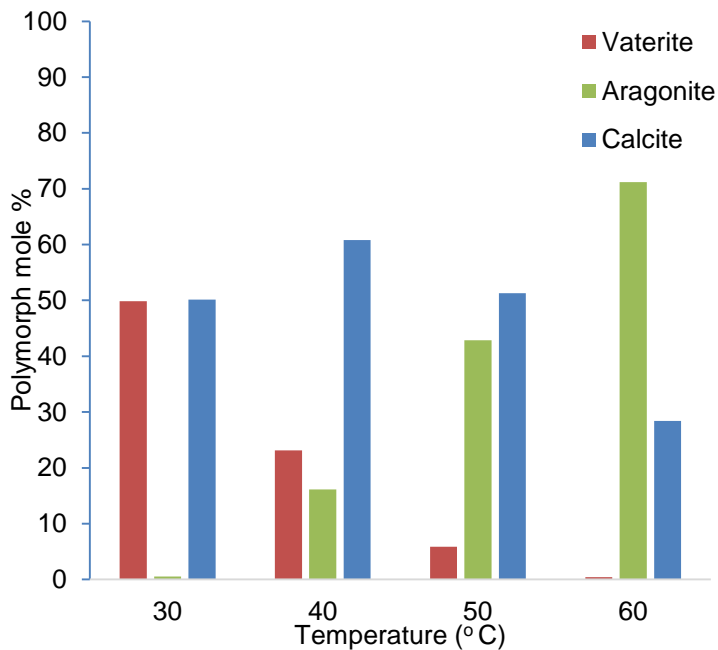


Figure 5-40 Effect of temperature on the polymorph abundance on the surface in the presence of 23% oil

Calcite is the predominant polymorph for the temperatures of 30° C to 50° C in oil-free system. This is because of the tendency for the scale to stabilise with time. Aragonite starts to appear at 40° C but with a low percentage and its presence increases with the temperature where it forms about 40% of the abundance at 60°

C. On the other hand vaterite presence is kept low by a percentage of less than 10% for all the temperatures.

In oil systems, the presence of the metastable phases can be more observed; vaterite at 30° C, vaterite and aragonite at 40 and 50° C and aragonite at 60° C. Vaterite percentage encounters a linear decline with temperature while aragonite percentage encounters a linear increase with temperature as shown in Figure 5-40.

It is worth mentioning that surface deposition process is taking place simultaneously to the bulk precipitation process. Therefore, the interaction between bulk precipitation and surface deposition should be linked together to better understand the kinetics of the crystallization process. Next chapter will focus on the crystallization process in the bulk solution.

5.4 Concluding Remarks

- Adding an oil phase as oil-in-water emulsions is found to exhibit a potential reduction in surface scaling where the scale formed in a 70% oil content system is found to reduce by 97% at 30° C and 80% at 60° C with reference to scale deposit in the absence of oil.
- The relationship between scale deposition amount and oil fractions is not clear for the close ranges of oil content but an overall decline in surface fouling is exhibited.
- An exception of the general reduction in scale formation is exhibited in the presence of oil for systems with oil fractions up to 40% at 60° C where scale is found to increase when adding an oil phase.
- The kinetics in the early stages of the crystallization at 30° C and 60° C show slower rates in the presence of oil than in the absence of oil.
- The presence of the metastable phase can be observed more in the presence of oil and this implies the delay in the transformation process.
- Analysis of the scaling process through estimating the rate at which each polymorph forms, grows and transforms can be a key factor for understanding the kinetics of the crystallization process.

6 Chapter Six The kinetics of the calcium carbonate bulk precipitation crystallization process in water and in oil/water emulsions;

6.1 Introduction

This chapter presents experimental results used to assess calcium carbonate precipitation in the absence and presence of an organic phase via different *in-situ* to *ex-situ* techniques. The Inductively Coupled Plasma-Optical Emission Spectroscopy (ICP-OES) to track the change in calcium ions in the solution during the crystallization process. Focused Beam Reflectance Measurement (FBRM) to measure particle size distribution *in-situ* and *in-real* time. This experiment was conducted under careful operating conditions to enable the tracking of both nucleation and crystal growth processes simultaneously. The produced precipitate was characterized using Scanning Electron Microscopy (SEM) and X-Ray Diffraction (XRD). A quantitative determination of CaCO₃ polymorphs was generated using correlations which are based on the intensity ratios of different polymorphs produced by XRD patterns at different times. This enabled a better understanding of the kinetics of formation and transformation of different polymorphic phases. This was in addition to Scanning Electron Microscopy (SEM) which provided visual evidence of the different stages of CaCO₃ scale formation.

6.2 Characterization of oil-saline water systems

6.2.1 Assessment of oil-in-water emulsions using Focused Beam Reflectance Measurement technique (FBRM)

FBRM has been used to characterize the oil/ water system. FBRM software produces the number of counts for specified chord length channels of 1 to 5, 10 to 23, 29 to 86, 100 to 251 and 293 to 1000 microns. Figure 6-1 shows the number of counts for different chord length channels for a 23% oil content system. The measurements show an increase in the number of counts with an increase in the impeller rotation speed and the existence of an equilibrium state at rotational speed of 650 to 750 rpm. This steady state indicates equilibrium between the rate of coalescence and break up of oil droplets. This is the optimum speed which assures homogeneous mixing of phases. Therefore, a rotation speed of 700 rpm is used for the experiments of high oil fractions of 23% and 30% whereas lower oil fractions of 10% and 17% were conducted at 550 rpm where a steady state was shown to exist between 500 and 600 rpm as in Figure 6-2. These measurements were recorded

after allowing the system to mix and equilibrate for at least 10 minutes between the different speeds.

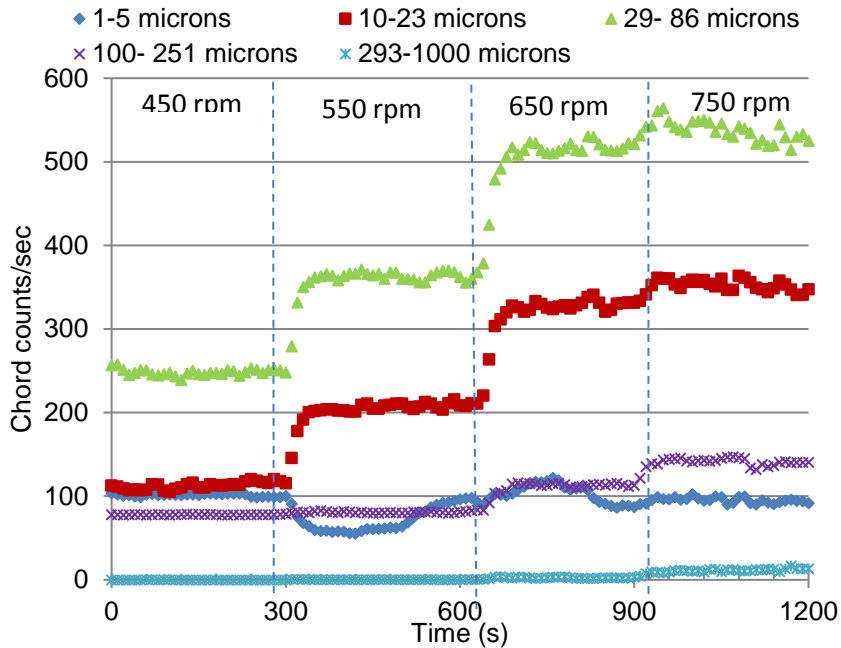


Figure 6-1 Effect of rotation speed for 23% oil- (0.3M) NaCl solution at 60° C

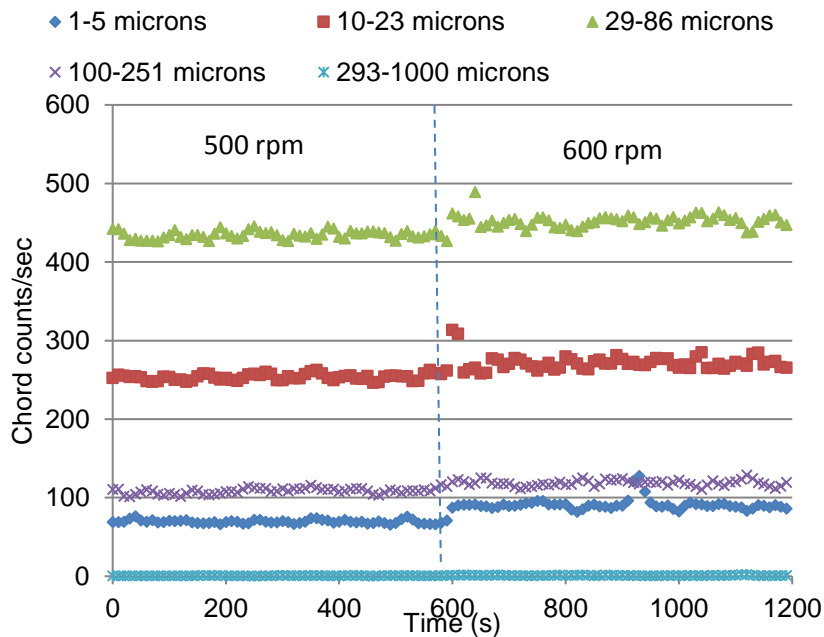


Figure 6-2 Effect of rotation speed for 10% oil- (0.3 M) NaCl solution at 60° C

Figure 6-3 shows droplet size distribution at different time intervals for systems containing 10% and 17% oil fraction. The results show the existence of a pseudo steady state where the mode of the peaks remain constant through time due to an equilibrium between droplet break up and coalescence rates.

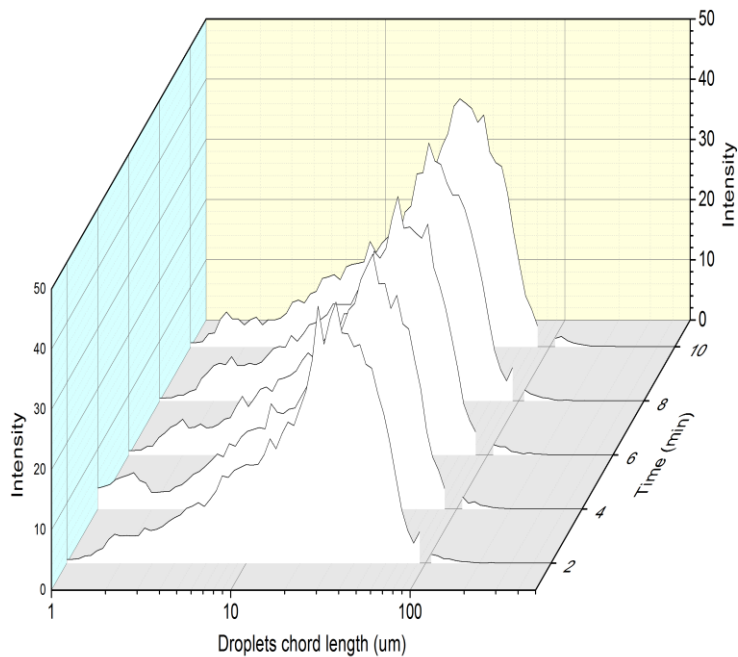
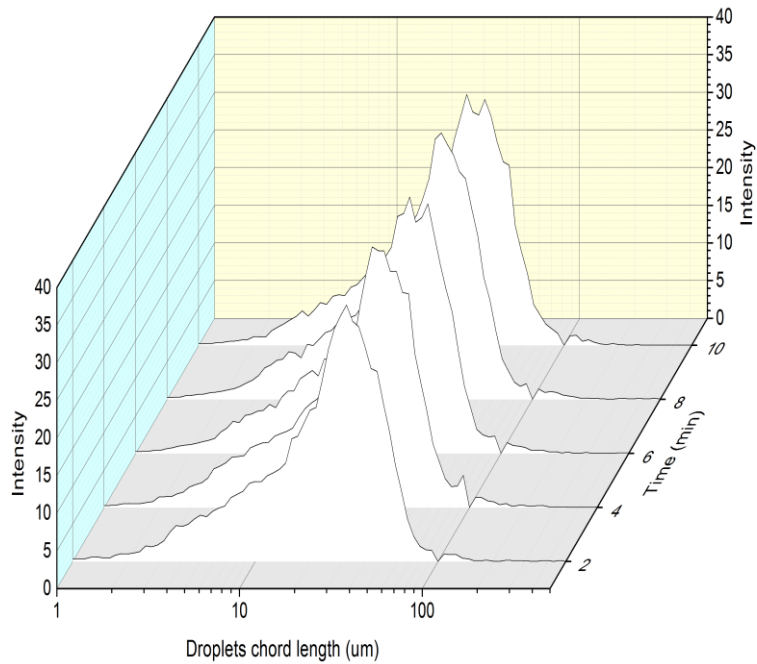


Figure 6-3 Droplet size distribution for oil-(0.3M) NaCl solution at different times, mixing speed of 550 rpm; top, 10% oil content; bottom, 17% oil content

Similar distribution profiles have been recorded at 30 and 60° C as shown in Figure 6-4. More peaks are detected at 30° C which indicates distinct sizes of droplets for the system. A separated peak at about 100 μm appears for both curves which most probably represents trapped air bubbles which are typically around this size [190].

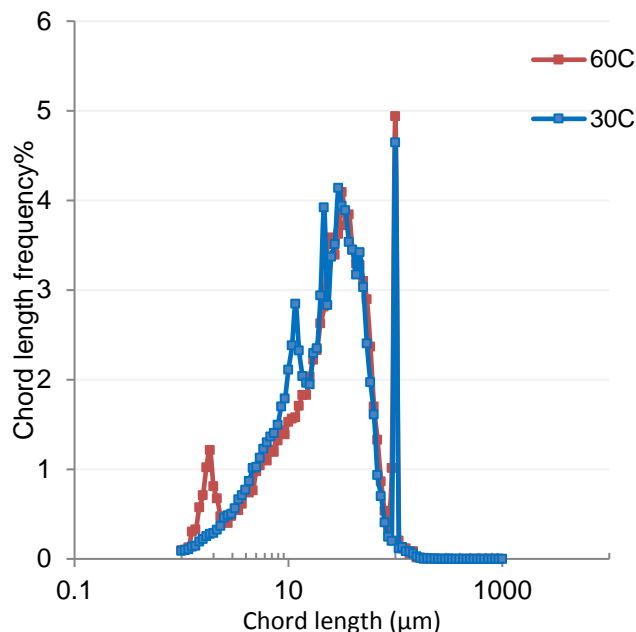


Figure 6-4 Frequency curves for 17% oil- (0.3M) NaCl solution, stirred at 550 rpm

The mean chord length for *O/W* emulsions at two different temperatures and for different oil volume fractions is shown to range between 18 to 29 μm . However, various weighting methods are used to approximate the measured particle size to the actual size. According to [191] square-weighted chord length distribution for spherical particles correlates similar to particle size distribution than un-weighted CLD. Applying square weight methods using equation 4.14 and 4.16, the mean chord length and chord length distribution for different oil content result in an average mean chord length (square-weighted) to range between 69 to 82 μm as shown in Table 6-1 and square-weighted chord length distribution as shown in Figure 6-5. The mean chord length has been calculated after removing of the 100 μm peak that has been detected as mentioned previously where the data and the calculations are shown in Table A-2 in appendix A-2 for the case of 10% oil content at 60°C.

Table 6-1 Mean diameter, droplet density and interfacial area for different fractions of saline water- emulsion at 60 °C

Oil content	Mean diameter (sq-wt), (μm)	Droplet density (no of droplets / cm^3)	Total interfacial area (m^2)
10%	65	691,637	12.89
17%	74	959,340	22.83
23%	78	1,179,620	32.05
30%	82	1,370,640	40.82

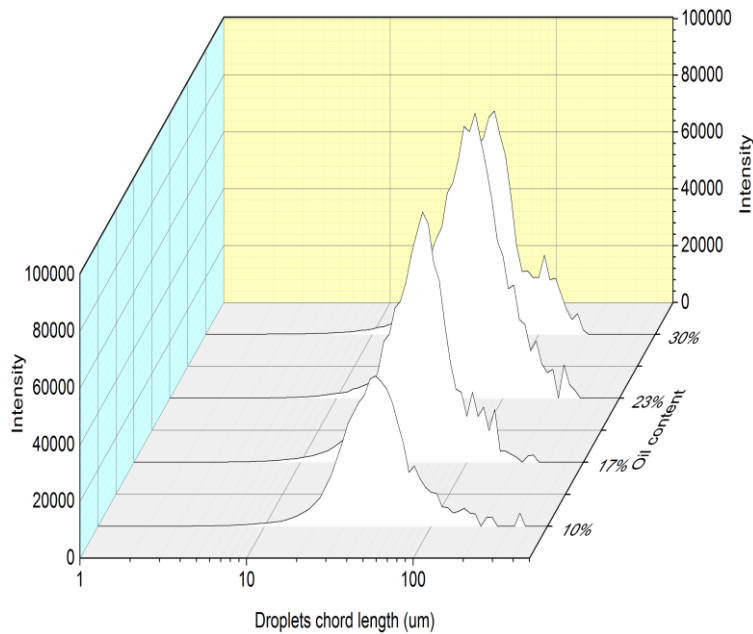


Figure 6-5 Applying square weight to chord length distribution for different oil contents at 60° C

Since oil droplets in oil-in-water emulsions are considered to have a spherical shape, mean chord length may be considered as mean droplet diameter. Table 6-1 shows the droplet mean diameter (square-weighted), droplet density in solution and total interfacial area. These values are calculated according to equations 4.17 to 4.21. Indeed, the mean droplet diameter increased from 65 μm in a system containing 10% of oil up to 82 μm ($\approx 20\%$ increase) when the oil content reaches 30%. This is attributed to the increase in droplet coalescence frequency as the fraction of oil in the system increases. The number of droplets and hence total interfacial area was also found to increase as shown in Table 6-1.

A plot between the total number of counts as detected from square-weighted method and droplet density as calculated based on square-weighted mean droplet diameter gave a linear relationship as shown in Figure 6-6. According to this finding, the number of droplets can be represented by the number of counts and the square-weighted chord length distribution and square-weighted mean chord length can better represent the droplet size distribution and the mean droplet diameter, respectively.

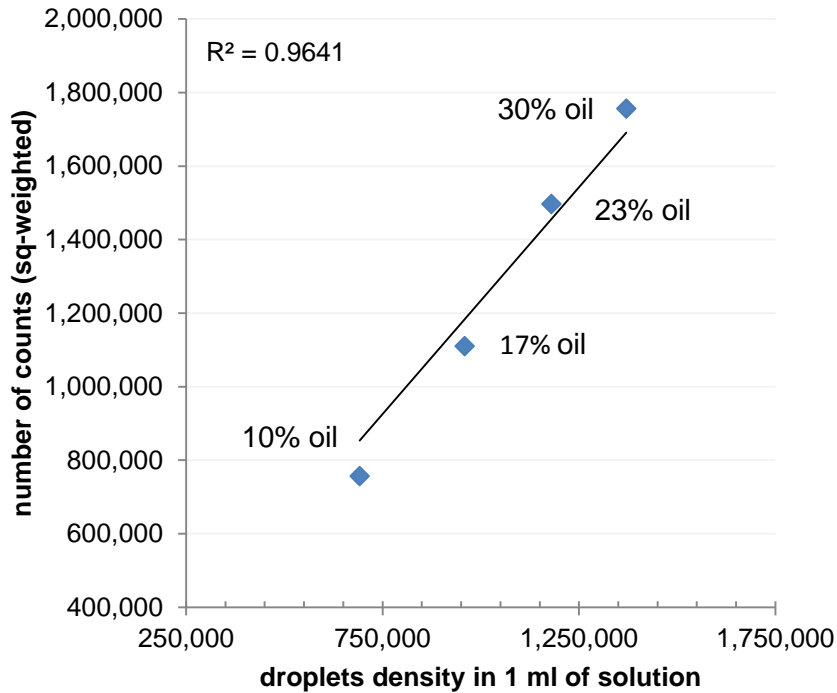


Figure 6-6 Comparing average total number of counts as estimated by applying square-weighted method and droplet density as estimated by square-weighted mean droplet diameter for different oil contents at 60° C

6.3 Assessment of bulk precipitation process

6.3.1 Turbidity measurements

The tendency for the brines to precipitate in an oil-free system was evaluated by measuring the solution turbidity. Figure 6-7 shows the turbidity for different brine concentrations at two different temperatures. All the brines show instantaneous precipitation with similar trend which indicates the rapid onset of nucleation at both temperatures. The degree of precipitation is similar for brine 2 (0.065M) at 30° C and for brine 3 (0.045M) at 60° C as shown in Figure 6-7 (a) and (b), this is because both the brines have similar range of saturation ratio. Brine 1 at 30° C shows about double degree of precipitation comparing to the other brines as shown in Figure 6-7 (c). This is reasonable as the saturation ratio has doubled for this brine. All the brines turbidity curves reaches to steady state after about 5 to 10 minutes. Steady state in this case could represent no more particles being formed and only crystal growth taking place over this period. Therefore, the turbidity profile could be used to differentiate between nucleation and crystal growth stages.

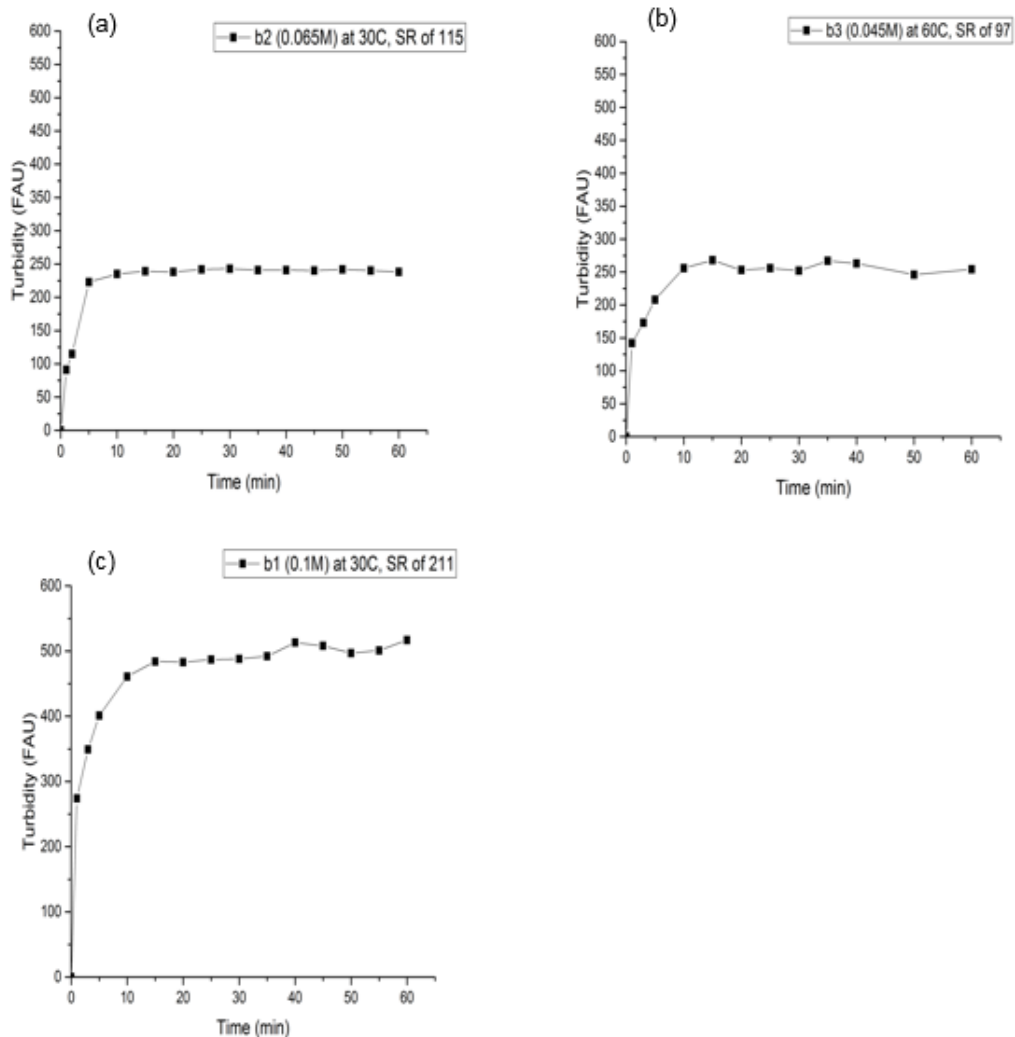


Figure 6-7 Turbidity (FAU); (a) brine 2 (0.065M) at 30° C, SR of 115, (b) brine 3 (0.045M) at 60° C, SR of 97, (c) brine 1 (0.1M) at 30° C, SR of 211

6.3.2 The pH measurements

The pH has been widely used as a method for characterizing scale formation particularly for estimating the induction time. The induction time is defined as the time elapsed from the moment of mixing the reactants to the moment of detectable crystals being observed. In order to estimate the induction time for nucleation, curves were plotted at different time intervals. The induction times are then estimated by a graphical method where the tangent of the pH slope curve is extrapolated and allowed to intersect with the time axis where an induction time is measured.

Assessment of the crystallization process using pH measurement is shown in Figures 6-8 to 6-10. The pH profiles showed similar trend between systems with and without oil at different temperatures. The pH drops initially with different slopes followed by a steadiness. The systems at 60° C exhibit an increase in the pH after a short period of steady behaviour as in Figure 6-10. The drop in pH is due to the

hydrogen release from the dissociation of carbonic acid and/ or bicarbonate ions. Therefore, carbonate ions would be freely available for the reaction with calcium ions to form calcium carbonate.

The pH drop for oil-free system is higher than for oil-systems. However, applying the tangent method to the curves produces various induction times which range between 4 and 5 minutes for oil-brine 2 (0.065M) and 3 and 4 minutes for oil-brine 1 (0.1M) at 30° C. The induction time ranges between 2 and 3 minutes for brine 3 (0.045M) at 60° C.

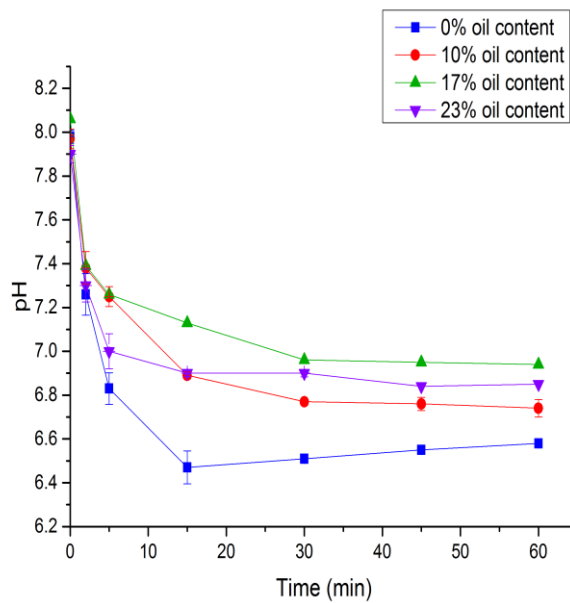


Figure 6-8 The pH profile for oil-brine 2 (0.065M) at 30° C

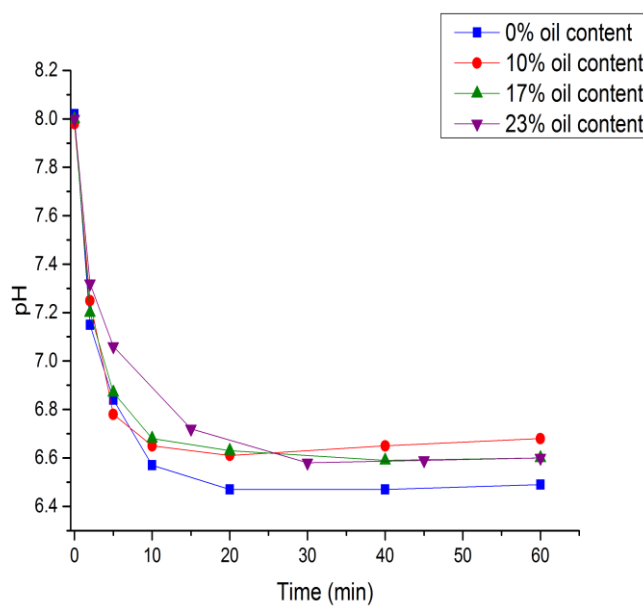


Figure 6-9 The pH profile for oil-brine 1 (0.1M) at 30° C

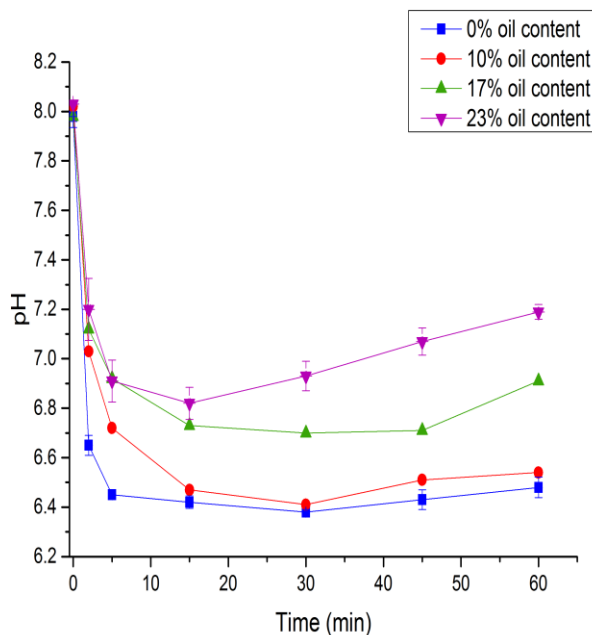


Figure 6-10 The pH profile for oil-brine 3 (0.045M) at 60° C

These induction times are a bit longer than what have been visually observed or detected by both the turbidity measurement in the previous section and the FBRM technique which will be illustrated in section 6.3.6. The induction times for all the previous methods were recorded as an instantaneous reaction in which a cloudiness was observed or the intensity was detected directly after mixing of the brines. Therefore, the induction times by tangent method did not accurately represent the induction times for the systems studied here.

6.3.3 Calcium concentration in solution

Since the brine solutions have equal concentration of calcium and carbonate ions, for each one mole of free calcium ions there will be one mole of free carbonate ions to react with to form one mole of calcium carbonate. It is expected that once nucleation is started there would be consumption or decrease in the calcium amount in the solution or unreacted. The drop in calcium ions can also be taken as an indication to the intensity of the reaction. A sharp decrease in calcium ions at the beginning of the crystallisation process may suggest instantaneous nucleation whilst a gradual decrease may suggest progressive nucleation in which nuclei continue to form as the reaction proceeds. Assessment of the crystallization process using the concentration of calcium ions remaining in solution is shown in Figures 6-11 and 6-12. The drop in calcium concentration is found to be low in the first 5 minutes of the precipitation then it started to increase with time at 30° C. This trend contradicts the results which are detected by other techniques such as pH, turbidity and FBRM measurements, in addition to visual observations of the system.

Nevertheless, a continuous decline in calcium concentration is exhibited in oil-free system at 30° C which implies a continuous formation of scale for the duration of the whole experiment.

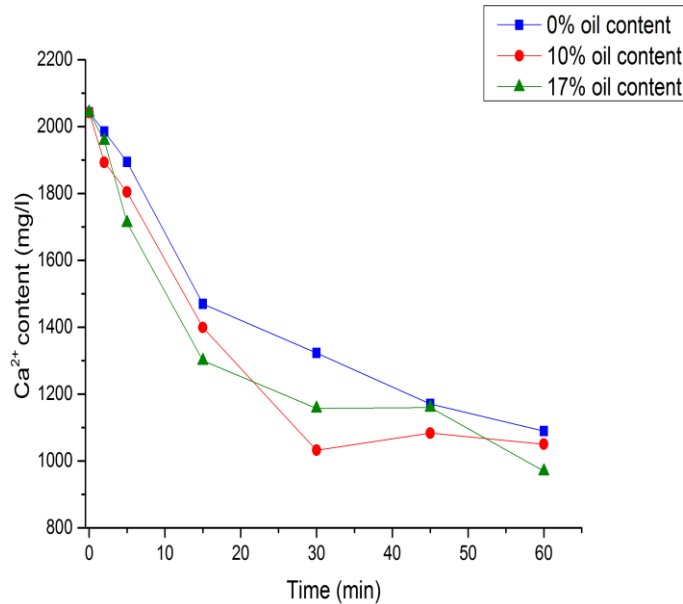


Figure 6-11 The concentration of calcium ions in mg/l for oil-brine 1 (0.1M) at 30° C

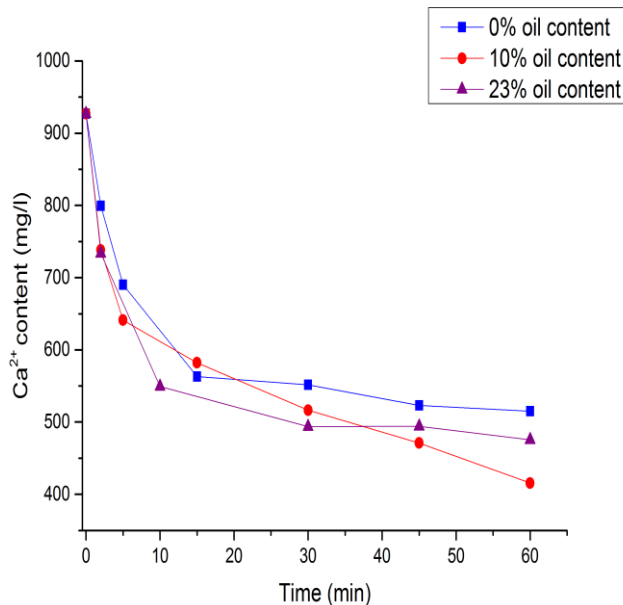


Figure 6-12 The concentration of calcium ions in mg/l for oil-brine 3 (0.045M) at 60° C

The decline in the calcium concentration for the oil-brine 3 at 60° C is faster in the early stages of precipitation than in the early stages of precipitation at 30° C. The oil-free system exhibited a similar trend to 23 % oil content system whereas 10% oil content showed a progressive reaction trend. The amount of unreacted calcium ions at both temperatures is higher in the oil-free system than in the oil system for the whole experiment duration.

6.3.4 Estimation of the de-supersaturation profile and the calcium carbonate produced based on measured pH and calcium concentration

Tracking the change in pH and calcium ions during the precipitation process is very important for studying the kinetics of the crystallization process in the bulk solution. Opposite behaviour existed for the precipitation progress between systems with and without oil; the drop in pH is higher for the oil-free system than for the oil systems which indicates a higher reaction rate exists in the oil-free system compared to the oil systems. On the other hand, the amount of unreacted calcium is higher in the oil-free system and this indicates a lower reaction rate compared to that in the oil systems. This contrast between the measured pH and the measured calcium ion concentrations in solution will be discussed in chapter 7.

Since calcium carbonate solubility and hence supersaturation and polymorph change are all affected by pH, it was necessary to combine the change in calcium concentration in solution with the measured pH to follow the precipitation process. Supersaturation and activity coefficients of Ca^{2+} and CO_3^{2-} were estimated using MultiScale™ software. These quantities are estimated at different measured pH and different concentrations of free calcium ions which were detected using ICP. The initial unreacted calcium ion concentration is considered equal to the value measured by ICP which corresponds to the concentration prior to any reactions. Knowing the SR, the solubility product of vaterite which is calculated using equation 2.35 and found as $1.11 \times 10^{-08} \text{ M}^2$ at 30° C and $5.34 \times 10^{-09} \text{ M}^2$ at 60° C and with the activity coefficients, the calcium and carbonate ions concentrations in solution can be calculated according to the following equation:

$$SR = \sqrt{\frac{a_{\text{Ca}^{2+}} a_{\text{CO}_3^{2-}}}{K_{sp, \text{vaterite}}}} \quad 6.1$$

or,

$$SR^2 K_{sp, \text{vaterite}} = IAP = a_{\text{Ca}^{2+}} a_{\text{CO}_3^{2-}} = \gamma_{\text{Ca}^{2+}} [\text{Ca}^{2+}] \gamma_{\text{CO}_3^{2-}} [\text{CO}_3^{2-}] \quad 6.2$$

where:

$a_{\text{Ca}^{2+}}$, $\gamma_{\text{Ca}^{2+}}$ and $[\text{Ca}^{2+}]$ are the activity (M), the activity coefficient and the concentration (M) for calcium ions, respectively.

$a_{\text{CO}_3^{2-}}$, $\gamma_{\text{CO}_3^{2-}}$ and $[\text{CO}_3^{2-}]$ are the activity (M), the activity coefficient and the concentration (M) for carbonate ions, respectively.

SR is the supersaturation ratio.

IAP is the ionic activity product.

$K_{sp,vaterite}$ is the solubility product of vaterite (M^2).

Tables 6-2 to 6-5 show the calculation of calcium carbonate produced based on the change in pH and with the aid of MultiScale™ software for oil-brine 1 (0.1M) at 30° C and oil-brine 3 (0.045M) at 60° C. The calculations for oil-brine 2 (0.065M) at 30° C is in Tables C-1 and C-2 in appendix C. The concentration of calcium ions detected using ICP analysis is higher than when correction was made (values in bold in the tables). Calcium ion concentrations detected by ICP is shown to drop at the end of the reaction by about 50% of its initial value for the oil-free system, whereas the reaction reached up to 94% when the drop in pH within the reaction was taken into account as shown in Table 6-2.

The concentration of the reacted calcium ions is calculated by subtracting the solution calcium ion concentration from the initial calcium concentration at different time intervals. The concentration of calcium carbonate produced within the experiment is calculated by applying mole balance between the reacted calcium and the produced calcium carbonate. Figures 6-13 and 6-14 represent the differences in the amount of calcium carbonate calculated directly from calcium ions measured in the solution and indirectly from the pH dependent on supersaturation. A higher amount of scale is produced when calculated than when measured. The trend of the curves for the measured $CaCO_3$ in case of oil-brine 1 at 30° C in Figure 6-13 suggests the continuous formation of scale over the whole period of the experiment and this contradicts other methods such as turbidity measurement in Figure 6-7(c) and pH in Figure 6-9. However, this behaviour is less observed in the case of oil-brine 3 (0.045M) system at 60° C in Figure 6-14 although the difference in the amount of scale measured and calculated are high in this case too. However, turbidity measurement for the brine 3 (0.045M) at 60° C shows a steady state intensity of about half the value which is detected for brine 1 (0.1M) at 30° C as shown in Figure 6-7 (b) and (c). This implies that the amount of precipitate for brine 3 at 60° C as detected from the calculated calcium and pH is a better representation of the system in this case too. The decrease in the amount of calcium carbonate for oil-brine 3 system after 30 minutes as shown on the right side of Figure 6-14 is theoretically unacceptable. This decrease in $CaCO_3$ is a result of the increase in the saturation ratio calculated which is affected by the increase in pH at 30 minutes as shown in Table 6-5 (values in bold).

Table 6-2 The calculation for correcting calcium ion that has reacted to form calcium carbonate for 0% oil-brine 1 (0.1M) at 30° C

Time (min)	Ca ²⁺ (mg/l) by (ICP)	Ca ²⁺ (mM) by (ICP)	pH	SR (Multiscale)	YCa ²⁺ (Multiscale)	YCO ₃ ²⁻ (Multiscale)	IAP= SR ² *K _{SPV} (M) ²	[Ca ²⁺]=[CO ₃ ²⁻] (mM) Corrected	Reacted [Ca ²⁺] (mM)	Produced CaCO ₃ (mg/l)
0	2042	50.954	7.6	211.46	-	-	-	50.954 *	0	0
2	1985	49.536	7.15	77.54	0.233	0.1478	6.6827E-05	44.051	6.903	690.258
5	1894	47.262	6.84	35.56	0.2336	0.149	1.40548E-05	20.094	30.859	3085.934
15	1470	36.680	6.57	12.24	0.237	0.156	1.66519E-06	6.711	44.243	4424.296
30	1323	33.007	6.47	8.05	0.239	0.159	7.20264E-07	4.353	46.600	4660.048
45	1170	29.203	6.47	6.43	0.241	0.165	4.59539E-07	3.399	47.555	4755.461
60	1089	27.175	6.49	5.63	0.242	0.165	3.52303E-07	2.970	47.984	4798.372

* The initial calcium concentration is considered as the value measured using ICP

Table 6-3 The calculation for correcting calcium ion that has reacted to form calcium carbonate for 17% oil-brine 1 (0.1M) at 30° C

Time (min)	Ca ²⁺ (ICP) (mg/l)	Ca ²⁺ (mM) by (ICP)	pH	SR	YCa ²⁺ (Multiscale)	YCO ₃ ²⁻ (Multiscale)	IAP= SR ² *K _{SPV} (M) ²	[Ca ²⁺]=[CO ₃ ²⁻] (mM) (corrected)	Reacted [Ca ²⁺] (mM)	Produced CaCO ₃ (mg/l)
0	2042	50.954	7.6	211.46	-	-	-	50.954 *	0.0	0.0
2	1958	48.861	7.2	84.61	0.233	0.1478	7.95689E-05	48.068	2.886	288.601
5	1712	42.714	6.87	31.81	0.2336	0.149	1.12468E-05	17.975	32.978	3297.844
15	1300	32.425	6.68	12.58	0.24	0.161	1.75898E-06	6.747	44.207	4420.705
30	1157	28.865	6.63	9.07	0.242	0.164	9.14355E-07	4.799	46.154	4615.422
45	1160	28.934	6.59	8.32	0.241	0.1628	7.6939E-07	4.428	45.526	4652.577
60	970	24.197	6.6	6.124	0.244	0.168	4.16841E-07	3.188	47.765	4776.521

* The initial calcium concentration is considered as the value measured using ICP

Table 6-4 The calculation for correcting calcium ion that has reacted to form calcium carbonate for 0% oil-brine 3 (0.045M) at 60° C

Time (min)	Ca ²⁺ (mg/l) by (ICP)	Ca ²⁺ (mM) by (ICP)	pH	SR (Multiscale)	YCa ²⁺ (Multiscale)	YCO ₃ ²⁻ (Multiscale)	IAP= SR ² *K _{SPV} (M) ²	[Ca ²⁺]=[CO ₃ ²⁻] (mM) Corrected	Reacted [Ca ²⁺] (mM)	Produced CaCO ₃ (mg/l)
0	926.925	23.128	7.56	97.66	-	-	-	23.128 *	0	0
2	799.241	19.942	6.65	10.56	0.226	0.15	5.95456E-07	4.191	18.937	1893.695
5	690.221	17.222	6.45	5.11	0.272	0.152	1.39432E-07	1.836	21.292	2129.159
15	563.031	14.048	6.42	3.26	0.229	0.156	5.67489E-08	1.260	21.868	2186.765
30	551.576	13.763	6.38	2.87	0.229	0.156	4.39831E-08	1.109	22.018	2201.843
45	523.136	13.053	6.43	2.91	0.23	0.157	4.52177E-08	1.119	22.009	2200.899
60	515.079	12.852	6.48	3.17	0.23	0.157	5.36588E-08	1.219	21.909	2190.902

* The initial calcium concentration is considered as the value measured using ICP

Table 6-5 The calculation for correcting calcium ion that has reacted to form calcium carbonate for 23% oil-brine 3 (0.045M) at 60° C

Time (min)	Ca ²⁺ (mg/l) by (ICP)	Ca ²⁺ (mM) by (ICP)	pH	SR (Multiscale)	YCa ²⁺ (Multiscale)	YCO ₃ ²⁻ (Multiscale)	IAP= SR ² *K _{SPV} (M) ²	[Ca ²⁺]=[CO ₃ ²⁻] (mM) Corrected	Reacted [Ca ²⁺] (mM)	Produced CaCO ₃ (mg/l)
0	926.925	23.128	7.56	97.66	-	-	-	23.128 *	0	0
2	733.669	18.306	7.2	31.03	0.228	0.153	5.14145E-06	12.140	10.988	1098.772
10	549.110	13.701	6.82	7.75	0.231	0.157	3.2072E-07	2.974	20.154	2015.426
30	493.604	12.316	6.93	6.34	0.232	0.159	2.14635E-07	2.412	20.716	2071.586
45	494.000	12.326	7.07	11.17	0.233	0.159	6.66237E-07	4.241	18.887	1888.732
60	475.366	11.861	7.19	13.59	0.233	0.16	9.86191E-07	5.143	17.985	1798.472

* The initial calcium concentration is considered as the value measured using ICP

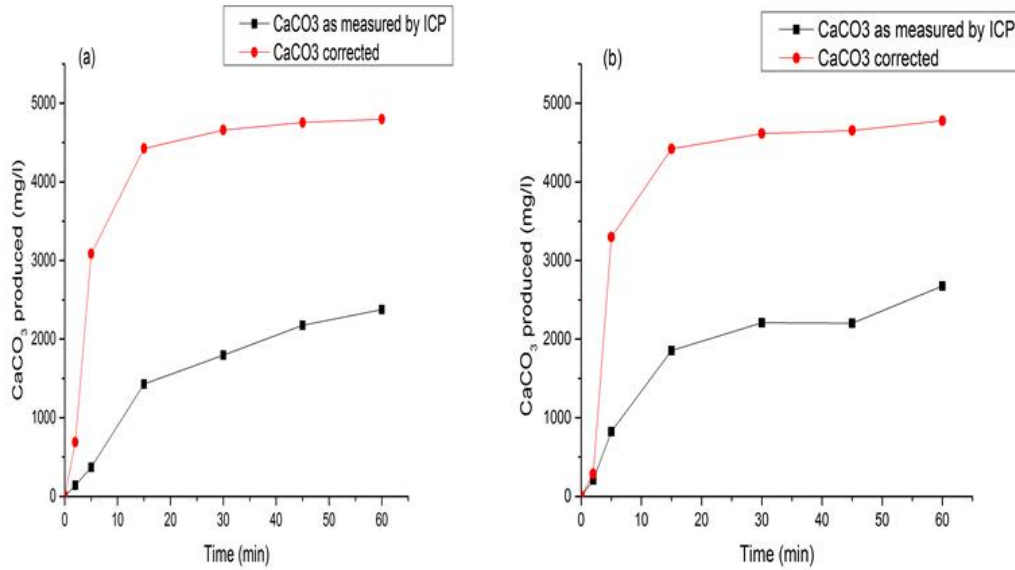


Figure 6-13 Comparing the amount of calcium carbonate produced as calculated by the reacted calcium ions detected by ICP to the amount produced as calculated by the reacted calcium ions detected from supersaturation dependent on pH for oil-brine 1 at 30° C; (a) 0% oil content, (b) 17% oil content

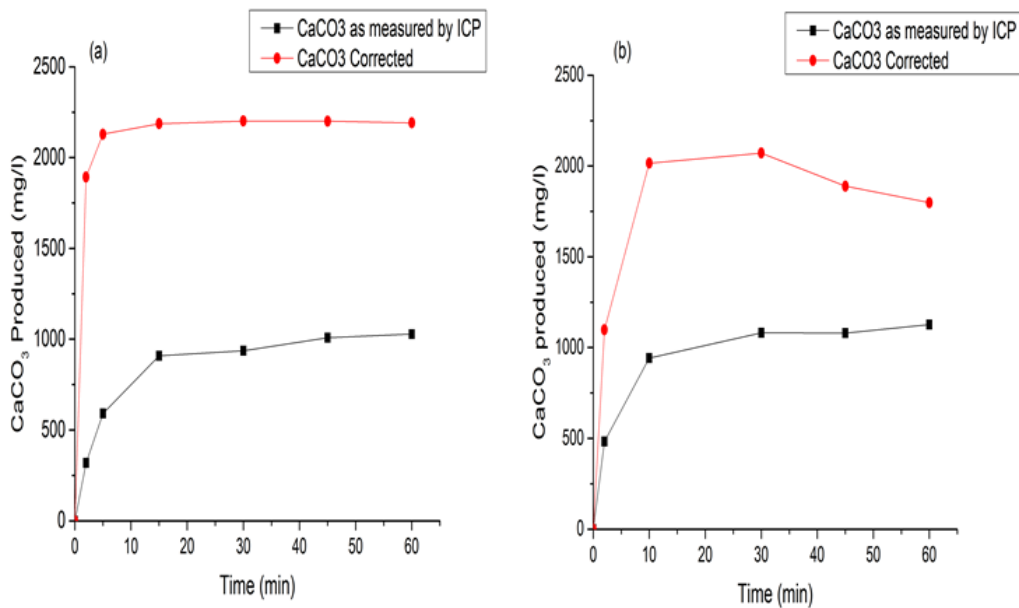


Figure 6-14 Comparing the amount of calcium carbonate produced as calculated by the reacted calcium ions detected by ICP to the amount produced as calculated by the reacted calcium ions detected from supersaturation dependent on pH for oil-brine 3 at 60° C; (a) 0% oil content, (b) 23% oil content

6.3.5 Assessment of the precipitation process using calcium carbonate concentration, pH and de-supersaturation profile

Figures 6-15 to 6-17 illustrate the comparison between the concentration of calcium carbonate produced with both pH and supersaturation change during the reaction. The yield of the CaCO_3 scale is high during the first 15 minutes and this is consistent with the reduction in the supersaturation of the brine and the change in the solution pH. The reactant is consumed as the reaction proceeds within this period which could be considered as the period of time where nucleation is taking place. After 15 minutes, changes in the slope of the curves for CaCO_3 produced, pH and supersaturation are exhibited. In this region a slight increase in the concentration of product occurs and this could be considered as the period where other process such as growth and agglomeration are progressed. The trend of the lines is similar for systems with and without oil at 30°C and this will be discussed in chapter 7. The rise in the pH profile for the system with oil at 60°C as shown in Figure 6-17 is of interest. This led to a decline in the amount of calcium carbonate produced with time as the rise in pH affected the calculation of the saturation ratio and hence the estimated calcium and carbonate ions concentrations in the solution.

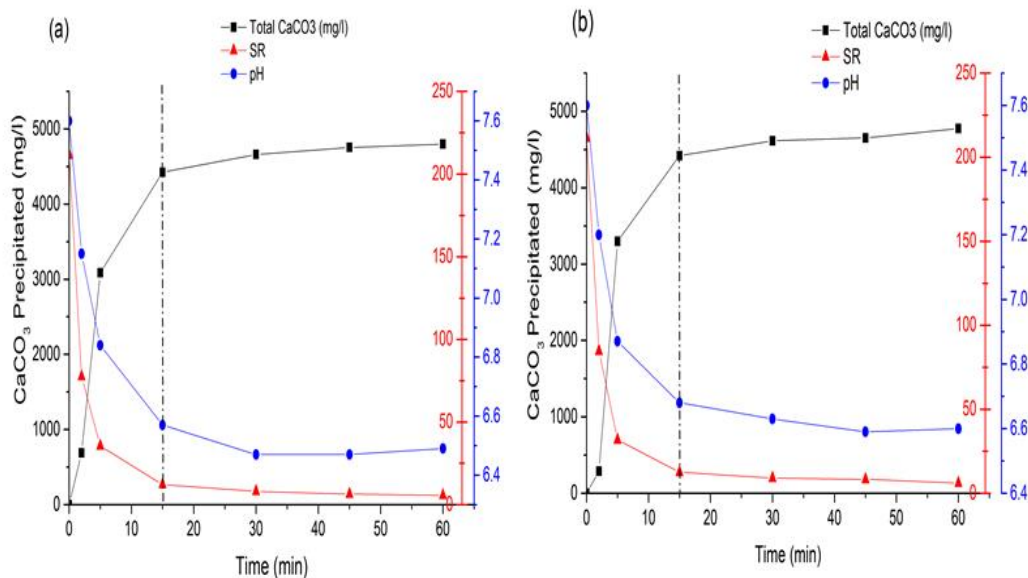


Figure 6-15 Comparing the amount of CaCO_3 formed with the change in supersaturation ratio and pH for oil-brine 1 (0.1M) at 30°C ; (a) 0% oil content, (b) 17% oil content

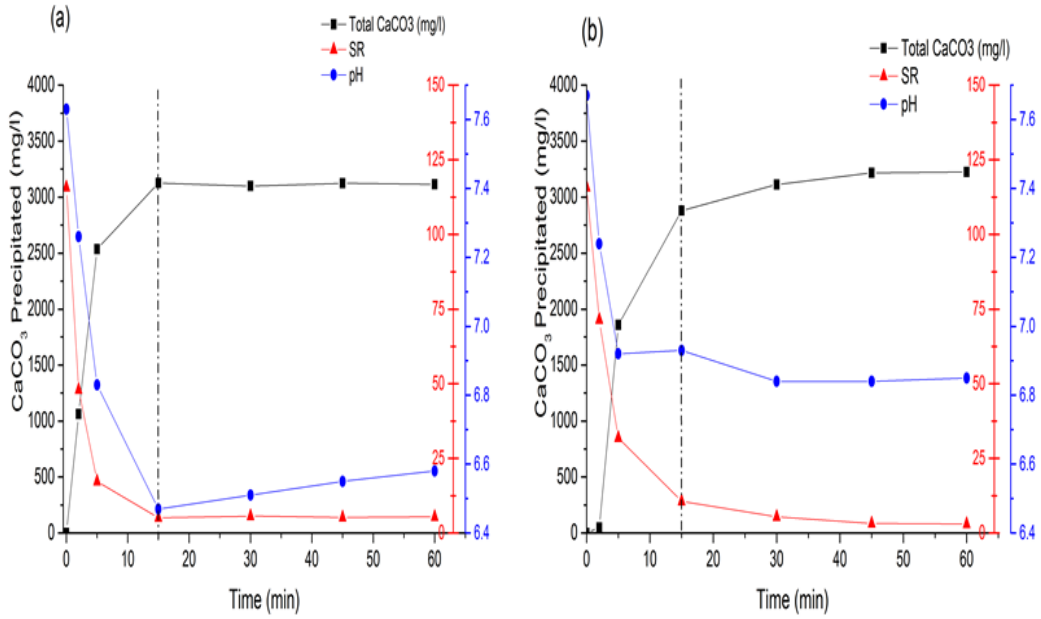


Figure 6-16 Comparing the amount of CaCO₃ formed with the change in supersaturation ratio and pH for oil-brine 2 (0.065M) at 30° C; (a) 0% oil content, (b) 23% oil content

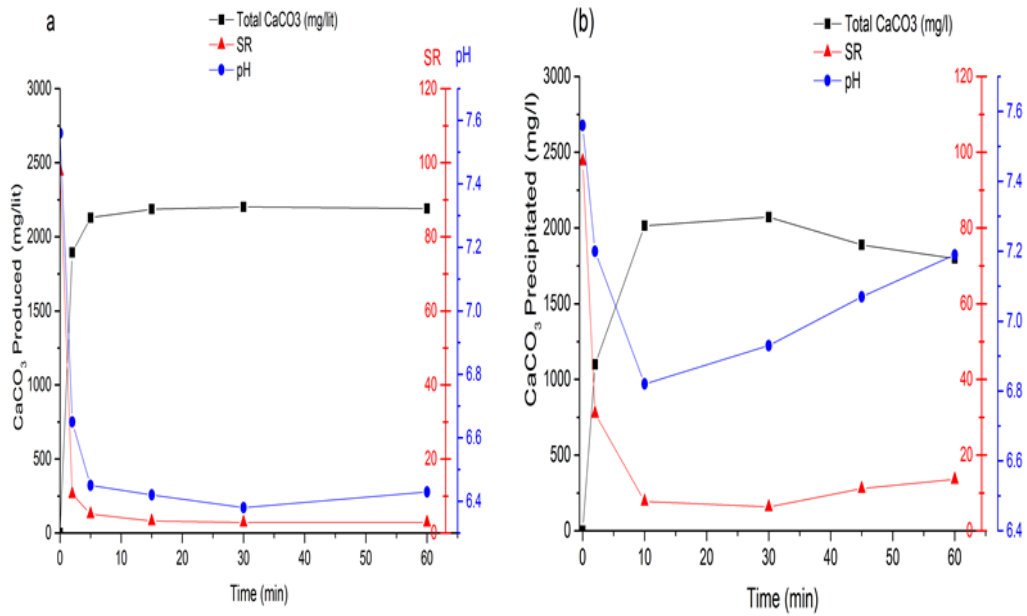


Figure 6-17 Comparing the amount of CaCO₃ formed with the change in supersaturation ratio and pH for oil-brine 3 (0.045M) at 60° C; (a) 0% oil content, (b) 23% oil content

6.3.6 Assessment of calcium carbonate precipitation process using Focused Beam Reflectance Measurement (FBRM) technique

6.3.6.1 Precipitation at 30° C

FBRM technique has been used to assess the nucleation and growth processes for calcium carbonate scale formation by analysing for particles (oil droplets and crystals) chord length distribution and the change in the total chord counts with time. The aim of using this technique is to enable *in-situ* characterization of the system to better understand the precipitation process.

Figures 6-18 and 6-19 show the number of chord counts for different chord length channels for oil-brine 3 (0.045M) at 30° C. The initial measurements are considered random, very intense and this is most probably because of the turbulence that happens inside the vessel when mixing the brines at the beginning of the experiment. In addition to the rapid precipitation and the tendency for the particles to adhere at the FBRM probe window which is very intense at the beginning of the experiment. Therefore, the first 5 minutes (300 s) of measurements are usually ignored. However an increase in the intensity can be observed from the time of mixing the brines which indicates instantaneous precipitation process. The reading of 1 to 5µm chord length is not stable because of the tendency for small particles to either adhere or nucleate at the probe window. This causes a high increase in the intensity and affects the measurements. The decrease of this small sized count after the initial increase is due to the regular cleaning of the probe which is very frequent at the beginning of the experiment. The gaps in the figure represent the peaks detected at the cleaning period of the probe which are removed. The raw data of the measurements before the removing of the cleaning periods are presented in appendix A-1.

Crystal particles of large chord lengths >10 µm have shown a lesser tendency to stick at the probe window as they showed relatively stable readings before and after the cleaning gaps. The tendency for the small particles to stick at the probe window is higher in the first 30 minutes of the experiment than in the last 30 minutes. However, the fact that only small particles of chord length of 1-5 µm have shown stickiness affinity to the probe window, in addition to the decrease in the tendency for the small particles to stick with time may suggest that this is due to the nucleation of crystals on the surface of the probe rather than the adhesion of crystals from the bulk solution.

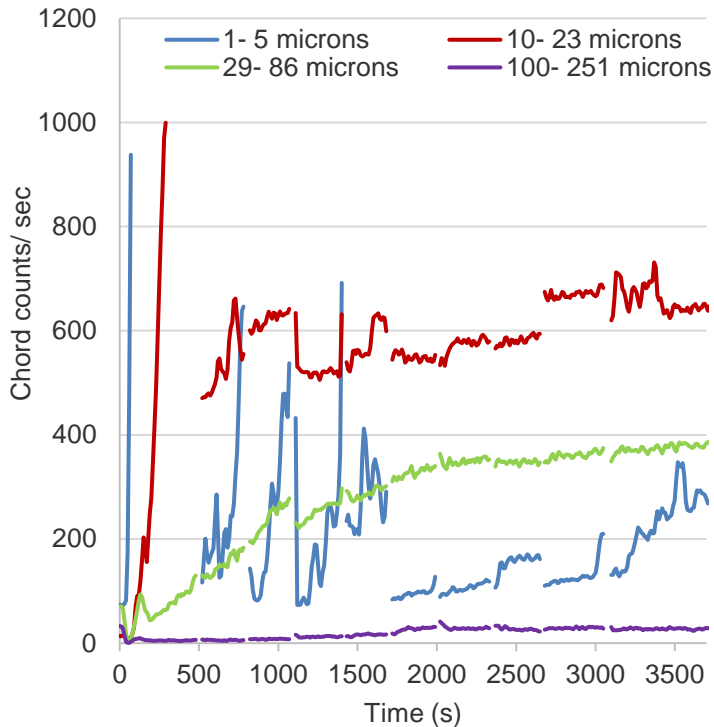


Figure 6-18 Chord counts for brine 3 (0.045M) at 30° C, agitated at 550 rpm

The continuous increase in the small particle counts throughout the experiment may suggest a progressive nucleation is taking place in the bulk solution throughout of the experiment for the oil-free system at 30° C as shown in Figure 6-18. The bulk nucleation period in the presence of oil is shown to be shorter as the small particles show a slight decline in the second half of the experiment as shown in Figure 6-19. The increase of the intensity of different chord length channels also suggests the occurrence of fast precipitation and rapid crystal growth rates immediately after mixing the brines. The increase in the channel intensity of ranges 10 to 23 μm and 29 to 86 μm is much higher at the beginning of the experiment than later on. However growth continues over all the experiment in the oil-free system by observing the increase in the large particle size counts. The continuous growth process occurs simultaneously to the continuous nucleation process in the oil-free system. On the other hand, the growth process starts to cease by about 25 min (1500 s) and this occurs in simultaneous to the nucleation process stopping in the oil system as shown in Figure 6-19. However, the difference between both systems is the existence of the high intensity of the particle chord length channel of 29-86 μm over the other particle size in the presence of oil and this will be discussed in chapter 7.

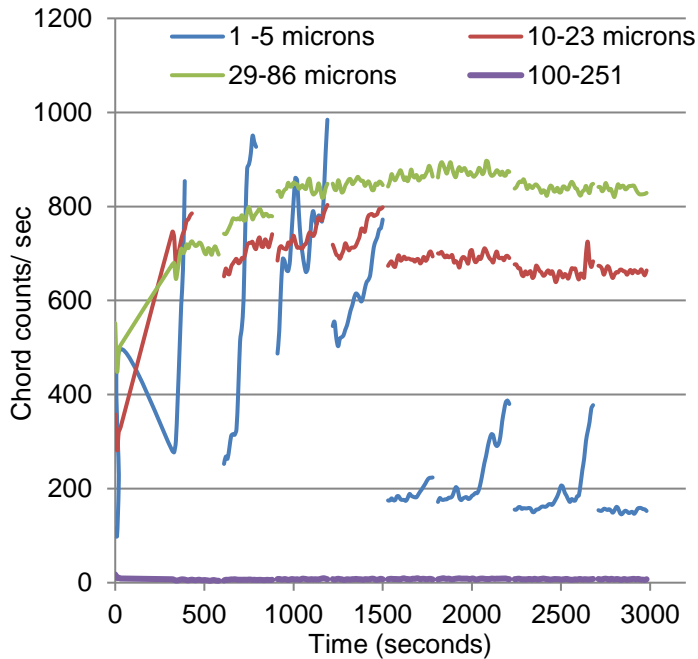


Figure 6-19 Chord counts for 10% oil- brine 3 (0.045M) at 30° C, agitated at 550 rpm

Figure 6-20 shows un-weighted chord length distribution for the oil-free system at 30° C. This is used as a reference for studying the impact of O/W emulsions on the crystallization process. The mode of the distribution clearly increases throughout the duration of the test and this is attributed to the growth of particles which makes the profile less broad and results in a slight shift to a larger crystal size. The continuous formation of small crystals (less than 5 μm) throughout the duration of the test can also be observed from the existence of the small peaks on the left side of the distribution and is attributed to the high nucleation rate contributing to creating new calcium carbonate crystals during the test.

The mean chord length (square-weighted) for the crystals that are formed in the oil-free system at 60 minutes is about 62 μm . This value corresponds to a mean chord length of about 21 μm (un-weighted). The calculations of the un-weighted and the square-weighted mean chord length are shown in Table A-1 in the appendix A-2. However SEM images in the next section show that the crystals are mainly formed of clusters of vaterite and calcite which are no larger than about 30 μm at 60 minutes. Therefore, un-weighted mean size and hence un-weighted chord length distribution may be considered to represent the system well in this case.

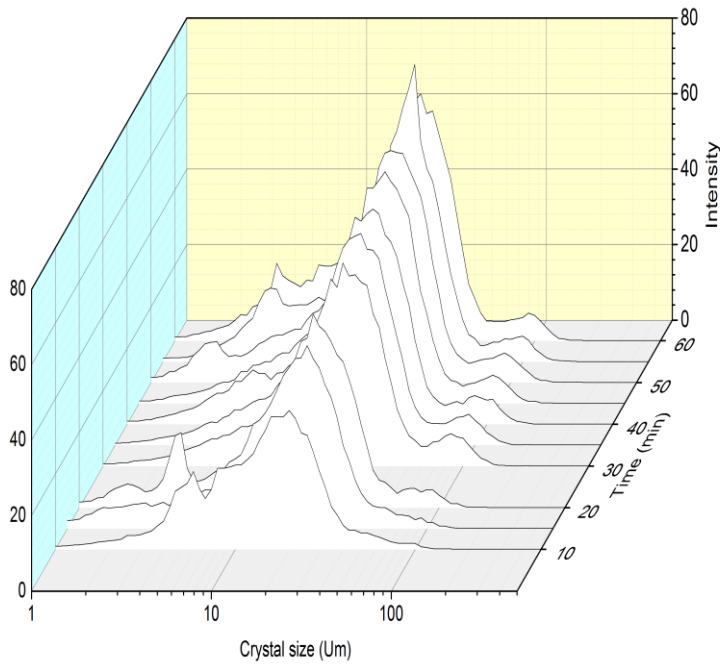


Figure 6-20 Chord length distribution (un-weighted) for brine 3 (0.045M) at 30° C

Figures 6-21 and 6-22 show the un-weighted chord length distributions for 10 and 23% oil content at 30° C, respectively. The first shaded profile represents oil droplet distribution which is detected from an oil-NaCl (0.3M) solution and used here as a reference for the precipitation process in the presence of oil. The mode of the chord length distribution is higher when the system encounters precipitation than when the system consists of only oil droplets. The mode of the chord length distribution continued to rise in a gradual manner throughout the duration of the test. The mean chord length (square-weighted) for the particles that are present in oil systems at 30 minutes are about 46 and 51 μm for the 10 and 23% oil-brine system, respectively. These values correspond to an average mean chord length of about 22 and 24 μm (un-weighted), respectively.

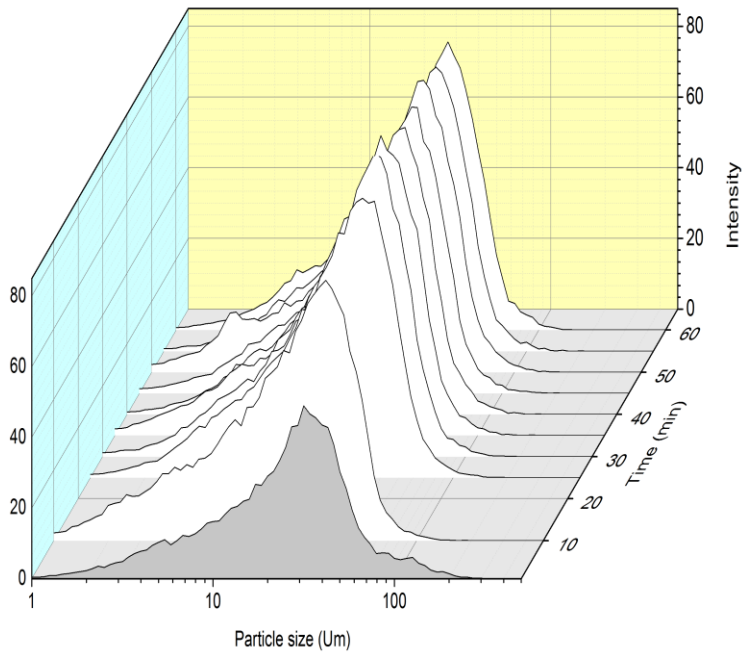


Figure 6-21 Chord length distribution (un-weighted) for 10% oil-brine 3 (0.045M) at 30° C

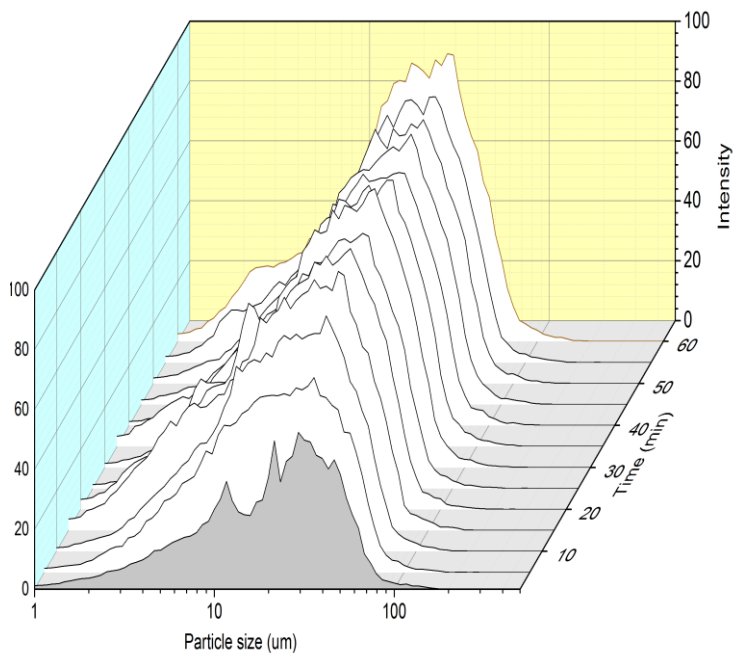


Figure 6-22 Chord length distribution (un-weighted) for 23% oil-brine 3 (0.045M) at 30° C

Applying weighting methods to a set of data as shown by equation 4-14 gives an extra influence to the larger particle weights in the data over the smaller particles. Therefore, representing the chord counts using square-weighted chord length distribution may better represent the oil-precipitate system in this case and this is shown in Figures 6-23 and 6-24.

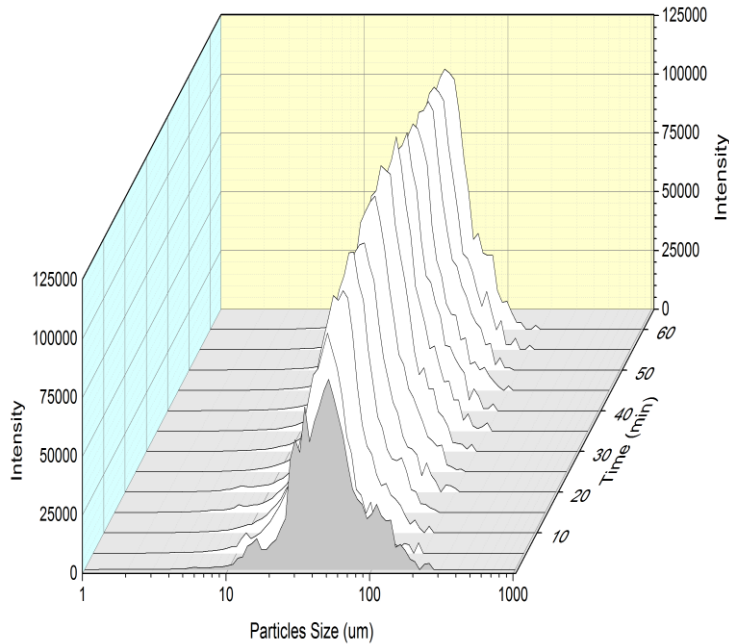


Figure 6-23 Chord length distribution (square-weighted) for 10% oil-brine 3 (0.045M) at 30° C

Square-weighted distribution is less broad than un-weighted distribution and the profile for the system containing only oil droplets shows a close distribution to the particle distribution which represents both crystals and oil droplets. The particle size distribution has encountered a gradual increase in the mode with a slight shift to larger size with time. However, the difference in the mode of the distribution profile between the system which contains only oil droplets and that which contains both colloid particles may indicate that crystals are formed in the bulk solution and this causes the mode to shift to the right. This could also be due to a change in the optical properties of the system as the scale builds-up at the oil-water interface. Although, it was reported that the FBRM technique provides reproducible and more accurate results for emulsions with high reflective properties than for transparent droplets [203]. It was also reported that the number of counts is affected by the change in the refractive index [204].

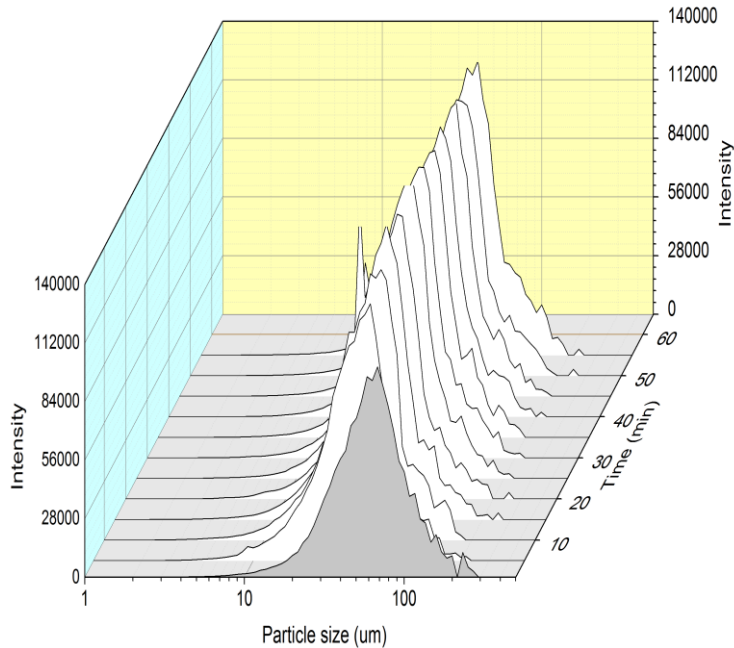


Figure 6-24 Chord length distribution (square-weighted) for 23% oil-brine 3 (0.045M) at 30° C

Comparing the total chord counts for systems with and without oil in order to ensure whether the precipitation increases or decreases with oil is illustrated in Figure 6-25. The left side shows the total chord counts which include both CaCO_3 crystals and oil droplets for the system with oil. The right side shows the measurement for the same system after subtracting the average count of oil droplets so that only the counts for CaCO_3 particles are shown. It is shown that the total chord counts are reduced by 1 to 1.5 times when the oil phase is removed from the system at 30° C. However, the total number of crystals as shown on the right side of Figure 6-25 showed a relatively similar level of precipitation for the system with and without oil, although the system with 23% oil content showed higher counts than the system with 10% oil content and this is most probably due to higher impeller mixing speed of 700 rpm than that used for 10% oil content system which is 550 rpm and this may promote precipitation. The oil-free system exhibited a clear increase in the total counts in the second half of the experiment. This increase in the total counts for the precipitate in the oil-free system is due to the increase in the small chord length channel of 1-5 μm counts which is shown to occur simultaneously with the increase of the larger chord length channels as shown in Figure 6-18.

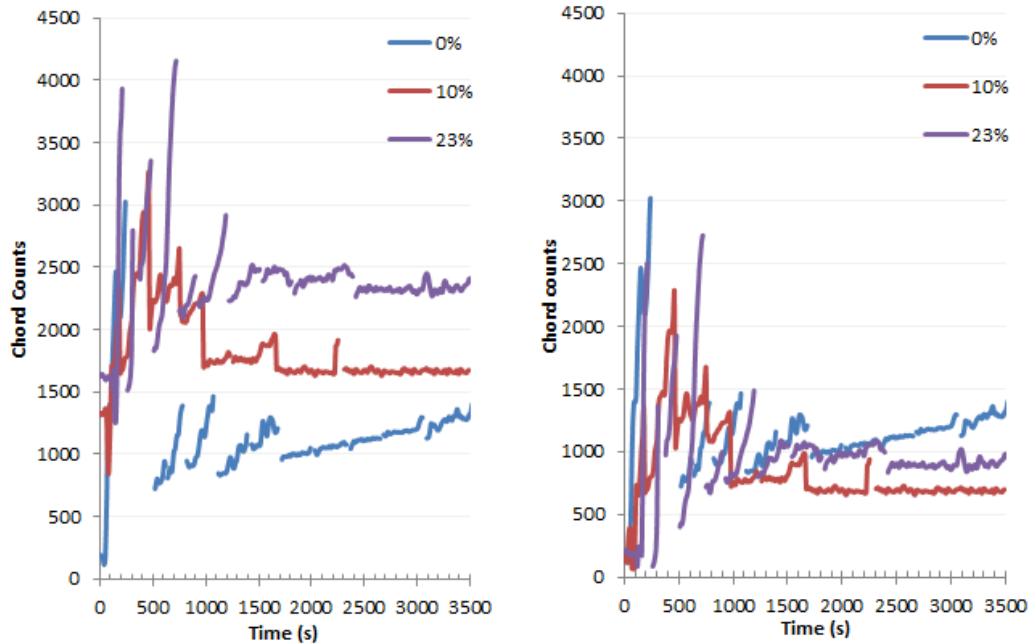


Figure 6-25 Total chord counts for oil-brine (3) at 30° C; LHS: total counts including oil droplets; RHS: total counts excluding oil droplets

6.3.6.2 Precipitation at 60° C

The number of counts for different chord length channels for the oil-free system at 60° C is shown in Figure 6-26. The intensity increased immediately after mixing the brine which indicates a spontaneous precipitation. The continuous increase in the smallest channel size of 1 to 5 μm indicates high nucleation rate which proceeded to about 40 minutes (2400 s) before it slowed down or stopped. The increase in the channel counts of ranges 10 to 23 μm and 29 to 86 μm from an early stage of the precipitation indicates a rapid growth process. The growth process continued to 30 minutes (1800 s) before it reached a steady state. The decrease in channel counts of 29 to 86 μm beyond 30 minutes is most probably due to the agglomeration of particles which led to a slight increase in the larger particle counts of 100-251 μm .

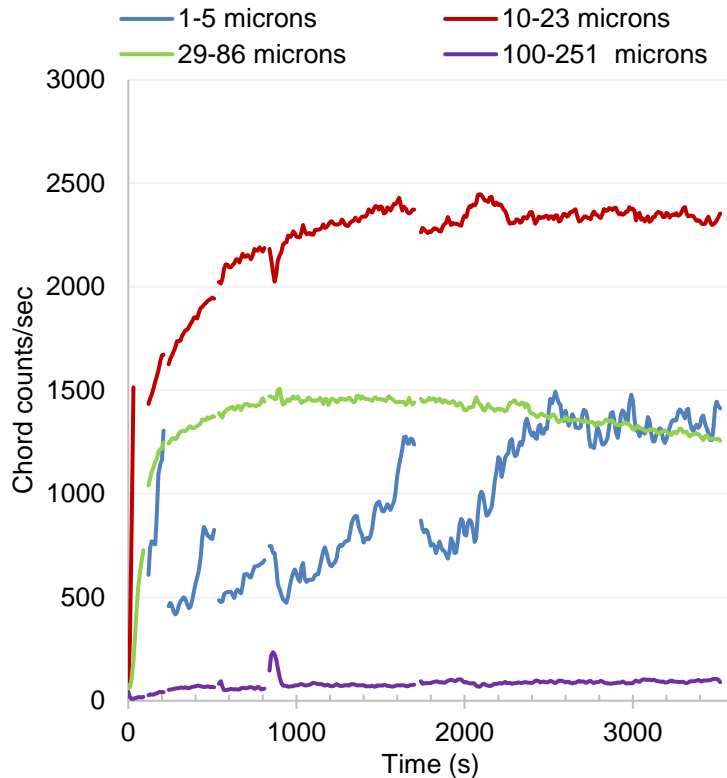


Figure 6-26 Crystals chord length counts for brine 3 (0.045M) at 60° C, agitated at 550 rpm

Figure 6-27 shows the number of counts for the different chord length channels for the 10% oil-brine 3 (0.045M) system. Again, precipitation took place immediately after mixing the brine and the increase in channel length counts of 10 to 23 μm and 29 to 86 μm in the early stages of the experiment indicates rapid crystal growth process which continued to the end of experiment. The low and relatively stable reading of the small channel size of 1 to 5 μm indicates the existence of equilibrium between nucleation and growth rates; as the growth in crystal size occurs, a switch to a larger size but with a potential decrease in their initial size is expected. However as the nucleation rate remains high, new nuclei are formed keeping the population of small crystals steady.

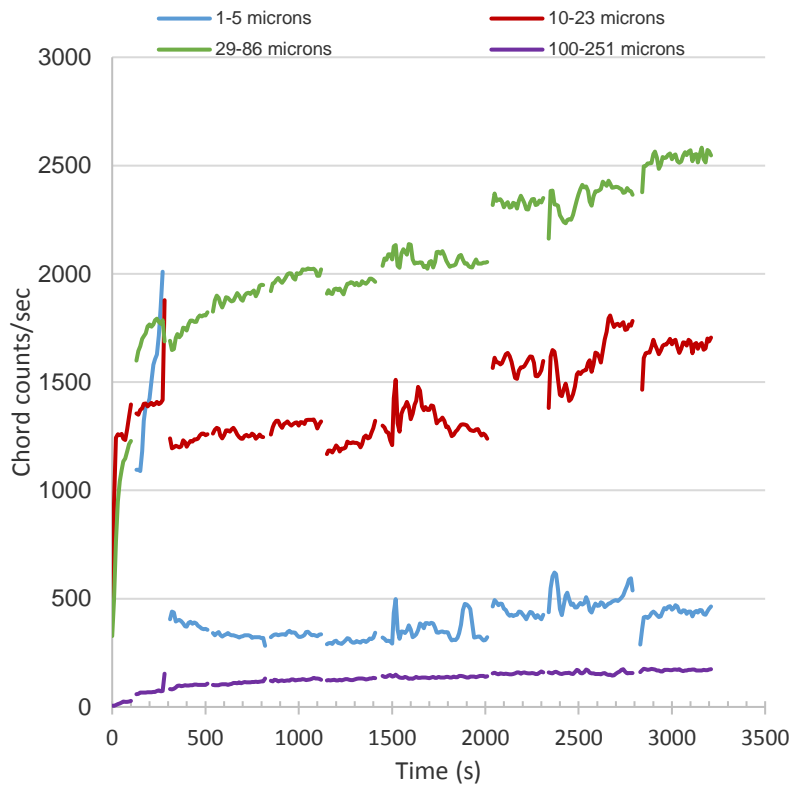


Figure 6-27 Change of chord counts with time for 10% oil-brine 3 at 60°C, agitated at 550 rpm

Figure 6-28 shows the chord length distribution over time for an oil-free system at 60° C. The population of small crystals (less than 10 μm) increased throughout the duration of the test and this is maybe attributed to a high nucleation rate. The mode of the distribution is also increased with a slight shift to the right or to a larger particle size and this is attributed to the growth of particles. The mean chord length (square-weighted) for the crystals that are formed in the oil-free system at 60 minutes is about 95 μm . This corresponds to a mean chord length of about 18 μm (un-weighted). The calculations of un-weighted and square-weighted chord length are shown in Table A-2 in the appendix A-2. However SEM images in the next section show that the crystals are mainly formed of clusters of aragonite which are needle shaped with high aspect ratio.

Figures 6-29 and 6-30 show the chord length distributions (un-weighted) for 10% and 17% oil at 60° C, respectively. It appears that the population of small crystals reduces and the distribution looks better when oil is added to the system and an o/w emulsion is formed.

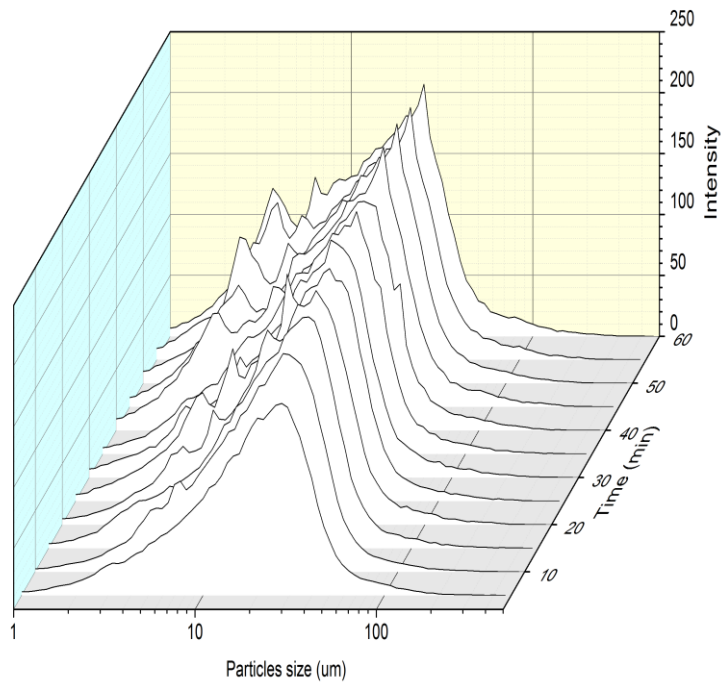


Figure 6-28 Chord length distribution for brine 3 (no oil) at 60° C

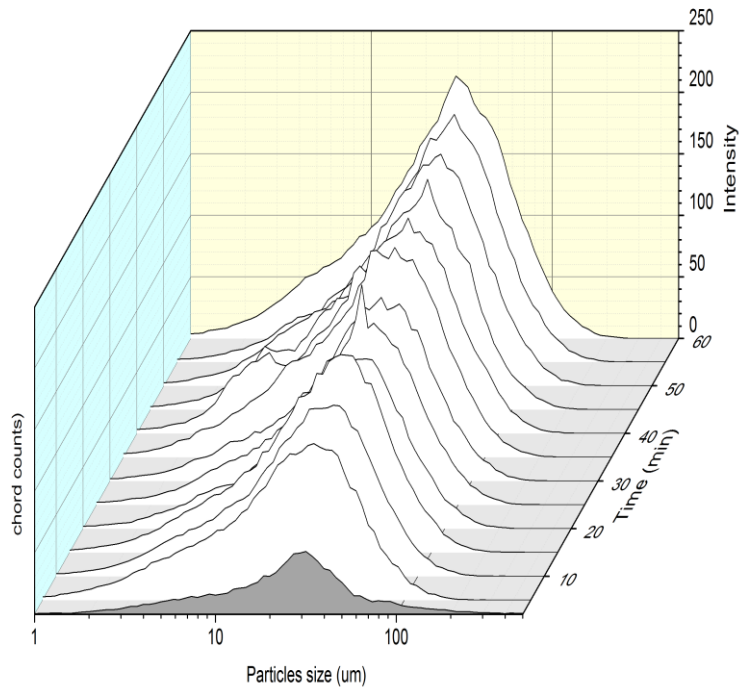


Figure 6-29 Chord length distribution for 10% oil-brine 3 (0.045M) at 60° C

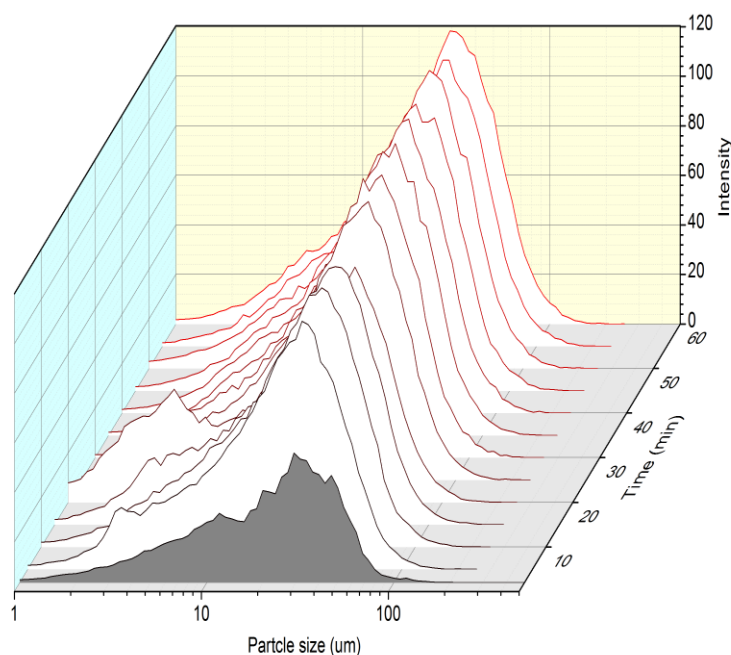


Figure 6-30 Chord length distribution for 17% oil-brine 3 (0.045M) at 60° C

The shaded profile represents the oil droplet distribution which is detected from an oil- NaCl (0.3M) solution and used here as a reference for the precipitation process in the presence of oil. The mode of the particle size distribution is much higher for the case where the system encounters precipitation than when the system contains only oil droplets. The mode of the peak continued to rise in a gradual manner throughout the duration of the test with a slight shift to larger particle size. The mean chord length (square-weighted) for the particles that are formed in oil systems at 60 minutes are about 74 and 58 μm for 10% and 17% oil content, respectively. These values correspond to mean chord lengths of about 32 and 28 μm (un-weighted) for 10% and 17% oil content, respectively as shown in Table A-2 in the appendix A-2 for 10% oil-brine system. Plots reproducing the particle size distribution as a square-weighted distribution are shown in Figures 6-31 and 6-32. A significant difference between the distribution profiles with and without CaCO_3 precipitate can be observed. The mode of the peak is intensively increased with time with a slight shift to the right. This may be attributed to the high precipitation rate combined with high agglomeration rate which is increased with time. This effect is more observed in the system with 10% oil content in Figure 6-31 than in the system with 17% oil content in Figure 6-32. The high tendency to agglomerate was also observed through a visual observation for the experiments in the presence of oil at 60° C when mixing was stopped. Dense flakes of agglomerated crystals collected at the water-oil interface and were oriented in the water phase. These clusters were found to be significant in the FBRM experiments compared to other experiments at 60°

C. This is maybe attributed to the change in the experimental conditions as there was no bubbling of CO₂ prior to these experiments.

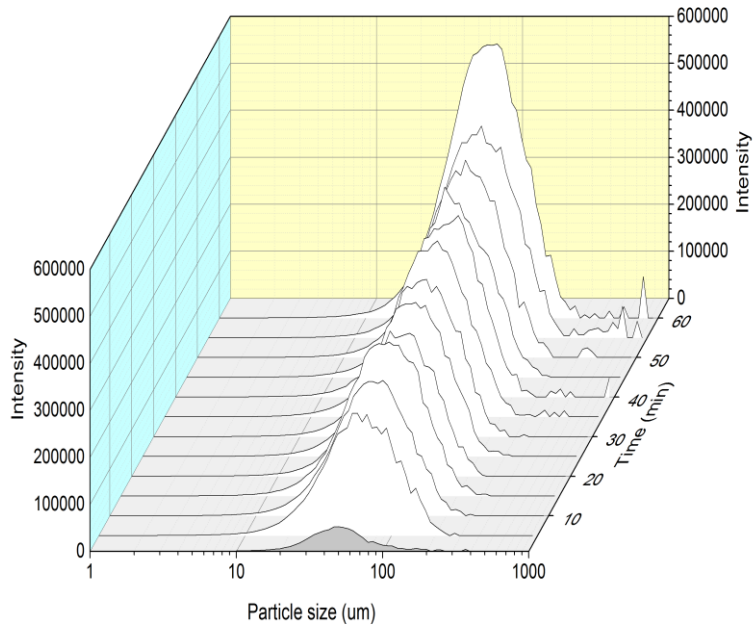


Figure 6-31 Chord length distribution (square-weighted) for 10% oil-brine 3 (0.045M) at 60° C

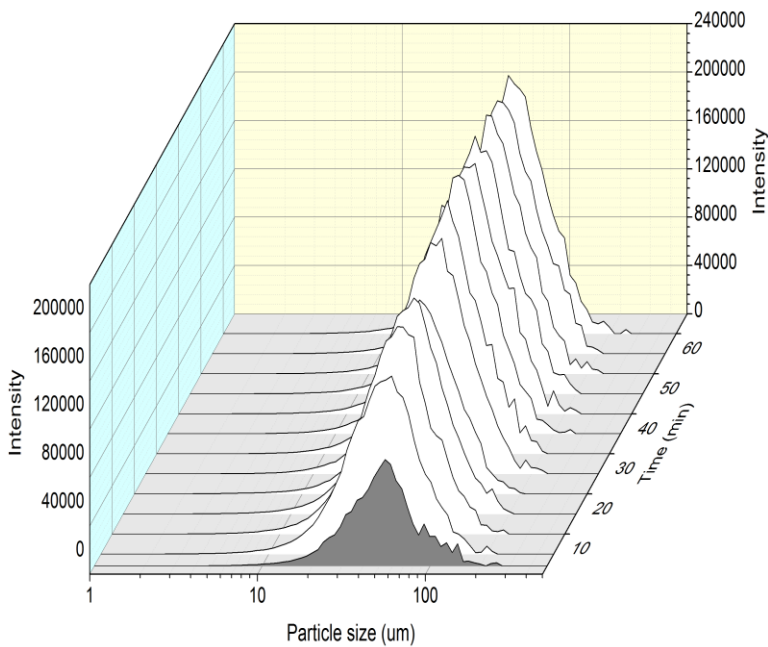


Figure 6-32 Chord length distribution (square-weighted) for 17% oil-brine 3 (0.045M) at 60° C

Comparing the total chord counts for systems with and without oil in order to ensure whether precipitation increases or decreases with the addition of oil is illustrated in Figure 6-33. The left side shows the total counts which includes the CaCO₃ crystals and the oil droplets for the

systems with oil. The right side shows the measurement for the same systems with the subtracting of the average counts of oil droplets so that only CaCO_3 precipitate counts are shown. The precipitation is found to decrease when adding an oil phase to the system at 60°C as fewer counts were detected in the presence of oil. The total chord count is reduced when removing the oil counts from the system by about 15% and 30% for 10% and 17% oil fraction, respectively. This suggests that the crystal counts are much higher than the oil droplet counts in this case. Both the oil-free system and 10% oil system at 60°C exhibited a clear increase in the total counts which proceed throughout the experiment whereas this increase was not detected in the 17% oil content system. This increase in the total counts for the oil-free system is due to the increase in the small chord length channel of 1-5 μm counts as shown in Figure 6-26 whereas the increase in the total counts is a result of an increase of the large particles in the 10% oil content as shown in Figure 6.27.

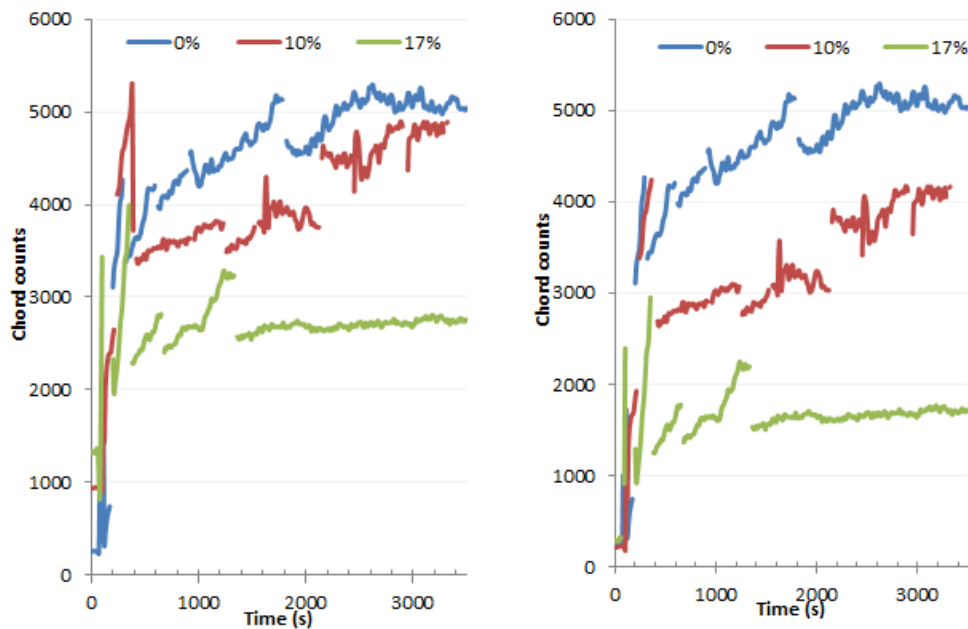


Figure 6-33 Total chord counts for oil-brine 3 at 60°C ; LHS: total counts including oil droplets; RHS: total counts excluding oil droplets

As a summary of the results detected by the FBRM technique, it is noted there is a high and instantaneous precipitation rate shown by the rapid and high counts recorded once the brines are mixed. The high growth rates cause an increase in the mode of the distributions with slight shifts to the right side to larger particle size for all cases at both temperatures. The continuous population of small particles throughout the experiment during the tests for the oil-free system at both temperatures takes place simultaneously with an increase in the large particles intensity. Oil systems have a much more ordered particle size distribution with less nucleation tendency but higher growth or agglomeration rates. The results also suggest that applying weighting methods can help in interpreting the FBRM data.

6.4 Characterization of calcium carbonate bulk precipitation

6.4.1 Analysis of crystal morphology using SEM

6.4.1.1 Morphology of precipitate at 30° C

The morphology of the scale formed in the bulk solution for systems with and without oil is analysed using Scanning Electron Microscopy (SEM). Figures 6-34 and 6-35 compare the crystal morphology at different time intervals for systems with and without oil at 30° C. The ImageJ analysis software is used to estimate the average size of vaterite and calcite at different time intervals for oil-brine 2 (0.065M) and oil-brine 1 (0.1M) as shown in Tables 6-6 and 6-7, respectively. Vaterite and calcite are the major morphology at this temperature. The Vaterite phase seems to take an initial spherical shape of an average size of about 3 μm which then grows to have a cauliflower or pine cone shape and reaches to an average size of 16 μm at 60 minutes. The cauliflower shape of vaterite is suggested by [205] to form as a result of agglomeration mechanism. It is shown by [206] that the success of an aggregation event of vaterite depends on the growth of a crystalline bridge between two colliding particles. However, the oil-free systems seem to promote vaterite growth more than in the oil system. The average size of vaterite in the oil systems is about 13 μm at 60 minutes.

The rhombohedral calcite crystals are shown to form as single crystals or as clusters of interconnected crystals. According to [48] the crystallization and growth of calcite on the surface of polycrystalline vaterite spheres results in various calcite superstructures. However, the calcite crystals are much bigger in the oil-free system with an average size of about 13 and 17 μm at 60 minutes for brine 2 (0.065M) and brine 1 (0.1M), respectively. Calcite crystals are smaller in the presence of oil with an average size of about 7 and 10 at 60 minutes for brine 2 (0.065M) and brine 1 (0.1M), respectively. This is in agreement to [207] who detected smaller size of calcium carbonate crystals formed in an oil-free system to those which formed in the presence of n-dodecane. The appearance of flat surfaces in some of vaterite clusters can be clearly observed in the systems with oil as shown in Figure 6-36. This gives rise to questions about its formation and will be discussed in chapter 7.

Aragonite is also found to form at this temperature and has taken the shape of a cluster of needles emerging from a central point which is usually connected to vaterite. This suggests that the origin of the aragonite is vaterite. However, the aragonite presence is more observed in brine 2 (0.065M) than in brine 1 (0.1M).

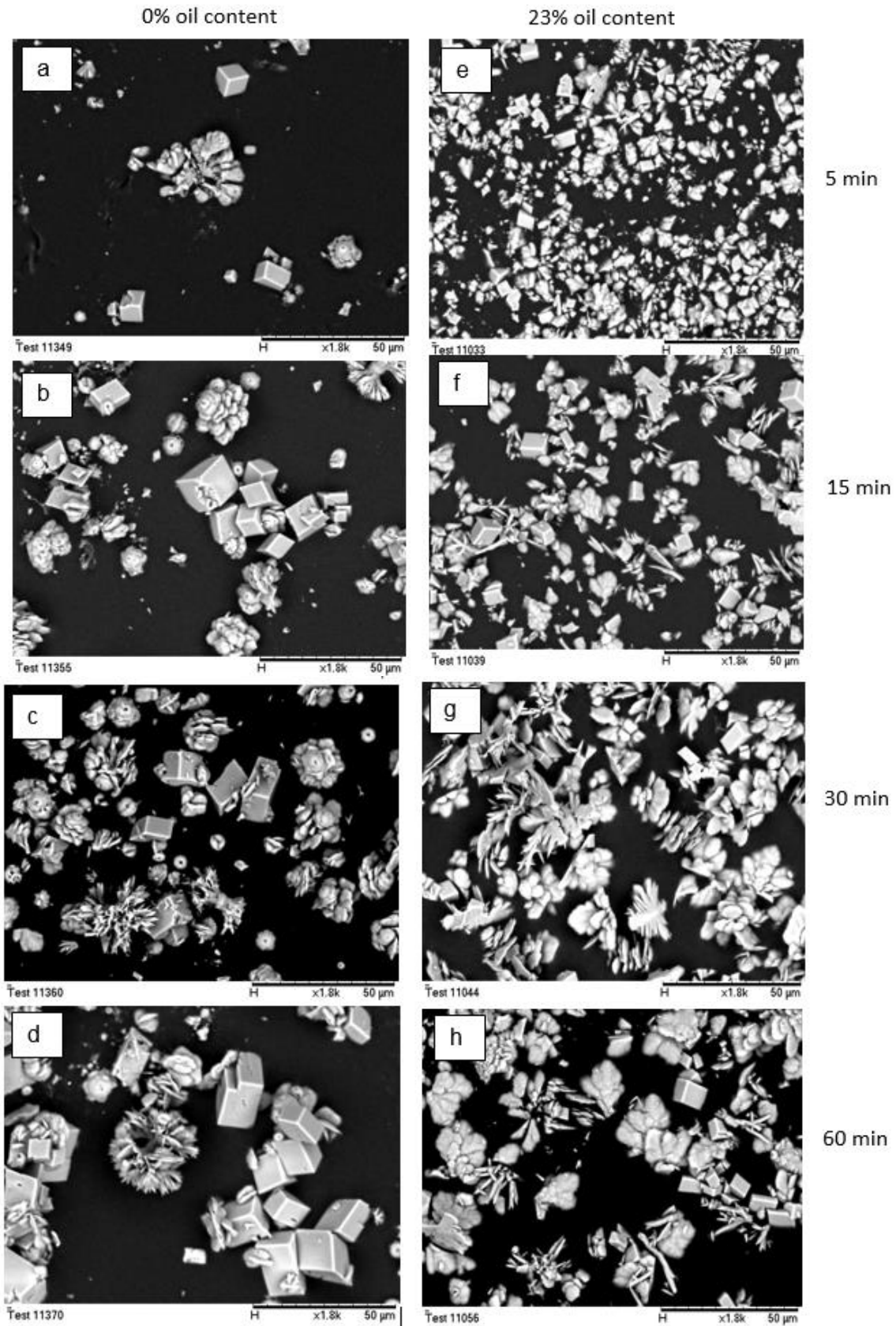


Figure 6-34 SEM images for CaCO_3 bulk precipitate for oil-brine 2 (0.065M) at 30° C; 0% oil content (a) 5 min, (b) 15 min, (c) 30 min, (d) 60 min; 23% oil content (e) 5 min, (f) 15 min, (g) 30 min, (h) 60 min

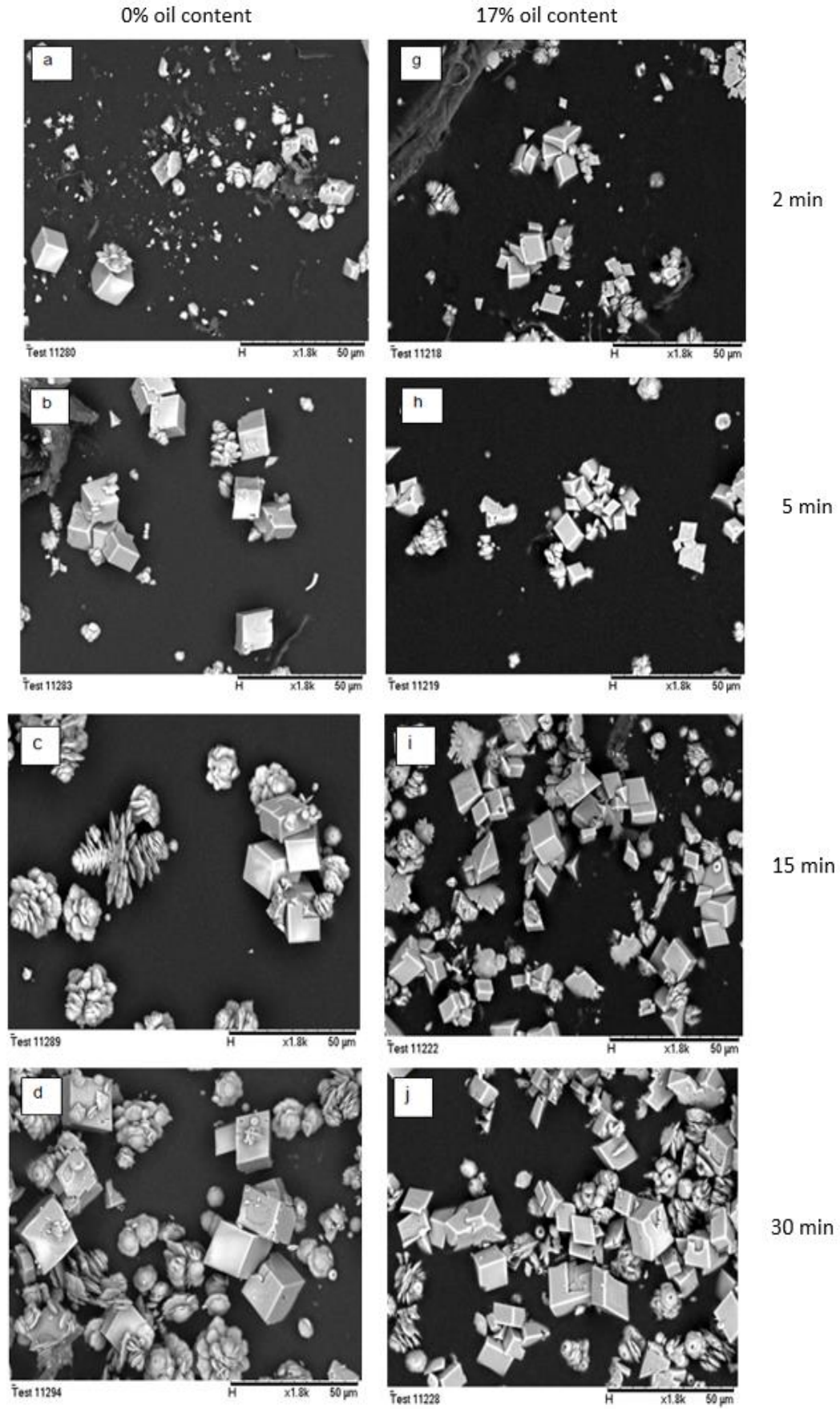


Figure 6-35 Continue

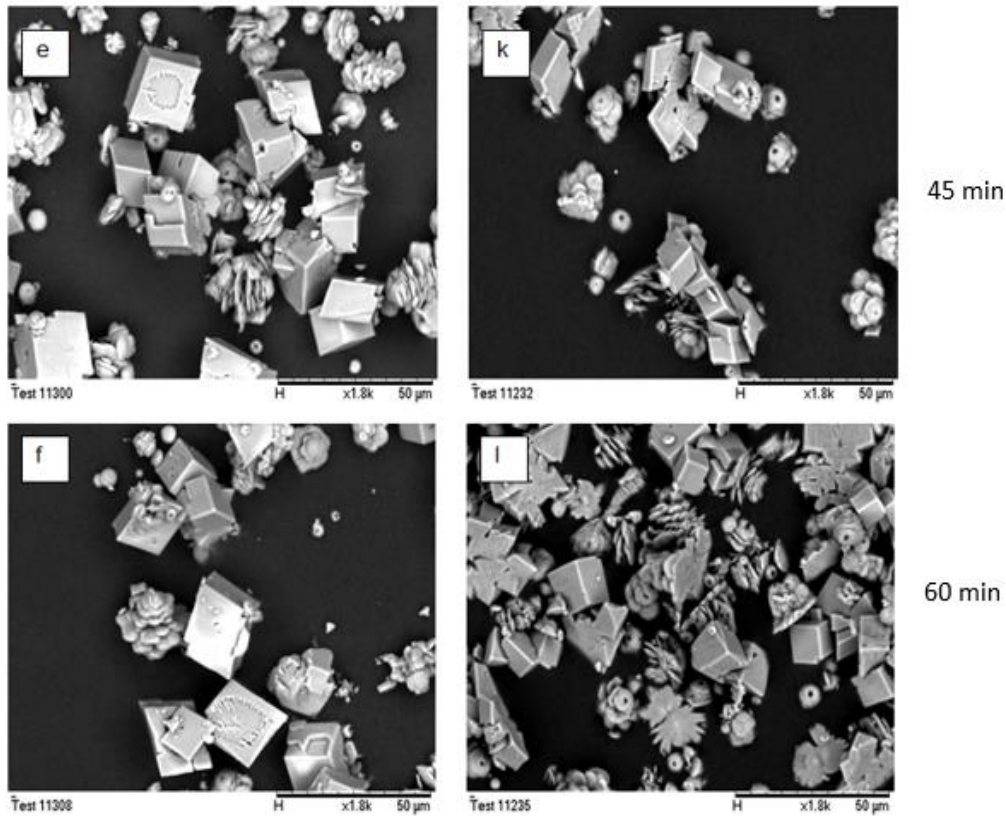


Figure 6-35 SEM images for CaCO₃ bulk precipitate for oil-brine 1 (0.1M); 0% oil (a) 2 min,(b) 5 min, (c) 15 min, (d) 30 min, (e) 45 min, (f) 60 min; 17% oil content, (h) 2 min, (i) 5 min, (j) 15 min, (k) 30 min, (l) 45min, (m) 60 min

Table 6-6 The change in precipitate average crystal size (μm) with time for oil-brine 2 (0.065M) system

Time (min)	0% oil content				23% oil content			
	Vaterite	Std.Dev.	Calcite	Std.Dev.	Vaterite	Std.Dev.	Calcite	Std.Dev.
5	5.82	2.88	5.23	2.01	3.84	1.91	4.43	1.67
15	9.66	4.49	8.69	1.94	5.73	2.61	5.98	1.62
30	10.71	5.92	10.39	2.32	11.2	4.89	7.28	1.65
45	13.48	8.42	11.91	3.212	12.39	4.03	6.26	1.79
60	15.82	6.67	12.67	1.72	12.29	3.94	6.78	2.27

Table 6-7 The change in precipitate average crystal size (μm) with time for oil-brine 1 (0.1M) system

Time (min)	0% oil content				17% oil content			
	Vaterite	Std.Dev.	Calcite	Std.Dev.	Vaterite	Std.Dev.	Calcite	Std.Dev.
2	3.57	1.41	6.94	2.44	5.74	1.86	6.51	2.39
5	5.74	2.95	10.67	1.19	6.76	2.95	6.39	1.84
15	14.72	5.74	12.64	0.53	7.26	1.9	8.03	1.68
30	14.59	5.98	14.68	2.85	10.52	2.87	9.25	2.17
45	14.09	5.42	16.33	2.47	9.82	3.63	9.72	2.48
60	16.52	6.18	16.97	2.00	11.75	3.58	10.22	2.83

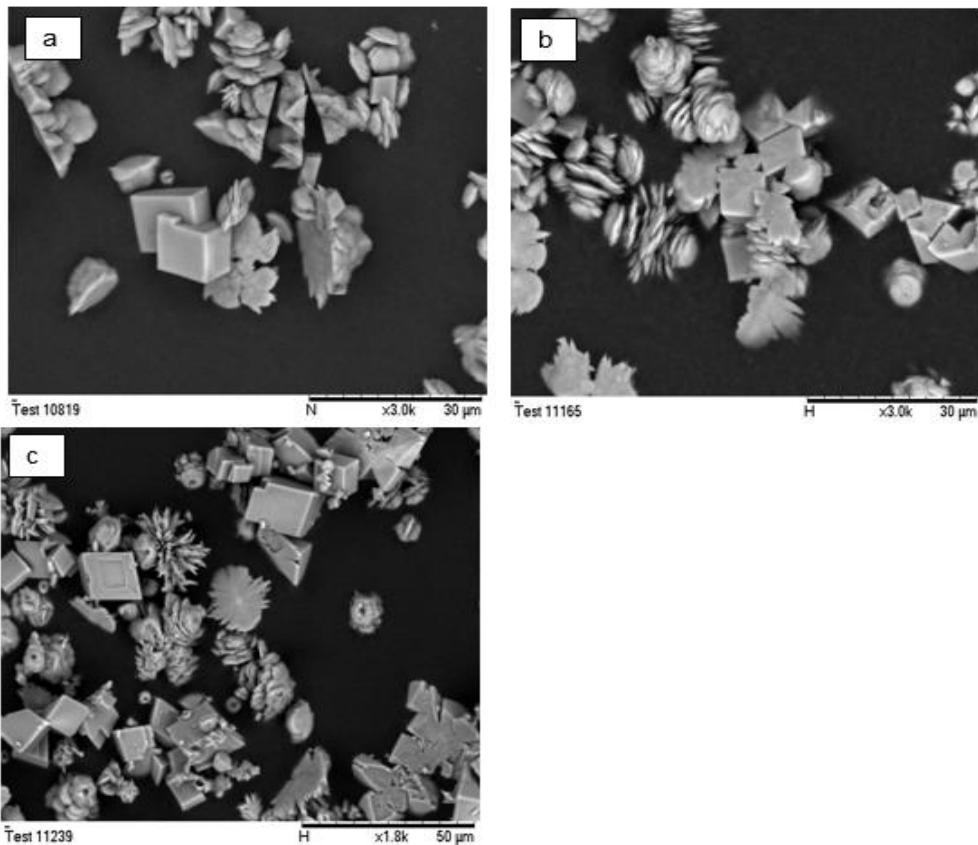


Figure 6-36 The appearance of flat and smooth surface on a side of vaterite in oil-brine systems at 30° C; (a) 23% oil-brine 2 (0.065M) sample at 60 min, (b) 17% oil-brine 1 (0.1 M) sample at 45 min, (c) 17% oil-brine 1 (0.1M) sample at 60 min

6.4.1.2 Morphology of precipitate at 60° C

Figure 6-37 compares between crystals morphology at different time intervals for the oil-free system to those for the oil system for oil-brine 3 (0.045M) at 60° C. The three CaCO_3 morphologies (vaterite, aragonite and calcite) can be clearly identified at this temperature; Aragonite with a needle like shape which appears as a single crystal in the beginning of the crystallization process as shown Figure 6-37 (a) and (f). These crystals are then tending to aggregate and/or branch in a later stage. Branched aragonite can be distinguished by the presence of small needles that have emerged from the surface of a previous formed one. This configuration can be observed more in the presence of oil and are most probably due to the onset of secondary nucleation. It was claimed that when the supersaturation is sufficiently high, secondary nucleation in the presence of prior crystals is induced [208]. The crystals are also appearing to agglomerate to large clusters with time.

Rhombohedral calcite crystals which are formed interconnected to each other are observed as early as 2 minutes in the oil system. Vaterite with a hexagonal plate is also presented and are observed more at the beginning of the crystallization process than later. Vaterite is observed more in the oil-free system than in the oil system.

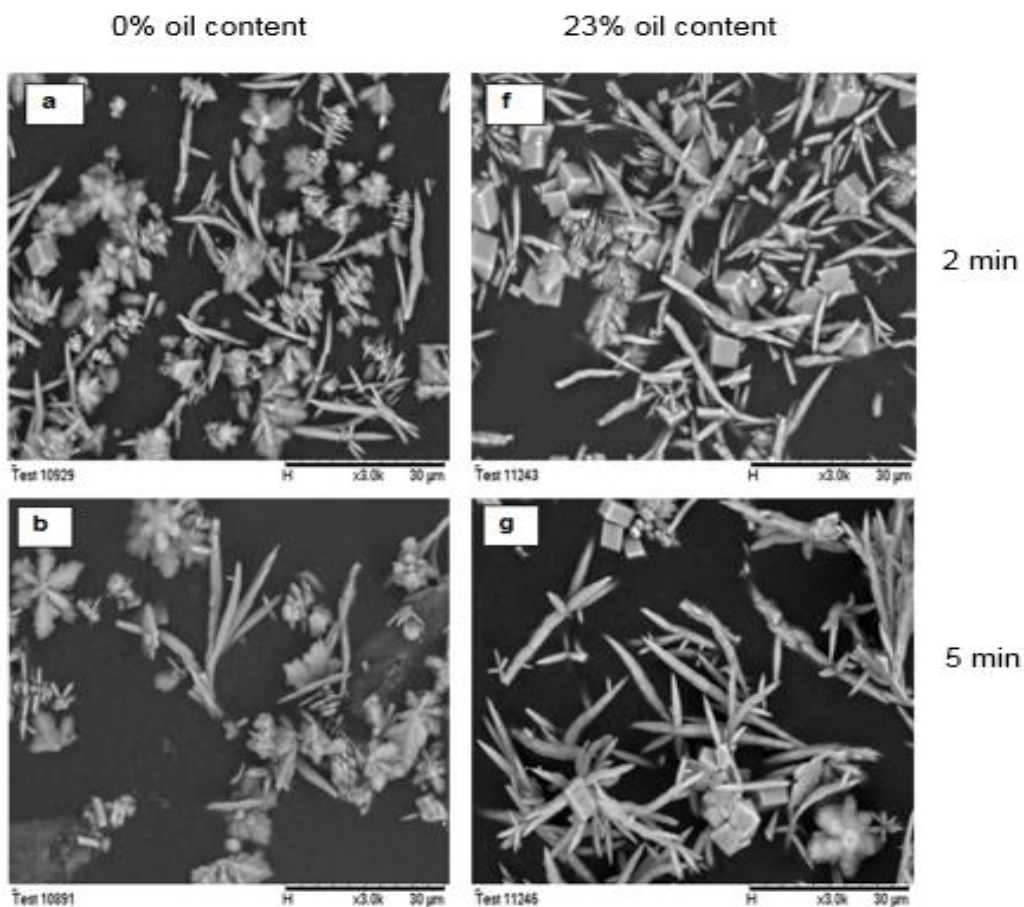


Figure 6-37 Continued

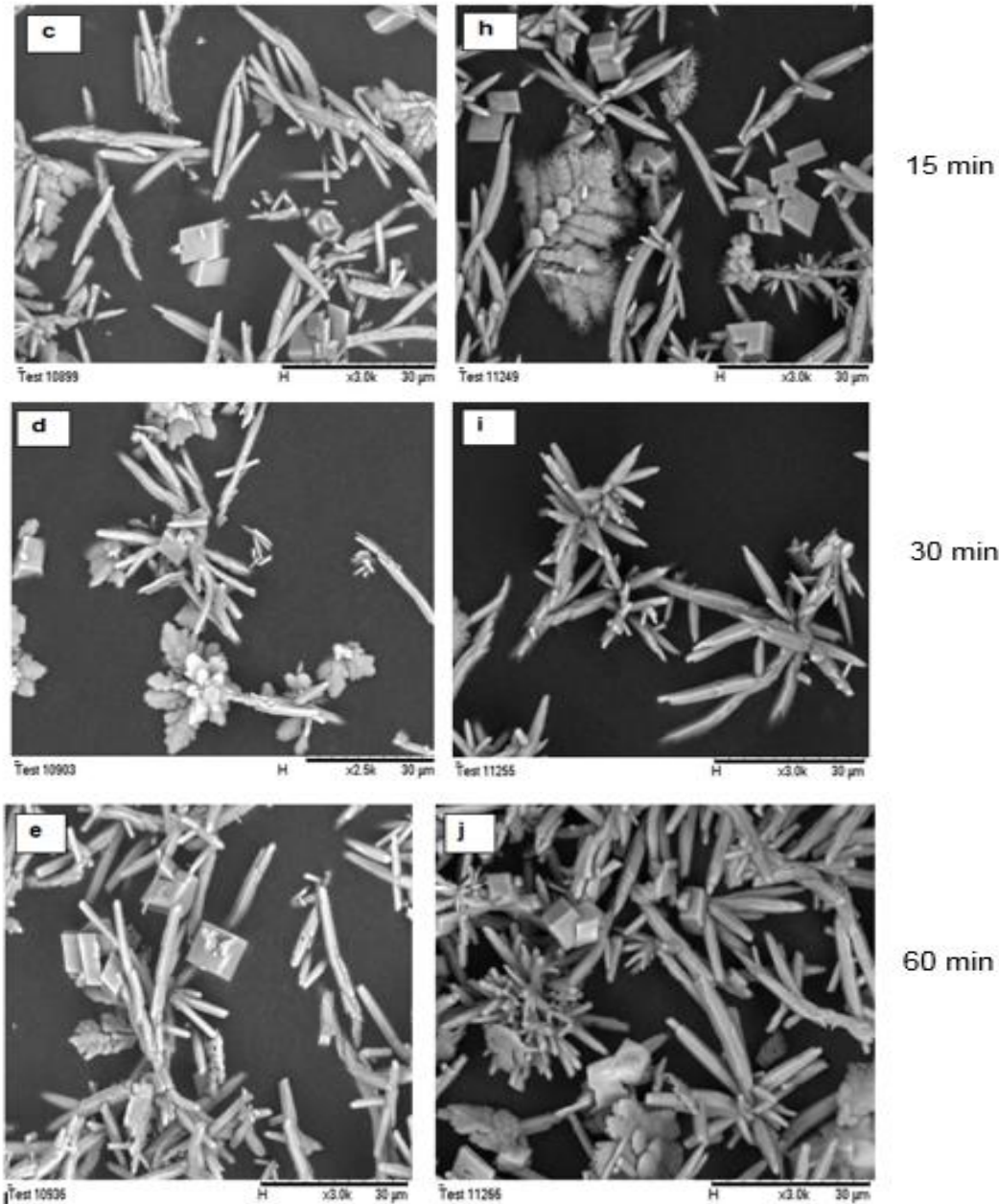


Figure 6-37 SEM for oil-brine 3 (0.045M) at 60° C; 0% oil content (a) 2 min, (b) 5 min, (c) 15min, (d) 30 min, (e) 60 min; 23% oil content (f) 2 min, (g) 5 min, (h) 15 min, (i) 30 min, (j) 60 min

6.4.2 Analysis of CaCO₃ scale using XRD

Calcium carbonate precipitate in the bulk solution is characterized using X Ray Diffraction (XRD). The three different crystalline polymorphs can be presented together under specific conditions of temperature, supersaturation, pH and mixing conditions [43, 45]. The diffraction peaks corresponding to the three calcium carbonate polymorphs calcite (C), vaterite (V) and aragonite (A) are detected at 60° C as shown in Figure 6-39, whereas only calcite (C) and vaterite (V) are at 30° C as shown in Figure 6-38.

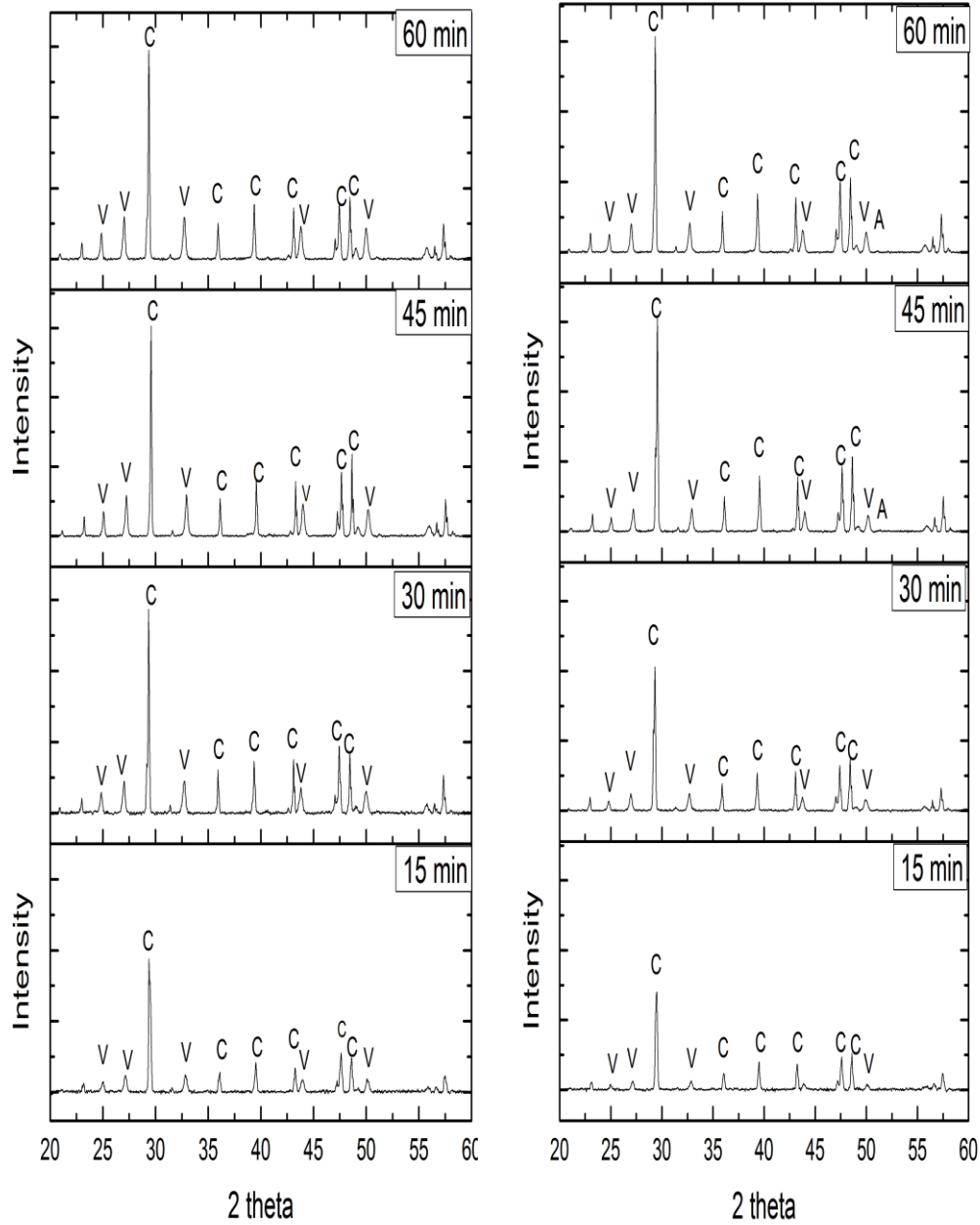


Figure 6-38 XRD patterns for oil-brine 2 (0.065M) at 30°C; LHS, 0% oil content; RHS, 23% oil content

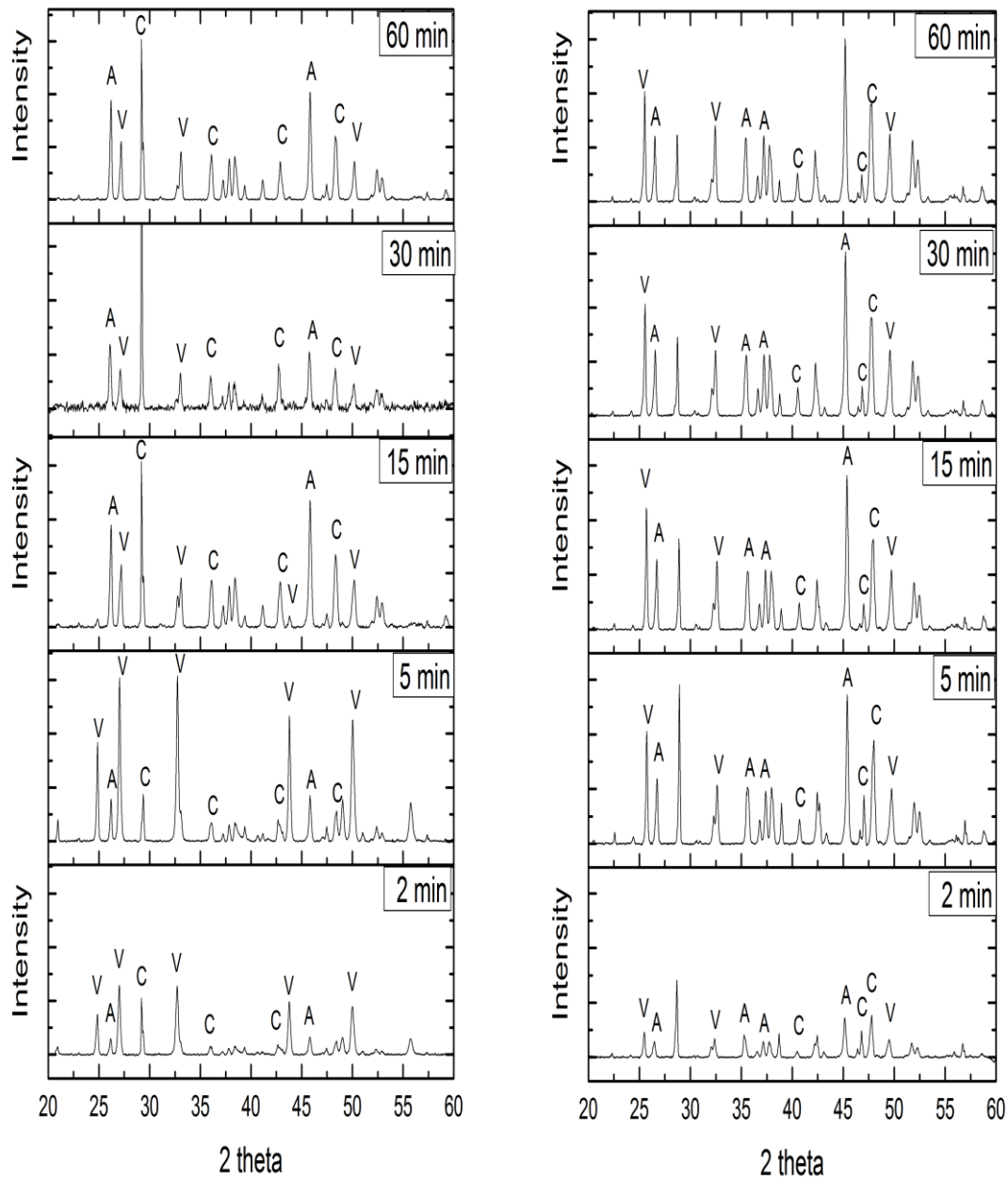


Figure 6-39 XRD patterns for oil-brine 3 (0.045M) at 60°C; LHS, 0% oil content; RHS, 23% oil content

6.4.3 Analysis of polymorphic abundance

In order to understand the kinetics of the precipitation process, the change in the composition of each polymorph was estimated based on the relative intensity of different phases which are detected using XRD and equations 4-22 to 4-24. The number of mmole of each polymorph per one litre of solution is calculated by multiplying the total mmole of calcium carbonate that is formed per one litre of solution by the mole fraction of each

polymorph. The concentration in mg/l of each polymorph is then calculated by multiplying the later quantity by the molecular weight of CaCO_3 . The change in the abundance, as well as the nucleation and growth rate of each polymorph can be evaluated.

6.4.3.1 Assessment of precipitate polymorphic abundance and growth at 30° C

Figures 6-40 to 6-47 represent the mole fractions and the concentrations of calcium carbonate crystalline phases that are formed in the bulk solution for two different brines with and without oil at 30° C. The mole fractions of Vaterite, calcite and aragonite are about 55, 40 and 5 % respectively at 15 minutes for brine 2 (0.065M) as shown in Figure 6-40. This is an indication of a relatively fast transformation rate where 45% of vaterite is transformed in 15 minutes. The change in vaterite composition beyond 15 minutes is slowed down; it requires about 45 minutes for the vaterite composition to reduce from 55% to 50%. Equal composition of vaterite and calcite requires about 90 minutes to achieve and a complete transformation would appear to require about 4 hours if the transformation persists with a similar rate. However the slowing of the apparent rate of vaterite conversion is not necessarily due to a slowing in transformation process from vaterite to calcite but it may be because of the high nucleation and/ or growth rate of vaterite which is exhibited simultaneously with the transformation to the more stable calcite. Some aragonite is also found to form at 30° C but in a very low amount and this also appeared in the SEM images in Figures 6-34. Aragonite is reported to form at this low temperature [43, 201].

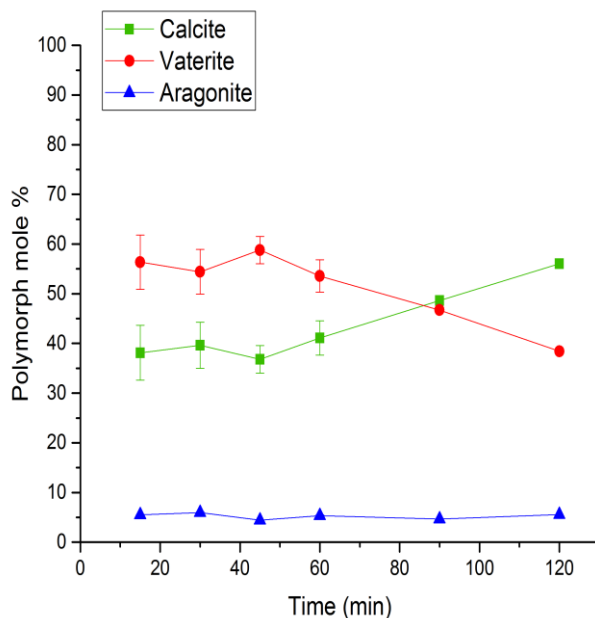


Figure 6-40 Polymorph abundance in the bulk solution for brine 2 (0.065M) at 30° C and at different times

The composition of vaterite, calcite and aragonite are about 60, 30 and 10 % respectively at 5 minutes for brine 1 (0.1M) as shown in Figure 6-41. This is also an indication of a fast initial transformation rate. The Vaterite abundance declines within the first 15 minutes followed by a rise which is continued to 60 minutes before it re-declined. The increase in the vaterite after the decline is most probably due to the continuous nucleation and/ or growth of vaterite which is continued to 60 minutes. Vaterite composition is then gradually decreased again as a result of the transformation of vaterite to calcite with time.

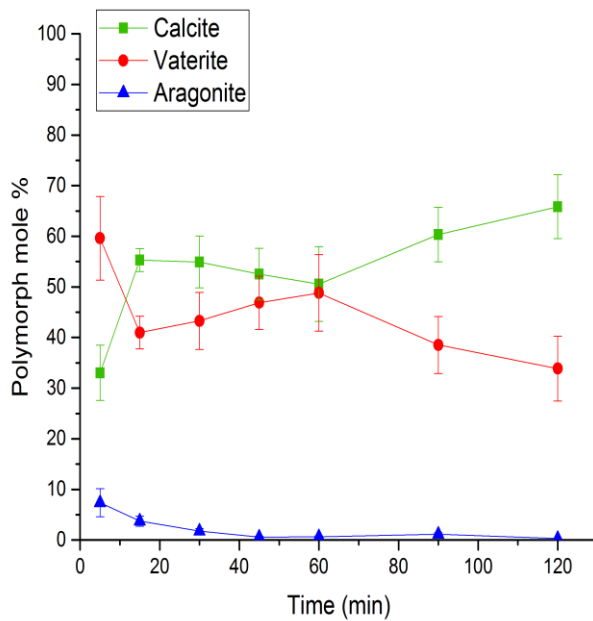


Figure 6-41 Polymorph abundance in the bulk solution for brine 1 (0.1M) at 30° C and at different times

Equal composition of vaterite and calcite requires about 60 minutes to reach. The composition of vaterite and calcite are about 70 and 30% respectively at 120 minutes and a complete transformation to a stable phase may require about 4 hours by extrapolating the vaterite abundance beyond 120 minutes. However the rise in vaterite abundance beyond 15 minutes indicates high nucleation and/ or growth rate of vaterite which is much higher than the rate of its transformation to calcite. Vaterite nucleation and/ or growth continued to 60 minutes before it slowed down or stopped with the continuous formation and growth of calcite.

Generally, the rate of transformation of vaterite and growth of calcite are much faster in the first 15 minutes for both the brines where the abundance of vaterite is decreased by about 40 to 60% of its initial value of 100%, provided that vaterite is the first crystalline phase to form. The rate of transformation beyond 15 minutes is slowed down and this may be due to the continuous nucleation and/ or growth of vaterite. The de-supersaturation profile was

also found to exhibit a significant drop in the first 15 minutes before it stabilised as shown in Figures 6-15 and 6-16. Therefore, the possibility of continuous nucleation beyond 15 minutes is eliminated and the reduction in the transformation process is most probably due to an extended period of vaterite growth. The evidence of vaterite growth in the oil-free system is also clearly observed by SEM in the left sides of Figures 6-34 and 6-35. FBRM also showed a high tendency to large particle sizes with time which shifts the distribution to the right side in the case of oil-free system at 30° C as shown in Figure 6-20.

The fraction of polymorph abundance can then be translated to concentration distribution in mg/l for each crystalline phase and compared to the amount of total CaCO₃ produced in the bulk solution as shown in Figures 6-42 and 6-43. Both vaterite and calcite concentrations increase within first 15 minutes which is considered as a nucleation period. The composition of vaterite and calcite are then found to be parallel to each other in the first hour for both brine systems. This is considered as the period of continuous growth for vaterite which is then transformed at a slow rate to stable calcite at the same time. This is also shown as a period of steady state in the concentration of the total CaCO₃ produced per litre of solution. Equilibrium exists between the rate of transformation of vaterite and the rate of growth of calcite beyond one hour as shown for brine 1 in Figure 6-43. This appears as a period of steady state for the total concentration of CaCO₃ which could be subject to another slight rise due to further growth of the stable phase if the solution saturation allowed further growth. However, the overall reaction stops when the concentration difference in the solution and at the crystal surface is zero.

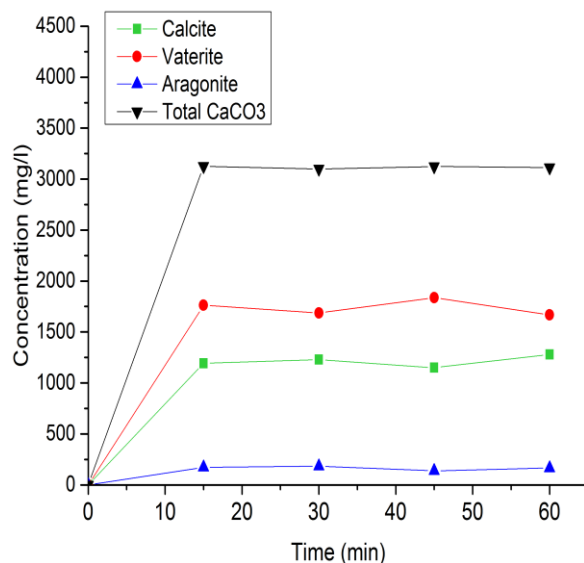


Figure 6-42 CaCO₃ polymorph concentrations in (mg/l) for brine 2 (0.065M) at 30° C and at different times

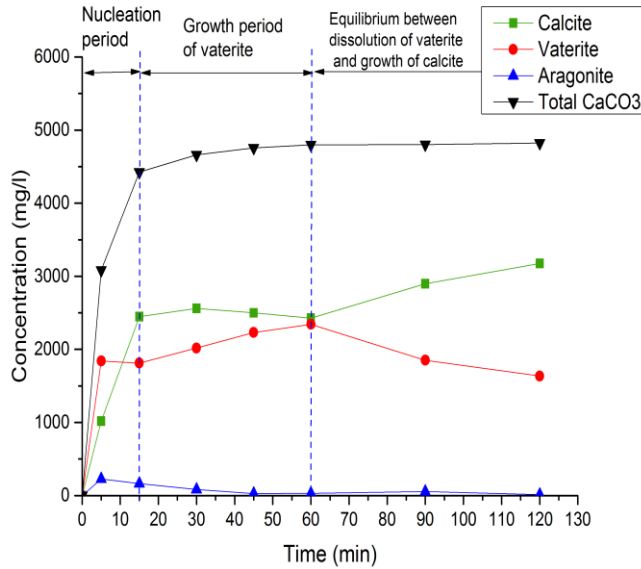


Figure 6-43 CaCO₃ polymorph concentrations in (mg/l) for brine 1 (0.1M) at 30° C and at different times

The assessment of polymorph abundance in the presence of an organic phase is illustrated in Figures 6-44 to 6-47. The mole percent of vaterite and calcite are about 70 and 30% respectively at 5 minutes for 23% oil-brine 2 (0.065M) as shown in Figure 6-44. Equal composition of phases requires about 60 minutes to reach and a complete transformation may require about 180 minutes at same rate. The change in vaterite composition and hence calcite composition is two times faster in the presence of oil than in the absence of oil by considering the slope of their abundance.

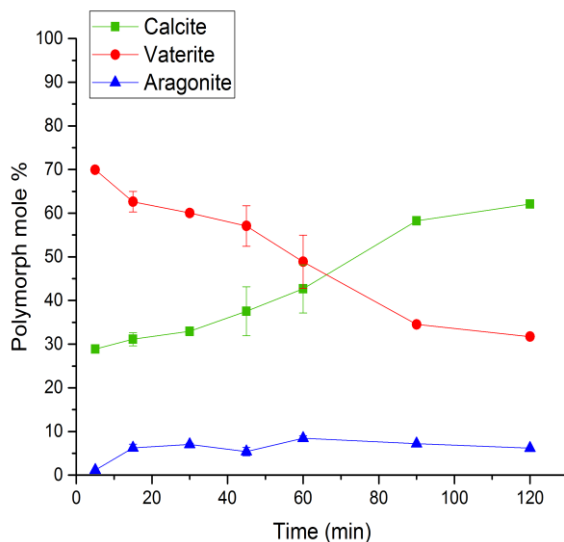


Figure 6-44 Polymorph abundance in the bulk solution for 23% oil-brine 2 (0.065M) at 30° C and at different times

The composition of vaterite and calcite is about 65 and 30% respectively at 5 minutes for 17% oil-brine 1 (0.1M) as shown in Figure 6-45. Brine 1 generally exhibits faster reaction

than brine 2 and a high rate of transformation is shown to exist within the first 15 minutes and an equal composition of both phases is achieved within this period. The transformation then slows down by a high degree once the compositions reach 30 and 70% for vaterite and calcite, respectively. The transformation is then continues with a very slow rate in the following 90 minutes.

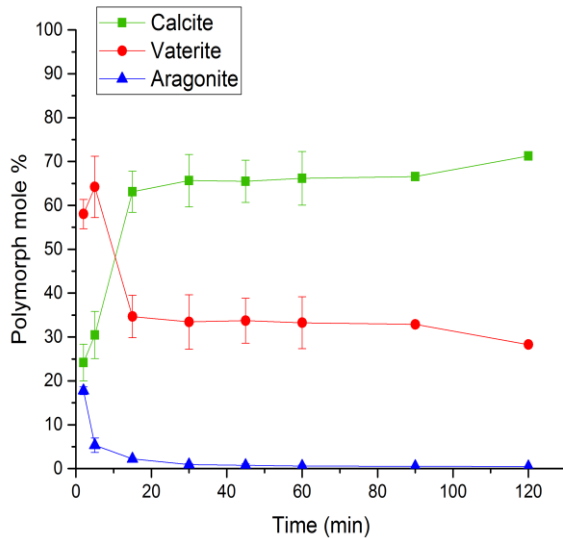


Figure 6-45 Polymorph abundance in the bulk solution for 17% oil-brine 1 (0.1M) at 30° C and different times

The concentration distribution of each polymorph in mg/l for 23% oil-brine 2 system in Figure 6-46 showed an increase in vaterite concentration within the first 15 minutes which is considered as the period of nucleation and growth. Transformation to the stable phase is also encountered during this period which resulted in an increase in the amount of calcite. A slow change in both vaterite and calcite concentration is shown after 15 minutes where calcite increased by a linear trend. This may be due to the growth of vaterite which is taking place simultaneously with the transformation to calcite.

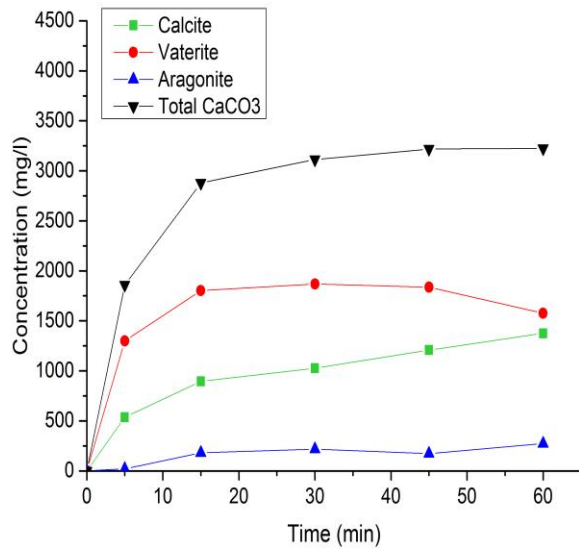


Figure 6-46 CaCO₃ polymorph concentration in (mg/l) for 23% oil-brine 2 (0.065M) at 30° C and different times

The higher saturation brine in Figure 6-47 showed an increase in vaterite concentration within the first 2 minutes which is considered as the period of nucleation. Transformation to a stable phase is also encountered during this period where calcite showed a clear increase in its presence after 15 minutes. This is due to further transformation of vaterite to calcite with the stopping of the vaterite nucleation process.

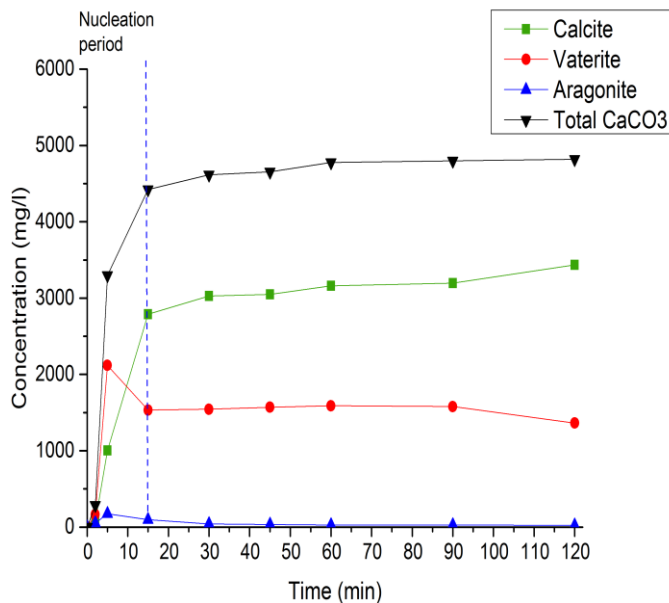


Figure 6-47 CaCO₃ polymorph concentration in (mg/l) for 17% oil-brine 1 (0.1M) at 60° C and different times

This results in a clear decrease in vaterite and a clear increase in calcite. The latter period is presented as a steady state in total CaCO₃ concentration where the transformation is very slow in this region. However, SEM images in the right side of 6-35 showed that vaterite had

less growth tendency in this case and this resulted in smaller calcite crystals when compared to the calcite in the oil-free system.

6.4.3.2 Assessment of precipitate polymorphic abundance and growth at 60° C

Figures 6-48 to 6-51 show the mole fractions and the concentrations of calcium carbonate crystalline phases that are formed in the bulk solution for oil-brine 3 (0.045M) at 60° C. Aragonite is known to be predominant at this temperature and its presence is combined with the presence of calcite and vaterite [51]. This is also confirmed by SEM in Figure 6-37 and XRD in Figure 6-39.

The distribution of phase fractions with time for brine 3 is shown in Figure 6-48. Initially vaterite was found as the predominant phase where it formed about 80 mole % of the total abundance at 2 minutes whereas aragonite and calcite were only about 15 and 5 mole%, respectively. The transformation at this temperature is considered to be from the metastable vaterite to aragonite which in turn transforms to the stable calcite. The nucleation of aragonite proceeded from the transformation of vaterite and was hence very fast as can be observed from the slope of the aragonite and vaterite fractions after 5 minutes. Aragonite is seen to reach a steady state beyond 15 minutes where it represents about 75% of the total fraction at 60 minutes. Calcite is also found to form during the first two minutes with very low abundance which represented about 5% of the phases. Calcite presence is increased with time where it represented about 20% of the phases at 60 minutes.

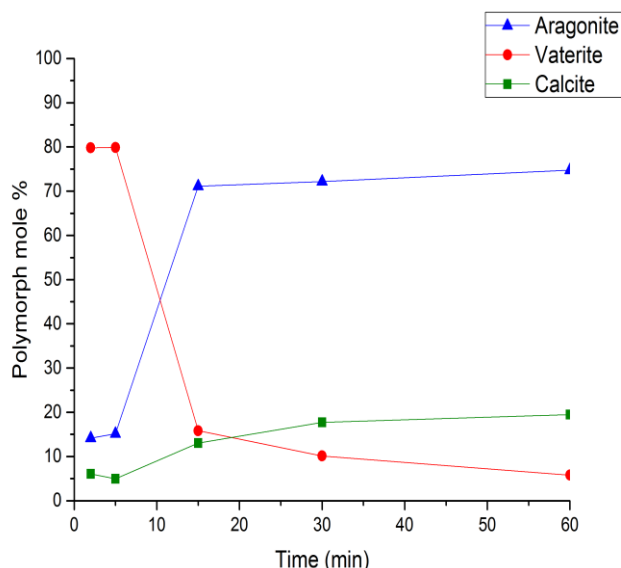


Figure 6-48 Polymorph abundance in the bulk solution for 0% oil-brine 3 (0.045M) at 60° C

Actually, it is not clear whether calcite was formed as a result of aragonite or vaterite transformation. However, the increase in calcite and the decrease in vaterite seemed to occur simultaneously beyond 15 minutes.

The change of the polymorphic concentration with time in Figure 6-49 illustrates the period of nucleation and growth for the three phases which seemed to take place within the first 5 minutes. This period was extended to 15 minutes for aragonite and calcite. In this region, the transformation of vaterite to aragonite was also taking place and this can be clearly observed by the clear decline in vaterite concentration after 5 minutes. Calcite seemed to increase slightly after 30 minutes and this is combined with a slight decrease in vaterite concentration in the same period.

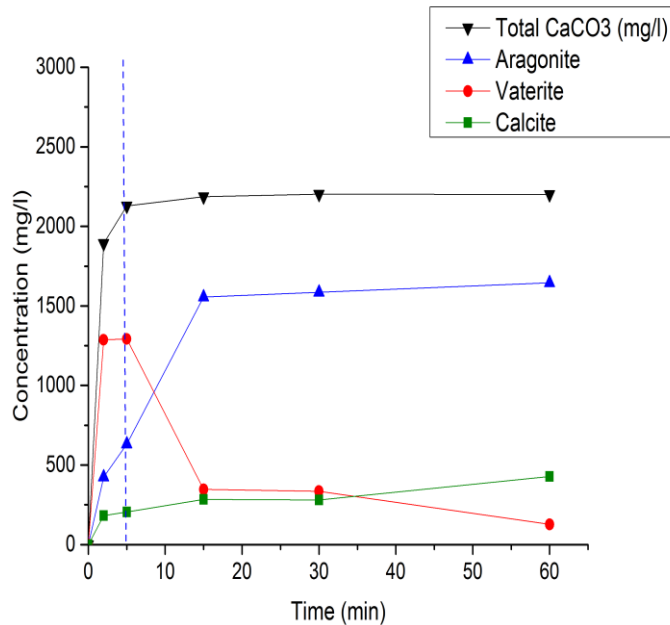


Figure 6-49 CaCO₃ polymorph concentration in (mg/l) for 0% oil-brine 3 (0.045M) at 60°C and different times

Combining the nucleation, the transformation and the growth processes to the total CaCO₃ concentration profile can lead us to consider the first 5 minutes to represent the period of nucleation and growth of vaterite which occurs simultaneously with its transformation. Therefore the nucleation and the growth of the other phases were as a consequence of the vaterite transformation process. Further transformation of vaterite to aragonite with the stopping of the vaterite formation resulted in an equilibrium between the rate of vaterite decline and the rate of aragonite increase and this is shown as a slight incline in the total CaCO₃ slope. The slight increase in the total CaCO₃ after 15 minutes is due to the growth of aragonite and the nucleation of calcite. The nucleation and growth of calcite are progressed very slowly and are combined with the decline in the vaterite concentration beyond 15 minutes. This may suggest that the formation of calcite is due to vaterite rather than aragonite transformation.

When the oil phase is introduced to the system the transformation from vaterite to aragonite seemed to exhibit differently as shown in Figures 6-50 and 6-51. Initially vaterite is found as

the predominant phase where it formed about 65 mole% of the total abundance at 2 minutes whereas aragonite and calcite were about 25 and 10 mole% respectively. The nucleation of aragonite proceeds with the transformation of vaterite and this process encountered periods of decline followed by steadiness until the composition of vaterite dropped to about 20% at 60 minutes as shown in Figure 6-50.

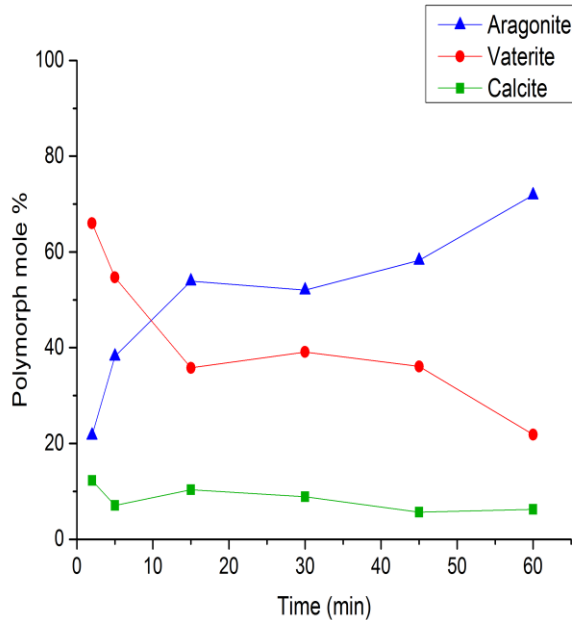


Figure 6-50 Polymorph abundance in the bulk solution for 23% oil-brine 3 (0.045M) at 60° C and different times

The concentration distribution in Figure 6-51 shows high vaterite concentration within first 2 minutes which is considered as a period of nucleation and growth of vaterite. Transformation to a stable phase is also encountered during this period as some aragonite and calcite also appeared within 2 minutes. Aragonite is showed a clear increase in its presence by 15 minutes. This is due to the high rate of transformation of vaterite to aragonite with continuous vaterite nucleation. This results in a steadiness in vaterite and an increase in aragonite polymorph at 15 minutes. Vaterite and aragonite then exhibit a region of steadiness followed by a slight increase in aragonite and decrease in vaterite. The last period showed a decline in the total CaCO_3 concentration which is theoretically unacceptable. The decrease in the total calcium carbonate detected results from the abnormal increase in pH in the presence of oil at 60° C as shown in Figure 6.17(b) which affected the saturation ratio calculations which calculated as shown in Table 6-5.

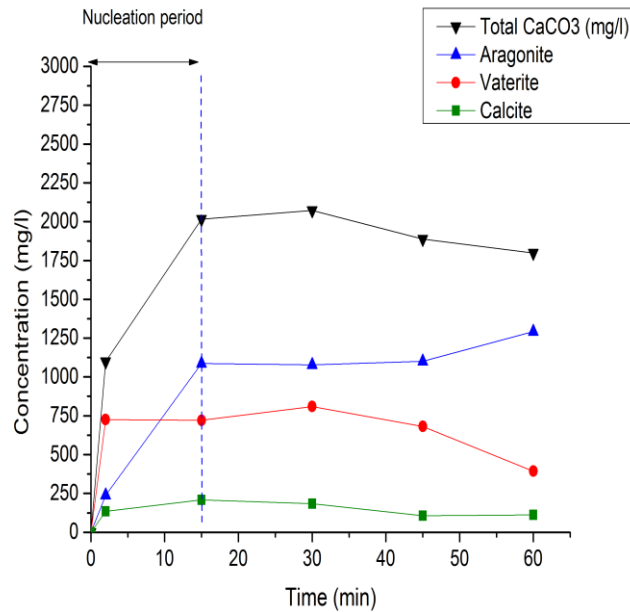


Figure 6-51 CaCO₃ polymorph concentration in (mg/l) for 23% oil-brine 3 (0.045M) at 60°C and different times

6.5 Concluding Remarks

- The pH measurement did not accurately measure the induction time for the system used in this study. This is most probably due to the high tendency for the brines to precipitate (high saturation brines). Also mixing of the phases with rotation speed of 520 rpm which is quite high and believed to promote and accelerate precipitation. Visual observations of the experiments ensure the existence of instantaneous precipitation for all the brines at both temperatures.
- Detection of the amount of calcium carbonate that is produced by measuring the amount of calcium remaining in the solution using inductively coupled plasma did not accurately represent the precipitation process. The amount of calcium that reacted or is consumed should be combined with the change in the solution pH to better represent the system.
- FBRM technique is used to track the nucleation and growth processes in the presence and absence of oil, to estimate mean particle size and distribution. Applying weighting methods can help in interpreting the FBRM data.
- Analysis of the polymorphic abundance and growth showed that the transformation from the metastable phase to stable phase at both temperatures is much faster in the early stages of the crystallization process. The transformation then slowed down when the process entered a long period where further transformation is expected.

7 Chapter Seven Discussion;

7.1 Introduction

The results in this thesis have covered aspects of surface deposition and bulk precipitation of calcium carbonate scale in the absence and presence of oil. The kinetics of the formation of scale has been followed and quantified and the transformation of the morphology of the scale has been studied. The new insights provided in this thesis are mainly around the effects of oil on all aspects of surface and bulk deposition and around the transformation of the polymorphs of calcium carbonate. Very little on these two subjects has been published in relation to oilfield scale. In this thesis chapter the results will be brought together, discussed in relation to the literature and the contribution that this work has made to the oilfield scaling field will be discussed.

7.1.1 Characterization of oil-water (brine) emulsions

In both the surface deposition tests and bulk crystallisation experiments the presence of oil complicates matters significantly. In a single phase system the situation is one where the surfaces in the solution are the seed crystals and the clusters of atoms in the early stages of nucleation. When there is oil phase present it is really important that the oil-water interface is described as this provides a different “surface” that can complicate matters in the determination of scale growth rates. In this section the emulsion properties are characterised.

An attempt to characterize the precipitation process in the presence of oil using Focused Beam Reflectance Measurement (FBRM) technique is presented in this study. This has not been reported previously in the literature and is a contribution made in this work. This has been achieved through estimation of the droplet mean chord length and the chord length distribution, the crystal mean chord length and the chord length distribution for an oil-free system and the particle (oil droplets and crystals) mean chord length and the chord length distribution for the oil-brine emulsion system.

A square weighting method was applied to approximate the chord length to the particle size where studies such as [191, 192] show that different chord weighting methods are found to correlate well with other sizing techniques for different systems. The agreement between square-weighted droplet chord counts with the density of droplets in the solution calculated based on the square-weighted mean droplet size is illustrated in Figure 6-6. This result led to suggested that the square-weighted mean droplet diameter and square-weighted droplet size distribution can reasonably represent the oil-in-water emulsion system. The square-weighted mean droplet diameter was found to be larger than the un-weighted one by about 3

to 4 times. Table 7-1 shows the difference between the number of droplets and the droplet density when calculated by the un-weighted and square-weighted methods for 23% oil content system at 60° C. The difference between the estimated values according to both methods changed the system characteristic and leads to better interpretation of the data as shown in Figure 6-6.

Table 7-1 Comparing the difference in the system characteristic as calculated by un-weighted and square-weighted mean droplet diameter

	Un-weighted	Square-weighted
Mean droplet diameter (µm)	27.45	78.62
Volume of a droplet (m³)	1.082×10 ⁻¹⁴	2.543×10 ⁻¹³
Number of droplets	3.88×10 ¹⁰	1.65×10 ⁰⁹
Droplets density/ 1ml of solution	27,715,060	1,179,620

However, many studies show that FBRM undersizes the droplets [192, 209, 210]. For oil in water emulsions, El-Hamouz et al. [209] compared FBRM mean chord length with mean droplet size detected by laser diffraction while Khatibi [210] compared FBRM chord length distribution (CLD) with droplet size distribution (DSD) measured by particle video microscope (PVM) technology. Both found that FBRM under-sizes large droplets, whereas [209, 211] found that it also overestimates small particles. It was claimed by [192] that FBRM can detect the change in the droplet size distribution with time but cannot measure the exact size of the droplets. They attributed this to the smooth exterior surface of the droplets as opposed to solid particles. According to Heath et al. [191] square-weighted CLD for a spherical particles correlate closer to the particle size distribution than un-weighted CLD. They applied different weighting methods to FBRM and compared them to laser diffraction as shown in Figure 7-1.

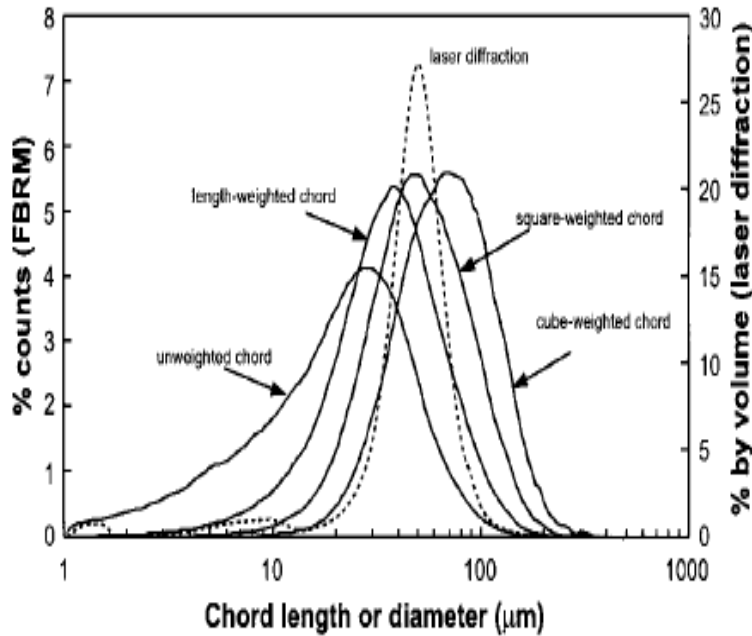


Figure 7-1 Comparison of different FBRM weighting methods of chord length distribution for aluminium particles (sieved 45-53 μm) to laser diffraction volume-weighted distribution [191]

Interpreting FBRM data when the system is encountering precipitation means it shows an increase in the intensity of particles for the large chord length channels of 10-23 and 29-86 μm which is considered as a growth events. This occurred simultaneously with an increase in the intensity of small chord length channels of 1-5 μm which are considered as a nucleation event as shown in Figures 6-18 and 6-19. The simultaneous nucleation and growth events are found to persist throughout all the experiment time of 1 hour in the oil-free system at 30° C whereas these events only occur up to about 25 minutes (1500 s) for the system with oil at 30° C. The situation is different at 60° C where the nucleation event is found to persist to about 40 minutes (2500 s) for the oil-free system whereas the growth event is found to cease by about 16 minutes (1000 s) as shown in Figure 6-26. The oil system at 60° C showed less nucleation events with high growth tendency as shown in Figure 6-27. A possible explanation of this is when the precipitated particles increase in size, the probability of detecting the edges of the randomly shaped particles becomes higher and hence affects the measurements by increasing the small chord size counts. This could be more easily observed in oil-free system than in oil-systems in which a considerable amount of crystals have appeared at the oil-water interface and this results in a more regular shape as the crystals are supposed to form at the droplet surface and retain the overall droplet shape. The difference in the nature of the crystals formed between 30 and 60° C may also affect the measurements; SEM images at 30° C showed the agglomeration of vaterite to form a cauliflower shape of an average size of about 15 μm for brine 2 (0.065M) at 60 minutes as shown in Table 6-6. The mean chord length detected for the precipitate at 60

minutes is 21 μm (un-weighted) as shown in Table 7-2. The precipitate at 60° C showed needle-like aragonite of a high aspect ratio which emerged from a central point forming an aggregate as shown in Figure 6-37. The shape of the aragonite and the existence of gaps between the aragonite needles which form the aggregate increase the probability of the detection of the width of the needle aragonite rather than the length of the needle. This may give rise to small chord length counts (nucleation) much more than large chord counts (growth) at 60° C as shown in Figure 6.26. However, in a study [20] which used FBRM technique for tracking nucleation and growth kinetics using polystyrene spheres in suspension; the growth process was studied by adding the same number of different sizes of polystyrene micro-particles separately in an ascending order in which particles were removed after measurement and replaced with the next size particles. It was found that the total number of chord counts increased due to the increase in small chord length counts when large particles were added although the number of particles remained the same. It was concluded that the number of particles does not give a good approximation to the number of chord lengths when the system exhibits a significant change in size. According to the same study, square-weighted mean chord lengths were found to track the changes in the average particle size reasonably. This suggests that the small chord length is not necessary translated as a nucleation event. The crystals morphology is also found as an important factor which may enhance or diminish this effect. According to this it may be expected that the system is better represented at 30° C than at 60°C using FBRM.

Table 7-2 summarizes the different mean chord length detected by applying weighting methods to the different systems at 30°C; 10% oil droplets (no precipitate), crystals that precipitated (no oil droplets) and when the precipitation occurs in the presence of 10% oil content (crystals and oil droplets). This may help in detecting which is the best method to rely on for each system (values in bold). The calculation of weighted mean size for the different systems is shown in Table A-1 in appendix A-2.

Table 7-2 Applying weighting methods to the mean particle size for 10% oil-brine emulsion at 30° C

System	Unweighted mean size (μm)	Square-weighted mean size (μm)
Oil droplets	27	68
Crystals	21	62
Particles (oil droplets and crystals)	25	46

As discussed previously the square-weighted method represents the mean droplet size reasonably. The un-weighted crystal size is much similar to the crystal size estimated using SEM than square-weight one and it is considered to represent the crystals in oil-free system. When the system contains both oil droplets and crystal particles a higher intensity for the large particle size of the range of 29-86 μm was detected over the other sizes for the 10% oil-brine system as shown in Figure 6-19. Moreover, the existence of similar distribution between the system containing only oil droplets and the system which precipitates in the presence of oil as shown in Figures 6-23 and 6-24, and the reduction of the total chord counts by 1 to 1.5 times when the oil droplets are removed from the total counts of the particles as shown in Figure 6.25, indicate that most of the colloids that exist in the system are closer in size to the oil droplets rather than to the crystals size. That means the counts for the oil droplets are higher than the counts for the crystals in the bulk solution. All of these support the application of the square-weighted method to the chord length distribution for oil-brine systems at 30° C.

However, this could not eliminate the expectation that some of the crystals may nucleate at the oil-water interface via heterogeneous type nucleation. Visual observations of the experiments of this study have shown evidence for a Pickering emulsion when mixing stops. These stabilized emulsions existed at different degrees of stabilization which mainly depends on the initial pH of the solution. High initial pH of 9 or above is found to stabilise the emulsion where a homogeneous layer of relatively small droplets are formed as shown on the right side of Figure 7.2. Lower initial pH of 8 (the experiment condition) showed droplets of various sizes which accumulated at the oil-water interface and sometimes diffused up into the upper oil layer as shown on the left side of Figure 7.2. Some camera and microscopic images for the Pickering emulsions are illustrated in appendix D.

The formation of the crystals at the surface of the oil droplets may retain the size of the oil droplets but may affect the oil droplet roughness and slightly increase the droplet size. This is difficult to isolate from other changes unless complete inhibition of the crystals formed in the bulk solution is achieved. In a study conducted by [212] using FBRM, the crystallization of water-in-oil emulsions into gas hydrates showed that the hydrate crystallization does not affect the size of the water droplets. Zhang et al. [41] using a glass-micromodel device observed the nucleation of CaCO_3 downstream of gas bubbles whereas no nucleation was observed in the absence of the gas bubbles. They claimed that the existence of a gas-water interface acted as a high energy surface where heterogeneous nucleation took place.

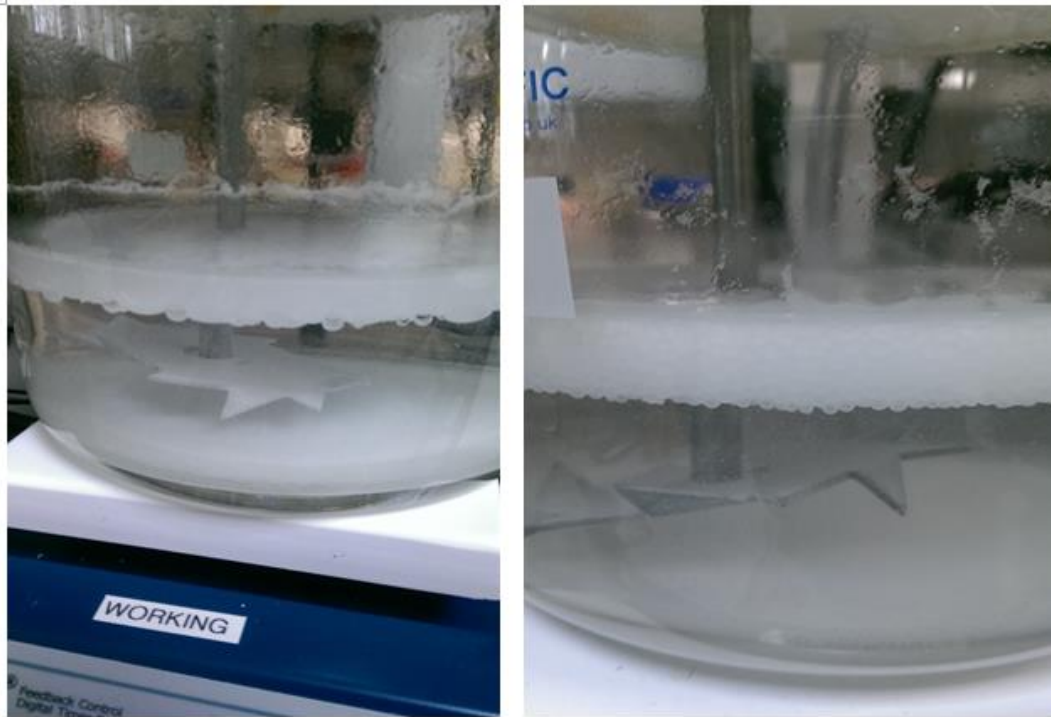


Figure 7-2 Varied behaviour of the colloidal system is shown when mixing stops; LHS, un-stabilized emulsion layer; RHS, stabilized emulsion layer

Figure 7-3 highlights the impact of oil-in-water emulsions on calcium carbonate precipitation at 30° C. The increase in the interfacial area with oil content minimizes the rate of calcium carbonate formed in the bulk solution by homogeneous type nucleation. The number of crystals that are formed when removing the oil droplets has shown a clear decline; the oil-free system exhibits a higher precipitation rate than the 10% O/W emulsion system which in turn exhibits higher precipitation than the 17% O/W emulsion system. This suggests that adding the oil droplets has decreased the potential of scale formation by reducing the number of crystals that are formed in the bulk solution according to homogeneous nucleation. On the other hand, this did not show whether the existence of an extra surface (oil droplets) has promoted the heterogeneous type nucleation as in this case the number of counts may stay constant to the oil droplet counts despite the crystals that are formed at the interface.

A better way to address the impact of the oil droplets on the scale formation in the bulk solution could be through the estimation of the de-supersaturation profile and the total amount of calcium carbonate formed in the system by both homogeneous and heterogeneous type of nucleation.

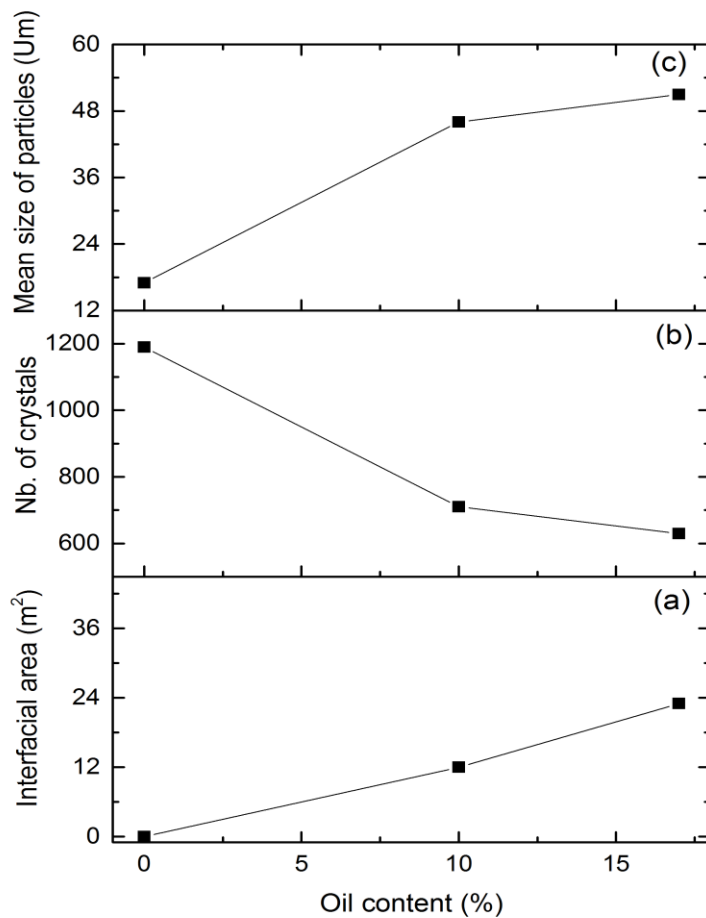


Figure 7-3 Effect of O/W emulsion on calcium carbonate scaling process at 30° C; (a) the impact of interfacial tension (b) the impact on total number of calcium carbonate crystals in bulk solution at 60 minutes; (c) the impact on mean particle size at 60 minutes

Table 7-3 summarizes the different mean chord length detected by applying weighting methods to the different systems at 60°C; 10% oil droplets (no precipitate), crystals that precipitated (no oil droplets) and when the precipitation occurs in the presence of 10% oil content (crystals and oil droplets). This may help in detecting which is the best method to rely on for each system (values in bold). The calculation of weighted mean size for the different systems is shown in Table A-2 in appendix A-2.

Table 7-3 Applying weighting methods to the mean particle size for 10% oil-brine emulsion at 60° C

System	Unweighted mean size (µm)	Square-weighted mean size (µm)
Oil droplets	29	65
Crystals	18	95
Particles (oil droplets and crystals)	32	74

The square-weighted mean chord lengths for both the crystals formed in the oil-free system and for the particles (oil droplets and crystals) are higher than the square-weighted mean chord length for the oil droplets. These high values can only reflect the agglomeration effect of the crystals at 60° C where applying weighting methods in this case gave rise to large particles among the small ones and this is clearly observed in Figures 6-31 and 6-32. The total chord counts are reduced by up to 30% when removing the oil counts from the oil-brine systems as shown in Figure 6-33. This suggests that the crystal counts are much higher than the droplet counts and hence the crystals are mainly formed in the bulk solution by homogeneous type nucleation. However the agglomeration of particles was also visually observed in the FBRM experiments at 60° C and is attributed to the change in the conditions of the experiments. According to this we may consider that the mean particle size and particle size distribution may be best represented by square-weighted methods at 60° C.

7.1.2 Comparing the pH and the free calcium ions in solution during the precipitation process

Conflicting behaviour for the precipitation progress between systems with and without oil has been detected as shown in Figures 7-4 and 7-5. The drop in pH is higher for the oil-free system than for the oil systems which indicate a higher reaction rate exists in the oil-free system compared to the oil systems. On the other hand, the amount of unreacted calcium is higher in oil-free system and this indicates a lower reaction rate compared to that in oil systems. Since the crystallization process consists of different stages; nucleation and growth stages where the energy required to grow a crystal after being formed is less than that required to form a new crystal in the bulk solution according to classic nucleation theory [30], it is expected that the drop in both the pH and the calcium ions in solution is much higher in the beginning of the crystallization process than later. The left images of Figures 7-4 and 7-5 show the high drop in pH during the first 5 and 15 minutes of the reaction for brine 3 at 60° C and brine 1 at 30° C, respectively. The drop in pH is then slowed down and a steady state to a slight increase in pH value is exhibited after about 15 and 30 minutes for the same brines, respectively. This high drop in pH in the early stage is an indication of the nucleation process. This is also supported by turbidity measurements for oil-free system in Figure 6-7 and the visual observation where a high degree of cloudiness for both the brines with and without the oil is observed straight after mixing the brines (instantaneous nucleation). However the change in calcium ion concentrations as detected using ICP did not support this theory. The drop in calcium concentrations display a progressive trend with lower drop detected initially and higher drop toward the end of experiment. This behaviour is less observed in the case of oil-brine 3 (0.045M) system at 60° C as shown on the right side of Figure 7-5. The explanation of why the ICP results did not support the other methods is

because of the procedure of quenching the sample before having it filtered. As the sample contains some crystals of calcium carbonate and the quench solution contains a chemical inhibitor, having the sample to be immediately quenched after sampling may dissolve the crystals. The procedure should be by filtering the sample from any crystals presence before having it quenched.

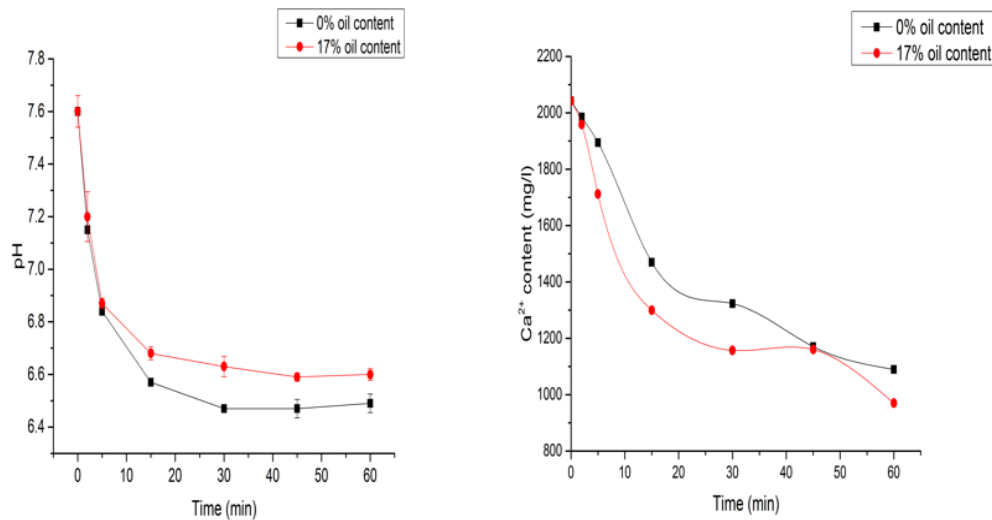


Figure 7-4 Comparing the reaction progress for oil-brine 1 at 30° C (0.1M) using two different techniques; LHS: by normal drift of pH during the reaction; RHS: by measuring the amount of unreacted calcium using ICP

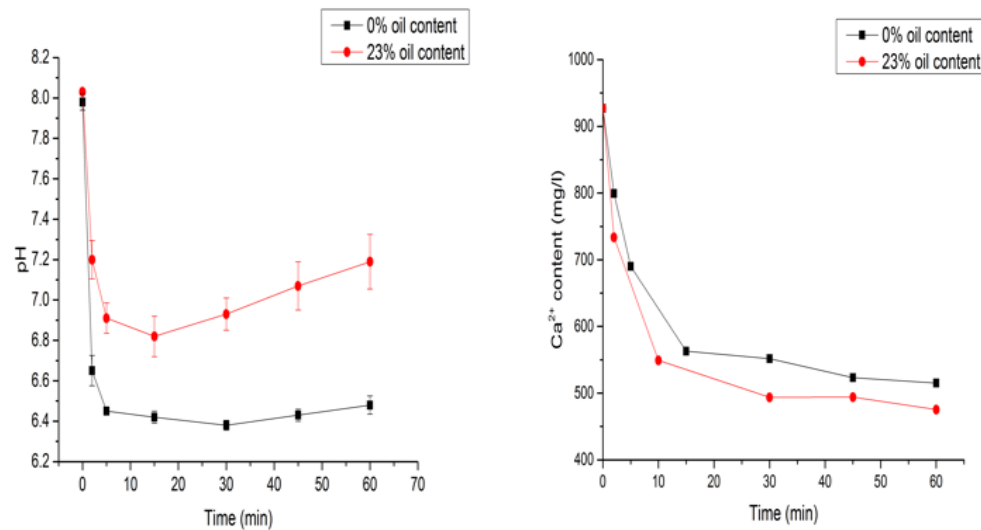


Figure 7-5 Comparing the reaction progress for oil-brine 3 (0.045M) at 60° C using two different technique; LHS, by normal drift of pH during the reaction; RHS, by measuring the amount of unreacted calcium using ICP

The amount of calcium carbonate produced is different between the measured calcium ions and the calculated from the supersaturation dependence on the pH as shown in Figures 6-13 and 6-14. Calcium carbonate is well known to exhibit different stages in which transformation from one polymorph to another is exhibited with time. This polymorphic

transformation is known to take place through dissolution and re-crystallization processes; vaterite is transformed to calcite via the dissolution of vaterite and the nucleation and growth of calcite [48, 68, 69]. Vaterite to aragonite and aragonite to calcite transformation is shown to transform via similar processes by [51]. Moreover, the dissolution and the re-crystallization processes are also found to be the case for ACC transformation to the different crystalline phases [49, 50, 77, 213]. According to this, calcium and carbonate ions are supposed to return to the solution during the dissolution process [69]. This may cause an increase in the concentration of calcium ions and the alkalinity of the solution and hence the increase in the pH due to the release of carbonate ions in the solution. Kralj et al. [73] followed the progress of the vaterite dissolution process by recording the pH as a function of time at temperatures ranging between 15 and 45° C. They found that pH is increased initially before it stabilises as shown in Figure 7-5. The increase in pH may not be observable because the dissolution process is usually accompanied by the nucleation and growth processes. These processes are usually more intense during the early stages of the precipitation process where they are supposed to cause a decline in the pH of the solution and thus eliminate the rise in pH due to the dissolution process. This may explain the slight increase in pH after a period of decline and steadiness in the later stages of the precipitation process as shown in chapter 6, section 6.2.2. This most probably is a result of the continuous dissolution processes as further transformation from the less stable to the more stable phase takes place. According to all of these, estimating the amount of calcium carbonate formed cannot be isolated from the effect of pH on the solubility and hence the solution supersaturation.

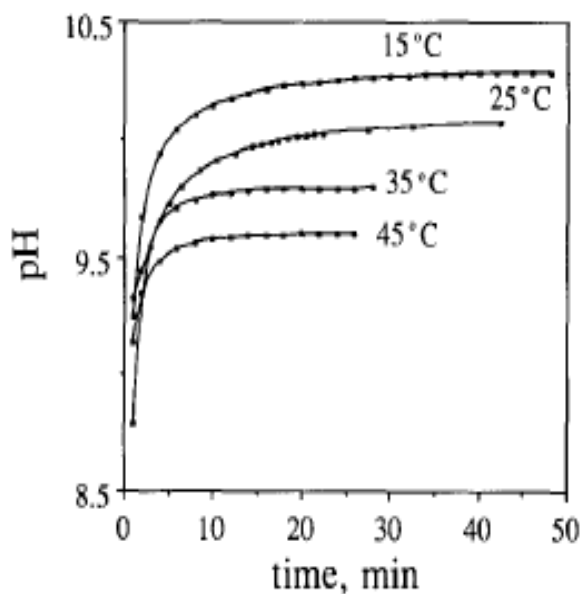


Figure 7-5 The change in pH during the dissolution process of vaterite at different temperatures [73]

In this study the molar concentrations of calcium and carbonate ions were estimated with the aid of MultiScale™ software. The activity coefficients of various species in the solution and

the saturation ratios are calculated by taking into account the change in pH with time. This can be considered as a correction for the effect of pH on the precipitation concentration. The calculation of calcium carbonate produced based on this correction is shown in Tables 6-2 to 6-5.

7.1.3 The kinetics of CaCO₃ surface deposition and bulk precipitation

The results show that surface fouling is reduced in the presence of an organic phase. The reduction reaches 90% for oil content up to 70% at 30° C. At high oil fractions the cleaner surfaces may be due to the surface being wetted by the oil phase which most probably prevents the scaling species to deposit on the surface. The presence of oil may not only wet the surface but also may act as a barrier for scaling species to transfer from the bulk solution and move to the surface. This may lead to low nucleation rate at the surface where with more oil, there are less nucleation sites and the larger the crystals are as shown in Figures 5-7 and 5-8.

The existence of different CaCO₃ phases as early as 1 minute is an indication of not only the fast nucleation reaction on the surface (low induction time) but also an indication of the fast transformation to a more stable species. Actually it is not clear whether the initial formation of the more stable phase with relatively high abundance is as a consequence of a rapid transformation of the metastable phase or it is just formed directly from the amorphous calcium carbonate ACC state. Although the latter contradicts the Ostwald's rule of stages [214] which states that a substance may exist in two or more solid phases with different stabilities where the unstable phase tends to transform to a stable phase through a metastable one, it was reported in the literature under some conditions that the more stable phase can be formed directly from ACC without a metastable precursor [63]. However, due to the low induction time for both the brines which is less than 1 minute, it is difficult to characterize the initial stage of the crystallization process and detect which is the first phase to form and what order the transformation takes.

The transformation of vaterite to calcite is known to occur by two kinetic processes; (i) the dissolution of vaterite (ii) the growth of calcite. The transformation process is controlled by the process which is slower. Assessment of the polymorphic mass growth in Figures 5-25 and 5-26 indicate the control of calcite growth in the oil-free system. The total mass growth of CaCO₃ follows the calcite growth profile where the dissolution of vaterite and hence the transformation to calcite seems to occur rapidly. However crystals usually dissolve much faster than they grow [215]. Converting the polymorphic mass growth to thickness in (μm) by dividing the polymorphic mass in (mg/cm^2) by both the polymorphic density and surface

coverage is shown in Figure 7.6. The densities of vaterite and calcite are taken as 2645 and 2710 mg/cm³ [216], respectively.

The thickness growth profiles for vaterite and calcite are shown in Figure 7-6. The profiles follow a polynomial growth function for the first 20 minutes as shown in Figure 7-6(b). The polymorphic growth fitted function is shown in Table 7-4 and the slope of the curves in the early stages of the deposition process represents the polymorphic growth rate constants which are shown in Table 7-5. The polymorphic growth rate constant decreases with time and this ensures the faster kinetics is taken place in the early stages of the process. The growth rates reduces by about 15% within the first 10 minutes for calcite whereas the vaterite growth reduction reaches to 75% within the same period of time.

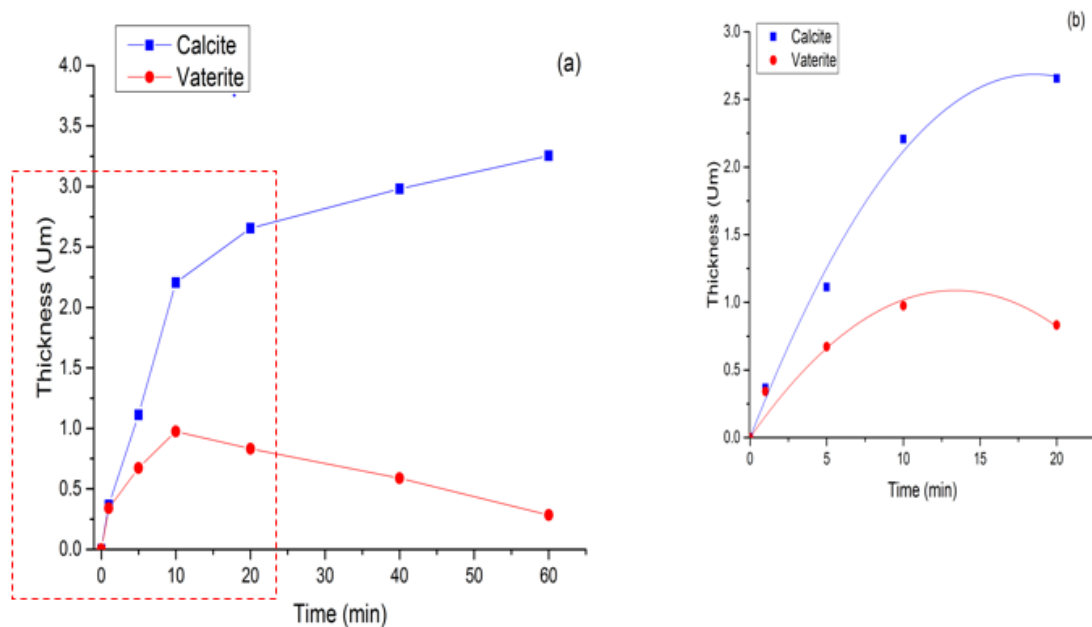


Figure 7-6 Polymorphic thickness versus time for brine 2 (0.065M) at 30° C; (a) calcite and vaterite thickness (µm), (b) curve fitting at an early stage of the crystallization process

Table 7-4 The growth profile fitted function for brine 2 (0.065M) at 30° C

Polymorph	Second order polynomial, $y = B_1x + B_2x^2$		
	Slope, $\frac{dy}{dx} = B_1 + 2B_2x$		
	B_1	B_2	R^2
Vaterite	0.1626	-0.0061	0.942
Calcite	0.2899	-0.0078	0.993

Table 7-5 The polymorphic growth constants in the early stages of the deposition process for brine 2(0.065M) at 30° C

Growth rate constant		Vaterite		Calcite	
Time (min)	$\mu\text{m}/\text{min}$	m/ sec	$\mu\text{m}/\text{min}$	m/ sec	
1	0.1504	2.51×10^{-9}	0.2743	4.57×10^{-9}	
5	0.1016	1.69×10^{-9}	0.2119	3.53×10^{-9}	
10	0.0406	6.76×10^{-10}	0.1339	2.23×10^{-9}	

The polymorphic growth rate constants are also estimated for brine 4 (0.06M) at 40° C, where it is found to obey an exponential function in which the reaction is very fast and decay rapidly within the first 5 minute as shown in Table B-2 in appendix B-1. According to this rapid reaction at 40° C, the growth rate constants are only considered at the first minute and the activation energy for vaterite and calcite growth is calculated using the Arrhenius equation 2.57 at both temperatures as shown in Table 7-6.

Table 7-6 The growth rate constants at 30 and 40° C and the growth activation energy for oil-free systems

polymorph	Growth rate constant (m/sec)		Growth activation energy (kJ/mol)
	30° C	40° C	
Vaterite	2.51×10^{-9}	9.03×10^{-9}	101.06
Calcite	4.57×10^{-9}	1.711×10^{-8}	104.04

Kralj et al. [68, 72] studied the individual rate for vaterite growth and calcite growth independently. Vaterite growth rate was found to follow a parabolic trend and the growth rate constant was 5.6×10^{-10} m/s at 25° C and 1.25×10^{-9} m/s at 33.8° C and the activation energy was 57 kJ/mol. The growth of calcite was found to follow a parabolic trend and the growth rate constant was 5×10^{-10} m/s at 25° C and 1.2×10^{-9} m/s at 35° C and the activation energy was 55 kJ/mol. They showed that the growth rate of calcite is lower than the growth rate of vaterite and according to this calcite growth is considered as the rate determining step for the transformation of vaterite to calcite. Andreassen et al. [206] studied vaterite growth rate by a seeded-batch precipitation process. The growth rate constant of vaterite was found as 5.27×10^{-10} m/s at 25° C and 1.98×10^{-9} m/s at 40° C, resulting in an activation energy of 68 ± 3 kJ/mol. Rodriguez-Blanco et al. [69] showed that the activation energy for calcite growth is

66 ± 2 kJ/mol, they suggested that this range of activation energy is for surface-controlled reactions.

To determine the activation energy for vaterite transformation to calcite, the fraction of vaterite (α) which is transformed to calcite at 30° C and 40°C is fitted into different models using model-fitting method of solid-state kinetics as shown in Tables B-5 and B-6 and Figures B-4 and B-5 in appendix B-2. The activation energy and the frequency factor can then be determined using the Arrhenius equation 2.57. It is difficult to choose which model represents the system by this method as all the models show relatively good fits [79]. An elimination of some models is done based on the shape of α -time curve. This curve showed a slowing trend in which the reaction rate decreases with the progress of the conversion as shown in Figure B-3 in the appendix. The range of the activation energy could then be estimated based on some selected models which also showed best fit to the data at both temperatures as shown in Tables B-9 in appendix B-2. The activation energy for the transformation of vaterite to calcite is found to be about ≈ 11 -22 kJ /mol for oil-free system. Kralj et al. [73] studied the dissolution of vaterite at temperatures between 15 and 45° C and found the activation energy of vaterite dissolution is 24 kJ/mol. They suggested that this range of activation energy supports the diffusion of the hydrated calcium and carbonate ions away from the crystal surface to be the rate determining step.

The activation energy for calcite growth which is shown to be 104 kJ/mol is much higher than the activation energy require for the dissolution process which is estimated to be in the range of 11-22 kJ/mol. This confirms the rapid dissolution process of vaterite and the slow growth process of calcite which is considered to control the process in this case. The rapid dissolution rate of vaterite and the slow growth rate of calcite are also confirmed by many other studies such as [67, 69]. During the dissolution process, calcium and carbonate ions are supposed to return to the solution [69], therefore vaterite is suggested to dissolve and return to the solution as Ca^{2+} and CO_3^{2-} by a fast process. This explains the low levels of vaterite during the crystallization process which is then re-crystallized to calcite as the solution in this case is saturated with respect to vaterite and supersaturated with respect to calcite [69, 202]. Since the process of calcite nucleation is slow, the Ca^{2+} and CO_3^{2-} ions may have sufficient time to move nearby and nucleate independently to calcite in the vicinity of its mother phase which is vaterite. This results in a spread of calcite nucleation sites with time which means calcite occupies a large surface area with small crystals and this is also confirmed by SEM in the left side of Figures 5-9 and 5-10 and the change in the slope of the total mass gain beyond 10 minutes is due to the re-nucleation of calcite as shown in Figures 5-25 and 5-26. The hypothesis regarding the formation and transformation of CaCO_3 in oil-free system is illustrated in Figure 7-7.

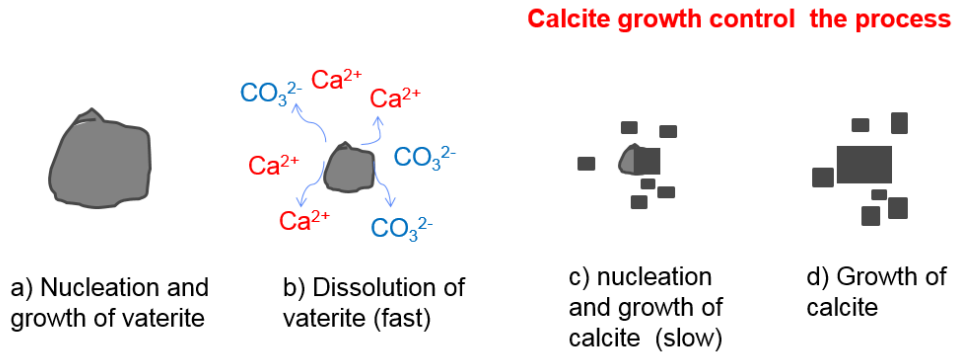


Figure 7-7 The hypothesis of surface crystallization kinetics for oil-free system at 30° C; Calcite growth controls the transformation process

The decrease in crystal population when vaterite is converted to calcite as shown in Figure 5-12 (b) and (c) and the existence of a variety of sizes of calcite crystals as shown in Figure 5-12 (c) may also suggest the existence of the joint effect of Ostwald ripening and particle size-solubility methods. The first states that there is a tendency for smaller particles to dissolve and the solute to settle down on the larger particles and this causes a further growth of the larger particles. The second method states as the small particles dissolve, the ratio of the surface area to the volume becomes larger and hence it exhibits higher surface free energy and hence a rapid transformation rate. This was also reported by [217] for a surface-controlled nucleation and growth processes of AgCl and AgBr crystals at 70°C. According to this study as the material is transported away from the surface (vaterite surface in this case), it leads to a decrease in the crystals size for a fraction of crystals and when the crystals size become less than the critical size required to grow, it dissolves and results in an overall decrease in the number of crystals.

The situation is different when adding an oil phase at 30° C; it is shown in Figure 5-29 that both vaterite and calcite mass gain increases in parallel to each other in a gradual manner. This gradual increase of calcite is due to the covering of vaterite with the newly formed calcite. This results in an increase in the surface area of the growing calcite with the progress of the transformation process [202]. The slow change in the composition of vaterite and calcite is most probably due to the slow dissolution process of vaterite which could be considered as the rate determining step in this case. According to [217] when the diffusion from or to the surface of a crystal controls the growth process (vaterite in this case), the dissolution process will retard and the number of crystals remains constant.

Figure 7-8 presents the polymorphic thickness (μm) at different times for the system with oil. The polymorphic profiles follow an exponential growth function for the first 20 minutes as shown in Figure 7-8(b). The polymorphic growth fitted function and the polymorphic growth rate constants are shown in Table 7-7 and Table 7-8, respectively. The growth rate

constants are reduced by about 90 and 75% within the first 10 minutes for vaterite and calcite, respectively.

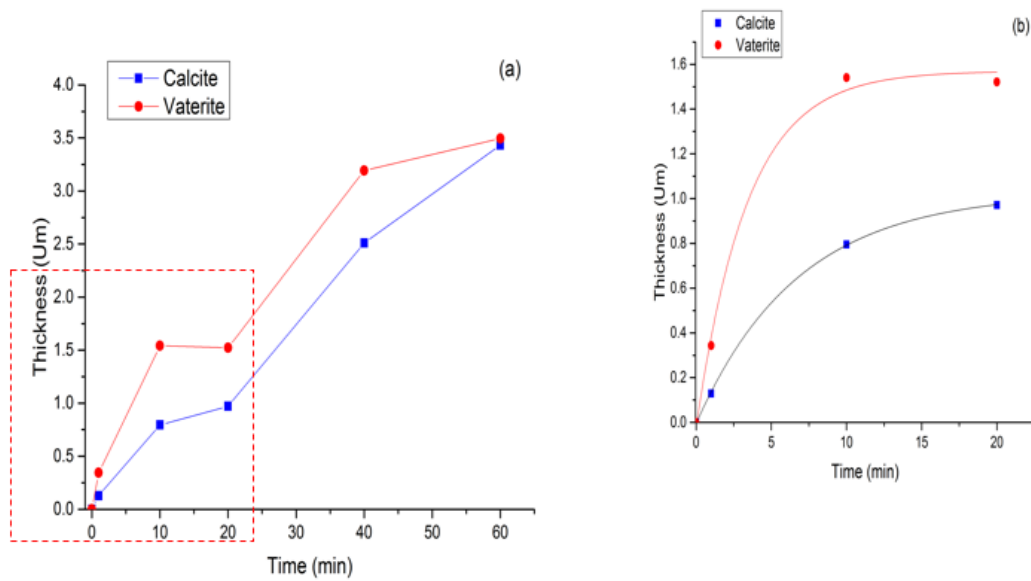


Figure 7-8 Polymorphic thickness versus time for 23% oil-brine 2 (0.065M) at 30° C; (a) calcite and vaterite thickness (µm), (b) the slope of curves at an early stage of the crystallization process

Table 7-7 The growth profile fitted function for 23% oil-brine 2 (0.065M) at 30° C

Polymorph	Exponential function, $y = A_1 - A_2 \exp(-kx)$			
	A_1	A_2	k	R^2
Vaterite	1.56957	1.59405	0.2931	0.996
Calcite	1.02623	1.03183	0.1482	0.999

Table 7-8 The polymorphic growth constants in the early stages of the deposition process for 23% oil-brine 2(0.065M) at 30° C

Growth rate constant	Vaterite		Calcite	
	µm/ min	m/ sec	µm/ min	m/ sec
Time (min)				
1	0.3485	5.81×10^{-9}	0.1318	2.19×10^{-9}
5	0.1079	1.79×10^{-9}	0.0729	1.21×10^{-9}
10	0.0249	4.15×10^{-10}	0.0347	5.79×10^{-10}

The polymorphic growth rate constants are also estimated for 23% oil-brine 4 (0.06M) at 40° C, where it is also found to obey an exponential function in which the growth is very fast and decay by about 95% within the first 10 minute as shown in Table B-4 in appendix B-1. According to this rapid process at 40° C, the growth rate constants are only considered for the first minute and the activation energy for vaterite and calcite growth is calculated using the Arrhenius equation 2.57 at both temperatures as shown in Table 7-9

Table 7-9 The growth rate constants at 30 and 40° C and the growth activation energy for oil systems

polymorph	Growth rate constant (m/sec)		Growth activation energy (kJ/mol)
	30° C	40° C	
Vaterite	5.81×10^{-9}	9.28×10^{-9}	36.98
Calcite	2.19×10^{-9}	8.751×10^{-9}	108.96

The activation energy for vaterite transformation to calcite is estimated according to the same method used in the oil-free system. The fraction of vaterite (α) which is transformed to calcite at 30° C and 40°C is fitted into different models as shown in Tables B-7 and B-8 and Figures B-6 and B-7 in appendix B-2. The range of activation energy could then be estimated based on some selected models which also showed best fit to the data at both temperatures as shown in Table B-10 in the appendix. Oil systems show much higher activation energy for the transformation where it found to range about ≈ 87 -107 kJ/mol.

The activation energy for calcite growth process is estimated to be 109 kJ/mol whereas the activation energy for the dissolution from vaterite to calcite is found to range between 87 and 107 kJ/mol. This high value for the transformation process confirms the slower dissolution process of vaterite growth process and therefore the vaterite dissolution process controls the oil/water system. It has to be mentioned here that these values are an approximation for the range of activation energy detected for both systems. More accurate values could be achieved under a range of isothermal conditions at different temperatures where the system exhibits conversion from vaterite to calcite but needs to avoid any aragonite formation and hence better represented at temperatures $\leq 30^\circ$ C. Model-free methods can also be used under a varied isothermal temperatures to estimate the activation energy. Khawam and Flanagan [218] have proposed a complementary approach that uses both model-free and model-fitting methods for kinetic data analysis. This approach utilizes a model-free method to obtain the activation energy and a model-fitting method to estimate the activation energy for different models. The most accurate model is chosen to be the one which produces an activation energy closest to that detected from the model-free analysis.

Therefore, Ca^{2+} and CO_3^{2-} ions that are released to the solution by a slow process may have not had sufficient time to move away from the mother phase which is vaterite. They may recrystallize as calcite at the surface of vaterite which then is subjected to further growth in size. As a result of this, calcite crystals grow with roughened surfaces which then become smooth when all vaterite is converted to calcite. This is also confirmed by SEM in the right side of Figures 5.9 and 5-10. The hypothesis regarding the formation and transformation of CaCO_3 in oil containing systems is illustrated in Figure 7-9.

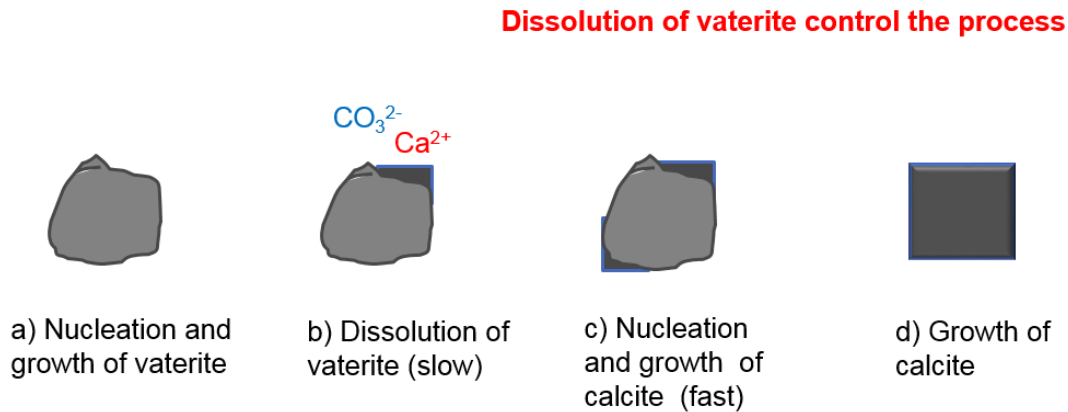


Figure 7-9 The hypothesis of surface crystallization kinetics for oil systems at 30° C; vaterite dissolution controls the transformation process

The mole percentage of vaterite and calcite for systems with and without oil in Figure 5-31 suggest that adding an organic phase to the brine in which oil-in-water emulsions are formed impacts the transformation process. The decrease in the nucleation process occurs either by retarding the rate at which reacting species reach the surface or by intermittent wetting of the surface in the presence of oil droplets in the bulk solution. This is confirmed by the existence of less nucleation sites in the first minute when the oil is in the system as shown in Figure 5-12 (a) and 5-13 (a), in addition to low mass gain in the early stages as shown in Figures 5-3 and 5-4. Moreover, the presence of an organic phase may also slow the dissolution of the metastable phase due to the wetting of the crystal surface by the oil and this causes a change in the transformation mechanism from a surface-controlled to diffusion-controlled mechanism. This caused a reduction in the overall surface deposition and suggests the existence of an inhibition effect when adding the organic phase to the overall crystallization process at 30° C. According to [59] when some scale inhibitors are added, both formation and transformation of the metastable phase are inhibited. It was also reported by [62] that adding monoethylene glycol (MEG) solvent to the water changes the growth mechanism from surface reaction control to diffusion control and yields a decrease in the growth rate of calcite.

In the bulk solution, the analysis of the polymorphic composition and concentration for the precipitate of two different brine saturations at 30° C shows the convergence between the

compositions and hence the concentration of vaterite and calcite for a duration of time ranging between 60 to 90 minutes for brine 1 (0.1M) and brine 2 (0.065M) respectively, as shown in Figures 6-40 and 6-41. The composition and concentration of vaterite and calcite diverges after this period of time; calcite increases and vaterite decreases in a relatively slow rate. The change in the polymorphic mole percentage with time for brine 1 and brine 2 at 30° C is in good agreement with Sawada and Ogino et al. [51, 202] who combined the change in the polymorphic composition at 25° C with the change in the Ionic Activity Product (IAP) as shown in Figure 7-10. The graph illustrates the existence of three regions; the unstable region which lasts for about 4 minutes and represents the region where ACC is transformed to crystalline forms of vaterite and calcite. The transformation is shown to occur by a rapid rate in which their abundance is increased rapidly. Calcite is shown to form prior to vaterite and this may suggest the direct formation of some of calcite phase from ACC. This is also shown by other studies such as [48, 63] who showed that calcite could be formed directly from ACC at room temperature. The metastable region where the gradual transformation of vaterite to calcite exists and is shown as a relatively slow process where equal compositions of vaterite and calcite can take about 100 minutes and a divergence of their abundance is then shown after this period of time. The stable region represents the period where all the metastable phase is transformed to calcite where the whole transformation process took up to 3.5 hours.

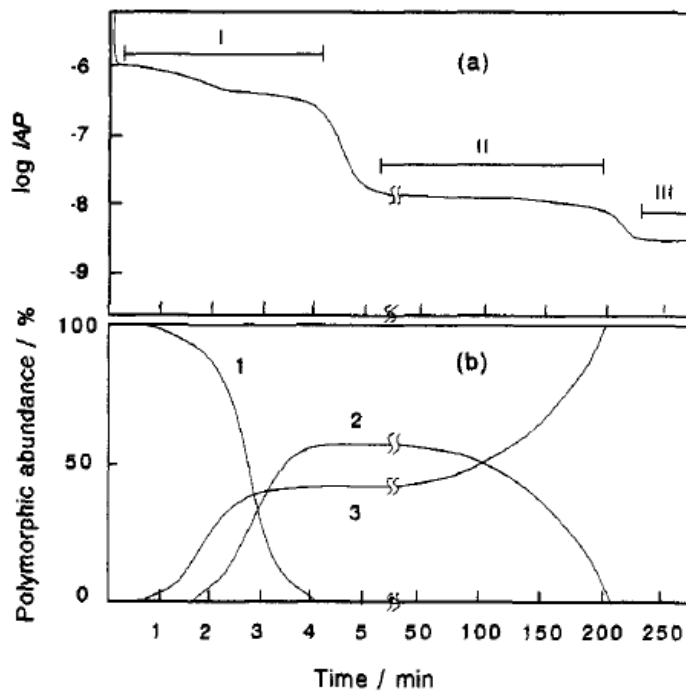


Figure 7-10 (a) The change in the ionic activity product with time at 25° C; (I) unstable stage, (II) metastable stage, (III) Stable stage; (b) The change in polymorphic abundance with time; (1) amorphous phase, (2) vaterite, (3) calcite [202]

The change in the polymorphic concentration in Figure 6-43, combined with both pH and de-supersaturation profiles in Figure 6-15(b) reveals the importance of the first 15 minutes (the nucleation period) compared to the later stages (the growth period) of the crystallization process. This early stage of the crystallization time represents the stage of formation of the crystals which causes the saturation ratio to decline by up to 97% of its initial value. The rate of formation of calcite fast within the nucleation period but since vaterite is supposed to form first, it is suggested that the first generation of vaterite is transformed by a rapid dissolution process and re-crystallizes to calcite according to the particle size-solubility dependence effect [215]. This states that as the particle size decreases, it exhibits higher solubility and hence higher dissolution rate than large particles. Small particles also exhibit larger surface area to volume ratio and this result in larger surface free energy and hence faster transformation tendency. Since the vaterite dissolution is considered fast in this process, the re-crystallization to calcite would be slower and this made the process controlled by the growth of calcite (surface-controlled) and is considered as process 1. This process takes place within the nucleation period and this explains the rapid increase in the concentration of calcite initially in Figure 6-43 which is in agreement with SEM in Figure 6-34 (a) and (b) and 6-35 (a) and (b). The hypothesis regarding the formation and transformation of CaCO_3 according to surface-controlled mechanism (process 1) is illustrated in Figure 7-11.

Oil- free systems

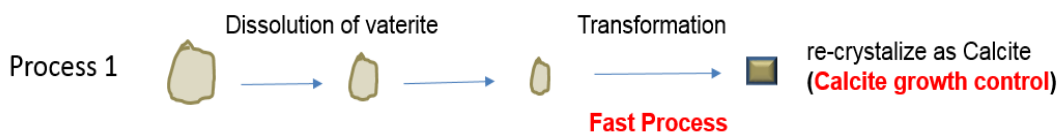


Figure 7-11 The hypothesis of formation and transformation of CaCO_3 in oil-free system which shows the dissolution of vaterite to calcite according to growth-control mechanism (process 1)

Due to the continuous formation of new crystals within the nucleation period in Figure 6-43 where this is also confirmed by the pH and the de-supersaturation profile in Figure 6-15 and the turbidity in the left side of Figure 6-7, the newly formed vaterite particles may then be subject to the Ostwald ripening phenomena [214]. This states that as small particles dissolve, the solute is then re-deposited onto larger particles and causes them to grow in size. Large particles in this case are vaterite particles which may survive from the early dissolution (process 1) and this is also reported by [50]. The growth of vaterite crystals in this case may slow the dissolution process according to the particle size-solubility dependence method [215]. This cause calcite to nucleate at the surface of vaterite in a process controlled by the dissolution of vaterite (diffusion-controlled mechanism) and this is considered as

process 2. Hence the existence of similar compositions for vaterite and calcite for a specific period of time in the growth period of Figure 6-43 is attributed to the slow dissolution of vaterite which may take several hours for a complete transformation from vaterite to calcite. The evidence of growing calcite on the surface of vaterite is also observed by many others such as [69, 77, 205]. The hypothesis regarding the formation and transformation of CaCO_3 according to the dissolution-controlled mechanism (process 2) is illustrated in Figure 7-12.

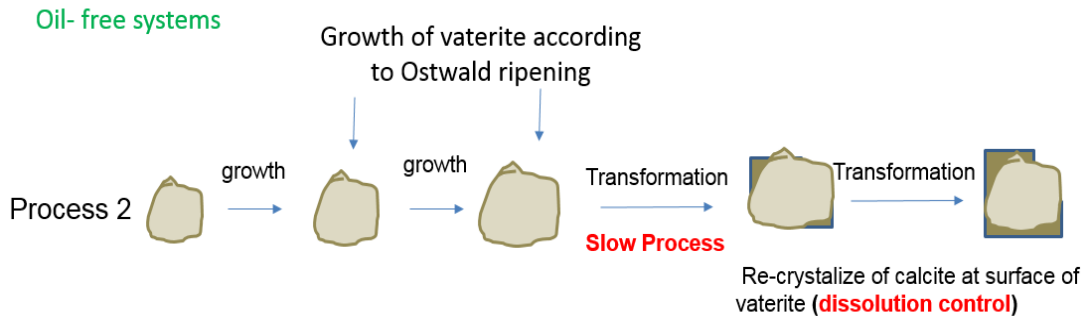


Figure 7-12 The hypothesis of formation and transformation of CaCO_3 in oil-free system which shows the growth of vaterite and the crystallization of calcite at surface of vaterite according to dissolution-control mechanism (process 2)

The evidence of vaterite growth in oil-free system at 30°C is also clearly observed by SEM in Figures 6-34 and 6-35 which is estimated in Tables 6-6 and 6-7 where an agreement between the average size of the crystals detected using un-weighted method for FBRM data in Table 7-2 and estimated by analysis of SEM images is shown; FBRM detected a mean chord length of $21\ \mu\text{m}$ at 60 minutes for brine 3 (0.045M) whereas the estimated average crystals size at 60 minutes for brine 2 (0.065M) in Table 6-6 is about $15\ \mu\text{m}$. The rate of the transformation of vaterite and the growth of calcite are then accelerated when the mole percentage of vaterite and calcite are equal and this causes a clear decline in vaterite composition and an increase in calcite composition beyond 60 minutes as shown in Figure 6-43. It was suggested by [51, 202] that the increase in the rate of transformation with time is a result of an increase in the surface area of calcite which proceeds with the transformation process. However the increase in the rate of transformation after a period of slowness may be due to the decrease in vaterite surface area with time rather than the increase in calcite surface area which results in higher dissolution rate and hence faster transformation to calcite.

The change in the total concentration of CaCO_3 combined with pH and de-supersaturation profiles in the presence of oil showed similar behaviour to that in absence of oil as shown in Figure 6-15. The change in the polymorphic concentration of vaterite and calcite are also found to behave similarly as in Figures 6-43 and 6-47 and this suggests the existence of the same two processes (the surface controlled and the dissolution controlled) in this system too. The tendency for the vaterite growth process according to the dissolution controlled

process is less in this case as less increase in vaterite concentration within the growth period is encountered in this case as shown in Figure 6-47. The decline in vaterite concentration within the nucleation process in the presence of oil may suggest the existence of a third process in which vaterite is transformed to calcite by a relatively fast process.

Although FBRM has not detected the formation of the crystals at oil/water interface, it showed a lower crystal count in the bulk solution than an oil droplet count. FBRM has also shown the decrease in the amount of homogeneous precipitation with the interfacial area as shown in Figure 7.3. A comparison between the total CaCO_3 that is formed between systems with and without oil is illustrated in Figure 7.13. A similar amount of CaCO_3 produced where the supersaturation is minimized by about 97% of its initial value for both cases. It seems that the oil phase has affected the bulk precipitation by reducing the homogeneous nucleation but at the same time the oil surface has provided an alternative place for the crystals to form. This causes a potential decrease in the supersaturation to a level that no more nucleation can take place and hence a similar yield of scale is detected in both cases. Similar rates of precipitation between an oil-free system and a system contains of 10% v/v n-dodecane has also been detected by [167].

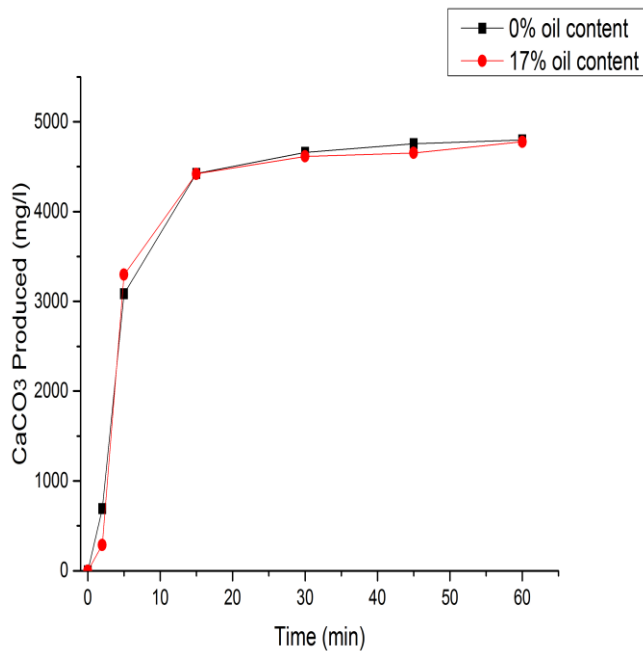


Figure 7-13 Comparing the total amount of CaCO_3 produced for oil-brine 1 at 30° C

The evidence of the formation of CaCO_3 crystals at the surface of oil droplets has also been observed using SEM images as observed in Figure 6.36. The existence of a flat surface at one side of some of vaterite clusters supports the idea of heterogeneous nucleation at the surface of the oil droplets. The vaterite clusters are shown to have an average size of 12 μm at 60 minutes for oil-brine systems at 30° C as shown in Tables 6-6 and 6-7, while the mean

diameter for the oil droplets at 30° C was found about 78 μm as measured using FBRM as shown in Table 6-1 . According to these values, the surface area of the oil droplets is about 40 times bigger than the surface area of vaterite by assuming a spherical shape of vaterite. This may also support the possibility of forming of the crystals at the surface of oil droplets and may also explain why the curvature shape of the oil droplets did not appear at vaterite flat surface.

The assumption of the nucleation of some of vaterite crystals at the oil-water interface could also explain why vaterite growth is less in the presence of oil where a competition surface with higher energy is found in which extra nucleation has taken place in this case. The heterogeneous nucleation at the oil-water interface is considered as a third process to encounter in the presence of oil. This process is also considered to take place within the nucleation period. The hypothesis regarding the formation and the transformation of CaCO_3 in oil systems is illustrated in Figure 7-14.

Oil- systems

Homogeneous nucleation, growth and transformation are taking place according to processes (1) and (2)

$$S_o > S_c \text{ by } 14$$

Heterogeneous nucleation is taking place at oil water interface according to process (3)

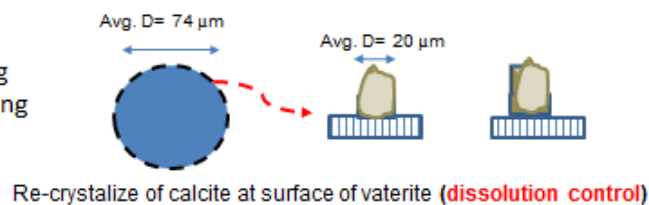


Figure 7-14 The hypothesis of formation and transformation of CaCO_3 in the presence of oil which shows the existence of three processes simultaneously; S_o and S_c denotes the surface area for an oil droplet and a crystal, respectively

SEM images in Figures 6-34 and 6-35 illustrate the polycrystalline nature of vaterite which takes a cauliflower shape. It was reported that vaterite is formed as a result of agglomeration of smaller particles [206]. It was also suggested by [43] that primary nucleation and secondary growth are common in the precipitation processes; primary nucleation is when nuclei are formed instantaneously at high supersaturation conditions and results in a drastic decline in supersaturation and secondary growth in which a larger particle is formed by the collision and the join of one or more particles together. The growth of vaterite in oil-free system with the agglomeration of vaterite units led to the formation of large vaterite clusters with size reaching to 16 μm in oil-free system. Since the transformation from vaterite to calcite at 30° C is believed to occur at the surface of the vaterite, calcite retains the

polycrystalline nature of vaterite and results in clusters of crystals that are interconnected and have an average size of 14 μm . The mechanism of formation of cauliflower vaterite is similar in the presence of oil but with fewer tendencies to form big vaterite units. However vaterite and calcite are formed with an average size of 12 μm and 8 μm , respectively for the systems with oil.

The crystallization kinetics at 60°C show relatively similar mechanisms of formation and transformation of CaCO_3 to that at 30°C. The reduction in the surface deposition in the presence of oil is also shown to exist at 60° C. An exception to this is found for the oil fractions of up to 40% where the amount of deposition is increased by one fold; the mass gain for an hour is higher in the presence of oil than in the absence of oil at 60° C as shown in Figure 5-2. However the amount of deposition for two different brine concentrations has showed a similar maximum deposition rate which is about 65% higher than the amount of deposition for oil-free system. This may be due to some of the crystals being sheared away when the thickness of the crystal layers reach the boundary layer thickness. A maximum limit on the amount of deposition is exhibited in this case.

Assessment of polymorphic abundance and mass gain on a surface for the oil-free system in Figures 5-32 and 5-33 suggest the transformation of aragonite to calcite occurs by a slow process and this slow process results in a gradual parallel rise in their masses. This suggests a dissolution controlled process in which the growth of calcite is taking place at the aragonite surface as an analogy to the transformation of vaterite to calcite at 30° C. This is in agreement with [219] who showed that the calcite nucleation during the aragonite-calcite transformation takes place on the aragonite surface.

In the presence of oil, the transformation of aragonite to calcite is faster as it only requires about 20 minutes for their fractions to equilibrate as shown in Figure 5-34. The increase in aragonite abundance after the decline is most probably due to new layers of aragonite crystals being formed and growing on old ones forming a dendrite or tree-like shape as shown in Figure 5-16 (c) to (e). This suggests the onset of secondary nucleation and this most probably attributed to the bulk behaviour which may have a direct impact on surface scaling behaviour. It was postulated by [208] that when the supersaturation is sufficiently high, secondary nucleation in the presence of prior crystals occurs. However, SEM images in the early stages of the crystallization process showed that aragonite is formed as aggregates of thin needles which emerged from a central point. These aggregates are less in average size but higher in quantity when compared to the aragonite aggregates in the oil-free system as shown in Figures 5-19 and 5-20. It is suggested that these first generation of aragonite thin needles are easier to transform to calcite by a fast transformation process according to surface-controlled mechanism and result in calcite spread over the surface in

the presence of oil as shown in Figure 5-17 (e) and (f). This may explain the rapid transformation of aragonite to calcite within the first 20 minutes in the presence of oil as detected in Figure 5-34. According to Bischoff et al. [219] aragonite of different origins and grain size gave significantly different rate of transformation. Bischoff et al. extensively studied the transformation of vaterite to aragonite and aragonite to calcite [219-221]. Apart from their work which is considered quite old today, there is a lack of studies in the literature concerned with the transformation to and from aragonite.

Comparing the mole percent of calcite to aragonite for systems with and without the oil and the amount of mass gain per hour for different oil fractions at 60° C in Figure 5-36, shows a similar abundance of calcite and aragonite for oil-free system whereas higher percentage of aragonite comparing to calcite is detected in the presence of oil. This is because of the mechanism of the transformation at this temperature where the diffusion-controlled process in the oil-free system caused the slow transformation of aragonite to calcite at 60° C, whereas the secondary nucleation in the presence of oil caused an increase in the abundance of aragonite.

It is found that equal composition of the metastable phase and the stable phase on the surface is achieved within first minute at 30° C and it requires about 50 minutes to achieve at 60° C in the single phase crystallization systems. This is contrary to the multiphase crystallization processes where equal composition of the metastable phase and the stable phase require about 60 minutes to achieve at 30° C and it only requires 20 minutes at 60° C. However, it was shown that the transformation is surface-controlled (fast) in the absence of oil at 30° C and at the first 20 minutes in the presence of oil at 60° C, whereas it was diffusion-controlled (slow) in the presence of oil at 30° C and in the absence of oil at 60° C. In the latter case, the stable phase is formed at the surface of the metastable phase and occupies the same area.

In the bulk solution, the analysis of the polymorphic composition and concentration of the precipitates at 60° C showed the domination of the aragonite phase in the presence and absence of oil. Vaterite is more observed in the solution at the beginning of the precipitation process in the oil-free system as shown in Figures 6-48 and Figure 6-49. Vaterite composition then declined rapidly and only requires 15 minutes for vaterite to reduce to about 15 mole%. The concentrations then diverge and the transformation seemed to cease beyond 15 minutes. Bischoff [220] suggested that the nucleation and the growth mechanisms that is applied to calcite is applied to aragonite. Therefore as an analogy to the transformation of vaterite to calcite at 30° C, the rapid transformation of vaterite to aragonite in this case is attributed to the rapid dissolution of vaterite and the re-crystallization of aragonite in the vicinity of vaterite which is a slow process and this makes the process

controlled by aragonite growth. On the other hand calcite seemed to form simultaneously with vaterite rather than aragonite as shown after 15 minutes in Figure 6-49. This may suggest that some of vaterite was transformed to calcite by a slow process which is diffusion-controlled as their concentrations were found to build together after 15 minutes. It was reported by [45] when diffusion and reaction play joint roles in the reaction system, a mixture of cubic and needle-like particles are formed. The last stage in the crystallization process in this case will be the transformation from aragonite to calcite which seemed to be a very slow process. However, Ogino et al. [51] showed that the time required for a complete transformation of aragonite to calcite took 1100 min (\approx 18 hours) at 60-80° C. This is much higher than that required for a complete transformation of vaterite to calcite which took up to 6 hours according to the same authors.

The change in the polymorphic concentration in Figure 6-49, combined with the pH and de-supersaturation profiles as shown on the left side of Figure 6-17 reveals the importance of the first 5 minutes (nucleation period) compared to the latter stage (growth period) of the crystallization process. This early stage of the crystallization time represents the stage of crystal formation which causes the supersaturation to decline by up to 95% of its initial value. Vaterite seemed to nucleate within the first 5 minutes at a relatively fast rate. The nucleation of vaterite caused a potential drop in the supersaturation and pH within this period of time as shown on the left side of Figure 6-17 and a high increase in the turbidity intensity as shown in Figure 6-7(b). At the same time vaterite is transformed to aragonite and this caused a clear increase in the aragonite concentration after 5 minutes. The dissolution process of vaterite is so fast and caused a significant drop in its concentration at 15 minutes allowing aragonite to become dominant.

The analysis of the polymorphic composition and concentration in the presence of oil behaves similarly to the oil-free system in the period of nucleation but with lower initial vaterite concentration in this case. The transformation to aragonite seemed to take place rapidly in the nucleation period and since vaterite is supposed to form first, it is suggested that some of the first generation of vaterite is transformed by a rapid dissolution process and re-crystallizes as aragonite. The rest of the vaterite has kept its presence and the transformation to aragonite in this case seemed to take place at a slower rate. An analogy to the transformation of vaterite to calcite at 30° C, the slow transformation of vaterite to aragonite in this case is attributed to the slow dissolution of vaterite and the re-crystallization of aragonite on the surface of vaterite and this makes the process controlled by vaterite dissolution.

However a decline in the total CaCO_3 seemed to take place after the nucleation period as shown in Figure 6-49 and this is combined with the abnormal rise in pH profile in the same

region as shown in the right side of Figure 6-17. This is most probably due to the initiation of the third process which causes the pH to increase and hence the calculations of the saturation ratio shows an increase and this results in a decrease in the total CaCO_3 produced as illustrated in Table 6-5. Theoretically, this is not possible as the system is going towards lowering the solubility as the reaction is progressed. However, FBRM shows the high tendency for the system to agglomerate at this temperature particularly in the presence of oil as discussed in section 7.1.1. The agglomeration process is defined as the formation of strong bonds when aggregate particles are cemented by a crystalline bridge and form an agglomerate [222]. The increase in the amount of scale formed on the surface is also encountered at this period of time as shown in Figure 5-35. This could be considered as a sensitive case which requires more investigation.

7.1.4 Linking between surface deposition and bulk precipitation

Comparing the polymorphic percentages of scale formed on a stainless steel surface with that formed in the bulk solution at 30° C highlights the importance of the first 10 to 20 minutes period of time as shown in Figures 7-15 and 7-16. This period is considered as the period when nucleation existed in simultaneous to the transformation of phases. The high drop in saturation ratio within this period supports this as illustrated in section 6.3.5 of chapter 6. Beyond this initial stage, nucleation ceases and the system is dominated by the further transformation of vaterite to calcite. However, it has been shown that the transformation from vaterite to calcite can exist by either a fast surface-controlled process or by a slow diffusion-controlled process. This is clearly observed for the kinetics of the crystallization on a surface. The kinetics of the crystallization in the bulk solution shows that both these processes are taking place simultaneously; part of the crystals exhibit a rapid surface-controlled mechanism and this process only requires about 15 minute to complete. The other part of the crystals exhibit a slow diffusion-controlled mechanism and this process takes place throughout the experiment and may persist much longer.

The fact that two processes occur in the bulk solution whereas only one process occur on the surface makes the polymorphic transformation faster on the surface than in the bulk for oil-free system as shown in Figures 7-15 and 7-16. Equal percentage of vaterite and calcite require only 1 minute to exist on a surface whereas in the bulk solution, it takes about 60 and 90 minutes for brine 1 (0.1M) and brine 2 (0.065M) to equilibrate respectively.

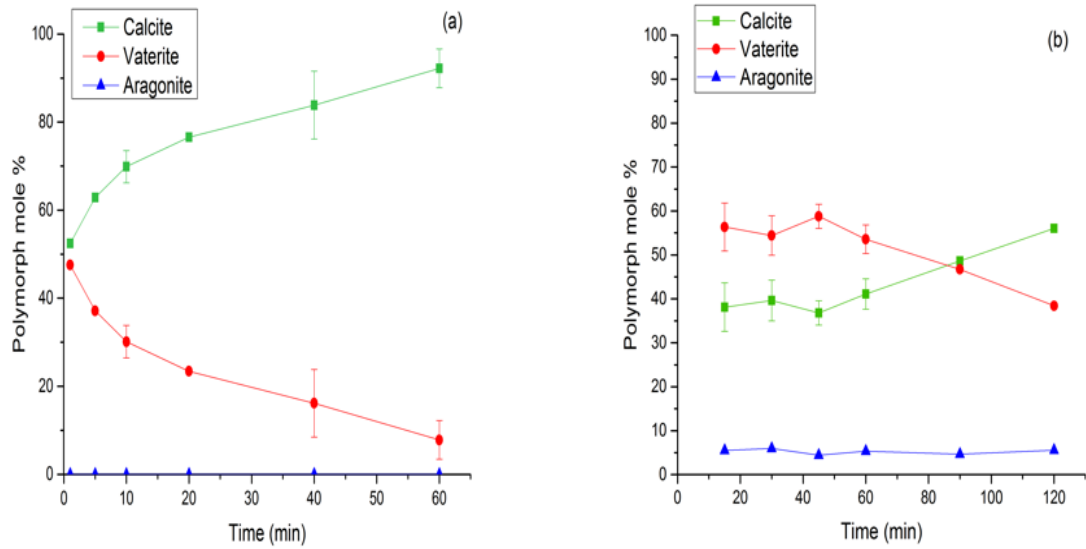


Figure 7-15 Comparing deposition and precipitation polymorphic abundance for brine 2 (0.065M) at 30° C; (a) on a surface, (b) in the bulk solution

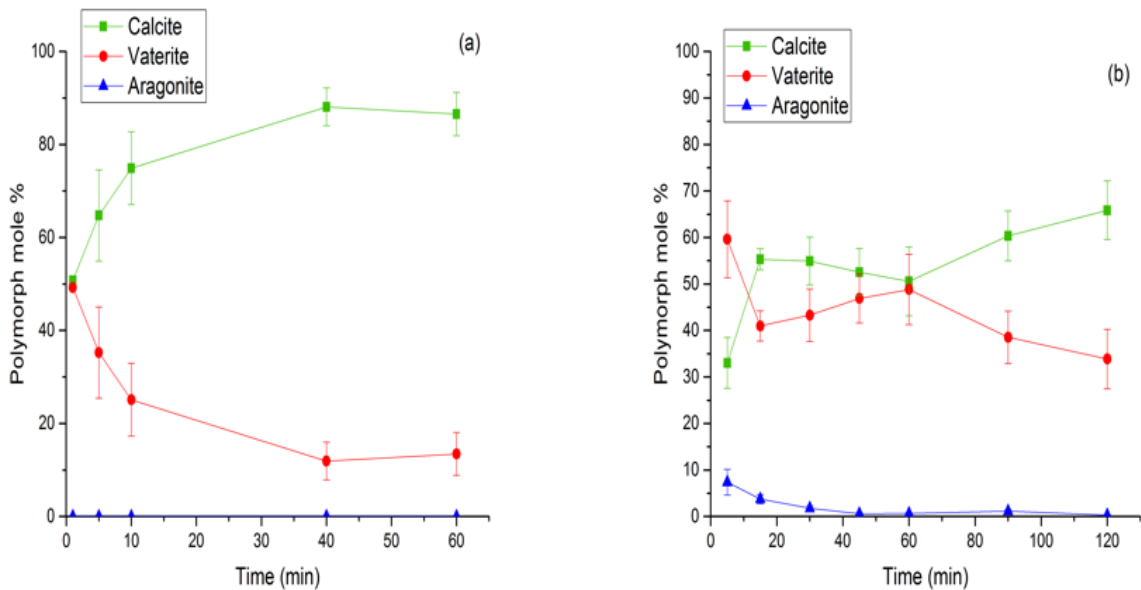


Figure 7-16 Comparing deposition and precipitation polymorphic abundance for brine 1 (0.1M) at 30° C; (a) on a surface, (b) in the bulk solution

In the presence of oil the existence of similar distribution of the phases between surface and bulk are clearly observed as shown in Figures 7-17 to 7-20. There are two possibilities for this similarity; surface deposition is diffusion-controlled which exhibited slow kinetics and this process is also found to dominate in the solution.

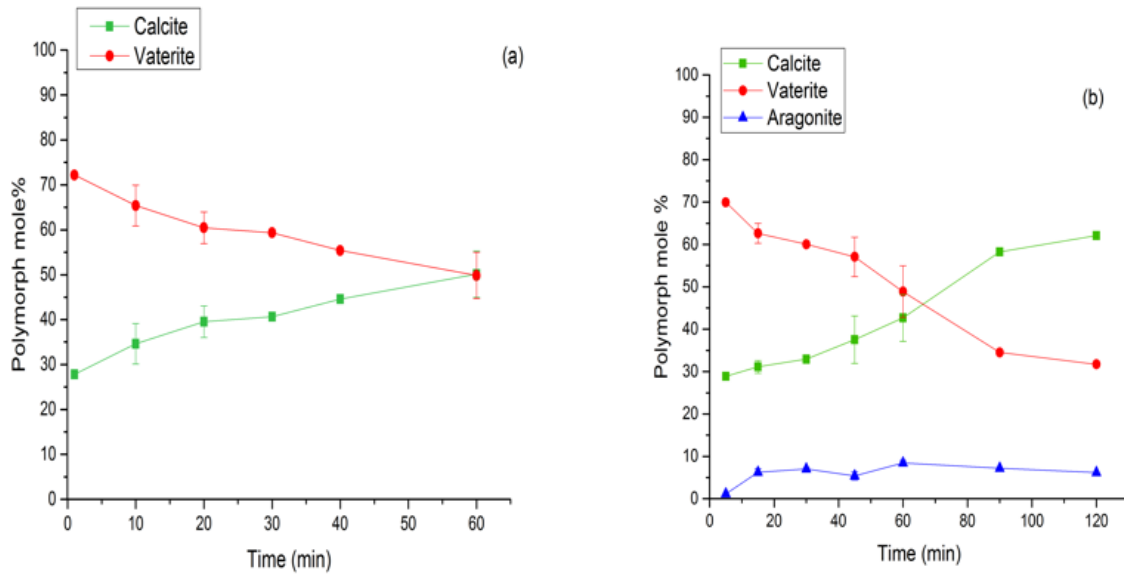


Figure 7-17 Comparing deposition and precipitation polymorphic abundance for oil-brine 2 (0.065M) at 30° C; (a) on a surface, (b) in the bulk solution

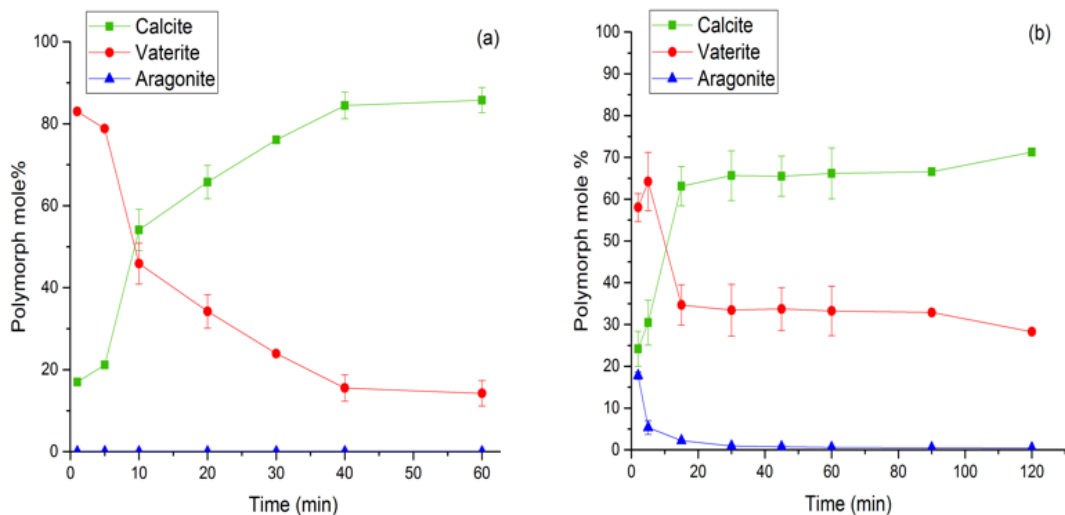


Figure 7-18 Comparing deposition and precipitation polymorphic abundance for oil-brine 1 (0.1M) at 30° C; (a) on a surface, (b) in the bulk solution

Another possibility to explain the similar polymorphic distribution observed on the surface and in the bulk in the presence of the oil is the role of heterogeneous nucleation on the crystallisation process; part of the bulk precipitate is believed to occur at oil-water interface. A competitive surface with low energy is found in this case and therefore more scale is formed and this may explain the existence of similar CaCO_3 produced in the bulk solution for systems with and without oil as shown in Figure 7-13.

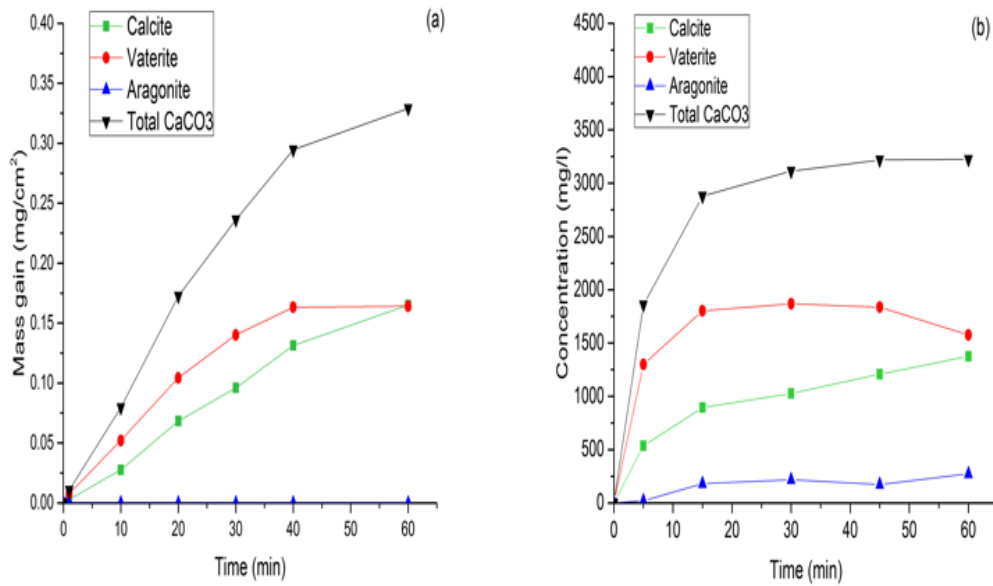


Figure 7-19 Comparing the polymorphic growth for 23% oil-brine 2 (0.065M) at 30° C; (a) on a surface, (b) in the bulk solution

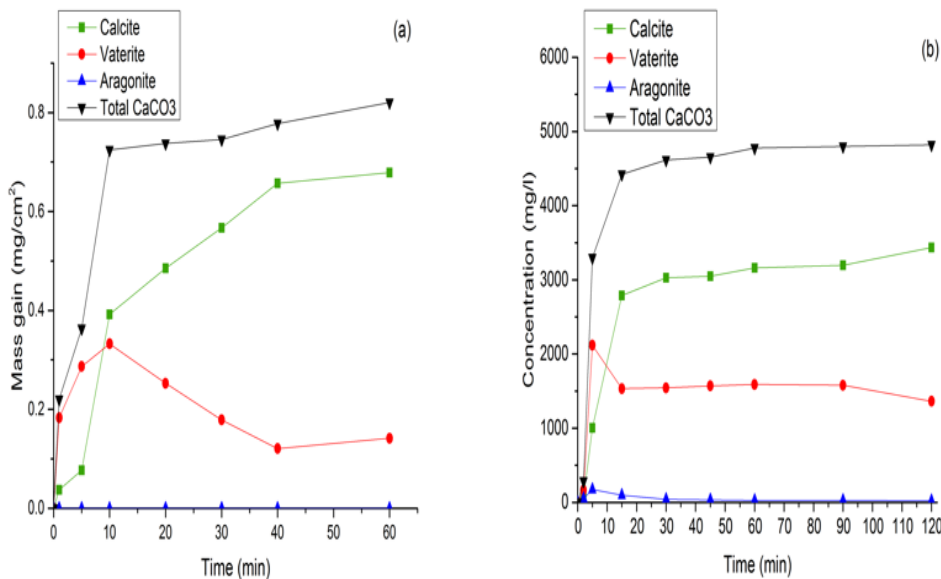


Figure 7-20 Comparing the polymorphic growth for 17% oil-brine 1 (0.1M) at 30° C; (a) on a surface, (b) in the bulk solution

At 60° C the situation is different as the three phases seen together in the bulk solution where the transformation of vaterite to aragonite and vaterite to calcite are taking place within the experiment. However, vaterite did not appear on a surface and the transformation seemed to take place from the metastable phase aragonite to the stable phase calcite. In the oil-free system the mole percentage of aragonite and calcite are about 80 and 20 mole % at first 1 minute on a surface. The same mole percentage of aragonite and calcite is detected by 30 minutes in the bulk solution as shown in Figure 7-21. This may suggest the fact that

polymorphic transformation is faster on a surface than in the bulk solution. It seems like a complete stage of transformation from vaterite to aragonite was eliminated on a surface in this case. However since the transformation time depends on the number of precursor stages being involved [201], and because the transformation process is much faster on a surface than in the bulk, it is suggested that aragonite is formed directly from the ACC precursor and then is transformed to the more stable calcite by the slow diffusion-controlled process on a surface. While the situation is different in the bulk where vaterite is formed first and transformed to aragonite by a relatively fast surface-controlled process which is then supposed to transform to calcite in a relatively slow process.

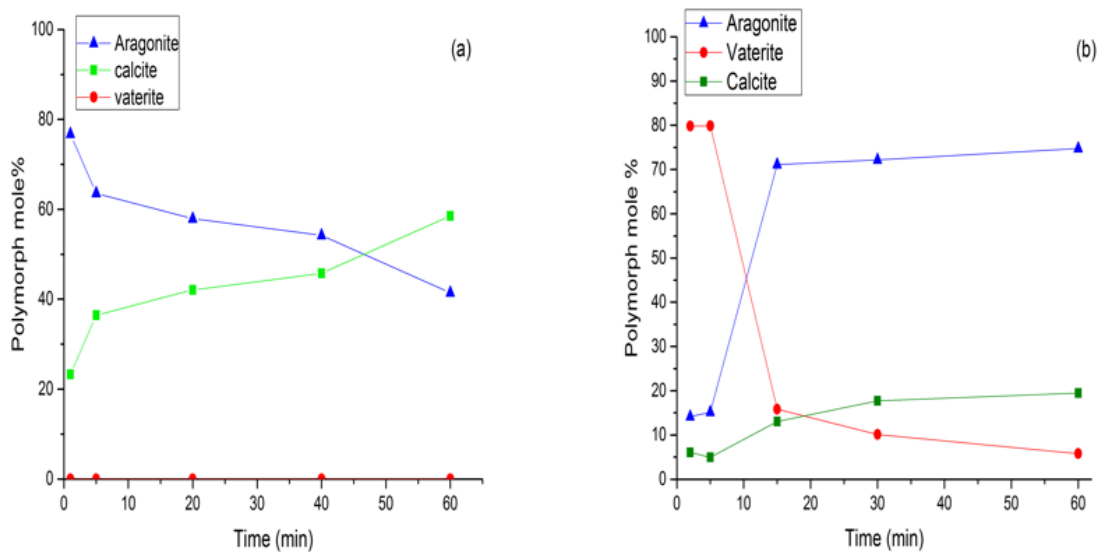


Figure 7-21 Comparing deposition and precipitation polymorph abundance for brine 3 (0.045M) at 60°C; (a) on a surface, (b) in the bulk solution

The mechanism of transformation in the presence of oil in Figure 7-22 shows the existence of two processes on a surface; the first is the rapid dissolution of aragonite to calcite according to surface-controlled mechanism. The second process is the onset of a secondary nucleation which causes the deposition to increase in this case. In the bulk solution two processes also existed in which vaterite is transformed to aragonite by both fast (surface-controlled) and slow (diffusion-controlled) mechanisms.

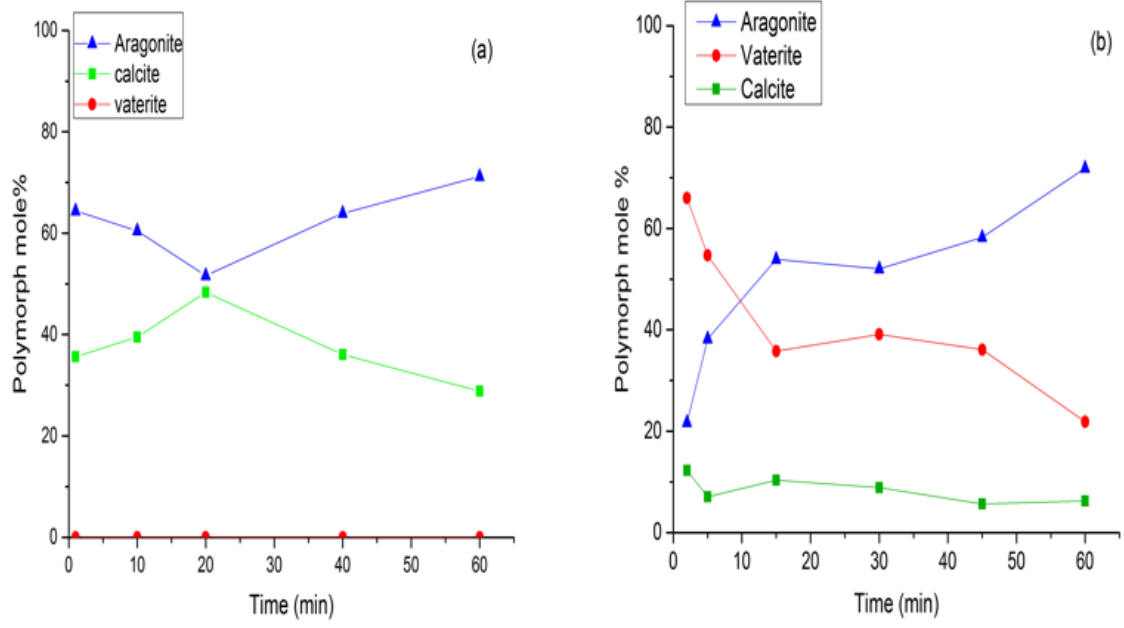


Figure 7-22 Comparing deposition and precipitation polymorph abundance for 23% oil-brine 3 (0.045M) at 60°C; (a) on a surface, (b) in the bulk solution

8 Chapter Eight Conclusions and future work;

8.1 Conclusions of the study

Despite the complexity of the system, FBRM has been acceptably used to track the nucleation and the growth processes in multiphase conditions. It was also used to detect where nucleation takes place; the high precipitation rate at 60° C where the crystals are mainly formed in the bulk solution and the low precipitation rate at 30° C where less crystals are formed in the bulk solutions and this led to the thinking that some of the crystals may have been formed at the oil-water interface. FBRM has also been used to characterize the oil-water system by estimating the mean droplets size and the interfacial area between phases and to estimate the particles (droplets and crystals) mean chord length and chord length distribution. Weight statistics have been used to interpret the data; square-weighted mean chord length and square-weighted chord length distribution are found to better represent the system when the oil droplets are dominant. Un-weighted mean chord length and un-weighted chord length distribution are found to better represent the system when precipitation is dominant. An overall characterizing of the system where the precipitation in the bulk solution according to homogeneous type nucleation is found to decrease in the presence of oil.

Kinetic measurements combined with microscopic observations have been monitored with time and found as a useful way for characterizing CaCO₃ scale formation on a surface and in the bulk solution. Analysing the surface crystallization process by estimating the rate at which each polymorph of CaCO₃ forms, grows and transforms can provide a microscale frame that enables a better understanding of the overall kinetics of the process compared to looking at the process through a macroscale frame by considering it as a stable structure.

The metastable phase is thermodynamically unstable and has a high tendency to transform and stabilise. The transformation from a metastable phase to a stable phase is agreed in the literature to take place by two steps: The first is the dissolution of the metastable phase and the second is the growth of the stable phase. How fast the transformation takes depends on which of these two steps is controlling the transformation process. The last stage in CaCO₃ crystallization is the growth of the stable phase. These various stages of CaCO₃ are believed to apply for the various phases; what applies between vaterite and calcite is applied between vaterite and aragonite or between aragonite and calcite with respect to the order of the transformation which is from a high solubility phase to a less solubility phase. This takes the order of vaterite, aragonite then calcite.

It is found that the formation of the more stable phase mainly depends on the formation and transformation of the less stable phase. The change in the kinetics of formation and transformation of vaterite on a surface, in the presence of oil at 30° C resulted in less nucleation sites with bigger crystals. Low nucleation sites was due to the lower ability for scaling species to diffuse and reach the surface in the presence of the oil droplets when an oil-in-water emulsion is formed. Big crystals were due to the slow dissolution process of vaterite which means it controlled the transformation process. This results in the nucleation and growth of calcite on the surface of the vaterite. Therefore it is suggested that the presence of an organic phase in the system acted by changing the mechanism of transformation process from surface-controlled to a diffusion-controlled mechanism and hence acted as an inhibition effect to the overall deposition process.

The presence of oil was shown to have more effect on the surface crystallization kinetics than on the bulk precipitation kinetics which was shown to behave similarly between the systems with and without oil at 30° C and 60° C. However, the growth of vaterite in the bulk solution is slightly lower and led to a faster transformation rate to calcite in the presence of oil. This is attributed to either the presence of oil which acted by reducing the nucleation sites in the bulk solution and led to less vaterite growth by the agglomeration process or due to the existence of heterogeneous nucleation where some vaterite were found to form at the oil-water interface. This acts as a competitive surface for crystals to nucleate at. Therefore less nucleation is found to take place in the solution by homogeneous type nucleation whereas some extra nucleation sites are found to occur at the oil-water interface according to heterogeneous type nucleation. The total yield of CaCO₃ scale is the same in the presence and absence of oil as what was reduced in the bulk solution found an alternative place to form, at the oil-water interface.

The kinetics of crystallization at 60° C is much complicated as the three polymorphs have been shown to appear during the reaction time in the bulk solution. However only aragonite and calcite present on the surface at 60° C and this is due to the fast kinetics that were taking place on the surface which caused vaterite to either disappear rapidly or be eliminated from the reaction. The kinetics of transformation of aragonite to calcite on a surface in the absence of oil at 60° C took place by a slow diffusion-controlled process in which calcite is supposed to form at the surface of aragonite. In the presence of oil at 60° C, two processes are found to exist on a surface. The first is the fast surface-controlled aragonite to calcite transformation. The second is the secondary nucleation of aragonite which caused layers of aragonite to form and led to high deposition rates. Bulk precipitation kinetics in the absence and presence of oil at 60° C showed similar mechanisms in which two processes took place simultaneously; the first in which vaterite is transformed by a fast surface-controlled process

to aragonite. The second is the transformation of vaterite to calcite by a slow diffusion-controlled mechanism in the oil-free system and the transformation of vaterite to aragonite by a slow diffusion-controlled mechanism in the oil systems.

According to all previous findings and as a rule of thumb we may summarize the trend of total calcium carbonate growth as:

- High slope: usually at the beginning of the crystallization process is the period at in which all the processes of nucleation and growth of the metastable phase, transformation to a more stable phase and nucleation and growth of a more stable phase are taken place simultaneously.
- Low slope: represents the period of growth of the metastable phase, transformation to a more stable phase, nucleation and growth of the more stable phase.
- Zero slope: represents the period of the transformation to a more stable phase, nucleation and growth of the more stable phase where an equilibrium between the rate of the metastable phase transformation and the rate of nucleation and growth of the more stable phase exists in this region.

Of particular interest is the relationship between surface crystallization and bulk precipitation kinetics. The similarity in the mechanism of the formation and the transformation of CaCO_3 scale between surface and bulk has been shown. It is suggested here that what applies in the bulk also applies on a surface. However, surface kinetics show much faster kinetics than bulk precipitation.

8.2 Suggestions for future research work

- Because the rate of formation and transformation of calcium carbonate scale on a surface and in the bulk, in the presence and absence of oil, for all experiment conditions in this study are extremely high, the early stage of the formation of different phases was not long enough to study. The results showed the great importance of this early stage of the crystallization process in terms of the detection of the mechanism of the formation of the different phases and their transformation. This early stage is shown to exist within 1 minute on a surface and it is extended to about 10 to 15 minutes in the bulk. This is considered as the nucleation period in which a potential supersaturation drop is exhibited. This period is considered to be very short and needs to be more focused on by more sampling and careful analysing. It is also recommended to work at much lower brine saturations in order to prolong this stage. This would allow the detection of the induction time in which the

metastable phase is formed and its abundance is 100%. Moreover, using an impeller with a rotation speed of 520 rpm may also promote the faster process. Therefore, it is also recommended to avoid vigorous mixing by using other techniques for emulsions creation such as using stabilizing agents but this is not a preferred option as it may affect the chemistry of the system, or by using homogenizing methods such as ultrasonic homogenization. It is also recommended to study the kinetics of surface deposition alone to avoid the interactions in their mechanisms. This can be done by using low saturation brine in which the energy required for homogeneous nucleation is much higher than that required for heterogeneous nucleation. This may also be applicable for studying the precipitation process by heterogeneous type nucleation in which the crystals are formed at the oil-water interface.

- The results in this study showed how the formation of a more stable phase is affected by the formation of the less stable phase. It has been shown that vaterite takes different morphologies at different experiment conditions. Vaterite is usually known to have a spherical shape, but this is not the only morphology that vaterite may appear with. Vaterite could also present as irregular shapes such as a leaf-like shape or as flower, cauliflower-like or pine cone shapes. This indicates the differences in the mechanisms of vaterite formation and since the amorphous calcium carbonate is known as the precursor for vaterite formation, understanding the stages and the mechanisms of formation and transformation of ACC to vaterite is very important. However, evidence of the formation and transformation of the ACC on the surface and in the bulk solution were detected during this study and are shown in appendix E. ACC should be looked at in more details.
- The increase in the pH with time and after a steady state period is also of interesting and needs more investigation. The primary explanations for this phenomena is that when further transformation is exhibited in the bulk solution the dissolution of the unstable phase causes the release of calcium and carbonate ions which return to the solution. This causes an increase in the pH of the solution. The existence of this phenomenon after the nucleation period explains why this could only be observed in a later stage but not in the early stage of the process. The increase in solution pH is observed more at 60° C where an abnormal rise in pH is exhibited and this is associated with the abnormal rise in the amount of surface deposition and the agglomeration of the crystals in the solution.
- The organic phase that was used in this study was an iso-paraffinic oil of which 55 wt% are paraffins and 45 wt% are naphthenic compounds. Using different type of oils

with different chemical composition such as a highly paraffinic oil or highly aromatic oils is recommended to evaluate the impact of the oil chemistry on the overall crystallization process.

- Understanding the kinetics of polymorphic formation and transformation of calcium carbonate could provide further insights for the development of new surface kinetics prediction models.
- The main finding in this study is the detection of the inhibition effect of the oil phase on surface deposition. The change in the kinetics from surface-controlled to diffusion-controlled at 30° C has caused an overall minimization of surface scaling. Assessment of the kinetics of polymorphic formation and transformation of calcium carbonate in the presence of different chemical scale inhibitors could help in developing a better understanding of the inhibition kinetics. This could help in detecting how different scale inhibitors act on the different stages of the polymorphic nucleation, growth and transformation mechanisms. Therefore, it could help in choosing which scale inhibitors work much more effectively at specific conditions.
- The existence of a similar mechanism of formation and transformation of CaCO_3 in the bulk solution and on a surface, may suggest that both type of scaling could be controlled in a similar way. It has also been shown in this study that surface deposition exhibited a faster process than bulk precipitation in the absence of oil whereas surface deposition exhibited similar behaviour to bulk precipitation in the presence of oil. The oil phase was found to act as an inhibitor to surface deposition causing slower kinetics whereas the presence of oil did not show a significant effect in the bulk solution. This may result in differences in the minimum inhibition concentration MIC required for surface inhibition from that required for bulk precipitation inhibition. However, Inhibitors still need to be further developed to be more effective and provide full scale prevention.

References

1. ExxonMobil. *2018 Outlook for Energy: A View to 2040*. 2018; Available from: Available from: <https://cdn.exxonmobil.com/~media/global/files/outlook-for-energy/2018/2018-outlook-for-energy.pdf>.
2. Statista. *Daily global crude oil demand 2006-2019*. 2018; Available from: Available from: <https://www.statista.com/statistics/271823/daily-global-crude-oil-demand-since-2006/>.
3. International, E., Agency,. *Oil market report*. November 2018; Available from: Available from: <https://www.iea.org/oilmarketreport/omrpublic/>.
4. Petroleum, B. *Global Oil Reserves 2017*; Available from: Available from: <https://www.bp.com/en/global/corporate/energy-economics/statistical-review-of-world-energy/oil/oil-reserves.html>.
5. Quanshu L., H.X., Jianjun L., Xiangchou L., *A review on hydraulic fracturing of unconventional reservoir*. *Petroleum*, 2015. **1**(1): p. 8-15.
6. Muggeridge A., C., A., Webb K., Frampton H., Collins I., Moulds T., Salino P., *Recovery rates, enhanced oil recovery and technological limits*. *Philosophical transactions. Series A, Mathematical, physical, and engineering sciences*. **372**(2006): p. 20120320-20120320.
7. Abarasi, H., *A review of technologies for transporting heavy crude oil and bitumen via pipelines*. *Journal of Petroleum Exploration and Production Technology*, 2014. **4**(3): p. 327-336.
8. Schramm, L., *Emulsions; Fundamentals and Applications in the Petroleum Industry*. Vol. 231. 1992, American Chemical Society.
9. Moghadasi J., M.H., Jamialahmadi M., Sharif A., *Model study on the kinetics of oil field formation damage due to salt precipitation from injection*. *Journal of Petroleum Science and Engineering*, 2004. **43**: p. 201-217.
10. Merdah A., Y.A., *Scale formation in oil reservoir during water injection at high-salinity formation water*. *Journal of applied sciences* 2007. **21**(7): p. 3198-3207.
11. Vrålstad, T., Fossen, M., Sjöblom, J., Randhol, P., *Influence of Interfacial Tension on Seeded Calcium Carbonate Scale Precipitation: Effect of Adsorbed Asphaltenes*. *Journal of Dispersion Science and Technology*, 2008. **29**(3): p. 440-446.
12. solutions, W.W. *Calcium Scale in Water Bores and BluBac Gold*. 2018 Available from: http://www.waterwellsolutions.com.au/mineral_scale_problems.html.
13. Lee E., J.J., Kang H. , Kim Y., *Thermal resistance in corrugated plate heat exchangers under crystallization fouling of calcium sulfate (CaSO₄)*. *International Journal of Heat and Mass Transfer* 2014. **78**: p. 908–916.
14. Albert F., A.W., Scholl S. , *Roughness and constriction effects on heat transfer in crystallization fouling*. *Chemical Engineering Science* 2011. **66**: p. 499–509.
15. Hoeka E., A.J., Knoell T., Jeong B., *Modeling the effects of fouling on full-scale reverse osmosis processes*. *Journal of Membrane Science* 2008. **314**: p. 33–49.
16. Gryta, M., *Fouling in direct contact membrane distillation process*. *Journal of Membrane Science* 2008. **325**: p. 383–394.
17. Crabtree M., E.D., Fletcher P, and King G., *Fighting scale- removal and prevention*. *Oilfield review*, 1999: p. 30-45.

18. Amer, M., Yassin, A., *Scale Formation in Oil Reservoir During Water Injection at High-Salinity Formation Water* Journal of Applied Sciences, 2007. **7**(21): p. 3198-3207.
19. Vetter, O., Farone, A., *Calcium Carbonate Scale in Oilfield Operations*, in *SPE Annual Technical Conference and Exhibition*. 1987, Society of Petroleum Engineers: Dallas, Texas
20. Hasson, D., Avriel, M., Resnick, W., Rozenman, T., Windreich, S., *Calcium carbonate scale deposition on heat transfer surfaces*. Desalination, 1968. **5**: p. 107-119.
21. Antony, A., Low, J. H., Gray, S., Childress, A. E., Le-Clech, P., Leslie, G., *Scale formation and control in high pressure membrane water treatment systems: A review*. Journal of Membrane Science, 2011. **383**: p. 1-16.
22. Merdah, A., Yassin, A., *The study of scale formation in oil reservoir during water injection at high-barium and high-salinity formation water*. J. of Applied Sciences, 2007. **21**: p. 3198-3207.
23. Walter, J.H., *Theoretical Mean Activity Coefficients of Strong Electrolytes in Aqueous Solutions from 0 to 100 °C*. National standard reference data series, NBS 24, 1968.
24. Witkowski, A., Majkut, M., Rulik, S., *Analysis of pipeline transportation systems for carbon dioxide sequestration*. Vol. 35. 2014. s. 117-140.
25. Segev, R., Hasson, D. and Semiat, R. , *Rigorous modeling of the kinetics of calcium carbonate deposit formation - CO₂ effect*. AIChE J., 2012. **58**: p. 2286–2289.
26. Eurybiades, P., Busenberg, L. N., *The solubilities of calcite, aragonite and vaterite in CO₂-H₂O solutions between 0 and 90°C, and an evaluation of the aqueous model for the system CaCO₃-CO₂-H₂O*. Geochimica et Cosmochimica Acta, 1982. **46**(6): p. 1011-1040.
27. Harned, W.J., Herbert, S. Hamer, , *The Ionization Constant of Water and the Dissociation of Water in Potassium Chloride Solutions from Electromotive Forces of Cells without Liquid Junction*¹. Journal of the American Chemical Society, 1933. **55**(6): p. 2194-2206.
28. Yeatts, L.B., Lantz, P. M., Marshall, W., L., *Calcium sulfate solubility in brackish water concentrates and applications to reverse osmosis processes; polyphosphate additives*. Desalination, 1974. **15**(2): p. 177-192.
29. Bott, T.R., *Aspects of crystallization fouling*. Experimental Thermal and Fluid Science, 1997. **14**(4): p. 356-360.
30. Mullin, J.W., *Crystallization*. 4 ed. 2004, Oxford: Elsevier Butterworth- Hienemann.
31. Sohnel, O., Garside, J. , *Precipitation: Basic principles and industrial applications*. 1992, Butterworth-Heinemann Ltd.: oxford.
32. Hindle, S., Povey, M., Smith, K., *Kinetics of Crystallization in n-Hexadecane and Cocoa Butter Oil-in-Water Emulsions Accounting for Droplet Collision-Mediated Nucleation*. Journal of Colloid and Interface Science, 2000. **232**(2): p. 370-380.
33. Mousaw, P., Saranteas, K., Prytko, B., *Crystallization Improvements of a Diastereomeric Kinetic Resolution through Understanding of Secondary Nucleation*. Organic Process Research & Development, 2008. **12**(2): p. 243-248.
34. Mazzarotta, B., *Abrasion and breakage phenomena in agitated crystal suspensions*. Chemical Engineering Science, 1992. **47**(12): p. 3105-3111.

35. Chernov, A., Zaitseva, N., Rashkovich, L. , *Secondary nucleation induced by the cracking of a growing crystal: KH_2PO_4 (KDP) and $K(H,D)2PO_4$ (DKDP)*. Journal of Crystal Growth, 1990. **102**(4): p. 793-800.
36. Garside, J., Rusli, I. T., Larson, M. A., *Origin and size distribution of secondary nuclei*. AIChE Journal, 1979. **25**(1): p. 57-64.
37. Clifford, Y.T., Jenn-Fang, Rousseau, Ronald, W. Wu,, *Interfacial supersaturation, secondary nucleation, and crystal growth*. Journal of Crystal Growth, 1992. **116**(3–4): p. 294-306.
38. Garside, J., Slobodan, J. J., *Measurement and scale-up of secondary nucleation kinetics for the potash alum-water system*. AIChE Journal, 1979. **25**(6): p. 948-958.
39. Yuping, Z.a.D., R., *The kinetics of calcite precipitation from a high salinity water*. Applied Geochemistry, 1998. **133**: p. 177-184.
40. Jones, A.G., *5 -Crystal formation and breakage*, in *Crystallization Process Systems*, A.G. Jones, Editor. 2002, Butterworth-Heinemann: Oxford. p. 123-154.
41. Dawe, R., Yuping, Z., *Kinetics of calcium carbonate scaling using observations from glass micromodels*. Journal of Petroleum Science and Engineering, 1997. **18** p. 179-187.
42. Davies, C.W., Jones, A. L., *The precipitation of silver chloride from aqueous solutions. Part 2 Kinetics of growth of seed crystals*. Transactions of the Faraday Society, 1955. **51**.
43. Tai, C.Y., *Experimental techniques for identifying operating variables of crystal growth and nucleation—From readily soluble salts to sparingly soluble salts*. Journal of the Taiwan Institute of Chemical Engineers, 2009. **40**.
44. Andritsos, N., Kontopoulou, M., Karabelas, A.J., Koutsoukos P. G., *Calcium carbonate deposit formation under isothermal conditions* The Canadian Journal of Chemical Engineering, 1996. **74**.
45. Wang, H., Huang, W., Han, Y., *Diffusion-reaction compromise the polymorphs of precipitated calcium carbonate*. Particuology, 2013. **11**(3): p. 301-308.
46. Al-Hadhrami, L., Quddus, A., Dhawi, A. Al-Otaibi, , *Calcium sulfate scale deposition on coated carbon steel and titanium*. Desalination and Water Treatment, 2013. **51**(13-15): p. 2521-2528.
47. Kabasci, S., Althaus, W., Weinspach, P., *Batch-precipitation of calcium carbonate from highly supersaturated solutions*. Vol. 74. 1996. 765-772.
48. Shen, Q., Wei, Hao, Z., Yong, H., Yaping, Y., Hengrui, W. Dujin, Xu Duanfu, *Properties of Amorphous Calcium Carbonate and the Template Action of Vaterite Spheres*. The Journal of Physical Chemistry B, 2006. **110**(7): p. 2994-3000.
49. Andreassen, J., *Formation mechanism and morphology in precipitation of vaterite— nano-aggregation or crystal growth?* Journal of Crystal Growth, 2005. **274**(1): p. 256-264.
50. Bots, P., Benning L. G., Rodriguez Blanco, J. D., Roncal-Herrero, T. Shaw, S., *Mechanistic Insights into the Crystallization of Amorphous Calcium Carbonate (ACC)*. Crystal Growth & Design, 2012. **12**(7): p. 3806-3814.
51. Ogino, T., Suzuki, T., Sawada, T., *The formation and transformation mechanism of calcium carbonate in water*. Geochim. Cosmochim. Acta 1987. **51**.
52. Blue, C.R., Giuffre, A., Mergelsberg, S., Han, N., De Yoreo, J. J., Dove, P. M., *Chemical and physical controls on the transformation of amorphous calcium*

- carbonate into crystalline CaCO₃ polymorphs*. *Geochimica et Cosmochimica Acta*, 2017. **196**: p. 179-196.
53. Wu, Z., Davidson, J., Francis, H., Lorraine, F., *Effect of water chemistry on calcium carbonate deposition on metal and polymer surfaces*. *Journal of Colloid and Interface Science*, 2010. **343**(1): p. 176-187.
 54. Saharay, M., Kirkpatrick, R. J., *Onset of Orientational Order in Amorphous Calcium Carbonate (ACC) upon Dehydration*. *Chemical Physics Letters*, 2014. **591**: p. 287-291.
 55. Chen, J., Xiang, L., *Controllable synthesis of calcium carbonate polymorphs at different temperatures*. *Powder Technology*, 2009. **189**(1): p. 64-69.
 56. Tai, C.Y., Chen, F.-B., *Polymorphism of CaCO₃ precipitated in a constant-composition environment* *AIChE Journal*, 1998. **44**(8): p. 1790-1798.
 57. Chen, T., Neville, A., *Calcium carbonate scale formation—assessing the initial stages of precipitation and deposition*. *Journal of Petroleum Science and Engineering*, 2005. **46**(3): p. 185-194.
 58. Wada, N., Kimihiro, Y. and Takao, U., *Effects of Carboxylic Acids on Calcite Formation in the Presence of Mg²⁺ Ions*. *Journal of Colloid and Interface Science*, 1999. **212**(2): p. 357-364.
 59. Qingfeng, Y., Yangqiao, L., Anzhong, G., Jie, D., Ziqiu, S., *Investigation of Calcium Carbonate Scaling Inhibition and Scale Morphology by AFM*. *Journal of Colloid and Interface Science*, 2001. **240**(2): p. 608-621.
 60. Koutsoukos, P.G., Klepetsanis, P., Spanos, N., Kanellopoulou, D. G., *Calcium Carbonate Crystal Growth and Dissolution Inhibitors*, in *CORROSION 2007*. 2007, NACE International: Nashville, Tennessee.
 61. Jin, D., Wang, F., Yue, L., *Phase and morphology evolution of vaterite crystals in water/ethanol binary solvent*. Vol. 46. 2011.
 62. Beck, R., Nergaard, M., Andreassen, J. P., *Crystal growth of calcite at conditions of gas processing in solvent mixtures of monoethylene glycol and water*. *Transactions of Tianjin University*, 2013. **19**(2): p. 79-85.
 63. Kim, W.-S., Hirasawa, Izumi, Kim, Woo-Sik, *Polymorphic Change of Calcium Carbonate during Reaction Crystallization in a Batch Reactor*. *Industrial & Engineering Chemistry Research*, 2004. **43**(11): p. 2650-2657.
 64. Radha, A.V., Forbes, T. Z., Killian, C. E., Gilbert, P. U. , Navrotsky, A., *Transformation and crystallization energetics of synthetic and biogenic amorphous calcium carbonate*. *Proceedings of the National Academy of Sciences*, 2010. **107**(38): p. 16438-16443.
 65. Cherkas, O., Beuvier, T., Breiby, Dag W., Chushkin, Y., Zontone, F., Gibaud, A., *Direct Observation of Microparticle Porosity Changes in Solid-State Vaterite to Calcite Transformation by Coherent X-ray Diffraction Imaging*. *Crystal Growth & Design*, 2017. **17**(8): p. 4183-4188.
 66. Cardew, P.T., Davey, R. J. , *The kinetics of solvent-mediated phase transformations*. *Proceedings of the Royal Society of London. A. Mathematical and Physical Sciences*, 1985. **398**(1815): p. 415.
 67. Ogino, T., Suzuki, T., Sawada, T., *The rate and mechanism of polymorphic transformation of calcium carbonate in water*. *Journal of Crystal Growth*, ,1990. **100**(1): p. 159-167.

68. Kralj, D., Brečević, L., Kontrec, J., *Vaterite growth and dissolution in aqueous solution III. Kinetics of transformation*. Journal of Crystal Growth, 1997. **177**(3): p. 248-257.
69. Rodriguez-Blanco, J.D., Shaw, S., Benning, L.G., *The kinetics and mechanisms of amorphous calcium carbonate (ACC) crystallization to calcite, viavaterite*. Nanoscale, 2011. **3**(1): p. 265-271.
70. Kitamura, M., *Crystallization and Transformation Mechanism of Calcium Carbonate Polymorphs and the Effect of Magnesium Ion*. Journal of Colloid and Interface Science, 2001. **236**(2): p. 318-327.
71. Spanos, N., Koutsoukos, P. G., *The transformation of vaterite to calcite: effect of the conditions of the solutions in contact with the mineral phase*. Journal of Crystal Growth, 1998. **191**(4): p. 783-790.
72. Kralj, D., Brečević, L., Nielsen, A. E., *Vaterite growth and dissolution in aqueous solution I. Kinetics of crystal growth*. Journal of Crystal Growth, 1990. **104**(4): p. 793-800.
73. Kralj, D., Brečević, L., Nielsen, A. E., *Vaterite growth and dissolution in aqueous solution II. Kinetics of dissolution*. Journal of Crystal Growth, 1994. **143**(3): p. 269-276.
74. Rao, M.S., *Kinetics and Mechanism of the Transformation of Vaterite to Calcite*. 1973. **46**(5).
75. Barriga, C., Morales, J., Tirado, J. L., *Changes in the kinetics of the vaterite-calcite transformation with temperature and sample crystallinity*. Journal of Materials Science, 1986. **21**(3): p. 947-952.
76. Khawam, A., Flanagan, D., *Solid-State Kinetic Models: Basics and Mathematical Fundamentals*. The Journal of Physical Chemistry B, 2006. **110**(35): p. 17315-17328.
77. Schlomach, J., Quarch, K., Kind, M., *Investigation of Precipitation of Calcium Carbonate at High Supersaturations*. Chem. Eng. Technol., 2006. **29**(2): p. 215-220.
78. Zaslavski, I., Shemer, H., Hasson, D., Semiat, R., *Rotating cylinder technique for assessing the effectiveness of anti-scalants*. Water Research, 2013. **47**(11): p. 3716-3722.
79. Khawam, A., Flanagan, D., *Basics and Applications of Solid State Kinetics: A Pharmaceutical Perspective*. Vol. 95. 2006. 472-98.
80. Khawam, A., Flanagan, D. R., *Role of isoconversional methods in varying activation energies of solid-state kinetics: I. isothermal kinetic studies*. Thermochimica Acta, 2005. **429**(1): p. 93-102.
81. Sanni, O., Bukuaghangin, O., Huggan, M., Kapur, N., Charpentier, T., Neville, A., *Development of a novel once-through flow visualization technique for kinetic study of bulk and surface scaling*. REVIEW OF SCIENTIFIC INSTRUMENTS, 2017. **88**(103903).
82. Eroini, V., Neville, A., Kapur, N., Euvrard, M., *New insight into the relation between bulk precipitation and surface deposition of calcium carbonate mineral scale*. Desalination and Water Treatment, 2013. **51**: p. 882-891.
83. Dove, P., Hochella, M. F., *Calcite precipitation mechanisms and inhibition by orthophosphate: In situ observations by Scanning Force Microscopy*. Geochimica et Cosmochimica Acta, 1993. **57**(3): p. 705-714.
84. Walton, A.G., *The formation and properties of precipitates* 2nd ed. 1979, Huntington, New York: Robert E. Krieger

85. Amor, A., Zgolli, M., Tlili, D., Manzola, M., *Influence of water hardness, substrate nature and temperature on heterogeneous calcium carbonate nucleation*. Desalination, 2004. **166**: p. 79-84.
86. Charpentier, T., Neville, A., *Controlling the Kinetic Versus Thermodynamic Growth of Calcium Carbonate Scale in the Bulk and on Surfaces*. 2016.
87. Quddus, A., Allam, I. M., *BaSO₄ scale deposition on stainless steel*. Desalination, 2000. **127**(3): p. 219-224.
88. Quddus, A., *Effect of hydrodynamics on the deposition of CaSO₄ scale on stainless steel*. Desalination, 2002. **142**(1): p. 57-63.
89. Quddus, A., Al-Hadhrami, L., *Hydrodynamically deposited CaCO₃ and CaSO₄ scales*. Desalination, 2009. **246**(1-3): p. 526-533.
90. Quddus, A., Al-Hadhrami, L., *Influence of solution hydrodynamics on the deposition of CaSO₄ scale on aluminum*. Journal of Thermophysics and Heat Transfer, 2011. **25**(1): p. 112-118.
91. Al-Hadhrami, L., Quddus, A., *Role of solution hydrodynamics on the deposition of CaSO₄ scale on copper substrate*. Desalination and Water Treatment, 2010. **21**(1-3): p. 238-246.
92. Quddus, A.A.-H., L., *Impact of solution hydrodynamics on the deposition of CaSO₄ on brass*. Desalination and Water Treatment, 2012. **50**(1-3): p. 285-293.
93. Levich, V.G. *Physicochemical hydrodynamics*. 1962; Available from: <http://books.google.com/books?id=DAtRAAAAMAAJ>.
94. Macadam, J., Parsons, S. A., *Calcium carbonate scale formation and control*. Reviews in Environmental Science and Biotechnology, 2004. **3**(2): p. 159-169.
95. Coey, J., Cass, M., Stephen, D., *Magnetic water treatment*. Journal of Magnetism and Magnetic Materials, 2000. **209**(1-3): p. 71-74.
96. Vazirian, M.M., Alvim, F. B. , de Oliveira, M. P., Charpentier, T., Neville, A., *Scale Deposition in the Oil and Gas Industry: From a Systematic Experimental Scale Study to Real-Time Field Data*, in *CORROSION 2016*. 2016, NACE International: Vancouver, British Columbia, Canada. p. 13.
97. Azimi, G., Cui, Y., Sabanska, A., Varanasi K., *Scale-resistant surfaces: Fundamental studies of the effect of surface energy on reducing scale formation*. Applied Surface Science 2014. **313**: p. 591-599.
98. Chaussemier, M., Pourmohtashama, E., Gelus D., Pécoul, N., Perrot, H., Lédion, J., Cheap-Charpentier, H., and Horner, O. , *State of art of natural inhibitors of calcium carbonate scaling. A review article*. Desalination, 2015. **356**: p. 47-55.
99. Estievenart, C., Kohler, N., Ropital, F., Fiaud, C., *Mechanisms of Scale and Corrosion Inhibition by Polyaspartates*. NACE International.
100. Hasson, D., Shemer, H., Sher, A., *State of the Art of Friendly "Green" Scale Control Inhibitors: A Review Article*. Industrial & Engineering Chemistry Research, 2011. **50**(12): p. 7601-7607.
101. Konstantinos, D., Neofotistou, E., Mavredaki, E., Tsiknakis, M., Sarigiannidou, E., Katarachia, S. D., *Inorganic foulants in membrane systems: chemical control strategies and the contribution of "green chemistry"*. Desalination, 2005. **179**(1-3): p. 281-295.
102. Kirboga, S., Öner, M., *The inhibitory effects of carboxymethyl inulin on the seeded growth of calcium carbonate*. Colloids and Surfaces B: Biointerfaces, 2012. **91**: p. 18-25.

103. Setta, F., Neville, A., *Efficiency assessment of inhibitors on CaCO₃ precipitation kinetics in the bulk and deposition on a stainless steel surface (316 L)*. Desalination, 2011. **281**: p. 340–347.
104. Riazi, M.R., *Characterization and properties of petroleum fractions*, ed. First. 2005, Philadelphia, PA: American Society for testing and materials.
105. Angeli, P., Hewitt, G. , *Flow structure in horizontal oil–water flow*. International Journal of Multiphase Flow, 2000. **26**(7): p. 1117-1140.
106. Al-Yaari, M., Abu-Sharkh, B. , *CFD Prediction of Stratified Oil-Water Flow in a Horizontal Pipe*. Asian Transactions on Engineering, 2011. **01**(05).
107. Mukhaimer, A., Al-Sarkhi, A., El Nakla, M., Ahmed, W. H., Al-Hadhrami, L., *Effect of water salinity on flow pattern and pressure drop in oil–water flow*. Journal of Petroleum Science and Engineering, 2015. **128**: p. 145-149.
108. Fairuzov, Y.V., Arenas-Medina, P., Verdejo-Fierro, J., Gonzalez-Islas, R., *Flow Pattern Transitions in Horizontal Pipelines Carrying Oil-Water Mixtures: Full-Scale Experiments*. Journal of Energy Resources Technology, 2000. **122**(4): p. 169-176.
109. Vralstad, T., Fossen, M., Sjoblom, J., Randhol, P., *Influence of interfacial tension on seeded calcium carbonate scale precipitation: Effect of adsorbed asphaltenes*. Journal of Dispersion Science and Technology, 2008. **29**(3): p. 440-446.
110. Sullivan, A.P. and P.K. Kilpatrick, *The effects of inorganic solid particles on water and crude oil emulsion stability*. Industrial & Engineering Chemistry Research, 2002. **41**(14): p. 3389-3404.
111. Poindexter, M.K., Mars, S. C., *Inorganic Solid Content Governs Water-in-Crude Oil Emulsion Stability Predictions*. Energy & Fuels, 2009. **23**: p. 1258-1268.
112. Khelifa, A., Stoffyn, P., Hill, P. S., Lee, K., *Characteristics of Oil Droplets Stabilized by Mineral Particles: Effects of Oil Type and Temperature*. Spill Science & Technology Bulletin, 2002. **8**(1): p. 19-30.
113. Khelifa, A., Hill, P., Stoffyn, P., Lee, K., *Characteristics of Oil Droplets Stabilized by Mineral Particles: The Effect of Salinity*. Vol. 2003. 2003. 963-970.
114. Clayton, T.C., John, D . Schwarzkopf, M. Sommerfeld, and Yutaka, T., *Properties of Dispersed Phase Flows*, in *Multiphase Flows with Droplets and Particles, Second Edition*. 2011, CRC Press. p. 17-38.
115. *Properties of Dispersed Phase Flows*, in *Multiphase Flows with Droplets and Particles, Second Edition*. 2011, CRC Press. p. 17-38.
116. Roisman, I.V., Oweis, G. F., Ceccio, S. L., Lyczkowski, R., Troutt, T. R., Mashayek, F., Tsuji, Y., Eaton, J. K., Tropea, C., Matsumoto Y. , *Multiphase Interactions*, in *Multiphase Flow Handbook*. 2005, CRC Press. p. 12-1-12-134.
117. Becher, P., *Emulsion: theory and practice*. 3 rd ed. 2001: American Chemical Society.
118. Kumar, R., Kumar, M., Mahadevan, N., *Multiple Emulsions: A review*. International Journal of Recent Advances in Pharmaceutical Research, 2012. **2**(1): p. 9-19.
119. Kralova, I., Sjöblom, J., Øye, G., Simon, S., Grimes, B. A., Pas, K., *Heavy Crude Oils/Particle Stabilized Emulsions*. Advances in Colloid and Interface Science, 2011. **169**.
120. Zhang, J., Li, L., Wang, J., Sun, H., Xu, J., Sun, D., *Double Inversion of Emulsions Induced by Salt Concentration*. Langmuir, 2012. **28**.

121. Palou, R., Mosqueira, M., *Transportation of heavy and extra-heavy crude oil by pipeline: A review*. Journal of Petroleum Science and Engineering, 2011. **75**.
122. Rimmer, D.P., Gregoli, A. A., Hamshar, J. A., Yildirim, E. , *Pipeline Emulsion Transportation for Heavy Oils*, in *Emulsions*. 1992, American Chemical Society. p. 295-312.
123. Sotgia, G., Tartarini, P., Stalio, E. , *Experimental analysis of flow regimes and pressure drop reduction in oil–water mixtures*. International Journal of Multiphase Flow, 2008. **34**: p. 1161–1174.
124. Gafonova, O.V., Yarranton, H. W., *The Stabilization of Water-in-Hydrocarbon Emulsions by Asphaltenes and Resins*. Journal of Colloid and Interface Science, 2001. **241**(2): p. 469–478.
125. Sztukowski, D.M., Yarranton, H. W. , *Oilfield solids and water-in-oil emulsion stability*. Journal of Colloid and Interface Science, 2005. **285**(2): p. 821-833.
126. Trallero, J.L., Sarica, C., Brill, J. P., *A study of oil/ water flow patterns in horizontal pipes*. SPE production and facilities 1997.
127. Mandal, A., Bera, A., *Modeling of flow of oil-in-water emulsions through porous media*. Petroleum Science, 2015. **12**(2): p. 273-281.
128. Kevin, C.T., B., Hawkins, F. , *Emulsions in Enhanced Oil Recovery*, in *Emulsions*. 1992, American Chemical Society. p. 263-293.
129. Peng, B., Jixiang, Guo, Zhaoxia, D., Mingyuan, Li, Zhaoliang, Wu, Meiqin, Lin, *Formation of Crude Oil Emulsions in Chemical Flooding*, in *Emulsions and Emulsion Stability*. 2005, CRC Press. p. 517-547.
130. Isaacs, E.E., Chow, R. S. , *Practical Aspects of Emulsion Stability*, in *Emulsions*. 1992, American Chemical Society. p. 51-77.
131. Fingasa, M., Fieldhouseb, B., *Studies on crude oil and petroleum product emulsions: Water resolution and rheology*. Colloids and Surfaces: Physicochem. Eng. Aspects, 2009. **333**(1-3): p. 67-81.
132. Farah, M.A., Oliveira, R. C., Caldas, J. N., Rajagopal, K., *Viscosity of water-in-oil emulsions: Variation with temperature and water volume fraction*. Journal of Petroleum Science and Engineering, 2005. **48**(3–4): p. 169-184.
133. Quintero, C., Noïk, C., Dalmazzone, C., Grossiord, J., *Modelling and characterisation of diluted and concentrated water-in-crude oil emulsions: comparison with classical behaviour*. Rheologica Acta, 2008. **47**(4): p. 417-424.
134. Hunter, R.J., Leyendekkers, J. V., *Viscoelectric coefficient for water*. Journal of the Chemical Society, Faraday Transactions 1: Physical Chemistry in Condensed Phases, 1978. **74**(0): p. 450-455.
135. Pal, R., Rhodes, E., *Viscosity/Concentration Relationships for Emulsions*. Journal of Rheology, 1989. **33**(7): p. 1021-1045.
136. Gisle, O., Marit-Helen, E., Trond, E., Havre, J. S., Hans, O., Øystein B., Harald K., , Glomm W., Hannisdal A., Knag M, Hemmingsen P. , *Modern Characterization Techniques for Crude Oils, Their Emulsions, and Functionalized Surfaces*, in *Emulsions and Emulsion Stability*. 2005, CRC Press. p. 415-476.
137. Kokal, S., *Crude oil Emulsions: A state of the art review*. SPE production and facilities, 2005.
138. Øystein, S., Westvik, A., Aulfem, A. H. , Hemmingsen, P. V., *Droplet Size Distributions of Oil-in-Water Emulsions under High Pressures by Video Microscopy*, in *Emulsions and Emulsion Stability*. 2005, CRC Press. p. 631-649.

139. Trifkovic, M., Sheikhzadeh, M., Rohani, S., *Kinetics Estimation and Single and Multi-Objective Optimization of a Seeded, Anti-Solvent, Isothermal Batch Crystallizer*. Industrial & Engineering Chemistry Research, 2008. **47**(5): p. 1586-1595.
140. Huimin, L., *Science and Engineering of Droplets - Fundamentals and Applications*. William Andrew Publishing/Noyes.
141. Kumar, V., Taylo, M. K., Mehrotra, A., Stagner W. C., *Real-Time Particle Size Analysis Using Focused Beam Reflectance Measurement as a Process Analytical Technology Tool for a Continuous Granulation–Drying–Milling Process*. AAPS PharmSciTech, 2013. **14**(2): p. 523-530.
142. Arellano, M., Gonzalez, J., Enrique, A., Graciela, B., Hayat, F., Denis, L.,, *Online ice crystal size measurements by the focused beam reflectance method (FBRM) during sorbet freezing*. Procedia Food Science, 2011. **1**: p. 1256-1264.
143. Benito, J.M., Ríos G., Pazos C., Coca J., *Droplet Size Distribution of Oil-Water Emulsions by Confocal Laser Scanning Microscopy*, in *Particle Sizing and Characterization*. 2004, American Chemical Society. p. 75-88.
144. Dukhin, A.S.a.G., P.J. , *Ultrasound for Characterizing Emulsions and Microemulsions*, in *Emulsion and Emulsion Stability*. 2005, CRC Press.
145. Brar, S.K., Verma, M., *Measurement of nanoparticles by light-scattering techniques*. Trends in Analytical Chemistry, 2011. **30**(1): p. 4-17.
146. Black, L.D., McQuay, M. Q., Bonin, M. P., *Laser-based techniques for particle-size measurement: A review of sizing methods and their industrial applications*. 1996. **22**(3).
147. Nicoli, D.F., Hasapidis, K., Hagan, P. O', McKenzie, D. C., Wu, J. S., Chang, Y. J., Schade, B. E. H., *High-Resolution Particle Size Analysis of Mostly Submicrometer Dispersions and Emulsions by Simultaneous Combination of Dynamic Light Scattering and Single-Particle Optical Sensing*, in *Particle Size Distribution III*. 1998, American Chemical Society. p. 52-76.
148. Haskell, R.J., *Characterization of submicron systems via optical methods*. Journal of Pharmaceutical Sciences, 1998. **87**(2).
149. Rao, F., Liu, Q., *Froth Treatment in Athabasca Oil Sands Bitumen Recovery Process: A Review*. Energy & Fuels, 2013. **27**(12): p. 7199-7207.
150. Dickinson, E., *Introduction to Food Colloids*. 1992, Oxford: Oxford University Press.
151. Mingyuan, L., Meiqin, L., Zhaoliang, W., Alfred, A. C.,, *The influence of NaOH on the stability of paraffinic crude oil emulsion*. Fuel, 2005. **84**(2–3): p. 183-187.
152. Arla, D., Siquin, A., Palermo, T., Hurtevent, C. Graciaa, A. Dicharry, C., *Influence of pH and Water Content on the Type and Stability of Acidic Crude Oil Emulsions†*. Energy & Fuels, 2007. **21**(3): p. 1337-1342.
153. *Emulsion Stability*, in *Food Emulsions*. 2015, CRC Press. p. 289-382.
154. Friberg, S., Larsson, K., Sjoblom, J., *Food Emulsions*. Boca Raton: CRC Press, 2003.
155. Rousseau, D., *Fat crystals and emulsion stability - a review*. Food Research International, 2000. **33**: p. 3-14.
156. McClements, D.J., *Crystals and crystallization in oil-in-water emulsions: Implications for emulsion-based delivery systems*. Advances in Colloid and Interface Science 2012. **174**: p. 1-30.

157. Coupland, J.N., *Crystallization in emulsions*. Current Opinion in Colloid & Interface Science, 2002. **7**(5–6): p. 445-450.
158. McCLEMENTS, D.J., DUNGAN, S.R., GERMAN, J.B., SIMONEAU, C., and KINSELLA, J.E., *Droplet Size and Emulsifier Type Affect Crystallization and Melting of Hydrocarbon-in-Water Emulsion*. Journal of food science, 1993. **58**(5).
159. McClements, D.J., Dungan, S. R., *Effect of Colloidal Interactions on the Rate of Interdroplet Heterogeneous Nucleation in Oil-in-Water Emulsions*. Journal of Colloid and Interface Science, 1997. **186**: p. 17-28.
160. Lei, M.L., P. G. Sun, Z. B. Tang, W. H., *Effects of organic additives on the morphology of calcium carbonate particles in the presence of CTAB*. Materials Letters, 2006. **60**(9): p. 1261-1264.
161. Aleksandra Szczes', E.C., Lucyna Hołysz *Influence of ionic surfactants on the properties of freshly precipitated calcium carbonate*. Colloids and Surfaces A: Physicochemical and Engineering Aspects, 2007. **297**: p. 14-18.
162. Aleksandra, S., *Influence of the surfactant nature on the calcium carbonate synthesis in water-in-oil emulsion*. Journal of Crystal Growth, 2009. **311**(4): p. 1129-1135.
163. Kaasa, B., Sandengen, K., Ostvold, T., *Thermodynamic Predictions of Scale Potential, pH and Gas Solubility in Glycol Containing Systems*, in *SPE International Symposium on Oilfield Scale*. 2005, Society of Petroleum Engineers: Aberdeen, United Kingdom. p. 13.
164. Flaten, E.M., Seiersten, M., Andreassen, Jens-Petter, *Induction time studies of calcium carbonate in ethylene glycol and water*. Chemical Engineering Research and Design, 2010. **88**(12): p. 1659-1668.
165. Bukuaghangin, O., Neville, A. and Charpentier, T. *Scale Formation in Multiphase Conditions*. in *Oilfield Chemistry Symposium*. 2015. Gielo.
166. Jaho, S., Sygouni, V., Rokidi, S. G., Parthenios, J., Koutsoukos, P. G., Paraskeva, C. A., *Precipitation of Calcium Carbonate in Porous Media in the Presence of n-Dodecane*. Crystal Growth & Design, 2016. **16**(12): p. 6874-6884.
167. Natsi, P.D., Rokidi, S., Koutsoukos, P. G., *Calcium Carbonate Scale Formation and Prevention in Aqueous Solutions and Mixed Solvents*, in *CORROSION 2016*. 2016, NACE International: Vancouver, British Columbia, Canada. p. 14.
168. Keogh, W., Neville, A., Huggan, Mich., Eroini, V., Olsen, J. H., Nielsen, F. M., Baraka-Lokmane, S., Bourdelet, E., Ellingsen, J. A., Bache, O., Charpentier, T., *Deposition of Inorganic Carbonate, Sulfate, and Sulfide Scales on Antifouling Surfaces in Multiphase Flow*. Energy & Fuels, 2017. **31**(11): p. 11838-11851.
169. Shell, C., *SHELLSOL OMS data sheet*. 22/07/2005.
170. Cervantes, T.A., Díaz, Cruz M., Domínguez, Aguilar, M. A., González Velázquez, J. L., *Effect of Flow Rate on the Corrosion Products Formed on Traditional and New Generation API 5L X-70 in a Sour Brine Environment*. Int. J. Electrochem. Sci., 2015. **10**: p. 2904-2920.
171. Rivero, E., Granados, P., River, F., Cruz, M., Gonzalez, I., *Mass transfer modeling and simulation at a rotating cylinder electrode (RCE) reactor under turbulent flow for copper recovery*. Chemical Engineering Science, 2010. **65**: p. 3042–3049.
172. Hesham, S., Abd El Moneim, A., *Electrowinning of Copper Using Rotating Cylinder Electrode Utilizing Lead Anode*. Engineering, 2011. **3**: p. 340-358.
173. Gabe, D.R., Wilox, G. D., *The rotating cylinder electrode: its continued development and application*. Journal of applied electrochemistry 1998. **28**.

174. Dong, H.Y., Kyung, S. Y., *Effects of schmidt number on turbulent mass transfer around a Rotating Circular Cylinder*. Journal of fluid engineering, 2011. **133**.
175. Silverman, D.C., *Study of Mass Transport Limited Corrosion Using Pine Rotated Cylinder Electrodes. An overview of theory and practice*. 2006.
176. Coulson, J.M., Richardson, J. F. , *Chemical engineering, fluid flow, heat transfer and mass transfer*. 6 ed. Vol. I. 1999: Butterworth- Hienemann.
177. Gabe, D.R., *The rotating cylinder electrode: a review of development*. Journal of applied electrochemistry, 1983: p. 3-22.
178. Heeg, B., Moros, T., Klenerman, D., *Persistency of corrosion inhibitor film on c-steel under multiphase flow [part I]: The jet- cylinder arrangement*. Corrosion Science, 1998. **39**.
179. Efir, K.D., Wright, E.J., Boros, J.A. , Hailey, T.G., *Correlation of Steel Corrosion in Pipe Flow with Jet Impingement and Rotating Cylinder Tests*. Corrosion, 1993. **49**(12): p. 992- 1003.
180. Hwang, A.J., Yang, K., Yoon, D., Bremhorst, K., *Flow field characterization of a rotating cylinder*. International Journal of Heat and Fluid Flow 2008. **29**.
181. Heeg, B., Moros, T., Klenerman, D., *Persistency of corrosion inhibitor films on C-steel under multiphase flow conditions. Part I: The jet-cylinder arrangement*. Corrosion Science, 1998. **40**(8): p. 1303-1311.
182. Pal, R., *Mechanism of Turbulent Drag Reduction in Emulsions and Bubbly Suspensions*. Industrial & Engineering Chemistry Research, 2007. **46**(2): p. 618-622.
183. Pal, R., *Pipeline flow of unstable and surfactant-stabilized emulsions*. AIChE Journal, 1993. **39**(11): p. 1754-1764.
184. Omer, A., Pal, R., *Effects of Surfactant and Water Concentrations on Pipeline Flow of Emulsions*. Industrial & Engineering Chemistry Research, 2013. **52**(26): p. 9099-9105.
185. Nestic, S., Solvi, G., Enerhaug, J. , *Comparison of the rotating cylinder and pipe flow tests for flow- sensitive carbon dioxide corrosion*. Corrosion 1995. **51**(10): p. 773-787.
186. Silverman, D.C., *Simplified Equation for Simulating Velocity-Sensitive Corrosion in the Rotating Cylinder Electrode at Higher Reynolds Numbers- A review*. Corrosion 2004. **60**(1003).
187. Silverman, D.C., *Conditions for Similarity of Mass-Transfer Coefficients and Fluid Shear Stresses Between the Rotating Cylinder Electrode and Pipe*. CORROSION, 2005. **61**(6): p. 515-518.
188. Al Nasser, W.N., Al Salhi, F. H., *Kinetics determination of calcium carbonate precipitation behavior by inline techniques*. Powder Technology, 2015. **270**, Part **B**(0): p. 548-560.
189. Leba, P., Cameirao, H., Herri, A., Darbouret, J., Peytavy M., Glénat J., *Chord length distributions measurements during crystallization and agglomeration of gas hydrate in a water-in-oil emulsion: Simulation and experimentation*. Chemical Engineering Science, 2010. **65**(3): p. 1185-1200.
190. *Malvern mastersizer 2000*. user manual, MAN0348, 2007(1).
191. Heath, A.R.F., P. D., Bahri, P. A., Swift, J. D., *Estimating Average Particle Size by Focused Beam Reflectance Measurement (FBRM)*. Part. Part. Syst. Charact., 2002. **19**: p. 84-95.

192. Maass, S., Wollny, S., Voigt, A., Kraume, M. , *Experimental comparison of measurement techniques for drop size distributions in liquid/liquid dispersions*. Exp. Fluids, article in press, 2010.
193. Khatibi, M., *Experimental study on droplet size of dispersed oil- water flow*, in *Department of energy and process engineering*. 2013, Norwegian university of science and technology.
194. James-Smith, M.A., K. Alford, and D.O. Shah, *A novel method to quantify the amount of surfactant at the oil/water interface and to determine total interfacial area of emulsions*. Journal of Colloid and Interface Science, 2007. **310**(2): p. 590-598.
195. TOLEDO, M., *LASENTEC D600 Hardware manual*, 2002.
196. Miriam, B., *Crystallization Kinetics of Calcium Carbonate in Relation to Surface Scale Formation*. 2014, University of Leeds.
197. SHAW, S.S., *Investigation into the mechanisms of formation and prevention of barium sulphate oilfield scale*, in *Institute of Petroleum Engineering*. 2012, Heriot-Watt University, Edinburgh.
198. Dickinson, S.R., McGrath, K. M., *Quantitative determination of binary and tertiary calcium carbonate mixtures using powder X-ray diffraction*. Analyst, 2001. **126**(7): p. 1118-1121.
199. Kontoyannis, C.G., Vagenas, N. V., *Calcium carbonate phase analysis using XRD and FT-Raman spectroscopy*. Analyst, 2000. **125**(2): p. 251-255.
200. Zhuona, Z., Yidong, X., Xurong, X., Haihua, P., Ruikang, T., *Transformation of amorphous calcium carbonate into aragonite*. Journal of Crystal Growth, 2012. **343**(1): p. 62-67.
201. Beck, R., Andreassen, J., *The onset of spherulitic growth in crystallization of calcium carbonate*. Journal of Crystal Growth, 2010. **312**(15): p. 2226-2238.
202. Sawada, K., *The mechanisms of crystallization and transformation of calcium carbonates*. Pure & Appl. Chem, 1997. **69**(5): p. 921-928.
203. Sparks, R.G., Dobbs, C. L., *The Use of Laser Backscatter Instrumentation for the On-line Measurement of the Particle Size Distribution of Emulsions*. Part. Part. Syst. Charact, 1993(10): p. 279-289.
204. Olivier, M., Jean-Paul, K., Christian, H., Berthe, R., *Particle Size Determination by Laser Reflection: Methodology and Problems*. Part. Part. Syst. Charact., 1996. **13**: p. 10-17.
205. Hostomsky, J., Jones, A. G., *Calcium carbonate crystallization, agglomeration and form during continuous precipitation from solution*. Journal of Physics D: Applied Physics, 1991. **24**(2): p. 165.
206. Andreassen, J., Hounslow, M. J., *Growth and aggregation of vaterite in seeded-batch experiments*. AIChE Journal, 2004. **50**(11): p. 2772-2782.
207. Jaho, S., Sygouni, V., Rokidi, S. G., Parthenios, J., Koutsoukos, P. G., Paraskeva, C. A., *Precipitation of Calcium Carbonate in Porous Media in the Presence of n-Dodecane*. Vol. 16. 2016.
208. Srisa-nga, S., Adrian, F. E., Edward, T. W., *The Secondary Nucleation Threshold and Crystal Growth of α -Glucose Monohydrate in Aqueous Solution*. Crystal Growth & Design, 2006. **6**(3): p. 795-801.
209. El-Hamouz, A.C., Stewart, A. M. , *On-Line Drop Size Distribution Measurement of Oil-Water Dispersion Using a Par-Tec M300 laser Backscatter Instrument*. Society of Petroleum Engineers.

210. Khatibi, M., *Experimental study on droplet size of dispersed oil- water flow*, in *Energy and Process Engineering*. 2013, Norwegian University of Science and Technology.
211. Qun, Y.Z., Chow, P., S., Tan, R. B., *Interpretation of Focused Beam Reflectance Measurement (FBRM) Data via Simulated Crystallization*. *Organic Process Research & Development*, 2008. **12**(4): p. 646-654.
212. Turner, D.M., Kleehammer, D. T., Miller, K. T., Carolyn, D., Talley, D. L., *Formation of hydrate obstructions in pipelines: Hydrate particle development and slurry flow*. 2005.
213. Giuffre, A.J., Gagnon, A. C., De Yoreo, J. J., Dove, P. M., *Isotopic tracer evidence for the amorphous calcium carbonate to calcite transformation by dissolution–reprecipitation*. *Geochimica et Cosmochimica Acta*, 2015. **165**: p. 407-417.
214. Ostwald, W., *Z. phys. chem*, 1897. **22**: p. 289-330.
215. Mullin, J.W., *6 -Crystal growth*, in *Crystallization (Fourth Edition)*. 2001, Butterworth-Heinemann: Oxford. p. 216-288.
216. *Minerology Database, Online*. 2014.
217. Leubner, I.H., *Crystal formation (nucleation) under kinetically-controlled and diffusion-controlled growth conditions*. *The Journal of Physical Chemistry*, 1987. **91**(23): p. 6069-6073.
218. Khawam, A., Flanagan D. R., *Complementary Use of Model-Free and Modelistic Methods in the Analysis of Solid-State Kinetics*. *The Journal of Physical Chemistry B*, 2005. **109**(20): p. 10073-10080.
219. Bischoff, J.L., Fyfe W. S., *Catalysis, inhibition, and the calcite-aragonite problem; [Part] 1, The calcite- aragonite transformation*. *American Journal of Science*, 1968. **266**: p. 59-79.
220. Bischoff, J.L., *Catalysis, inhibition, and the calcite-aragonite problem; [Part] 2, The vaterite-aragonite transformation*. *American Journal of Science*, 1968. **266**: p. 80-90.
221. Bischoff, J.L., *Temperature controls on aragonite-calcite transformation in aqueous solution1*. *American Mineralogist*, 1969. **54**(1-2): p. 149-155.
222. Jones, A.G., *6 - Crystal agglomeration and disruption*, in *Crystallization Process Systems*. 2002, Butterworth-Heinemann: Oxford. p. 155-189.

Appendix A-1

Raw data from FBRM measurement

Figures A-1 to A-4 show the high intensity peaks which are detected during the cleaning period of the FBRM probe. These peaks are removed when interpreting the results.

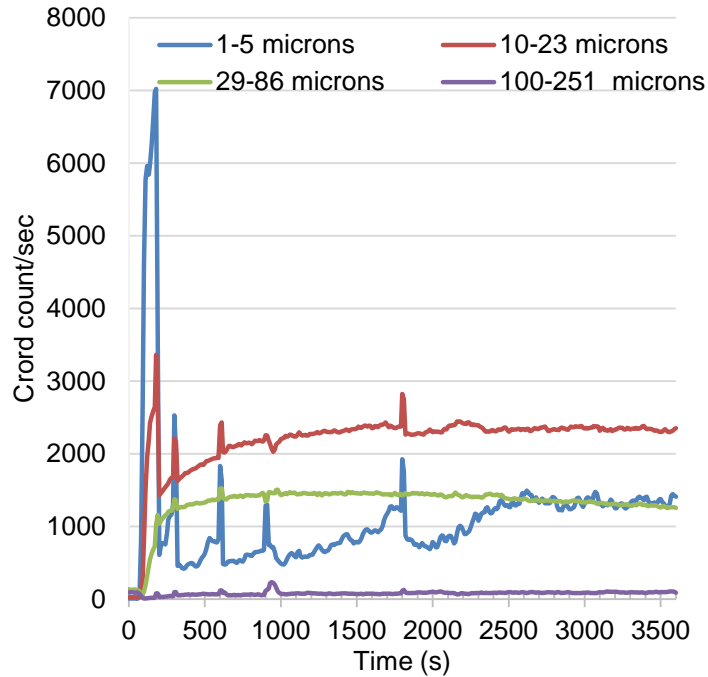


Figure A- 1 Chord counts (un-weighted) for brine 3 (0.045M) at 60° C, agitated at 550 rpm

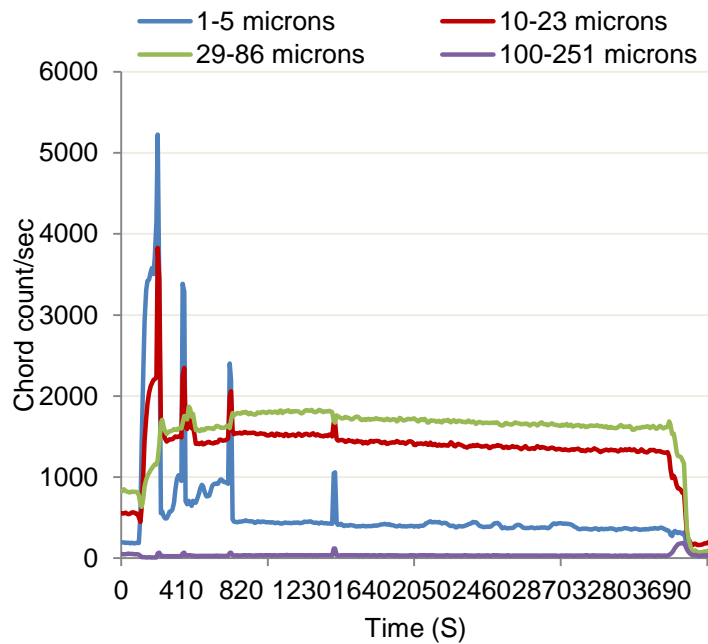


Figure A- 2 Chord counts (un-weighted) for 23% oil-brine 3 (0.045M) at 60° C, agitated at 750 rpm

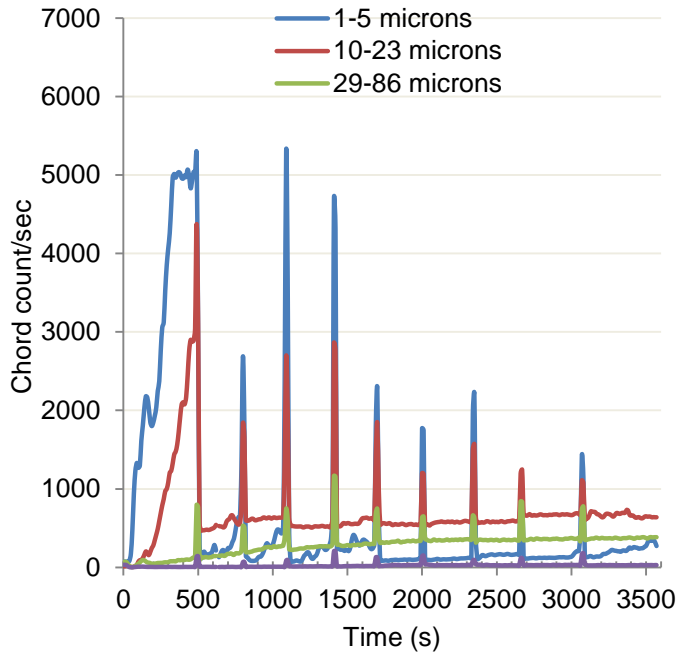


Figure A- 3 Chord counts (un-weighted) for brine 3 (0.045M) at 30° C, agitated at 550 rpm

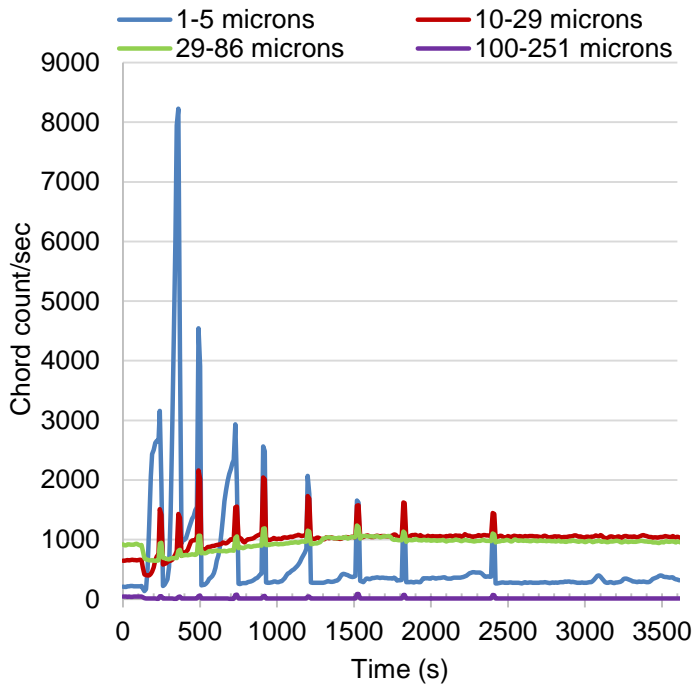


Figure A- 4 Chord counts (un-weighted) for 10% oil-brine 3 (0.045M) at 30° C, agitated at 550 rpm

Appendix A-2

Different weighted mean size

Table A- 1 Calculation of un-weighted and square-weighted mean size for different systems at 30° C

Chord	10% oil-saline system				Brine 3 system (no oil droplets)				10% oil-brine 3 (0.045M) system			
L_i	f_i	$f_i \times L_i$	$f_i \times L_i^2$	$f_i \times L_i^3$	f_i	$f_i \times L_i$	$f_i \times L_i^2$	$f_i \times L_i^3$	f_i	$f_i \times L_i$	$f_i \times L_i^2$	$f_i \times L_i^3$
1	0.166	0.166	0.166	0.166	0.063	0.063	0.063	0.063	0.044	0.044	0.044	0.044
1.08	0.179	0.193	0.209	0.225	0.068	0.073	0.079	0.086	0.047	0.051	0.055	0.059
1.166	0.201	0.234	0.273	0.319	0.079	0.092	0.107	0.125	0.053	0.062	0.072	0.084
1.259	0.299	0.376	0.474	0.597	0.146	0.184	0.231	0.291	0.078	0.098	0.124	0.156
1.359	0.323	0.439	0.597	0.811	0.158	0.215	0.292	0.397	0.084	0.114	0.155	0.211
1.468	0.576	0.846	1.241	1.822	0.198	0.291	0.427	0.626	0.106	0.156	0.228	0.335
1.585	0.716	1.135	1.799	2.85	0.225	0.357	0.565	0.896	0.121	0.192	0.304	0.482
1.711	0.79	1.352	2.313	3.95	0.263	0.450	0.770	1.317	0.149	0.255	0.436	0.746
1.848	0.86	1.589	2.937	5.42	0.293	0.541	1.001	1.849	0.169	0.312	0.577	1.067
1.995	0.502	1.001	1.998	3.98	0.413	0.824	1.644	3.279	0.195	0.389	0.776	1.548
2.154	0.447	0.963	2.074	4.46	0.537	1.157	2.492	5.367	0.236	0.508	1.095	2.359
2.326	0.375	0.872	2.029	4.71	0.705	1.640	3.814	8.872	0.289	0.672	1.564	3.637

2.512	0.409	1.027	2.581	6.48	0.859	2.158	5.420	13.616	0.328	0.824	2.070	5.199
2.712	0.361	0.979	2.655	7.20	0.765	2.075	5.627	15.259	0.366	0.993	2.692	7.300
2.929	0.38	1.113	3.260	9.54	0.793	2.323	6.803	19.927	0.432	1.265	3.706	10.855
3.162	0.438	1.385	4.379	13.84	0.952	3.010	9.518	30.097	0.478	1.511	4.779	15.112
3.415	0.473	1.615	5.516	18.83	1.197	4.088	13.960	47.672	0.568	1.940	6.624	22.621
3.687	0.472	1.740	6.416	23.65	1.834	6.762	24.931	91.922	0.681	2.511	9.257	34.132
3.981	0.634	2.524	10.048	40.00	2.683	10.68	42.521	169.277	0.809	3.221	12.821	51.042
4.299	0.645	2.773	11.921	51.24	1.478	6.354	27.316	117.429	0.851	3.658	15.728	67.613
4.642	0.782	3.630	16.851	78.221	1.112	5.162	23.962	111.230	1.042	4.837	22.453	104.228
5.012	1.024	5.132	25.723	128.92	1.013	5.077	25.447	127.539	0.989	4.957	24.844	124.517
5.412	1.687	9.130	49.412	267.41	1.122	6.072	32.863	177.855	1.047	5.666	30.666	165.966
5.843	2.248	13.13	76.748	448.44	1.221	7.134	41.686	243.570	1.106	6.462	37.760	220.629
6.31	1.418	8.948	56.459	356.25	1.602	10.10	63.785	402.486	1.103	6.960	43.917	277.117
6.813	0.959	6.534	44.514	303.27	1.856	12.64	86.150	586.939	1.21	8.244	56.165	382.649
7.356	0.932	6.856	50.431	370.97	1.616	11.88	87.443	643.230	1.357	9.982	73.428	540.138
7.943	1.088	8.642	68.643	545.23	1.471	11.68	92.807	737.168	1.512	12.010	95.394	757.714
8.577	1.025	8.791	75.404	646.74	1.573	13.49	115.71	992.510	1.666	14.289	122.559	1051.19
9.261	1.115	10.32	95.629	885.62	1.641	15.19	140.74	1303.414	1.703	15.771	146.060	1352.66

10	1.207	12.07	120.700	1207.00	1.72	17.20	172.00	1720.000	1.852	18.520	185.200	1852.00
10.798	1.338	14.44	156.007	1684.55	1.912	20.64	222.93	2407.231	1.959	21.153	228.413	2466.41
11.659	2.474	28.84	336.296	3920.88	2.004	23.36	272.40	3176.008	2.096	24.437	284.914	3321.81
12.589	2.353	29.62	372.910	4694.56	2.318	29.18	367.36	4624.738	2.256	28.401	357.537	4501.04
13.594	3.766	51.19	695.945	9460.67	2.673	36.33	493.96	6714.919	2.356	32.027	435.381	5918.57
14.678	3.592	52.72	773.874	11358.91	3.193	46.86	687.91	10097.168	2.624	38.515	565.324	8297.83
15.849	3.669	58.15	921.619	14606.74	3.474	55.05	872.63	13830.421	2.826	44.789	709.865	11250.65
17.113	2.02	34.56	591.567	10123.48	3.766	64.44	1102.8	18873.775	3.226	55.207	944.749	16167.50
18.478	1.761	32.54	601.270	11110.26	4.242	78.38	1448.3	26763.047	3.224	59.573	1100.79	20340.42
19.953	1.922	38.35	765.191	15267.85	4.76	94.97	1895.0	37812.166	3.528	70.394	1404.57	28025.49
21.544	1.916	41.27	889.300	19159.07	4.712	101.5	2187.0	47117.724	3.923	84.517	1820.83	39228.11
23.263	2.267	52.73	1226.82	28539.65	4.813	111.9	2604.6	60591.684	3.974	92.447	2150.59	50029.37
25.119	2.419	60.76	1526.30	38339.18	4.565	114.6	2880.3	72351.547	4.227	106.178	2667.08	66994.52
27.123	8.285	224.7	6094.91	165312.49	4.355	118.1	3203.7	86896.309	4.577	124.142	3367.10	91325.93
29.286	8.356	244.7	7166.68	209883.64	4.261	124.7	3654.5	107026.59	4.765	139.548	4086.79	119685.92
31.623	3.49	110.3	3490.04	110365.82	3.7	117.0	3700.0	117006.75	4.964	156.977	4964.07	156978.79
34.145	4.154	141.8	4843.07	165366.61	3.45	117.8	4022.2	137341.07	4.726	161.369	5509.95	188137.37
36.869	2.799	103.1	3804.74	140277.16	2.595	95.67	3527.4	130053.31	4.513	166.390	6134.62	226177.50

39.811	2.777	110.5	4401.31	175220.59	1.802	71.73	2856.0	113700.93	4.119	163.982	6528.26	259896.87
42.987	2.611	112.2	4824.82	207404.55	1.274	54.76	2354.2	101200.07	3.652	156.989	6748.46	290096.29
46.416	2.473	114.7	5327.94	247301.78	0.702	32.58	1512.4	70200.507	3.087	143.286	6650.77	308702.23
50.119	2.256	113.0	5666.87	284018.27	0.569	28.51	1429.2	71634.042	2.578	129.207	6475.71	324556.35
54.117	1.762	95.35	5160.28	279258.91	0.484	26.19	1417.4	76709.032	1.915	103.634	5608.36	303507.84
58.434	1.341	78.36	4578.88	267562.73	0.401	23.43	1369.2	80009.438	1.293	75.555	4414.99	257985.55
63.096	1.003	63.28	3993.04	251945.39	0.415	26.18	1652.1	104244.60	0.894	56.408	3559.10	224565.48
68.129	0.673	45.85	3123.77	212819.34	0.352	23.98	1633.8	111311.15	0.503	34.269	2334.70	159061.12
73.564	0.442	32.51	2391.95	175961.75	0.4	29.42	2164.6	159241.40	0.461	33.913	2494.77	183525.72
79.433	0.332	26.37	2094.78	166395.27	0.524	41.62	3306.2	262623.86	0.315	25.021	1987.52	157875.03
85.77	0.264	22.64	1942.11	166575.12	0.525	45.02	3862.1	331257.35	0.261	22.386	1920.04	164682.23
92.612	0.177	16.39	1518.12	140596.67	0.539	49.91	4622.9	428144.68	0.224	20.745	1921.2	177930.26
100	0	0	0	0	0.495	49.50	4950.0	495000.00	0.101	10.100	1010.00	101000.00
107.978	0.167	18.03	1947.09	210243.37	0.406	43.83	4733.6	511130.58	0.061	6.587	711.214	76795.48
116.591	0.118	13.7	1604.02	187015.27	0.343	39.99	4662.5	543612.20	0.054	6.296	734.047	85583.26
125.893	0.091	11.45	1442.26	181570.85	0.156	19.63	2472.4	311264.32	0.028	3.525	443.773	55867.96
135.936	0.08	10.87	1478.28	200952.51	0.099	13.45	1829.3	248678.73	0.01	1.359	184.786	25119.06
146.78	0.031	4.550	667.875	98030.75	0.044	6.458	947.95	139140.42	0.008	1.174	172.355	25298.26

630.957	0	0	0	0	0	0	0	0	0	0	0	0
681.292	0	0	0	0	0	0	0	0	0	0	0	0
735.642	0	0	0	0	0	0	0	0	0	0	0	0
794.328	0	0	0	0	0	0	0	0	0	0	0	0
857.696	0	0	0	0	0	0	0	0	0	0	0	0
926.119	0	0	0	0	0	0	0	0	0	0	0	0
1000	0	0	0	0	0	0	0	0	0	0	0	0
Sum	99.9	2739.7	129551.2	8840201.0	100	2139.4	82505.0	5139949.7	100.002	2527.5	91636.7	4246878.3
(Un-wt)	$\frac{\sum f_i \times l_i}{\sum f_i}$		27.39		$\frac{\sum f_i \times l_i}{\sum f_i}$		21.39		$\frac{\sum f_i \times l_i}{\sum f_i}$		25.27	
(Sq-wt)	$\frac{\sum f_i \times l_i^3}{\sum f_i \times l_i^2}$		68.23		$\frac{\sum f_i \times l_i^3}{\sum f_i \times l_i^2}$		62.29		$\frac{\sum f_i \times l_i^3}{\sum f_i \times l_i^2}$		46.34	

Table A- 2 Calculation of un-weighted and square-weighted mean size for different systems at 60° C

Chord	10% oil-saline system				Brine 3 system (no oil droplets)				10% oil-brine 3 (0.045M) system			
L_i	f_i	$f_i \times L_i$	$f_i \times L_i^2$	$f_i \times L_i^3$	f_i	$f_i \times L_i$	$f_i \times L_i^2$	$f_i \times L_i^3$	f_i	$f_i \times L_i$	$f_i \times L_i^2$	$f_i \times L_i^3$
1	0.051	0.051	0.051	0.051	0.118	0.118	0.118	0.118	0.046	0.046	0.046	0.046
1.08	0.055	0.059	0.064	0.069	0.128	0.138	0.149	0.161	0.049	0.053	0.057	0.062
1.166	0.063	0.073	0.086	0.100	0.143	0.167	0.194	0.227	0.056	0.065	0.076	0.089
1.259	0.1	0.126	0.159	0.200	0.205	0.258	0.325	0.409	0.088	0.111	0.139	0.176
1.359	0.108	0.147	0.199	0.271	0.222	0.302	0.410	0.557	0.095	0.129	0.175	0.238
1.468	0.131	0.192	0.282	0.414	0.287	0.421	0.618	0.908	0.113	0.166	0.244	0.357
1.585	0.147	0.233	0.369	0.585	0.329	0.521	0.827	1.310	0.126	0.200	0.317	0.502
1.711	0.179	0.306	0.524	0.897	0.414	0.708	1.21	2.074	0.144	0.246	0.422	0.721
1.848	0.203	0.375	0.693	1.28	0.473	0.874	1.62	2.99	0.16	0.296	0.546	1.01
1.995	0.202	0.403	0.804	1.60	0.599	1.195	2.38	4.76	0.192	0.383	0.764	1.52
2.154	0.253	0.545	1.17	2.53	0.687	1.480	3.19	6.87	0.226	0.487	1.05	2.26
2.326	0.323	0.751	1.75	4.06	0.794	1.847	4.30	9.99	0.269	0.626	1.46	3.39
2.512	0.372	0.934	2.35	5.90	0.863	2.168	5.45	13.68	0.314	0.789	1.98	4.98
2.712	0.462	1.25	3.40	9.22	0.979	2.655	7.20	19.53	0.402	1.09	2.96	8.02
2.929	0.49	1.44	4.20	12.31	1.176	3.445	10.09	29.55	0.465	1.36	3.99	11.68
3.162	0.585	1.85	5.85	18.49	1.438	4.547	14.38	45.46	0.493	1.56	4.93	15.59

3.415	0.664	2.27	7.74	26.44	1.702	5.812	19.85	67.78	0.517	1.77	6.03	20.59
3.687	0.801	2.95	10.89	40.15	2.019	7.444	27.45	101.19	0.571	2.11	7.76	28.62
3.981	0.853	3.40	13.52	53.82	2.318	9.228	36.74	146.25	0.661	2.63	10.48	41.70
4.299	0.941	4.05	17.39	74.76	2.197	9.445	40.60	174.56	0.765	3.29	14.14	60.78
4.642	1.076	4.99	23.19	107.63	2.031	9.428	43.76	203.15	0.852	3.95	18.36	85.22
5.012	1.161	5.82	29.16	146.17	1.812	9.082	45.52	228.13	0.859	4.31	21.58	108.15
5.412	1.185	6.41	34.71	187.84	1.718	9.298	50.32	272.33	0.871	4.71	25.51	138.07
5.843	1.206	7.05	41.17	240.58	1.751	10.23	59.78	349.30	0.938	5.48	32.02	187.12
6.31	1.296	8.18	51.60	325.61	2.023	12.76	80.55	508.26	1.06	6.70	42.28	266.82
6.813	1.512	10.30	70.18	478.15	2.495	16.99	115.81	789.02	1.04	7.10	48.37	329.52
7.356	1.45	10.67	78.46	577.16	2.242	16.49	121.32	892.40	1.14	8.39	61.74	454.16
7.943	1.566	12.44	98.80	784.78	2.215	17.59	139.75	1110.01	1.21	9.58	76.09	604.37
8.577	1.698	14.56	124.91	1071.38	2.396	20.55	176.26	1511.80	1.34	11.45	98.21	842.34
9.261	1.648	15.26	141.34	1308.97	2.463	22.81	211.24	1956.31	1.39	12.89	119.39	1105.64
10	1.806	18.06	180.6	1806	2.445	24.45	244.50	2445	1.51	15.11	151.10	1511.00
10.798	1.713	18.50	199.73	2156.69	2.507	27.07	292.31	3156.34	1.67	18.05	194.95	2105.07
11.659	1.946	22.69	264.52	3084.09	2.525	29.44	343.23	4001.71	1.90	22.09	257.59	3003.26
12.589	1.844	23.21	292.24	3679.04	2.737	34.46	433.77	5460.70	1.91	24.04	302.70	3810.72

13.594	2.102	28.57	388.44	5280.49	2.795	38.00	516.51	7021.40	2.15	29.27	397.87	5408.61
14.678	2.149	31.54	462.99	6795.74	2.938	43.12	632.97	9290.79	2.27	33.29	488.63	7172.06
15.849	2.261	35.83	567.94	9001.32	2.956	46.85	742.52	11768.20	2.58	40.92	648.57	10279.3
17.113	2.5	42.78	732.14	12529.06	3.078	52.67	901.41	15425.78	2.65	45.37	776.36	13285.8
18.478	2.708	50.04	924.61	17084.94	3.174	58.65	1083.7	20024.97	2.93	54.07	999.04	18460.3
19.953	2.959	59.04	1178.04	23505.50	3.277	65.39	1304.6	26031.61	3.16	63.11	1259.2	25126.0
21.544	2.934	63.21	1361.80	29338.58	3.455	74.43	1603.6	34548.33	3.37	72.65	1565.0	33718.4
23.263	3.388	78.82	1833.47	42652.11	3.452	80.30	1868.1	43457.82	3.49	81.09	1886.5	43885.9
25.119	3.616	90.83	2281.57	57310.67	3.618	90.88	2282.8	57342.36	3.77	94.80	2381.2	59814.8
27.123	3.754	101.8	2761.66	74904.42	3.954	107.2	2908.7	78895.06	3.69	100.14	2716.0	73667.3
29.286	4.431	129.7	3800.33	111296.61	3.123	91.46	2678.5	78442.63	3.82	111.99	3279.7	96050.2
31.623	4.176	132.0	4176.06	132059.51	2.741	86.68	2741.0	86679.87	3.97	125.39	3965.0	125387.0
34.145	3.582	122.3	4176.19	142595.87	2.423	82.73	2824.9	96457.23	3.70	126.20	4309.1	147134.1
36.869	3.438	126.7	4673.35	172301.85	1.922	70.86	2612.6	96324.65	3.74	137.96	5086.5	187537.4
39.811	3.358	133.6	5322.15	211879.99	1.591	63.34	2521.6	100387.45	3.82	152.24	6060.7	241283.2
42.987	3.243	139.4	5992.68	257607.42	1.181	50.77	2182.3	93812.63	3.66	157.29	6761.4	290652.3
46.416	3.175	147.3	6840.36	317502.29	0.875	40.61	1885.1	87500.63	3.27	151.92	7051.5	327302.4
50.119	2.935	147.1	7372.47	369500.73	0.732	36.69	1838.7	92154.87	3.25	162.89	8163.7	409157.5

54.117	2.807	151.9	8220.72	444880.69	0.554	29.98	1622.4	87803.31	2.90	156.99	8496.0	459778.7
58.434	2.739	160.0	9352.40	546498.38	0.514	30.04	1755.0	102555.74	2.45	143.16	8365.6	488835.7
63.096	2.394	151.0	9530.77	601353.20	0.385	24.29	1532.7	96708.85	2.19	137.93	8702.7	549105.3
68.129	1.981	134.9	9194.93	626441.50	0.355	24.19	1647.7	112259.83	1.91	129.85	8846.8	602724.6
73.564	1.666	122.5	9015.83	663240.45	0.317	23.32	1715.5	126198.81	1.64	120.94	8896.7	654482.2
79.433	1.18	93.73	7445.33	591404.88	0.284	22.56	1791.9	142338.12	1.29	102.71	8158.3	648039.4
85.77	0.764	65.53	5620.36	482058.33	0.303	25.99	2229.0	191182.82	1.16	99.06	8496.7	728766.2
92.612	0.53	49.08	4545.80	420995.70	0.268	24.82	2298.6	212880.84	0.94	86.87	8045.2	745083.0
100	0	0	0	0	0.222	22.20	2220.0	222000	0.73	72.70	7270.0	727000.0
107.978	0.239	25.81	2786.56	300887.22	0.188	20.30	2191.9	236681.15	0.57	61.01	6587.4	711302.4
116.591	0.184	21.45	2501.20	291617.04	0.155	18.07	2106.9	245655.66	0.44	51.07	5953.9	694175.4
125.893	0.144	18.13	2282.26	287320.91	0.138	17.37	2187.1	275349.21	0.37	47.08	5927.5	746236.3
135.936	0.07	9.52	1293.50	175833.45	0.119	16.18	2198.9	298916.87	0.24	32.35	4397.9	597833.7
146.78	0.062	9.10	1335.75	196061.51	0.078	11.45	1680.4	246658.03	0.18	26.86	3942.6	578697.7
158.489	0.066	10.46	1657.84	262749.14	0.086	13.63	2160.2	342370.10	0.1	15.85	2511.8	398104.8
171.133	0.025	4.28	732.16	125297.18	0.065	11.12	1903.6	325772.67	0.08	13.69	2342.9	400951.0
184.785	0.05	9.24	1707.27	315478.78	0.058	10.72	1980.4	365955.38	0.04	7.39	1365.8	252383.0
199.526	0.022	4.39	875.83	174751.60	0.043	8.58	1711.8	341559.95	0.019	3.79	756.40	150921.8

857.696	0	0	0	0	0	0	0	0	0	0	0	0	0
926.119	0	0	0	0	0	0	0	0	0	0	0	0	0
1000	0	0	0	0	0	0	0	0	0	0	0	0	0
Sum	99.9	2739.7	129551.2	8840201.0	100	2139.4	82505.0	5139949.7	100.002	2527.5	91636.7	4246878.3	
(Un-wt)	$\frac{\sum f_i \times l_i}{\sum f_i}$		29.31		$\frac{\sum f_i \times l_i}{\sum f_i}$		18.83		$\frac{\sum f_i \times l_i}{\sum f_i}$		32.27		
(Sq-wt)	$\frac{\sum f_i \times l_i^3}{\sum f_i \times l_i^2}$		65.13		$\frac{\sum f_i \times l_i^3}{\sum f_i \times l_i^2}$		94.99		$\frac{\sum f_i \times l_i^3}{\sum f_i \times l_i^2}$		74.31		

Appendix B-1

Growth rate constants and the activation energy for growth at 40° C

a) For 0% oil-brine 4 (0.06M) at 40° C

The polymorphic thickness profiles follow an exponential growth function as shown in Figure B-1(b). Only the first 20 minutes are fitted for vaterite as it exhibit a clear decline after this time. Table B-1 shows the growth fitted function and parameters. Table B-2 shows the growth rate constants for the first 5 minutes which exhibits a high decrease by about 99 and 65% for vaterite and calcite, respectively within this time and this indicates the rapid growth behaviour for the brine at 40° C.

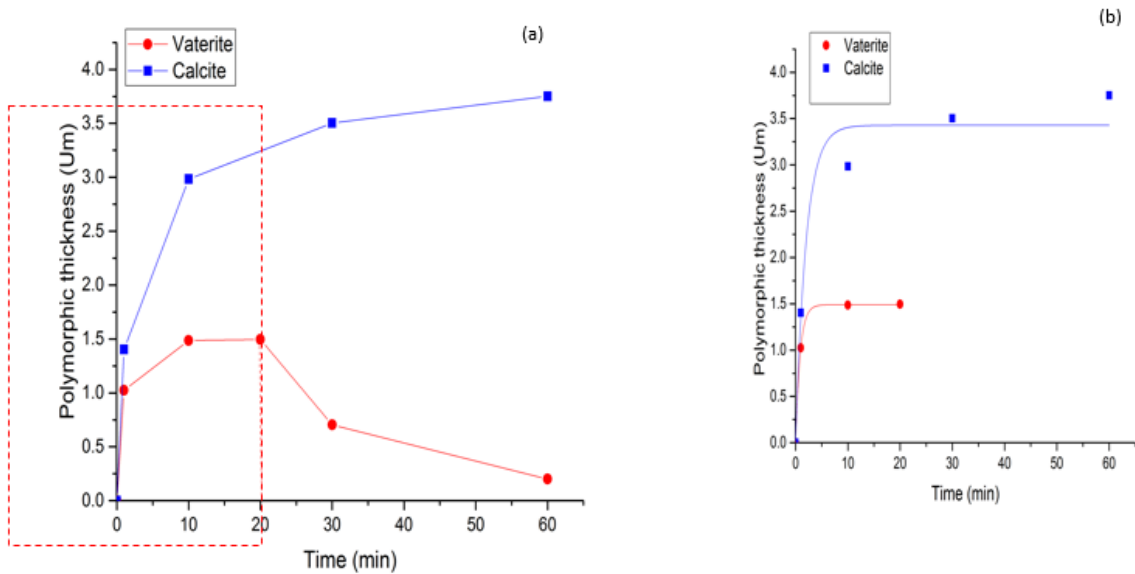


Figure B- 1 Polymorphic thickness versus time for brine 4 (0.06M) at 40° C; (a) calcite and vaterite thickness (μm), (b) curve fitting of the data

Table B- 1 The growth profile fitted function and parameters for brine 4 (0.06M) at 40° C

Polymorph	Exponential function, $y = A_1 - A_2 \exp(-kx)$			
	A_1	A_2	k	R^2
Vaterite	1.49050	1.49050	1.1617	0.999
Calcite	3.42816	3.40133	0.4950	0.971

Table B- 2 The polymorphic growth rate constants in m/sec in the early stages of the deposition process for brine 4 (0.06M) at 40° C

Growth rate constant		Vaterite		Calcite	
Time (min)	$\mu\text{m}/\text{min}$	m/ sec	$\mu\text{m}/\text{min}$	m/ sec	
1	0.5419	9.031×10^{-9}	1.026	1.711×10^{-8}	
2	0.1696	2.826×10^{-9}	0.6256	1.043×10^{-8}	
5	0.0052	8.662×10^{-11}	0.1417	2.362×10^{-9}	

b) For 23% oil-brine 4 (0.06M) at 40° C

The polymorphic thickness profiles follow an exponential growth function for the oil system at 40° C as shown in Figure B-2(b) and Table B-3. Only the first 10 minutes are fitted for vaterite as it exhibit a high decrease after this time. Table B-4 shows the growth rate constants for the first 10 minutes where the growth reduces by about 80 within 5 minutes and the growth reduction reaches to about 95% within 10 minutes. This is also an indication for the rapid growth behaviour in this temperature.

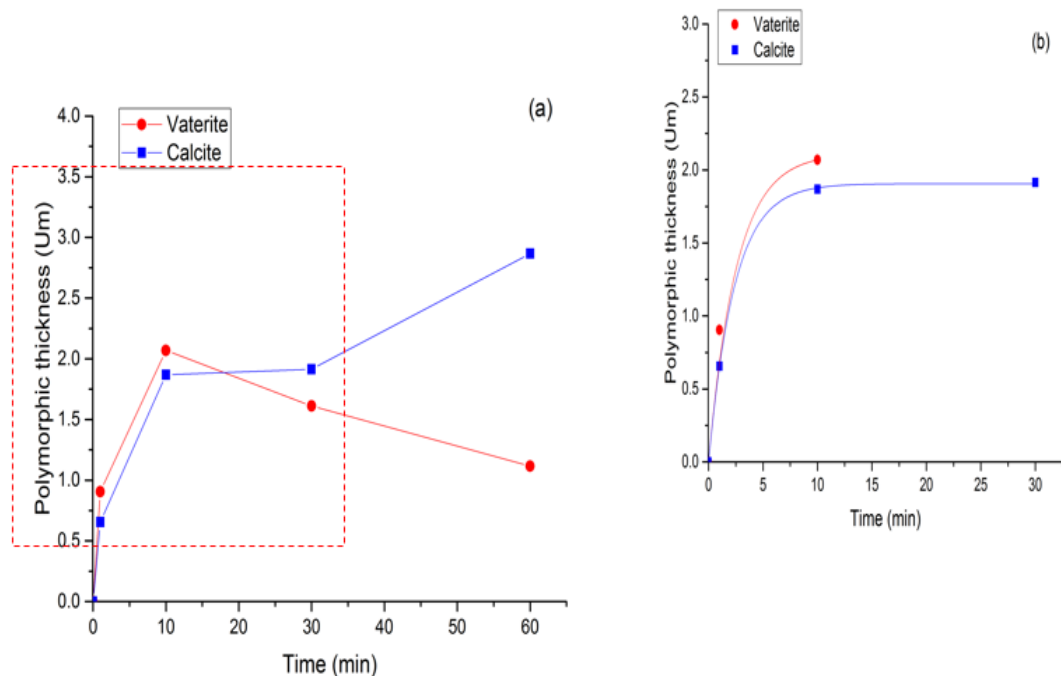


Figure B- 2 Polymorphic thickness versus time for brine 4 (0.06M) at 40° C; (a) calcite and vaterite thickness (μm), (b) curve fitting of the data

Table B- 3 The growth profile fitted function and parameters for 23% oil-brine 4 (0.06M) at 40° C

Polymorph	Exponential function, $y = A_1 - A_2 \exp(-kx)$			
	Slope, $\frac{dy}{dx} = kA_2 \exp(-kx)$			
	A ₁	A ₂	k	R ²
Vaterite	2.11229	2.11229	0.3892	0.976
Calcite	1.90656	1.90536	0.4189	0.999

Table B- 4 The polymorphic growth rate constants in the early stages of the deposition process for 23% oil-brine 4 (0.06M) at 40° C

Growth rate constant		Vaterite			Calcite	
Time (min)	µm/ min	m/ sec		µm/ min	m/ sec	
1	0.55701	9.283×10 ⁻⁹		0.52498	8.749×10 ⁻⁹	
5	0.11745	1.957×10 ⁻⁹		0.09829	1.638×10 ⁻⁹	
10	0.01678	2.797×10 ⁻¹⁰		0.01210	2.017×10 ⁻¹⁰	

Appendix B-2

Calculation of the activation energy for the transformation of vaterite to calcite by solid-state kinetics

a) Fraction of vaterite converted to calcite α is calculated according to the following:

$$\alpha = \frac{x_0 - x_t}{x_0 - x_\infty} \quad \text{B.1}$$

Where: x_0 is the initial mole fraction of vaterite which is assumed to be 1 as vaterite is the first phase to form. x_t : is of vaterite mole fraction at time t and x_∞ is vaterite mole fraction at the end of reaction which is equal zero at the end of the transformation process. Plots of α -time at 30 and 40° C in the absence and presence of oil are shown in Figure B-3 (a) and (b). The figures show a decelerator relation in which the reaction progress decreases with time.

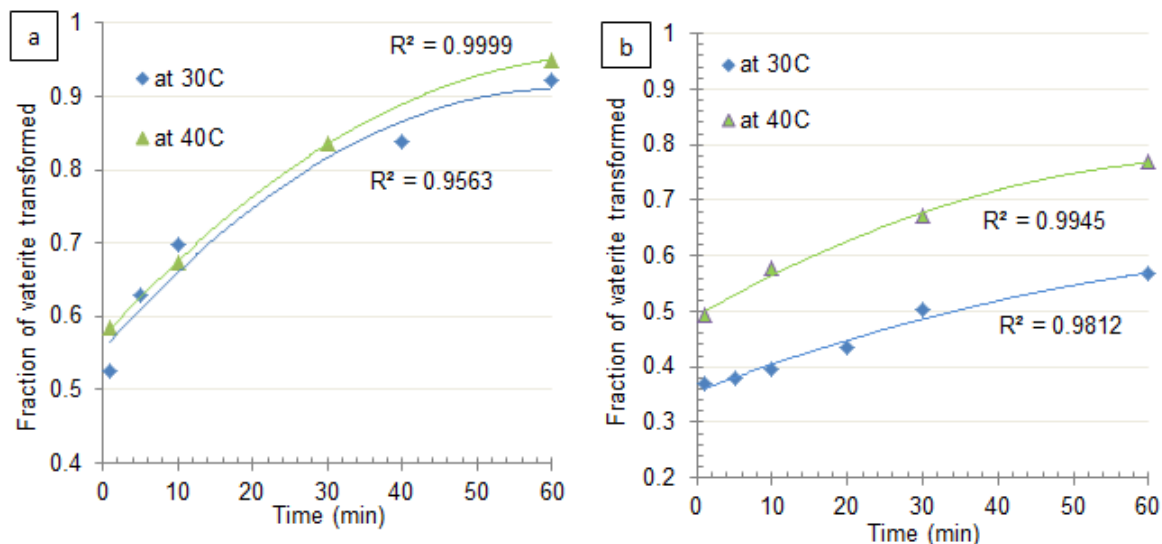


Figure B- 3 α - time plots for isothermal transformation of vaterite to calcite at 30° C and 40° C; (a) in the absence of oil, (b) In the presence of oil

b) Analysis of the data using model- fitting methods

The conversion fraction α is fitted into the different models as shown in Tables B-5 to B-8 and a relation of the form $g(\alpha) = kt$ is plotted as shown in Figures B-4 to B-7. The reaction rate constant is estimated and the activation energy is calculated using the Arrhenius for different models at 30 and 40° C in the absence and presence of oil as shown in Tables B-9 and B-10.

Table B- 5 Model fitting of the conversion fraction α into different models for brine 2 (0.065M) at 30° C

Assume model		Avarami model			Geometrical contraction		Power law			Diffusion models				Reaction order models		
Time (min)	α	A2	A3	A4	R2	R3	P2	P3	P4	D1	D2	D3	D4	F1	F2	F3
1	0.524	0.862	0.906	0.928	0.762	0.841	0.262	0.159	0.216	0.275	0.171	0.048	0.041	0.743	1.103	1.711
5	0.629	0.995	0.997	0.998	0.814	0.876	0.314	0.124	0.249	0.395	0.261	0.079	0.064	0.991	1.694	3.128
10	0.699	1.095	1.063	1.047	0.849	0.900	0.349	0.100	0.274	0.488	0.337	0.109	0.085	1.200	2.320	5.010
40	0.839	1.350	1.222	1.162	0.919	0.946	0.419	0.054	0.338	0.703	0.544	0.208	0.144	1.824	5.195	18.691
60	0.922	1.596	1.366	1.263	0.961	0.974	0.461	0.026	0.399	0.850	0.723	0.328	0.203	2.549	11.789	81.278

Table B- 6 Model fitting of the conversion fraction α into different models for brine 4 (0.06M) at 40° C

Assume model		Avarami model			Geometrical contraction		Power law			Diffusion models				Reaction order models		
min	α	A2	A3	A4	R2	R3	P2	P3	P4	D1	D2	D3	D4	F1	F2	F3
1	0.584	0.937	0.957	0.968	0.792	0.861	0.292	0.139	0.234	0.341	0.219	0.064	0.053	0.877	1.404	2.391
10	0.673	1.057	1.038	1.028	0.836	0.891	0.336	0.109	0.264	0.453	0.307	0.097	0.077	1.118	2.057	4.173
30	0.836	1.345	1.218	1.160	0.918	0.945	0.418	0.055	0.336	0.699	0.540	0.205	0.143	1.809	5.104	18.129
60	0.950	1.733	1.443	1.316	0.975	0.983	0.475	0.017	0.433	0.903	0.801	0.400	0.231	3.002	19.127	202.05

Table B- 7 Model fitting of the conversion fraction α into different models for 23% oil-brine 2 (0.065M) at 30° C

Assume model		Avarami model			Geometrical contraction		Power law			Diffusion models				Reaction order models		
Time (min)	α	A2	A3	A4	R2	R3	P2	P3	P4	D1	D2	D3	D4	F1	F2	F3
1	0.278	0.571	0.688	0.755	0.639	0.759	0.139	0.241	0.143	0.077	0.043	0.011	0.010	0.326	0.385	0.459
20	0.395	0.709	0.795	0.842	0.698	0.798	0.198	0.202	0.177	0.156	0.091	0.024	0.021	0.503	0.654	0.868
30	0.407	0.722	0.805	0.850	0.703	0.802	0.203	0.198	0.181	0.165	0.097	0.025	0.023	0.522	0.685	0.920
40	0.446	0.769	0.839	0.877	0.723	0.815	0.223	0.185	0.192	0.199	0.119	0.032	0.028	0.591	0.805	1.129
60	0.502	0.835	0.886	0.914	0.751	0.834	0.251	0.166	0.209	0.252	0.155	0.043	0.037	0.696	1.007	1.513

Table B- 8 Model fitting of the conversion fraction α into different models for 23% oil- brine 4 (0.06M) at 40° C

Assume model		Avarami model			Geometrical contraction		Power law			Diffusion models				Reaction order models		
min	α	A2	A3	A4	R2	R3	P2	P3	P4	D1	D2	D3	D4	F1	F2	F3
1	0.493	0.824	0.879	0.908	0.746	0.831	0.246	0.169	0.206	0.243	0.149	0.041	0.036	0.679	0.972	1.445
10	0.577	0.927	0.951	0.963	0.788	0.859	0.288	0.141	0.232	0.333	0.213	0.062	0.052	0.860	1.362	2.290
30	0.671	1.055	1.036	1.027	0.836	0.890	0.336	0.110	0.264	0.451	0.306	0.096	0.076	1.113	2.043	4.129
60	0.769	1.210	1.136	1.100	0.884	0.923	0.384	0.077	0.303	0.591	0.430	0.149	0.111	1.465	3.328	8.864

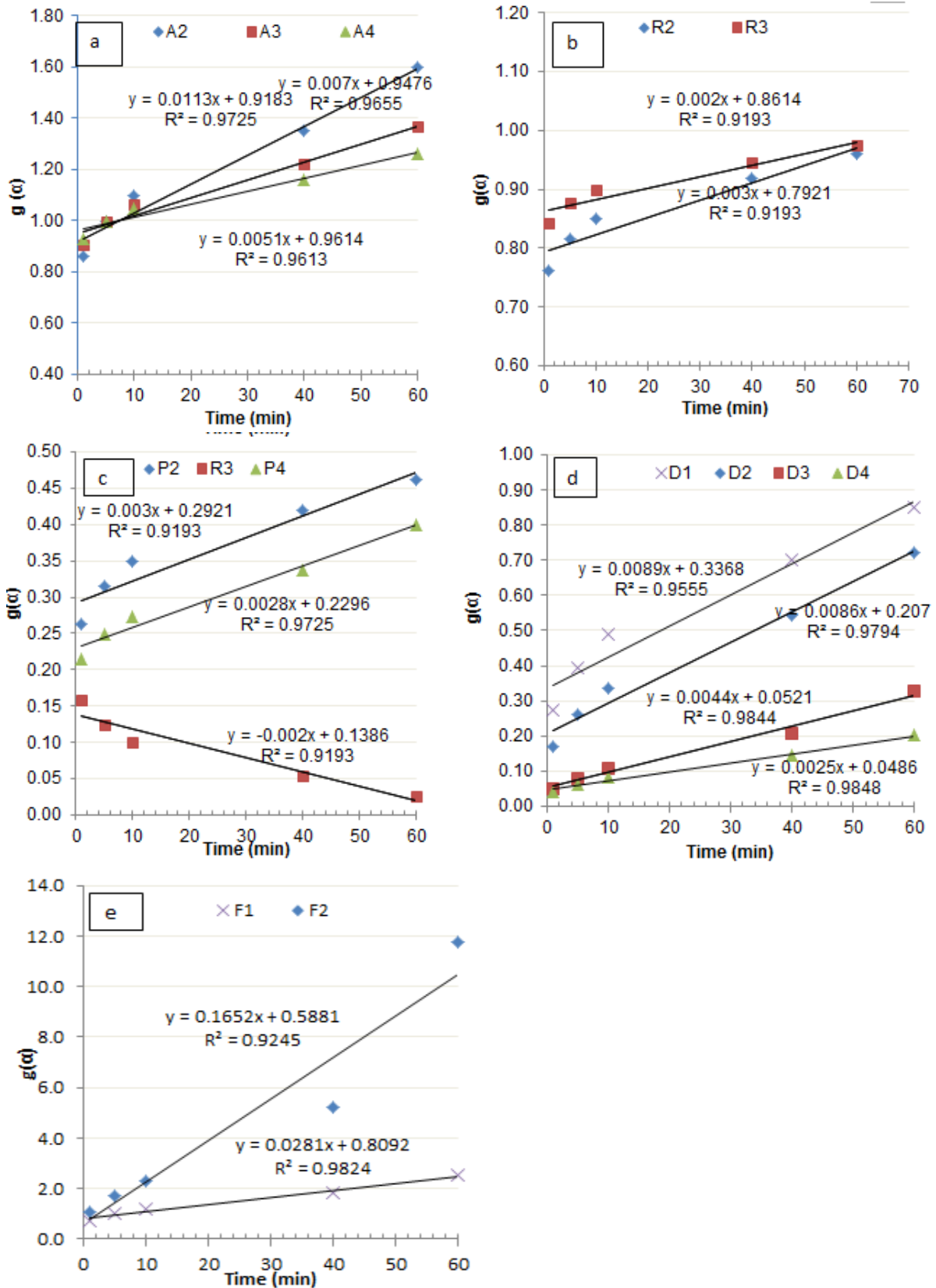


Figure B- 4 $g(\alpha)$ -time plot of different models for brine 2 (0.065M) at 30° C, a) Avrami, b) geometrical contraction, c) power law, d) diffusion, e) reaction order models

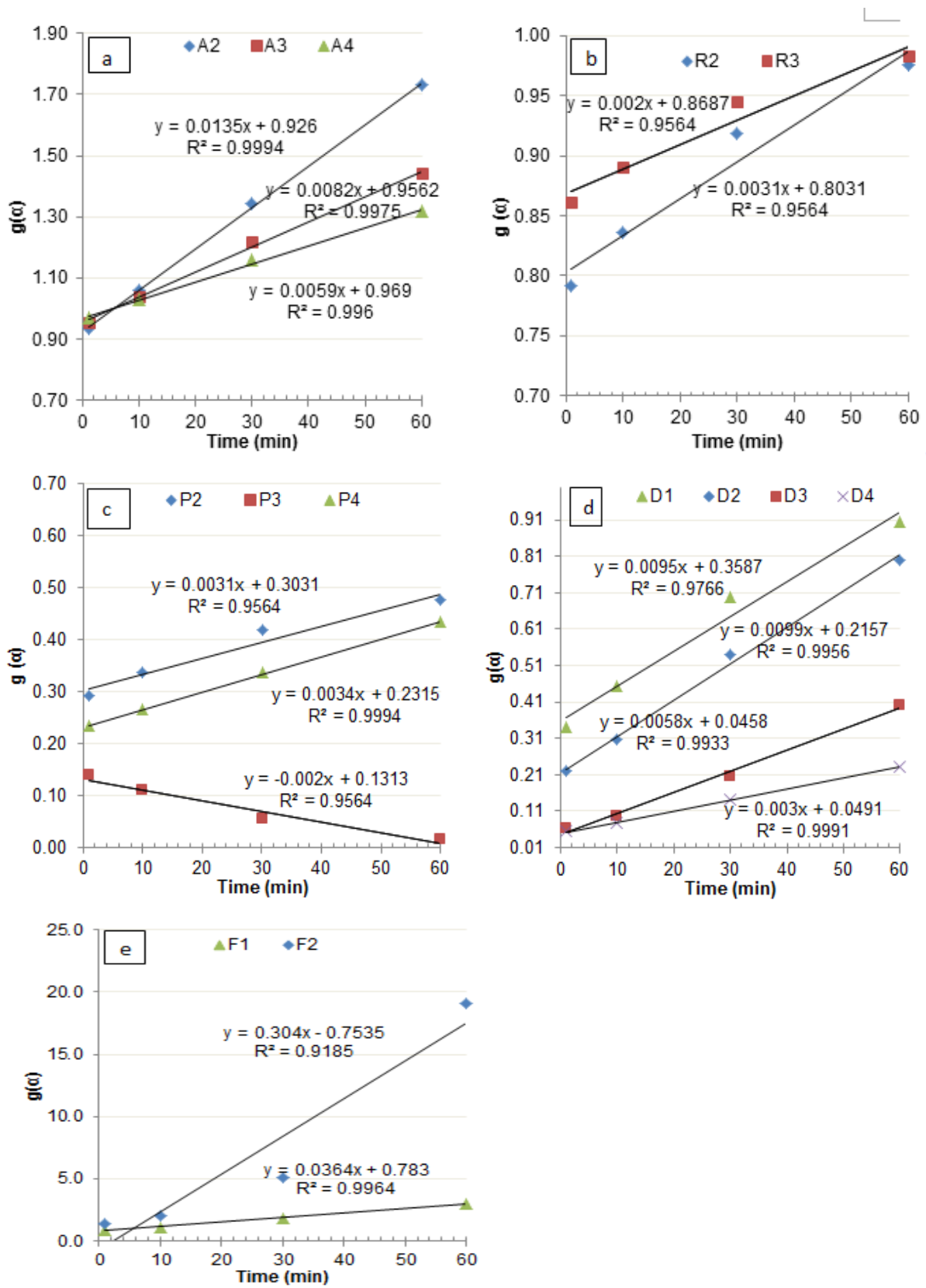


Figure B- 5 $g(\alpha)$ -time plot of different models for brine 4 (0.06M) at 40° C; a) Avarami, b) geometrical contraction, c) power law, d) diffusion, e) reaction order models

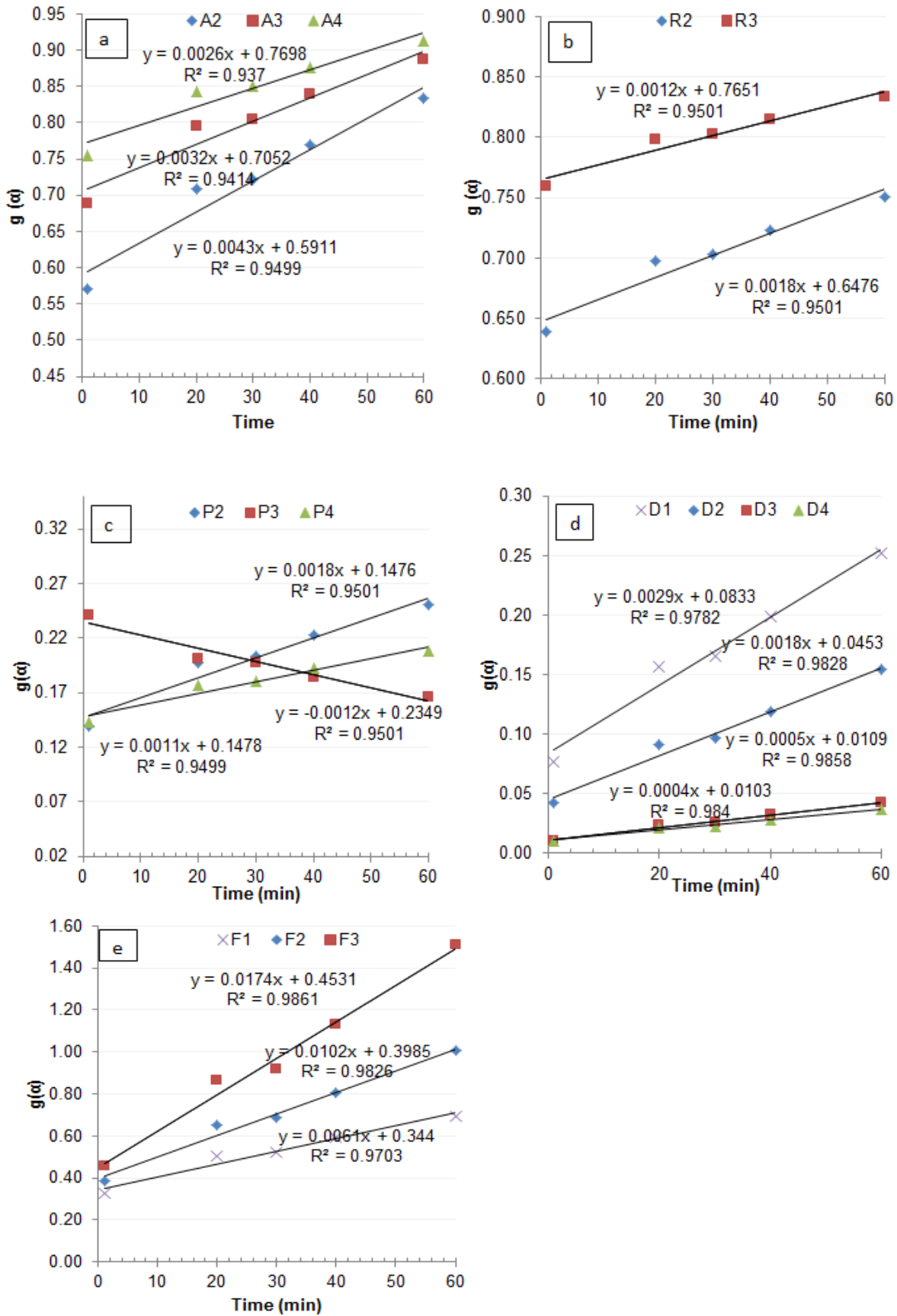


Figure B- 6 $g(\alpha)$ -time plot of different models for 23% oil-brine 2 (0.065M) at 30° C, a) Avarami, b) geometrical contraction, c) power law, d) diffusion, e) reaction order models

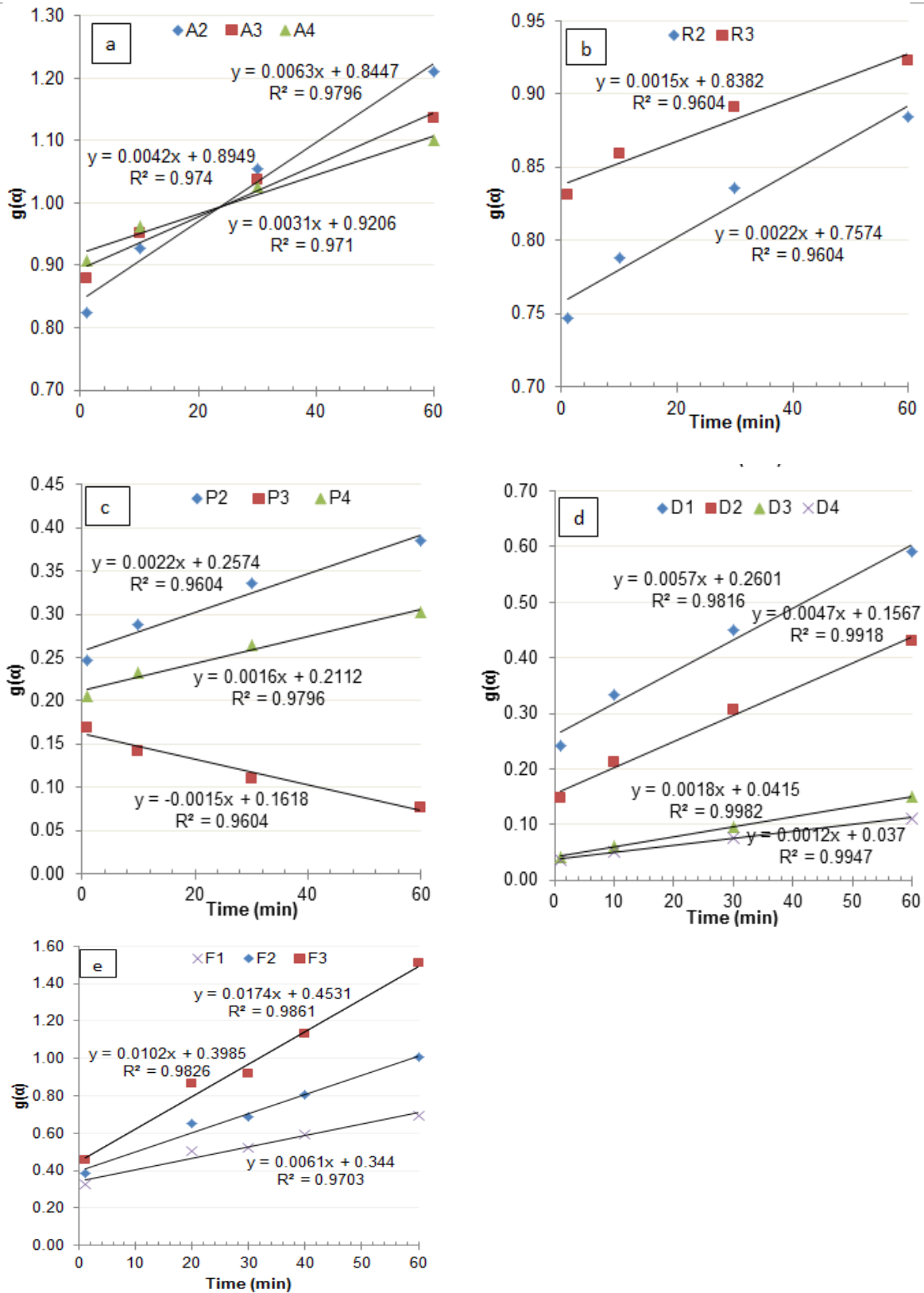


Figure B-7 $g(\alpha)$ -time plot of different models for 23% oil-brine 4 (0.06M) at 40° C, a) Avarami, b) geometrical contraction, c) power law, d) diffusion, e) reaction order models

Table B- 9 Calculation of the activation energy between 30 and 40° C in the absence of oil

Model	30° C			40° C			Activation energy	
	K ₁	R ²	Ln K ₁	K ₂	R ²	Ln K ₂	-E/R	E (KJ/mole)
A2	0.011	0.972	-4.483	0.014	0.999	-4.305	-1687.062	14.03
A3	0.007	0.965	-4.962	0.008	0.997	-4.804	-1500.581	12.47
A4	0.005	0.961	-5.278	0.006	0.996	-5.133	-1381.923	11.49
R2	0.003	0.919	-5.809	0.003	0.956	-5.776	-310.975	2.58
R3	0.002	0.919	-6.215	0.002	0.956	-6.215	0	0
P2	0.003	0.919	-5.809	0.003	0.956	-5.776	-310.975	2.58
P3	-0.002	0.919	-	-0.002	0.956	-		-
P4	0.0028	0.972	-5.878	0.003	0.999	-5.684	-1841.356	15.31
D1	0.0089	0.955	-4.722	0.010	0.976	-4.656	-618.735	5.14
D2	0.0086	0.979	-4.756	0.010	0.996	-4.615	-1335.073	11.10
D3	0.0044	0.984	-5.426	0.006	0.993	-5.150	-2619.96	21.78
D4	0.0025	0.984	-5.991	0.003	0.991	-5.809	-1729.119	14.37
F1	0.0281	0.912	-3.572	0.0036	0.996	-3.313	-2454.425	20.41
F2	0.156	0.924	-1.801	0.030	0.918	-3.493	16053.523	133.47
F3	1.1933	0.819	0.177	3.407	0.840	1.226	1676.019	13.93

Table B- 10 Calculation of the activation energy between 30 and 40° C in the presence of oil

Model	30° C			40° C			Activation energy	
	K ₁	R ²	Ln K ₁	K ₂	R ²	Ln K ₂	-E/R	E (KJ/mole)
A2	0.0043	0.949	-5.449	0.006	0.979	-5.067	-3622.23	30.11
A3	0.0032	0.941	-5.745	0.004	0.974	-5.473	-2578.99	21.44
A4	0.0026	0.937	-5.952	0.003	0.971	-5.776	-1668.13	13.87
R2	0.0018	0.950	-6.319	0.002	0.960	-6.119	-1903.14	15.82
R3	0.0012	0.950	-6.725	0.002	0.960	-6.502	-2116.27	17.59
P2	0.0018	0.950	-6.319	0.002	0.960	-6.119	-1903.14	15.82
P3	-0.0012	0.950	-	-0.002	0.960	-	-	-
P4	0.0011	0.949	-6.812	0.002	0.979	-6.437	-3553.56	29.54
D1	0.0029	0.978	-5.843	0.006	0.982	-5.167	-6408.8	53.28
D2	0.0018	0.983	-6.319	0.005	0.992	-5.360	-9102.42	75.67
D3	0.0005	0.986	-7.601	0.002	0.998	-6.320	-12148.2	101.00
D4	0.0004	0.984	-7.824	0.001	0.995	-6.725	-10419.13	86.62
F1	0.0061	0.970	-5.099	0.013	0.992	-4.343	-7176.09	59.66
F2	0.0102	0.983	-4.585	0.04	0.998	-3.231	-12840.4	106.75
F3	1.0174	0.986	-4.051	0.126	0.981	-2.074	-18753.7	155.92

Appendix C

Table C- 1 The calculations for correcting calcium ion that has reacted to form calcium carbonate for 0% oil- brine 2 (0.065M) at 30° C

Time (min)	Ca ²⁺ (mg/lit) by (ICP)	Ca ²⁺ (mmol/lit) by (ICP)	pH	SR (Multiscale)	YCa ²⁺ (Multiscale)	YCO ₃ ²⁻ (Multiscale)	IAP= SR ² *K _{SPV} (M) ²	[Ca ²⁺]=[CO ₃ ²⁻] (mmol/lit) Corrected	Reacted [Ca ²⁺] (mmol/lit)	Produced CaCO ₃ (mg/lit)
0	1349.00	33.659	7.63	115.81	-	-	-	33.659*	0.000	0
2	1258.20	31.394	7.26	48.01	0.2578	0.1864	2.56191E-05	23.0358	10.624	1062.357
5	1222.98	30.515	6.83	17.3	0.2579	0.1872	3.32654E-06	8.301	25.359	2535.861
15	980.31	24.460	6.47	5.11	0.2579	0.1872	2.9023E-07	2.400	31.259	3125.903
30	986.63	24.618	6.51	5.67	0.261	0.193	3.57327E-07	2.663	30.996	3099.598
45	897.27	22.388	6.55	5.23	0.261	0.193	3.04021E-07	2.422	31.237	3123.699
60	883.88	22.054	6.58	5.44	0.263	0.197	3.28926E-07	2.515	31.145	3114.450

Table C- 2 The calculations for correcting calcium ion that has reacted to form calcium carbonate for 23% oil- brine 2 (0.065M) at 30° C

Time (min)	Ca ²⁺ (mg/lit) by (ICP)	Ca ²⁺ (mmol/lit) by (ICP)	pH	SR (Multiscale)	YCa ²⁺ (Multiscale)	YCO ₃ ²⁻ (Multiscale)	IAP= SR ² *K _{SPV} (M) ²	[Ca ²⁺]=[CO ₃ ²⁻] (mmol/lit) Corrected	Reacted [Ca ²⁺] (mmol/lit)	Produced CaCO ₃ (mg/lit)
0	1349	33.659	7.6	115.81	-	-	-	33.659*	0.000	0
2	1242	30.979	7.45	71.445	0.2588	0.188	5.67341E-05	32.148	1.511	151.136
5	1133	28.281	7.16	31.886	0.2605	0.191	1.13006E-05	15.070	18.589	1858.879
15	886	22.107	6.87	10.603	0.265	0.199	1.24956E-06	4.868	28.792	2879.160
30	907	22.633	6.56	5.455	0.263	0.196	3.30742E-07	2.533	31.126	3112.634
45	879	21.931	6.35	3.185	0.263	0.196	1.12751E-07	1.479	32.180	3218.041
60	871.92	21.756	6.34	3.068	0.2628	0.196	1.04619E-07	1.425	32.234	3223.420

Appendix D

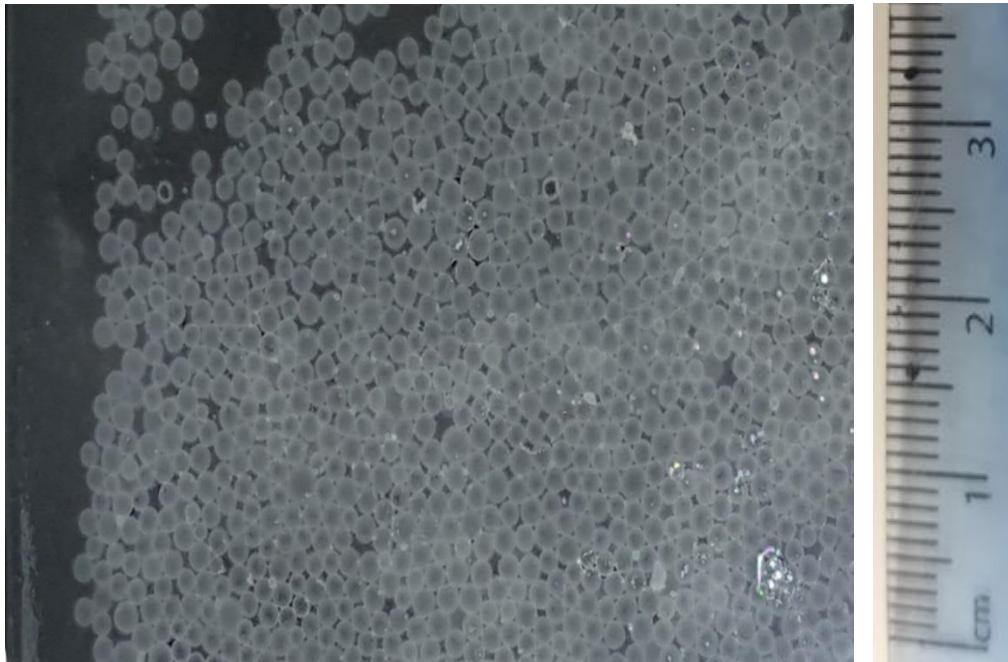


Figure D- 1 Camera image for stabilized emulsion, experiment conducted for oil-brine (0.1M), pH of 9 at 30° C

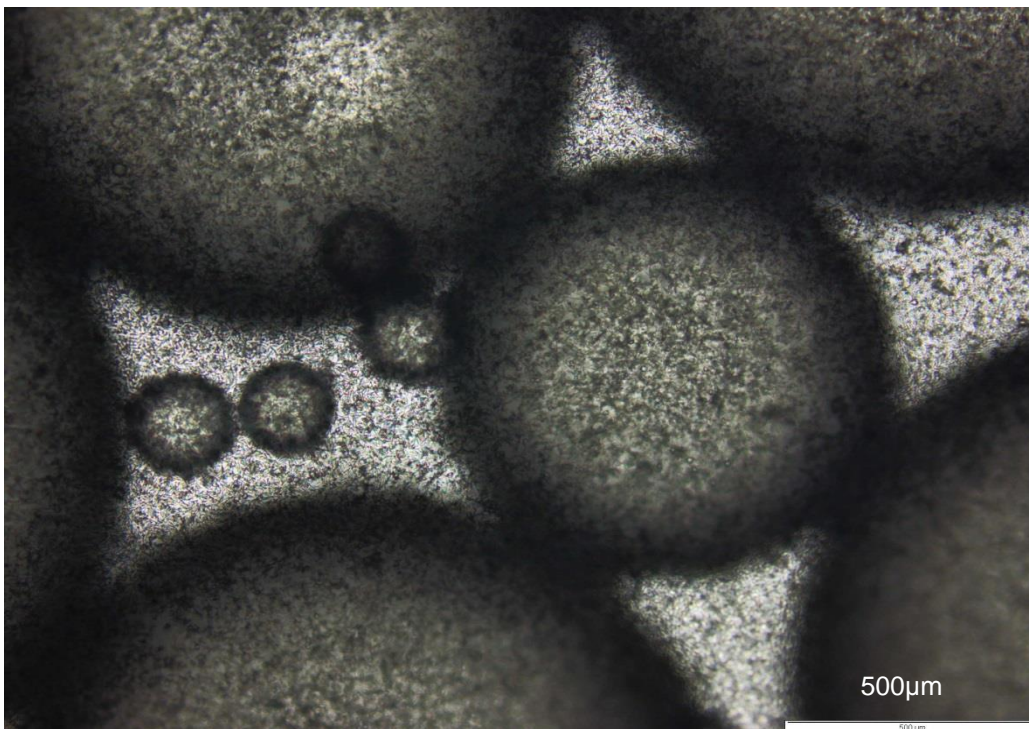


Figure D- 2 Microscopic image shows stabilized emulsion of different droplets sizes ranges from 200 µm to 1500 µm; experiment conducted for oil-brine 2 (0.065M), pH of 9 and 60° C

Appendix E

a) Evidences on the presence of amorphous CaCO_3 (ACC) in the bulk solution

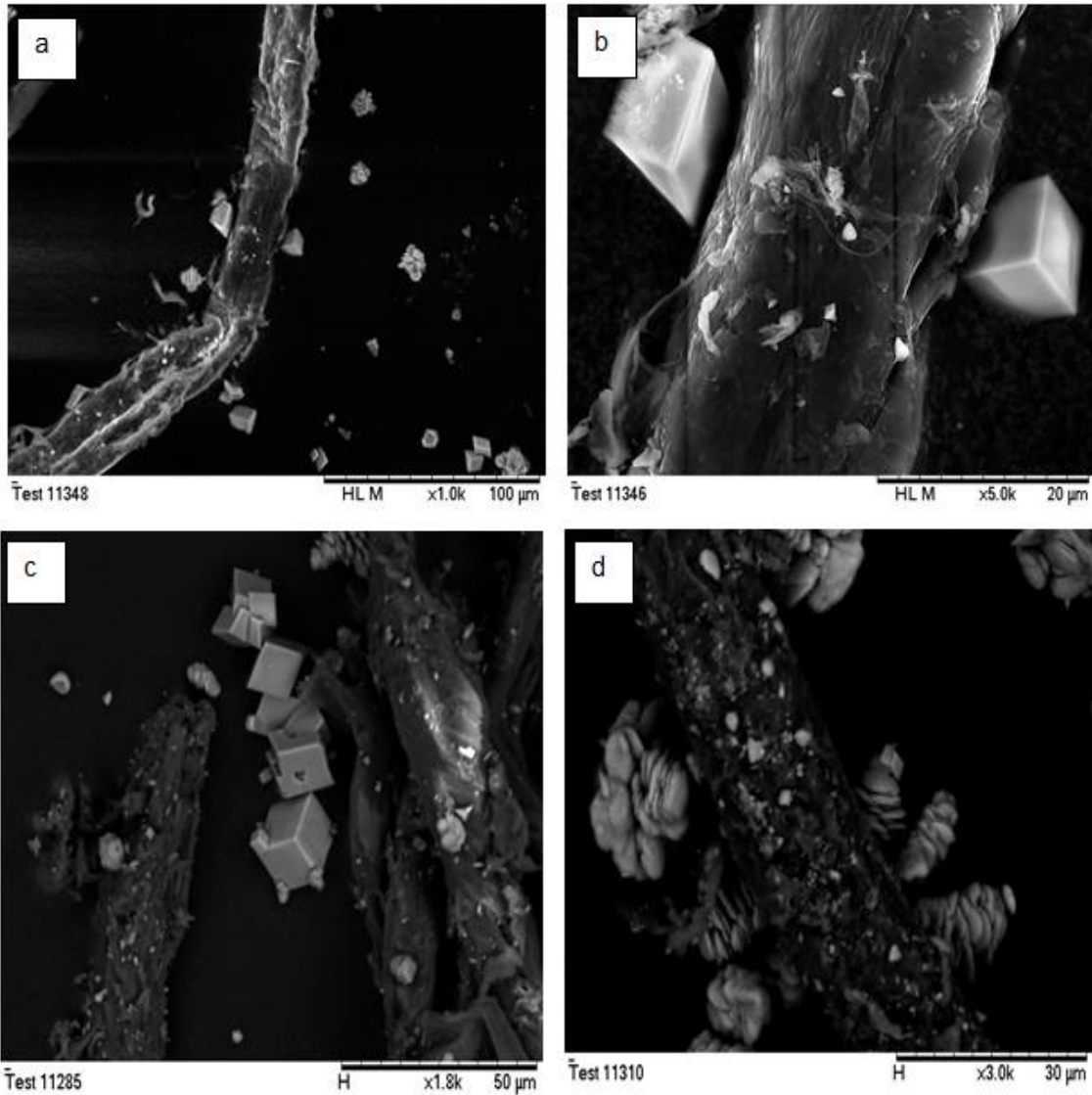


Figure E- 1 Evidence of amorphous calcium carbonate presence in the bulk solution for 23% oil-brine 3 (0.045 M) at 60° C. The experiment was conducted under high pH conditions of 9. Sample was taken at 10 minutes

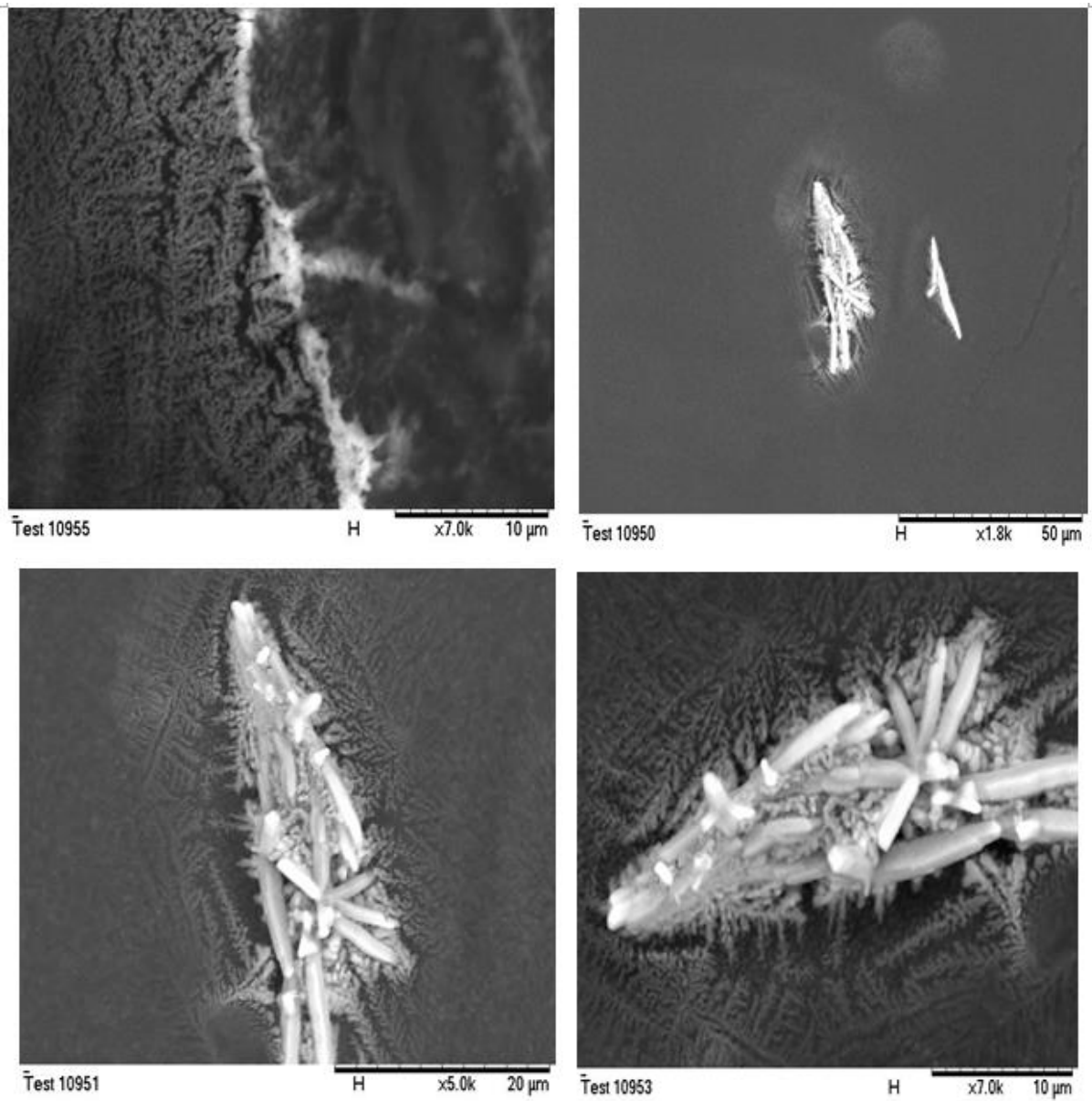


Figure E- 2 Evidence of amorphous calcium carbonate presence in the bulk solution for 23% oil-brine 3 (0.045 M) at 60° C. The experiment was conducted under high pH conditions of 9. Sample was taken at 10 minutes

b) Evidences on the presence of amorphous calcium carbonate ACC on the surface

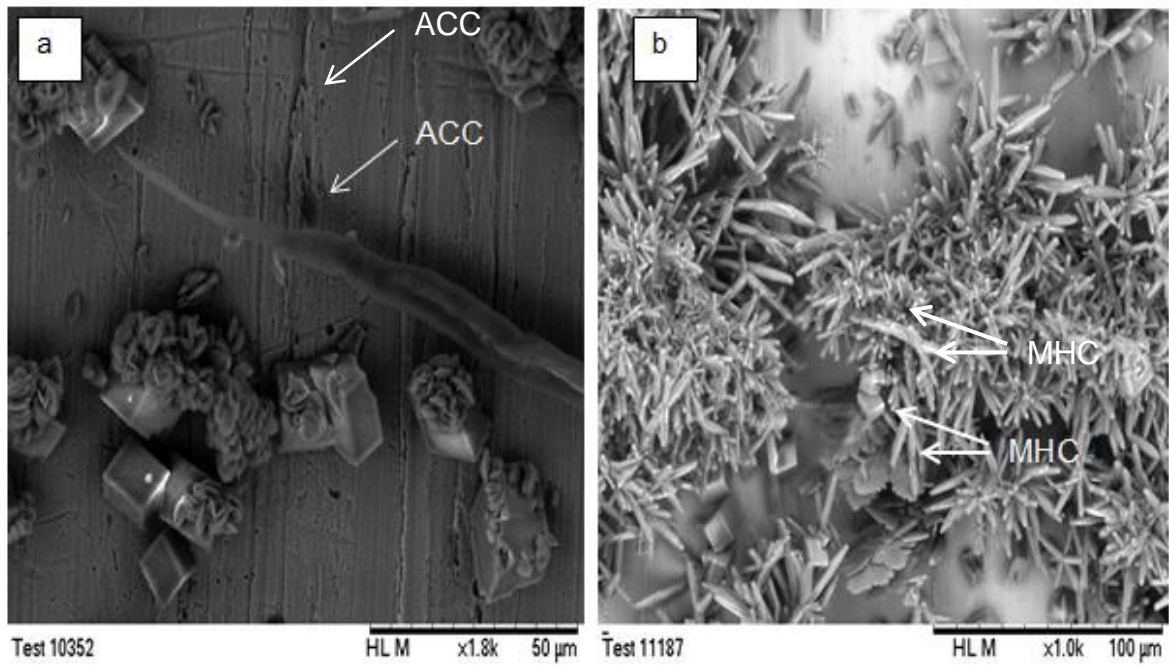


Figure E- 3 ACC presence on the surface, a) b1 23% brine 1 (0.1 M) at 30° C, sample at 30 minutes; b) 23% oil brine 3 (0.045 M) at 60° C, Monohydrocalcite presence, sample at 45 minute